
Space and Ground Based Studies of Transpolar Arcs

Thesis submitted for the degree of
Doctor of Philosophy
at the University of Leicester

Atousa Goudarzi

Radio and Space Plasma Group
Department of Physics and Astronomy
University of Leicester

June 2009

به نام خالق یکتا

دل گرچه در این بادیه بسیار شناخت
یک موی ندانست ولی موی شکافت
اندر دل من هزار خورشید بتافت
آخر به کمال ذره‌ای راه نیافت

(حکیم ابوعلی سینا)

To My great homeland

When I die, give my hair to the old woman in Hiroshima; may it dance in the ocean breeze forever.

When I die, give my nose to the shepherd of a Nomadic tribe in Somalia; may it smell the sharp scent of camel milk forever.

When I die, give my mouth to the little Buddhist in Narita; may the sweet hymn of inner peace be sung forever.

When I die, give my hands to the Sikh women in Amritsar; may they bake fresh bread for pilgrim old men forever.

When I die, give my heart to all men and women who have never been in love; may the fragile feeling of falling in love for the first time stay there forever.

When I die, give my legs to all men and women in border cities of Iran and Iraq who stepped on mines while picking wild poppies; may they run in mine free lands forever.

When I die, place my eyes on top of the Damavand Mountains; may they gaze at my great homeland forever.

Contents

Abstract	
Declarations	
Acknowledgments	
Chapter 1 Solar-terrestrial phenomena.....	1
1.1 Introduction	1
1.2 The Sun.....	2
1.3 The solar wind and interplanetary magnetic field.....	4
1.4 The Earth's magnetosphere.....	7
1.4.1 Magnetospheric current systems.....	8
1.4.1.1 The magnetopause current.....	8
1.4.1.2 The ring current.....	8
1.4.1.3 The cross tail current.....	9
1.4.1.4 The field-aligned current.....	9
1.4.2 Magnetospheric plasma population.....	10
1.5 The Earth's atmosphere.....	10
1.5.1 The structure of the ionosphere.....	12
1.6 The aurora.....	13
1.7 Summary.....	14
Chapter 2 Magnetosphere-Ionosphere coupling and the transpolar arc.....	15
2.1 IMF control of reconnection location.....	16
2.1.1 Reconnection under the southward IMF and B_y -associated Asymmetry.....	17
2.1.2 Reconnection under the northward IMF condition.....	19
2.2 IMF northward related phenomena.....	20
2.2.1 Lobe reconnection.....	20
2.2.2 Dual lobe reconnection.....	21
2.2.3 Substorm in the magnetosphere.....	23
2.2.4 Tail reconnection during IMF northward non-substorm intervals.....	25
2.2.5 The transpolar arc.....	26

2.2.5.1	Formation and dynamics of the transpolar arcs.....	30
2.2.5.2	Particle precipitations associated with transpolar arcs.....	31
2.3	Field-aligned currents.....	32
2.4	Summary.....	35
Chapter 3 Instrumentation and experimental techniques.....		36
3.1	The Super Dual Auroral Radar Network.....	36
3.1.1	The SuperDARN radars.....	37
3.1.2	Nature of coherent backscatter.....	37
3.1.3	The map potential model.....	40
3.2	ACE spacecraft.....	42
3.3	DMSP auroral particle instruments.....	43
3.4	Imaging ultraviolet aurora.....	44
3.5	The Iridium satellite constellation.....	45
3.5.1	FACs from the Iridium satellite constellation.....	46
3.6	NOAA satellites.....	48
3.7	Summary.....	48
Chapter 4 Multi-instrument observations of a transpolar arc in the Northern Hemisphere.....		49
4.1	Introduction.....	49
4.2	Event overview.....	51
4.2.1	Interplanetary magnetic field data	51
4.2.2	IMAGE FUV data.....	52
4.3	Ground-based SuperDARN convection.....	54
4.4	Particle precipitation overview.....	56
4.5	Field Aligned Current (FAC) observations.....	58
4.5.1	Data and observation.....	59
4.5.1.1	Comparison of auroral images and field-aligned currents....	61
4.5.1.2	Comparison of averaged auroral images and field-aligned currents.....	62
4.5.1.3	Comparison of averaged ionospheric flows with FACs measured from two different sources.....	64
4.6	Discussion.....	65

4.6.1	Variation of the polar cap flux content.....	66
4.6.2	Formation and motion of the transpolar arc.....	68
4.6.3	Evidence of field-aligned currents in polar cap arcs.....	70
4.7	Summary.....	74
Chapter 5 Five further transpolar arc studies.....		77
5.1	Introduction.....	77
5.2	Event selection.....	78
5.2.1	TPA1: 25th November 2001.....	79
5.2.2	TPA2: 2nd March 2002.....	83
5.2.3	TPA3: 4th March 2002.....	85
5.2.4	TPA4: 11th March 2002.....	87
5.2.5	TPA5: 12th March 2002.....	90
5.3	Discussion.....	92
5.3.1	IMF effects.....	92
5.3.2	Effects of ionospheric flows on the dynamics of TPAs.....	93
5.3.3	Observation of TRINNIs associated with TPA.....	96
5.3.4	Particle precipitation overview.....	97
5.4	Summary.....	99
Chapter 6 Summary and future work.....		102
6.1	Motivation.....	102
6.2	Summary of results.....	103
6.3	Future directions.....	105
6.3.1	IMF Bx effects of TPAs.....	105
6.3.2	Detailed study of vortical flows at the nightside.....	106
6.3.3	Statistical study of TRINNIs associated with TPAs.....	107
Bibliography.....		108

Abstract

Space and Ground Based Studies of Transpolar Arcs

Atousa Goudarzi

This thesis presents a study of the formation and dynamics of 6 transpolar arcs. This work was undertaken primarily using auroral emission data from the Imager Magnetopause-to-Aurora Global Exploration (IMAGE) spacecraft along with the ionospheric convection flow patterns from the Super Dual Auroral Radar Network HF radars located in the auroral regions of both hemispheres. Particle precipitation data from Defence Meteorological Satellite Program (DMSP) and National Oceanic and Atmosphere Administration (NOAA) satellites were also used, together with Field Aligned Current data from the Iridium satellite constellation. A detailed study is first presented concerning the nature of the ionospheric convection flows on the nightside during an isolated transpolar arc. The results of this study demonstrated: a) the occurrence of cross midnight azimuthal flows, which are thought to be associated with the formation of the transpolar arc; and b) that ionospheric flows caused by dayside reconnection were responsible for the motion of the transpolar arcs. Five further case studies of transpolar arcs, which exist during intervals of northward but different IMF B_y components, are also discussed. The flows during a number of transpolar arc events have been studied, which confirm that the excitation of flow appears to accompany transpolar arc dynamics in general. Also, a detailed study of particle precipitation data suggests that the particles associated with the transpolar arcs are located on closed field lines. Evidence presented in this thesis suggests that the transpolar arcs mentioned above lie on closed field lines. Finally, a discussion of possible future work is given, suggested by the results of the studies described above.

Declarations

The research detailed in chapter 4 of this thesis has led to the publication of the following scientific paper in a refereed journal:

Goudarzi, A., M. Lester, S. E. Milan, and H. U. Frey, Multi-instrumentation observations of a transpolar arc in the northern hemisphere, *Annales Geophysicae*, **26**, 201-210,2008.

Acknowledgements

For their help in developing and completing this thesis, my heartfelt gratitude goes to:

Professor Stan Cowley, for allowing me to study in the Radio and Space Plasma group, and especially for his help and support during the final year of my PhD.

I would like to acknowledge the graduate research funding from the Dorothy Hodgkin Postgraduate Awards (DHPA) scheme of the Research Councils UK, which gave me a wonderful opportunity to study at one of the top universities in the UK.

Much appreciation goes to Professor Mark Lester, who always treated me as a colleague rather than a supervisee; taking such an attitude towards me greatly helped me to build my professional confidence. I would especially like to thank Mark for teaching me so many things besides science, such as how to maintain my enthusiasm even when the outcome of the STFC meetings was rather disheartening.

Further appreciation goes to Dr. Steve Milan, whose love and passion for science showed me how one can do what they love and get paid for it.

I would like to express my gratitude to those listed below who provided us with data central to this research; The PIs of the SuperDARN radars, Mike Ruohoniemi for provision of the “map-potential” software, Norman Ness (ACE/MAG), David McComas (ACE/SWEPAM), Harald Frey (IMAGE/FUV), Brian Anderson and Colin Waters (Iridium/FAC), Kjellmar oksavik (NOAA), and Pat Newell (DMSP).

My deepest thanks go to my beloved parents for their unconditional love and support; living so far away from them has been the most difficult thing I have ever done. I would also like to thank my dearest brother Omid who introduced me to Persian Rap!!!

Tennessee Williams once said: ‘Life is partly what we make it, and partly what it is made by the friends we choose’. Hence, I believe now is the time to thank those who made part of my life. Friends from 33° 52' S, 151° 13' E down in the Southern Hemisphere to 49° 11' N, 123° 10' W up in the Northern Hemisphere, who would occasionally forget the time difference, call me up at 0300 Magnetic Local Time and ask for a certain recipe, or whether I had any plans for the summer (you know who are!); friends at RSPP who literally made working in this group an unforgettable experience (in the most positive way, of course!); and friends who accompanied me on my mad adventures, which included, jumping out of an airplane at 10,000 ft, travelling to India with no solid plans and ending up taking a taxi for a 12 hour journey!; finally, a big fat thank you to you all who have made the years of my PhD life a delightful experience and one which I will always look back on with much pride.

Chapter 1

Solar-Terrestrial Phenomena

1.1 Introduction

The interaction between the solar wind and the Earth's magnetosphere results in a highly dynamic terrestrial space environment, which affects many aspects of the near-Earth environment, for example, the ionosphere that is crucial for the transmission of HF radio waves. The high-latitude electrodynamics of the Earth are studied by the analysis of two separate regions of interaction, the solar wind-magnetosphere and the magnetosphere-ionosphere interfaces. The solar wind carries a weak magnetic field amounting to a few nanoteslas, while streaming through interplanetary space at supersonic velocities. The magnetic field is said to be “frozen in” to the plasma as the electrical conductivity is very large, and the plasma controls the motion of the total magnetoplasma because it has the greater energy density. As the solar wind approaches the Earth, it interacts with the Earth's magnetic field and carves out the geomagnetic cavity. This cavity, referred to as the magnetosphere, is three-dimensional with a blunt nose region on the dayside and an extended tail on the night side. The frozen-in-flow approximation suggests that there should be little other interaction between the solar wind and the magnetosphere. However, coupling does take place, and the effects of this interaction on the upper atmosphere of the Earth are the subject of this thesis.

The main coupling process between the solar wind, and the magnetosphere is magnetic reconnection which is a fundamental process in magnetized plasmas, whereby magnetic field lines are broken and topologically reconnected. Introduced by *Dungey* (1961), the concept of magnetic reconnection at the dayside magnetopause has been accepted as the most important process conditioning the interaction between the solar wind and the Earth's

magnetosphere. In the magnetosphere, the solar wind sweeps back the newly opened Earth's magnetic field to form a tail. Occasionally, the field in the tail can reconnect in an explosive manner, producing a geomagnetic substorm. This interaction also results in energetic particles from the solar wind and the geomagnetic tail penetrating into the Earth's atmosphere which, in colliding with the atmospheric constituents results in the production of a magnificent phenomenon called the Aurora.

It is the aim of this thesis to investigate this interaction by looking at the patterns of ionospheric flow excited by the solar wind-magnetosphere coupling, in either one hemisphere or sometimes in both hemispheres simultaneously, in conjunction with observations of the aurora.

1.2 The Sun

Our Sun, a star approximately 1.4 million km in diameter, is a prodigious source of energy. The Sun is made up of various regions. Figure 1.1 is a schematic of the Sun's interior and atmosphere. According to theoretical models, there is a strong fusion reactor in the core of the Sun, which results in the temperature at the core being of order 1.5×10^7 K. The temperature decreases with the radius rapidly and the energy transfer continues through convection, creating a turbulent convection zone. There is a region between the core and the convection zone where the radiation undergoes many reflections, known as the radiation zone.

The Sun's atmosphere is made of three different layers, the photosphere, chromosphere, and corona. The photosphere is a thin layer (approximately 500 km thick) with a density of 10^{23} m^{-3} . Right above the photosphere exists a more transparent layer called the chromosphere with density of 10^{17} m^{-3} . The corona, with a density of 10^{15} m^{-3} is the outermost layer of the sun. The corona is hotter than some of the inner layers. Its average temperature is 1 million K but in some places it can reach 3 million K.

By observing the sun at different wavelengths, pictures of the atmosphere at different altitudes can be obtained. In white-light images darker regions on the

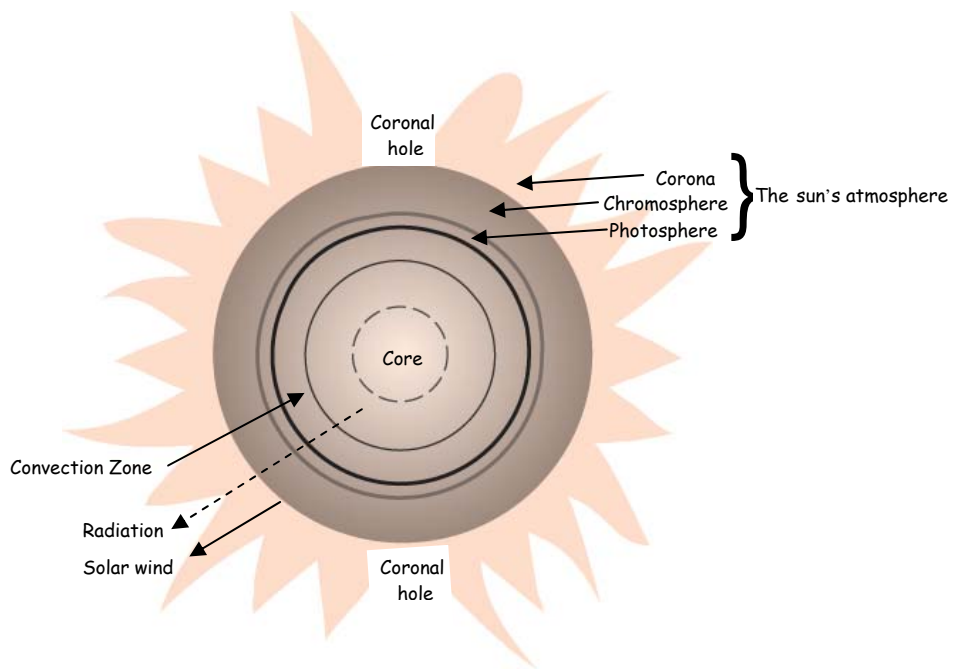


Figure 1.1 Schematic of the Sun's structure

Chapter 1: Solar-Terrestrial Phenomena

surface of the Sun, known as sunspots, are observed and these have stronger magnetic fields and different patterns of motion from their surroundings. Sunspots are a good diagnostic as they provide us with information about the overall activity state of the Sun.

The first serious study of sunspots was reported in 1610 when the first telescopes were designed to be used for astronomical purposes. *Heinrich Schwabe*, a German amateur astronomer, discovered in 1850 that the number of sunspots rose and fell in an irregular cycle of about 11 years; Fig. 1.2 illustrates the sunspot cycle since A.D. 1610. The Maunder minimum, when there were few sunspots for an extended time, corresponded to a very cold period in the Earth's climate.

There are a number of time scales associated with the magnetic activity of the Sun. It rotates approximately every 27 days, so persistent active features on the surface are presented to the Earth with this periodicity. The overall level of solar activity changes with the 11-year solar cycle, and the Sun reverses its magnetic polarity after every solar cycle to give a 22-year cycle. During solar minimum the number of sunspots is a minimum and the heliospheric current sheet lies close to the ecliptic plane. At solar maximum the number of sunspots increases and the heliospheric current sheet can form above or below the ecliptic.

A link between the Sun's magnetic field and a particular feature of the corona was discovered by the Skylab missions of May 1973 to February 1974. There are areas which emit less light at all wavelengths than other regions, but they are most marked at X-ray wavelengths. Such areas have been named coronal holes. Coronal holes are often the source of solar particles streaming into space. Although they are usually located near the poles of the Sun, especially at solar minimum, coronal holes can extend to low latitudes such that the fast streams can impinge on the Earth.

Violent discharges of hot, electrically charged gas (plasma) from the Sun's corona occur and these are known as Coronal Mass Ejections (CMEs). CMEs hurl up to 11 billion tons of plasma into space. We observe about one CME a week at solar minimum and an average of 2 to 3 per day near solar maximum, but only those ejected toward Earth are potentially dangerous. They travel the ~150 million

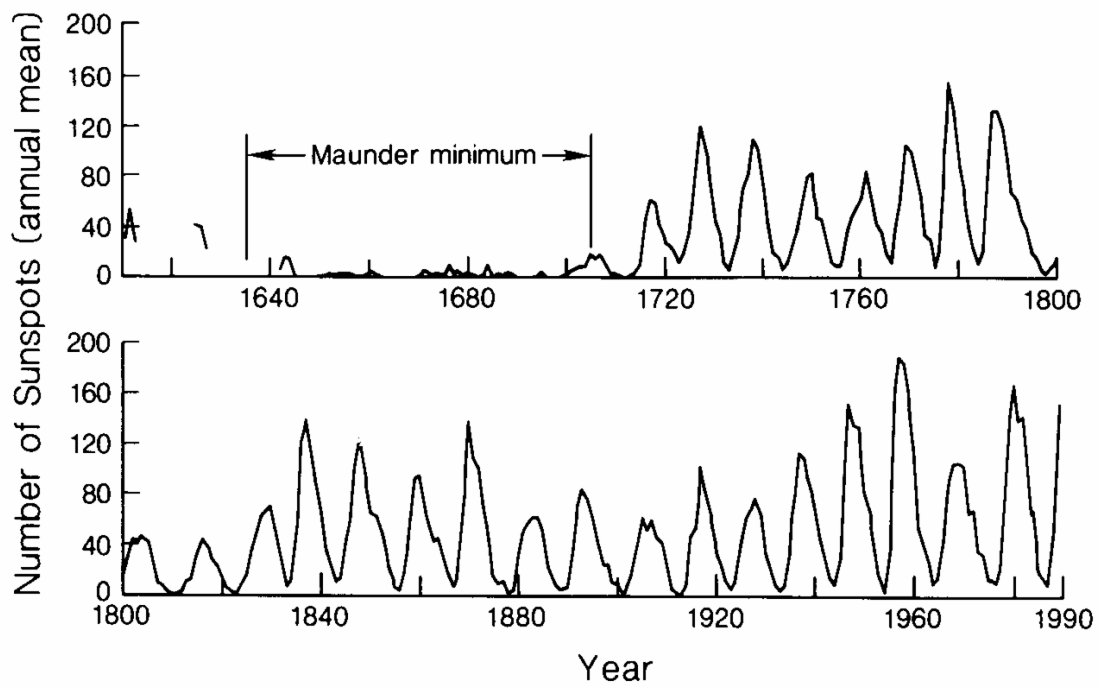


Figure 1.2 Sunspot cycle since A.D. 1610 (*Kivelson and Russell, 1995*).

kilometers between the Sun and the Earth in 2.5 to 5 days and the consequences of their interaction with the Earth's magnetosphere can lead to damage satellites, disrupt communications networks and cause power outages. CMEs are five times more likely to occur during solar maximum than solar minimum.

1.3 The solar wind and interplanetary magnetic field

In addition to coronal mass ejections, there is also a continuous outflow of plasma called the solar wind. *Ludwig Biermann* proposed the existence of a low-density, high speed solar wind in 1951 (*Biermann, 1951*). *Eugene Parker* followed this suggestion by analyzing the structure of the solar corona (*Parker, 1958*). Describing mathematically the structure of the corona, Parker claimed that the atmosphere around the sun should not be static, and the material in the corona must flow out into interplanetary space. The temperature of the gas in the solar wind is quite high, over 10^6 K, which explains the fact that the gas is fully ionized. The solar wind is primarily composed of electrons and protons, along with a small fraction of helium nuclei and an even smaller percentage of heavier nuclei. The solar wind has a very low density; for instance the number density of protons in the solar wind is about $7 \times 10^6 \text{ m}^{-3}$ in the vicinity of the Earth. The solar wind plasma streams past the Earth travelling at super-Alfvénic speeds between 200 and 800 km s^{-1} . The solar wind plasma carries the Sun's magnetic field into the interplanetary medium due to the so called "frozen-in" condition. The Sun's magnetic field in the interplanetary medium is called the interplanetary magnetic field (IMF).

We must also consider that the Sun is rotating. Its rotating winds up the magnetic field into a large spiral. The magnetic field is primary directed outward from the sun in one of its hemispheres, and inward in the other. This causes opposite magnetic field directions in the Parker spiral above and below the "heliospheric current sheet". Figure 1.3 illustrates the Sun's magnetic field lines, which are wound into an Archimedean spiral. Since this dividing line between the outward and inward field direction is not exactly on the solar equator, the rotation of the Sun causes the current sheet to become "wavy", and this waviness is carried

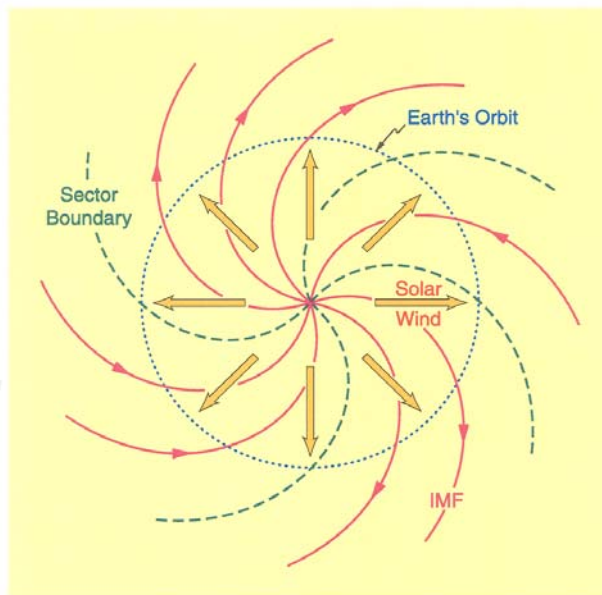


Figure 1.3 Simplified model for the spiral interplanetary magnetic field lines which remain attached to the sun but frozen into a radial solar wind expansion at 400 km s^{-1} . (Image credit: *Baumjohann/Treumann/Mayr-Ihbe*)

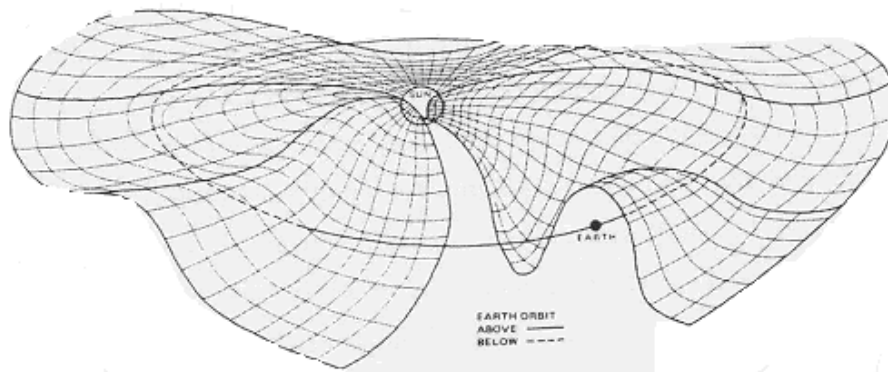


Figure 1.4 The “ballerina skirt” effect which is produced by the effect of the tilt of the solar magnetic axis with respect to the rotation axis (from *Kivelson and Russell 1995*).

out into interplanetary space by the solar wind. The wavy current sheet (sometimes likened to a ballerina skirt) of the Sun is shown in Figure 1.4.

As has been mentioned above the solar wind is formed of very high conducting plasma, which is frozen to magnetic field lines of the IMF. Below there is a simplified version of the proof of this theorem. Faraday's Law becomes as follows,

$$\nabla \times \mathbf{E} = - \frac{\partial \mathbf{B}}{\partial t} \quad (1.1)$$

where \mathbf{B} is the magnetic field strength, \mathbf{E} is the electric field strength. In addition we consider the Ohm's law,

$$\mathbf{J} = \sigma (\mathbf{E} + \mathbf{V} \times \mathbf{B}) \quad (1.2)$$

where σ is the conductivity of the plasma, \mathbf{V} the plasma velocity, and \mathbf{J} is the current density. Combination of equations 1.1 and 1.2 leads us to the frozen in flow equation:

$$\frac{\partial \mathbf{B}}{\partial t} = \nabla \times \left[\mathbf{V} \times \mathbf{B} - \frac{\mathbf{j}}{\sigma} \right] \quad (1.3)$$

Using standard vector identity ($\nabla^2 \mathbf{A} = \nabla (\nabla \cdot \mathbf{A}) - \nabla \times \nabla \times \mathbf{A}$), along with Ampère's law ($\nabla \times \mathbf{B} = \mu_0 \mathbf{j}$), and Monopoles law ($\nabla \cdot \mathbf{B} = 0$), we have,

$$\begin{aligned} \frac{\partial \mathbf{B}}{\partial t} &= \nabla \times \left[\mathbf{V} \times \mathbf{B} - \frac{\nabla \times \mathbf{B}}{\sigma \mu} \right] \\ \frac{\partial \mathbf{B}}{\partial t} &= \nabla \times \mathbf{V} \times \mathbf{B} - \frac{\nabla \times \nabla \times \mathbf{B}}{\sigma \mu} \end{aligned}$$

using the vector identity, we have,

$$\frac{\partial \mathbf{B}}{\partial t} = \nabla \times \mathbf{V} \times \mathbf{B} - \frac{\nabla^2 \mathbf{B}}{\sigma \mu} + \frac{\nabla (\nabla \cdot \mathbf{B})}{\sigma \mu}$$

where the last term must be zero, from $\nabla \cdot \mathbf{B} = 0$, so

$$\frac{\partial \mathbf{B}}{\partial t} = \nabla \times (\mathbf{V} \times \mathbf{B}) + \eta \nabla^2 \mathbf{B} \quad (1.4)$$

where $\eta = \frac{1}{\mu_0 \sigma}$ is the magnetic diffusivity. The magnetic Reynold's number is

defined as the ratio of the first to the second term of the right-hand side of equation 1.4, with L as the characteristic length over which the fields change,

$$R_m \equiv \mu_0 \sigma uL$$

where u is the average velocity perpendicular to the magnetic field. The magnetic Reynolds number gives an indication of the extent to which Alfvén's theorem is valid in a plasma; a large value of R_m indicates that the field and the plasma are frozen, while a small value is indicative of a diffusion dominated plasma (*Baumjohann and Treuman, 1997*).

The change of magnetic flux Φ across a closed boundary is given by:

$$\frac{d\Phi}{dt} = \iint \frac{\partial \mathbf{B}}{\partial t} \cdot d\mathbf{a} + \int \mathbf{B} \cdot (\mathbf{v} \times d\mathbf{l}) \quad (1.5)$$

where the first term on the right describes the change in the magnetic flux due to time variation of the magnetic field, and the second term on the right describes the change in the magnetic flux due to motion of the boundary. Equation 1.5 reduces to:

$$\frac{d\Phi}{dt} = \iint \left[\frac{\partial \mathbf{B}}{\partial t} - \nabla \times (\mathbf{v} \times \mathbf{B}) \right] \cdot d\mathbf{a} \quad (1.6)$$

but when the conductivity is extremely high the integrand tends to zero. Therefore, the magnetic flux through any closed loop moving with the highly conducting plasma is constant in time, i.e. the magnetic field lines are “frozen” into the plasma. In terms of the plasma and fields, Equation 1.4 reduces to the familiar frozen-in approximation:

$$\mathbf{E} = -\mathbf{v} \times \mathbf{B}$$

When Alfvén's theorem breaks down, magnetic reconnection occurs between oppositely directed field lines. However, mass conservation requires that there must be an outflow as long as there is a plasma inflow and a second dimension is introduced that sets a limit to the extension of the diffusion region. This simplified two-dimensional picture results in the so-called x-line reconnection configuration of *Sweet (1958)* and *Parker (1957)*, which is illustrated in Figure 1.5. The magnetic field approaches zero only along a single line, called the neutral line, and not in an entire plane. The plasma outflow is driven by the same external electric field that drives the inflow and magnetic flux is carried away from the diffusion region rather than being annihilated. Two elements of plasma initially on the same magnetic flux tube flowing toward the

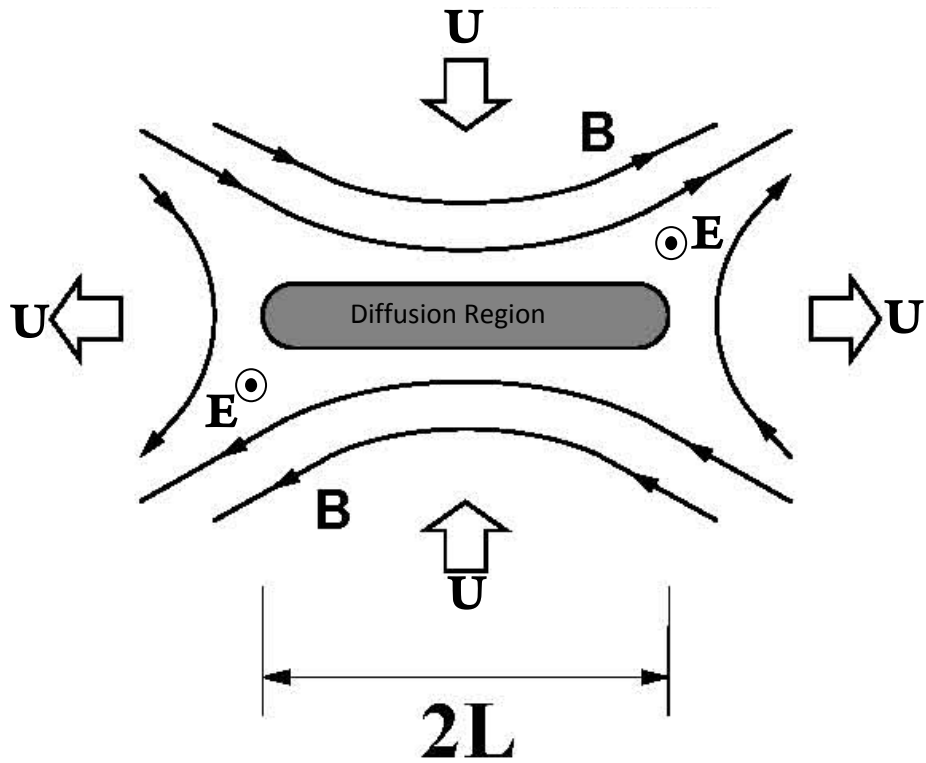


Figure 1.5 Sweet-Parker magnetic reconnection configuration. \mathbf{B} and \mathbf{U} are the magnetic field and plasma flow velocity convecting toward and leaving the diffusion region of dimension L (from *Kivelson and Russell, 1995*).

diffusion region may be located on two different flux tubes at a later time flowing away from the diffusion region. It can be considered as a process by which the initial magnetic field is “cut” and later “reconnected.” The boundary is no longer closed, since a normal component of \mathbf{B} , exchanging mass, momentum, and energy between the two regions.

1.4 The Earth’s magnetosphere

Sydney Chapman and his student *Vincenzo Ferraro* (1931) first deduced the basic nature of the interaction between the solar wind and the Earth’s magnetic field, which led to the concept of the Earth’s magnetosphere. Plasmas which come from the Sun interact with the Earth’s magnetic field lines as if they are “frozen” together as discussed above. In the absence of the solar wind, the ionized part of the upper atmosphere, the outer ionosphere would consist of a proton and electron plasma with concentration determined by diffusion along the magnetic field, which would merge gradually into the plasma of outer space. In reality, when the Earth’s plasma and the solar wind plasma meet each other, they do not mix but a sharp boundary then divides an outer region, where the solar wind continues to flow, from an inner region that contains the compressed geomagnetic field, and from which the wind is excluded. The boundary is called the magnetopause and the inner region the magnetosphere. The magnetopause is roughly spherical on the dayside and is observed at a geocentric distance of about 10 R_E . Figure 1.6 illustrates the noon-midnight cross section of the magnetosphere. The solar wind plasma travels around the obstacle at a velocity that is less than that of the solar wind flow, following the development of a shock wave upstream, which is called the bow shock. The magnetosheath is the region between the bow shock and the magnetopause. The magnetic field in the magnetosheath is stronger than the IMF but still weaker than the magnetospheric field, and it is deflected from the near-IMF orientation in the outer magnetosheath toward a draped orientation near the magnetopause. On the nightside, the magnetosphere extends into a geomagnetic tail, hundreds of Earth radii long, which contains low density plasma (less than 0.1 cm^{-3}).

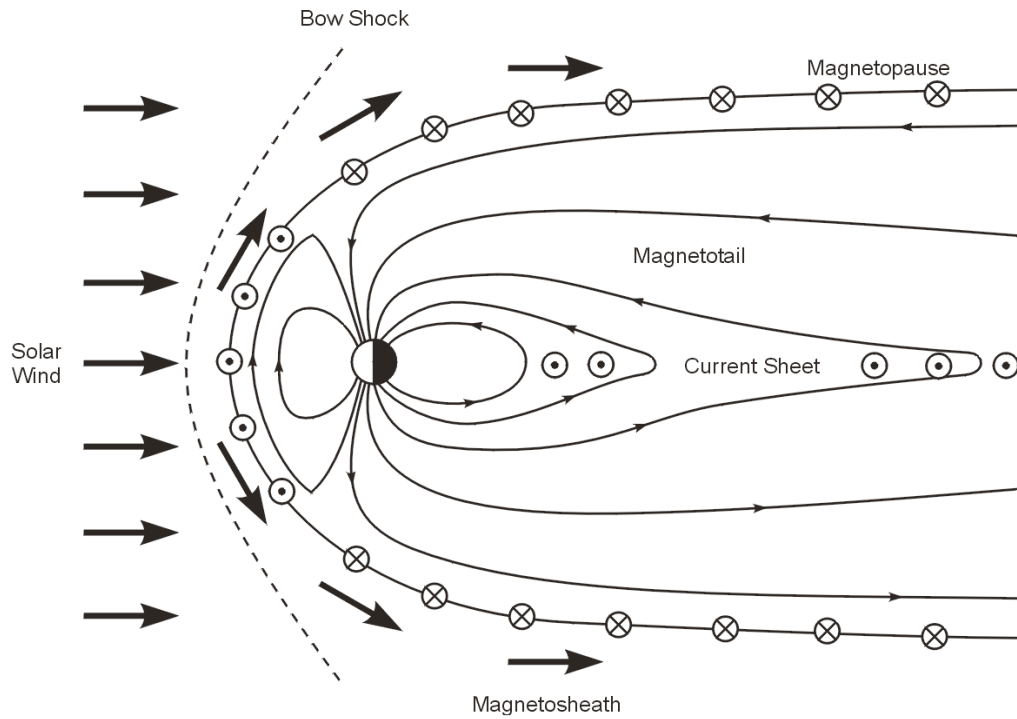


Figure 1.6 Cross section of the simplest model of the magnetosphere in the noon-midnight meridian. Thick arrows indicate the solar wind flow which is deflected at the bow shock and flows around the magnetosphere, forming the magnetosheath (from *Kivelson and Russell, 1995*)

1.4.1 Magnetospheric current systems

The solar wind drives a very complex system of currents within the magnetosphere. The plasmas are not stationary in the magnetosphere but move under the influence of the external and internal forces. The combination of plasma and electric field in the magnetosphere allows electric currents to flow. Figure 1.7 illustrates the magnetospheric current configuration within the magnetosphere. The currents, which are believed to exist in the magnetosphere are: the magnetopause current, the ring current, the cross tail current sheet, and the field-aligned currents.

1.4.1.1 The Magnetopause Current

The outer boundary of the geomagnetic field is the magnetopause in which the magnitude of the current flowing cancels the geomagnetic field outside the boundary. The magnetopause current is associated with the compression of the terrestrial magnetic field by the IMF and solar wind flow. This current is also referred to as the Chapman-Ferraro current (*Chapman and Ferraro, 1931*). Its effect on the inner magnetosphere is small compared to the earth's dipole field.

1.4.1.2 The Ring Current

Another large-scale current system, which influences the configuration of the inner magnetosphere, is the ring current. This current is one of the major current systems in the Earth's magnetosphere. It circles the Earth in the equatorial plane and is associated with the gradient and curvature drift trajectories of energetic ions and electrons trapped in the dipolar field of the inner magnetosphere. The current may be detected by magnetometers at equatorial latitudes on the surface of the earth. A clockwise ring current is produced by the drift of trapped particles since protons drift to the west and electrons to the east. The particles responsible for the ring current are low energy particles, and are mainly protons of 10 to 100 keV.

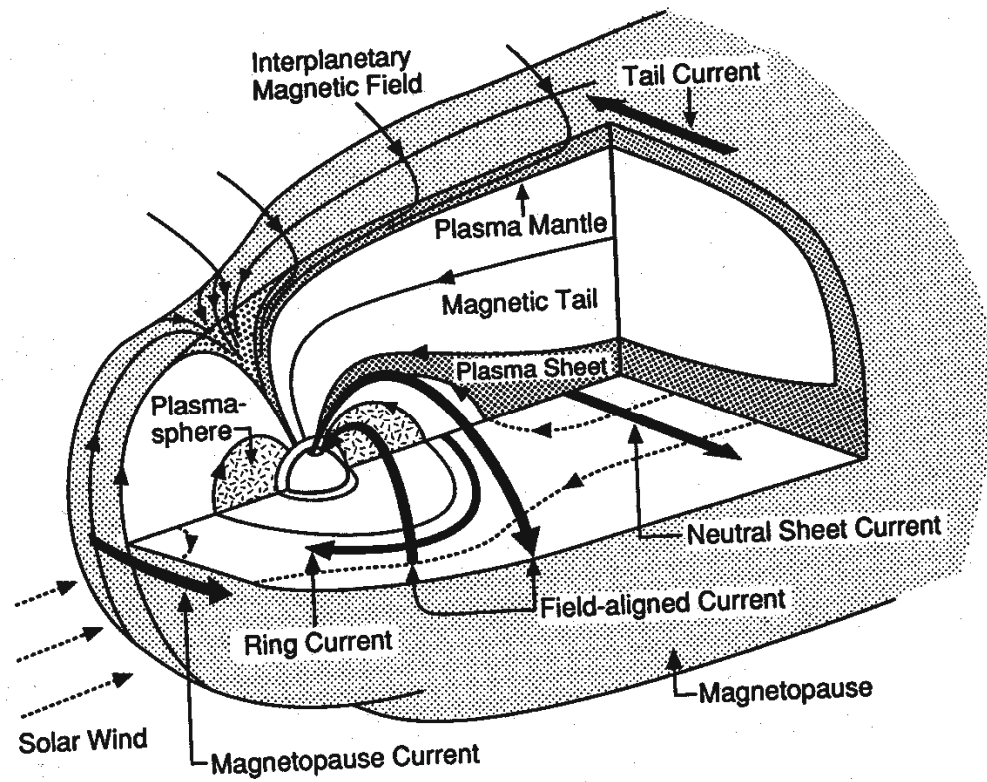


Figure 1.7 Three dimensional cutaway view of the magnetosphere showing currents, field, and plasma regions (from *Kivelson and Russell, 1995*)

The ring current is generally located between 4 and 6 R_E , close to the inner edge of the plasma sheet and to the outer edge of trapping zone where the magnetospheric convection is the main cause of the concentration of particles. The inward convection of the tail field on the Earthward side of the reconnection point accelerates particles inward, but they eventually mirror in the stronger field nearer the Earth and this is where the inner edge of the plasma sheet forms.

1.4.1.3 The Cross tail current

A third system is the cross-tail current the presence of which is indicated by the solar wind extension of the magnetosphere into a tail, flowing across the plasma sheet from dusk to dawn side. This current is associated with the highly elongated non-dipolar field lines of the tail. This cross tail current closes through currents flowing in the tail magnetopause; viewed along the Sun-Earth line, it can be seen that they both are connected and form a Θ -like current system.

1.4.1.4 The field-aligned current

In addition to the perpendicular currents discussed above, there are also currents, which flow along geomagnetic field lines. As shown in Figure 1.7, the field-aligned current, or Birkeland currents (*Birkeland*, 1908) connect the magnetospheric current system in the magnetosphere to those flowing in the polar and auroral ionosphere. The field-aligned currents are essential for the exchange of energy and momentum between these regions and are mainly carried by electrons. In the dayside, the field-aligned currents are directly affected by solar wind conditions, particularly the IMF orientation, with variations in the north-south component affecting the size of the auroral oval, the east-west component affecting the relative position of the observed field-aligned currents (*Iijima et al.*, 1978) and the strength of observed field-aligned currents (*Iijima and Potemra*, 1982).

1.4.2 Magnetospheric plasma populations

The plasma within the magnetosphere has two sources. The first is plasma generated internally by photo-ionization of the Earth's atmosphere (the ionosphere). Plasma diffuses up field lines to populate the inner magnetosphere (the plasmasphere) and to a lesser extent the outer magnetosphere. Magnetic reconnection (see discussion later on in chapter 2) produces open field lines, which cross the magnetopause, from the magnetosheath to the magnetosphere, along which solar wind plasma can gain entry. This then is the second source of magnetospheric plasma. Figure 1.8 illustrates the different populations of magnetospheric plasma. The magnetosheath plasma flows down the newly opened field lines toward the Earth, forming the "dayside cusp" population, where the "magnetic mirror" effect reflects particles such that they populate the mantle. The magnetosheath, the boundary layer and the plasma mantle of the outer tail lobes, which have been shown in Figure 1.8 using green dots, are primarily composed of solar wind plasma. The second population which is known as the plasma sheet consists roughly equally of solar wind and ionospheric plasma, it flows into the central current sheet, and has been shown by red dots. This plasma is accelerated toward the Earth and back into the solar wind by reconnection in the tail. The plasma which is directed toward the Earth will be on closed field lines; mirroring between conjugate hemisphere results in the plasma becoming trapped by the "bounce" motion. If a particle's mirror point is at sufficiently low altitude it can collide with an atmospheric atom or molecule, producing aurora and excess ionization, in which case it is lost from the trapping region. Such particles are said to be within the loss cone.

1.5 The Earth's atmosphere

The Earth's atmosphere is a thin layer of gas that surrounds the Earth. It is primarily composed of Nitrogen (N₂, 78%), Oxygen (O₂, 21%), and Argon (Ar, 1%), (CO₂, 0.03%) carbon dioxide, and trace amounts of other gases. This thin

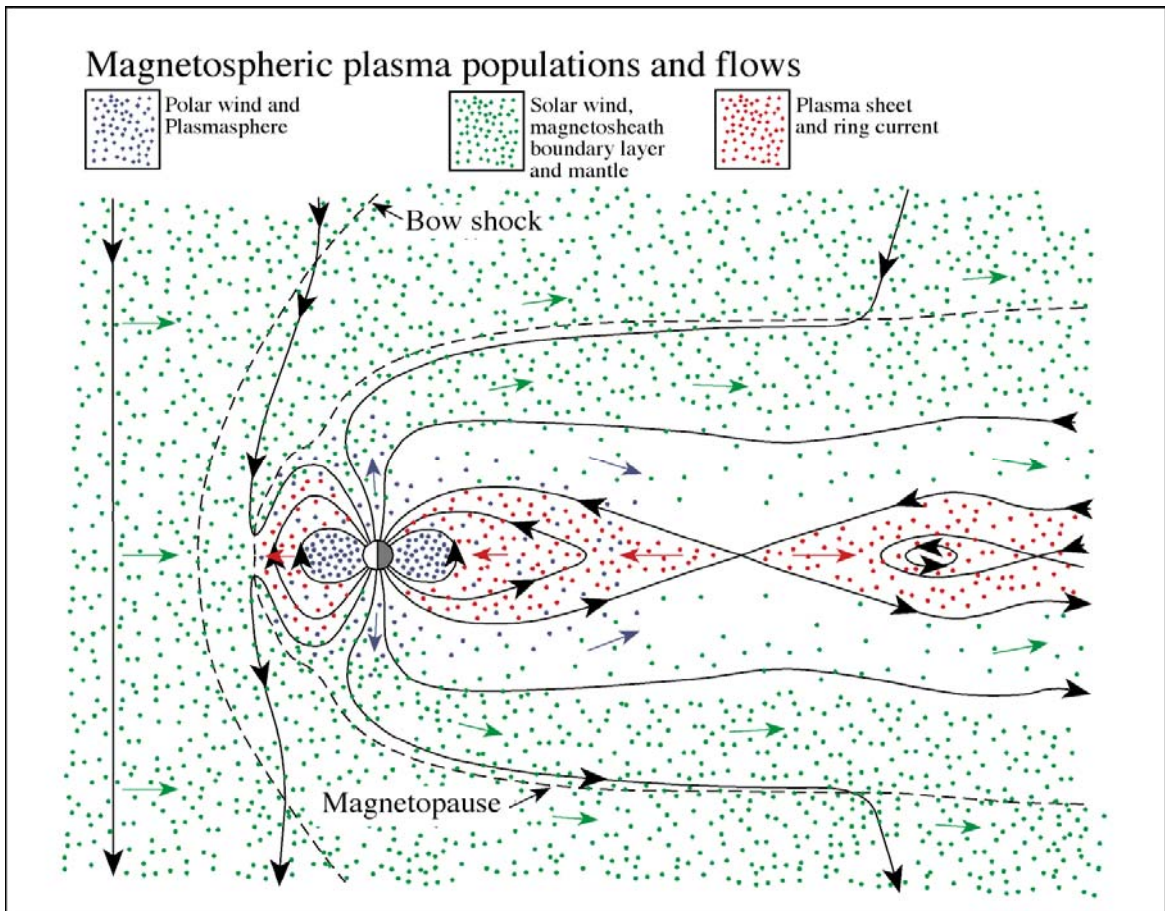


Figure 1.8 Schematic of different plasma population in Earth's magnetosphere in the noon-midnight meridian (after *Cowley et al.*, 2003)

Chapter 1: Solar-Terrestrial Phenomena

gaseous layer protects the Earth from extreme temperatures; it keeps heat inside the atmosphere and it also blocks the Earth from much of the Sun's incoming ultraviolet radiation. Most of the atmosphere (about 80%) is within 16 km of the surface of the Earth but neutral gases can extend out into the magnetosphere. Considering the vertical temperature structure, we can subdivide the atmosphere into four main regions although there is no exact place where the atmosphere ends. Figure 1.9 shows the structure of the neutral atmosphere in a typical temperature profile (left-hand side) and ionospheric plasma density (right-hand side).

The troposphere, which is the densest part of the atmosphere starts at the Earth's surface and extends between 8 to 14.5 km high. The temperature drops from about 17 to -25°C as the height increases in this layer.

The next layer is separated from the troposphere by the tropopause. Right above the tropopause is the stratosphere, which extends to 50 km altitude. This part of the atmosphere is dry and less dense compared to the troposphere. Due to the absorption of ultraviolet radiation, the temperature in this region increases gradually to -3°C at the stratopause. The ozone layer, which absorbs and scatters the solar ultraviolet radiation, is the main source of heat in this layer. The stratopause separates the stratosphere from the next layer.

Just above the stratosphere there is a layer called the mesosphere, which extends to 85 km high. This layer is known to be the coldest region of the atmosphere as the temperatures drop as low as -93°C at the mesopause.

The mesopause separates the mesosphere from the thermosphere. The thermosphere starts right above the mesosphere and is the layer, which is first exposed to the Sun's radiation and heated by the Sun. The thermosphere extends to approximately 600 km altitude and is the region of the Earth's atmosphere where ultraviolet radiation causes ionization to form the ionosphere.

Beyond the ionosphere there is a region known as the exosphere where collisions are so infrequent that atoms moving with sufficient velocity have a high probability of escaping from Earth's gravitational field into interplanetary space.

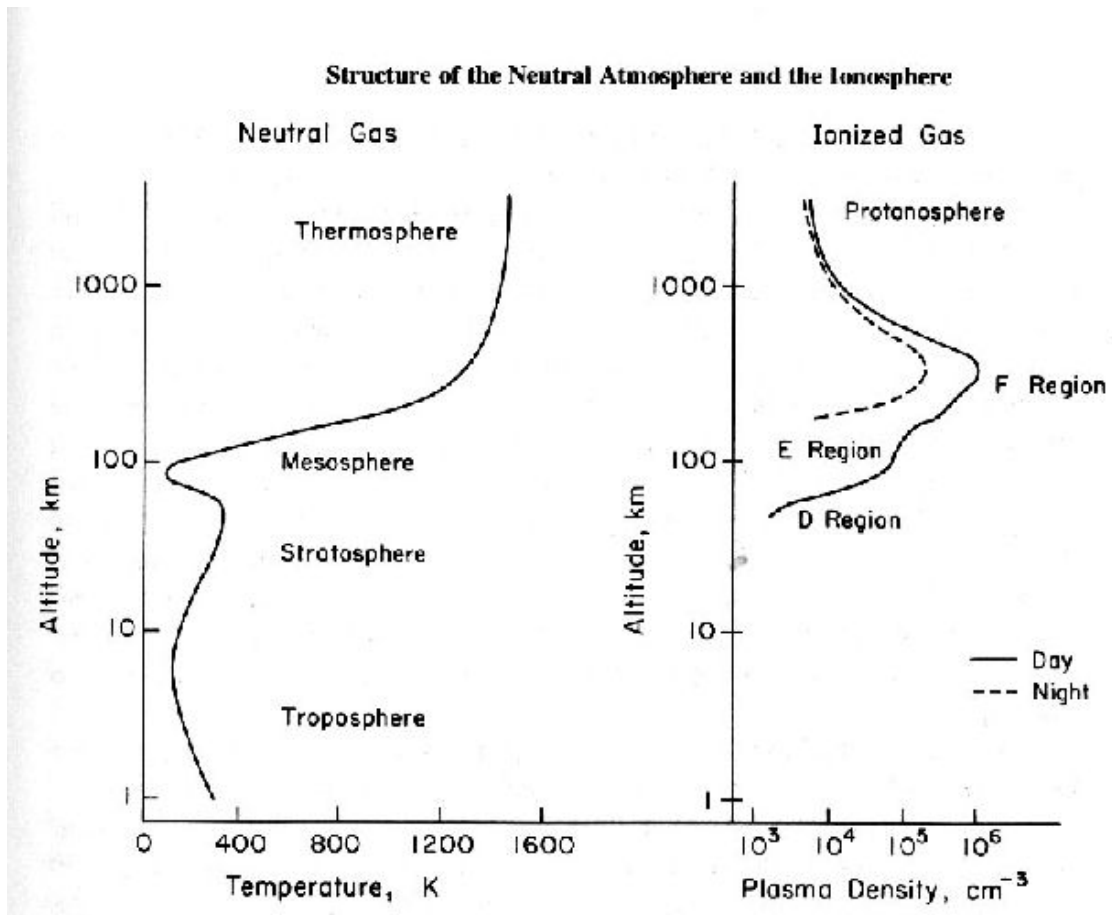


Figure 1.9 An altitude profile of the neutral atmospheric temperature (left-hand side) and ionospheric plasma density for day and night (right-hand side) (from *Kelly, 1989*).

1.5.1 The structure of the ionosphere

The ionosphere is the partly ionized thermosphere. Photoionization sometimes causes a molecule to become ionized, and therefore, the ionosphere and thermosphere overlap. The ionosphere is the transition region from the essentially fully ionized magnetospheric plasma to the neutral atmosphere and acts both as a source and a sink of plasma for the magnetosphere. Three principal regions of the ionosphere are identified as the composition of the atmosphere changes with height, (termed the D, E and F regions). Figure 1.9 (right-hand side) illustrates these three regions defined by peaks in the plasma concentration.

The D region is the lowest in altitude, lies between about 60 and 90 km, and absorbs the most energetic radiation and hard X-rays. This region is characterized by the presence of complex photochemical reactions, NO^+ , water cluster ions, and the presence of negative ions as well as electrons.

The E region electron density peak occurs between 105 and 115 km. It absorbs soft X-rays. This region is dominated by molecular ions, O_2^+ and NO^+ . Collisions between the neutral atmosphere particle and ions cause a drift between ions and electrons, which generates the ionospheric currents. The ions are motionless with respect to the neutral atmosphere at the base of the E region, and that is because the ion-neutral collision frequency is so high in this region. The electrons then drift in the direction perpendicular to both the electric and magnetic field, in the $\mathbf{E} \times \mathbf{B}$ direction, termed the Hall current. As the neutral density decreases at high altitude, the ions tend to have some mobility in the direction of the electric field, which is transverse to the magnetic field. This introduces a current flow along \mathbf{E} termed the Pedersen current, which peaks at an altitude of ~ 125 km. At this altitude ion mobility in the E direction is equal to that in the direction of $\mathbf{E} \times \mathbf{B}$ which means that the Pedersen and Hall conductivities are approximately equal. Further up in altitude ion motion increases in the $\mathbf{E} \times \mathbf{B}$ direction, the relative drift between ions and electrons decreases, and the current vanishes. In the next section, the horizontal pattern of these currents in the ionosphere is discussed in more detail.

The F region starts above the E region and has a maximum electron

density around 300 km. It is here that the highest ionospheric electron densities are found. Extreme ultra-violet radiation (EUV) is absorbed there. The plasma obeys the frozen-in flow approximation as there are negligible collisional effects in this region. This results in ionospheric flow, which mirrors the magnetospheric convection above. Details of which will be discussed in chapters 4, 5, and 6.

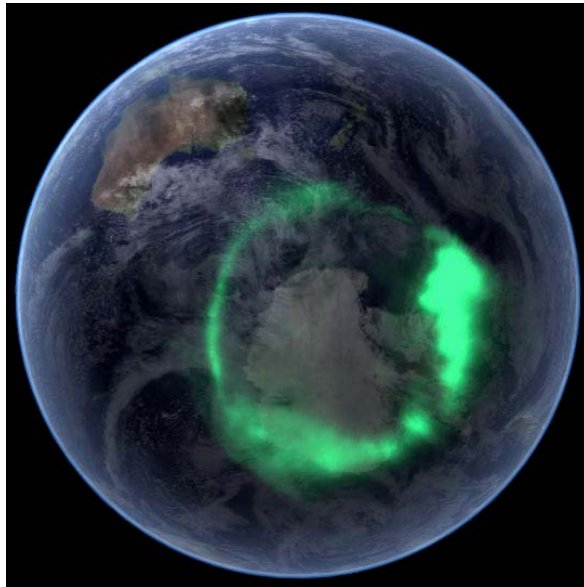
1.6 The Aurora

The aurora is certainly one of the most spectacular of nature's phenomena also known as (northern lights and polar lights).

The auroral radiation is emitted by atmospheric constituents that are excited by precipitating particles. These emission are primarily due to a two-step process in which precipitating energetic auroral particles (electrons and ions) collide with the atoms and molecules of the earth's upper atmosphere converting their kinetic energy, in part, into energy stored in the chemically excited states of atmospheric species. The chemically excited states relax, giving off photons of wavelengths determined by the energy transitions in the relaxation processes. The size and the form of the aurora thereby reflect the forces acting on these auroral particles as they journey from their source to the earth's upper atmosphere.

The advantage of using aurora as a monitor of those near-earth processes that arise through the link to the magnetosphere, rather than any conceivable system of in situ measurements, is that the size of the aurora oval differs in scale from the magnetosphere by perhaps a factor of 10^6 . The high spatial and temporal resolution available through ground-based observations provides another advantage of studying the aurora from below. Figures 1.10a and b show examples of spatial and ground based auroral observations.

The first International Polar Year (1882-3) can be regarded as marking the beginning of modern auroral research. The driving force behind the effort was Kristian Birkeland, the great auroral pioneer (*Birkeland*, 1908, 1913). In his day, only the simplest ground instruments were available for auroral investigations. Today, aurora research is conducted mainly through the use of sophisticated instruments on board rockets and satellites, as well as advanced balloon and



(a)



(b)

Figure 1.10 (a) Satellite observation of the auroral oval in the Southern Hemisphere (Courtesy of NASA). (b) Ground-based observation of aurora Australis.

ground-based equipment.

1.7 Summary

This chapter has provided a general introduction to the basic nature of the solar-terrestrial environment, Earth's magnetosphere and its interaction with the interplanetary magnetic field. Chapter 2 is comprised of a detailed explanation of the coupling process between the solar wind, magnetosphere, and ionosphere. It will also provide a brief introduction on the aurora and its characteristics. In particular, transpolar arc formation models will be reviewed as this thesis is concerned with the ground space observations of transpolar arcs. The third chapter will discuss the technical aspects of a variety of scientific instruments from which data have been used in the transpolar arc studies. These studies are presented in full in the fourth and fifth chapters. Finally, a conclusion section will summarize the work undertaken and also make suggestions for further work.

Chapter 2

Magnetosphere-Ionosphere coupling and the transpolar arc

As explained in chapter 1 reconnection is a crucial process that controls the interaction between the solar wind and planetary magnetosphere. However, the issue of when and where on the magnetopause reconnection occurs on the dayside under certain conditions has not been solved yet.

If the electrical conductivity of a fluid is large enough, the magnetic flux linking a particular fluid element remains fixed. The frozen-in flow approximation then determines that the magnetic field lines convect with the fluid. Magnetic reconnection is a process, which takes place only if this criterion breaks down, which at first sight seems very unlikely in the collisionless plasma of space. Nevertheless, there is plenty of evidence that this physical phenomenon occurs and much remains open to debate. As mentioned above magnetic reconnection controls the interaction between the solar wind and planetary magnetosphere and drives magnetospheric activity, which results in the convection in the ionosphere as well as the production of the aurora. This extraordinary phenomenon is the most readily observed consequence of the dynamic magnetosphere and the most obvious characteristic of the high-latitude ionosphere. Images of the ionospheric auroral emissions can be used to diagnose physical processes such as particle acceleration in the magnetosphere, reconnection processes in the tail, formation, and dynamics of the transpolar arcs amongst other things. A detailed explanation about the transpolar arc and how it is formed is given later on in this chapter. This chapter also aims to introduce the coupling process between the solar wind, magnetosphere and ionosphere and the various subsequent effects on the ionosphere in more detail.

2.1 IMF control of reconnection location

Magnetic reconnection at the dayside magnetopause mainly tends to happen in regions where the magnetospheric magnetic field and magnetosheath magnetic field adjacent to the magnetopause are oppositely directed. Hence, the location of the reconnection on the magnetopause is controlled by the strength and orientation of the transverse Geocentric Solar Magnetic Coordinates (GSM), y and z components of the IMF. The GSM coordinate system is generally used when studying the Sun's influence on the geomagnetic field is geocentric solar magnetic coordinates. In this system we have the X direction along the Sun-Earth line, with $GSM-X = 0$ at the Earth, and positive X is towards the sun. The $GSM-Z$ direction is perpendicular to X and lies in the plane containing the X -axis and Earth's dipole moment, being positive towards the North. The $GSM-Y$ direction completes the right-handed set, and is positive in the direction opposite to the motion of the Earth in its orbit around the Sun.

The direction of the IMF is given by the “clock angle” ($\theta = \text{atan } B_y/B_z$), with respect to north. For purely southward IMF the clock angle would be 180° , 0° for purely northward, 90° for purely duskward and -90° for completely dawnward IMF orientations. Under southward orientation of the IMF, reconnection is expected to occur at low latitudes, at or close to the subsolar point, as here the magnetic field inside the magnetopause points northwards. When the IMF turns from southward to northward, reconnection can happen between northward IMF and open field lines of the tail lobes which were produced by earlier intervals of southward field; these tail lobe field lines point southward at the magnetopause. Thus the IMF B_z controls whether reconnection occurs with closed ($B_z < 0$) or open ($B_z > 0$) terrestrial magnetic field lines. The average ionospheric convection as a result of magnetic reconnection at the dayside magnetopause is now well understood. Below are some details about the reconnection process and convection flow patterns under different IMF orientations.

2.1.1 Reconnection under southward IMF conditions and B_y -associated asymmetry

When reconnection occurs during southward IMF conditions closed geomagnetic field lines become open and are swept anti-sunward by the flow of the solar wind. Whether they are carried preferentially dawnward or duskward depends on tension forces introduced by the B_y component of the IMF.

The anti-sunward flow of the solar wind causes anti-sunward flow in the ionosphere in those regions that map to open field lines. Reconnection in the tail then closes open field lines, which subsequently return to the dayside, with corresponding return flow in the ionosphere. This cyclical convection is known as the Dungey cycle. The combination of anti-sunward/sunward and dawn/dusk flows results in the orange/banana twin-cell flows characteristic of southward IMF as shown in Figure 2.1. This figure illustrates the expected ionospheric convection patterns in the Northern Hemisphere for extended intervals of steady reconnection balanced on the dayside and the nightside, with noon at the top of each diagram and dusk to the left. In the upper row of diagrams, the corresponding ionospheric flows in the Northern Hemisphere are shown for near-zero or negative IMF B_z and different IMF B_y orientation. In this situation the twin cell Dungey cycle flows are well-developed, and the region of open field lines is relatively expanded, while dawn-dusk asymmetries in the flow are produced by the IMF B_y component with newly-opened cusp field lines flowing east for B_y negative, and west for B_y positive. In the southern hemisphere the simultaneous east-west flows are opposite or, more accurately a mirror image reflected in the noon-midnight meridian.

Figure 2.2 illustrates the geometry of newly-reconnected field lines that gives rise to the B_y -related asymmetry in the ionospheric convection. The field lines which are produced by this kind of reconnection, do not convect solely in the anti-sunward direction anymore, but are pulled towards dusk and dawn by the field tension effect. In the top diagram, representative of positive IMF B_y , newly reconnected flux tubes are pulled from postnoon across to the dawnside of the

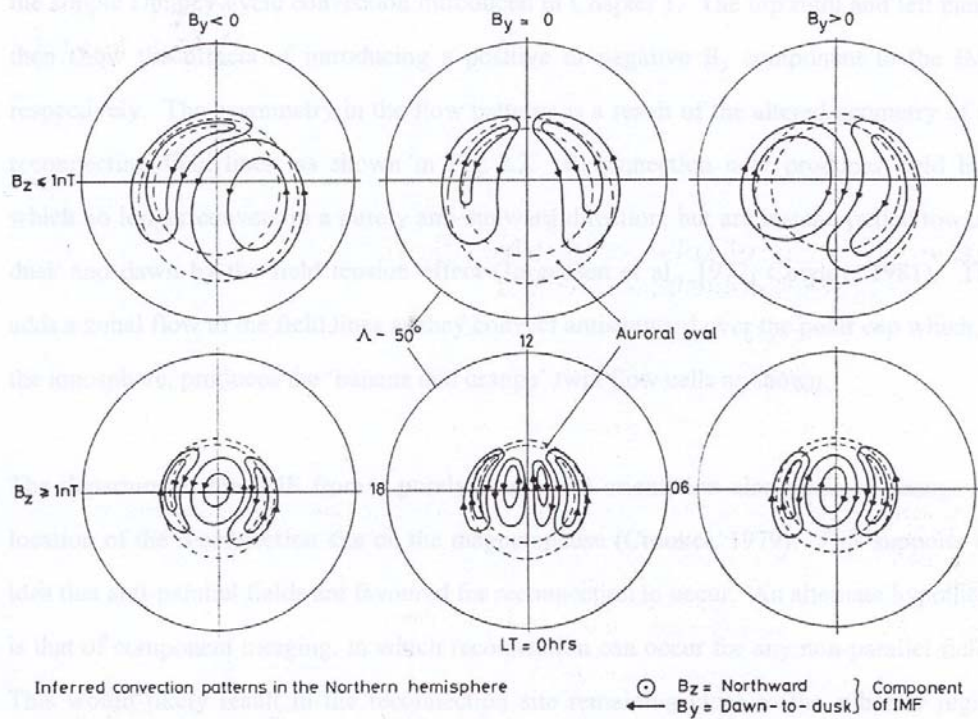


Figure 2.1 Sketches of the high-latitude ionospheric flows in the northern hemisphere ordered according to different orientations of the IMF. The dashed line shows the open-closed field line boundary, and the arrowed solid lines show the plasma streamlines (after *Lockwood, 1991*).

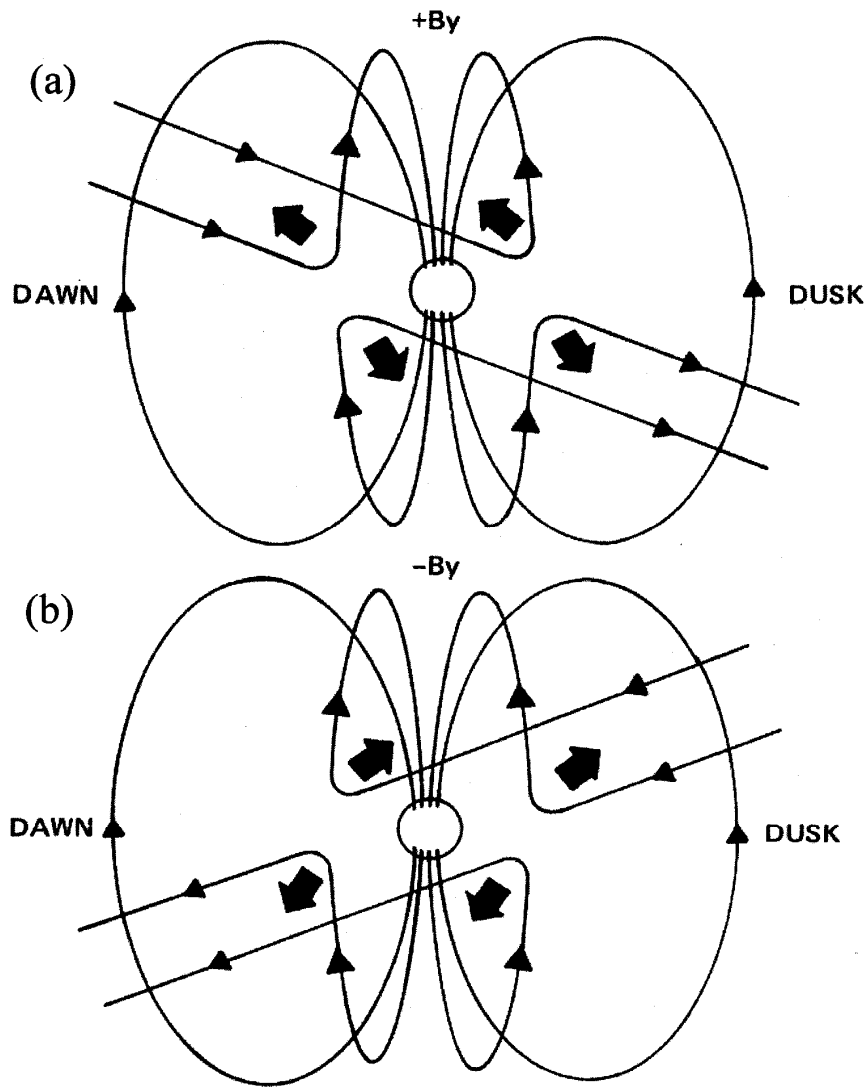


Figure 2.2 Sketches of the newly reconnected field lines for the cases when the IMF has (a) negative B_z and positive B_y components and (b) negative B_z and B_y components, viewed from the Sun. the short broad arrows show the direction that magnetic tension will tend to pull these field lines (adapted from *Gosling et al.*, 1990).

northern polar cap. In the southern hemisphere, we expect to see recently reconnected flux tubes, which are pulled from prenoon across to the duskside of the polar cap. This IMF-dependent asymmetric flow in the polar cap gives rise to the field aligned currents, which produce the Svalgaard-Mansurov effect (*Mansurov, 1969; Svalgaard, 1973*). This effect was discovered some 30 years ago. The key observation in the discovery was that in magnetograms from certain high-latitude stations (especially stations between 83° and 88° geomagnetic when near local noon) the deflection of the Z trace depended on the east-west component of the IMF as measured on a spacecraft in the solar wind. At the time of its discovery the Svalgaard-Mansurov effect was important because it proved that the IMF exerted a direct influence on the polar ionosphere. It is also important in a practical way because it allows the direction of the inner-planetary field to be determined by a ground-based technique at times when there is no spacecraft in the solar wind, which is valuable information that would not be available otherwise.

Much work has been done on the excitation of flow in the dayside ionosphere during intervals of southward IMF (e.g. *Etemadi et al., 1988; Todd et al., 1988; Ruohoniemi et al., 1993; Khan and Cowley, 1999*). Some scientists claimed that during intervals when IMF is southward and $|B_y| \sim |B_z|$, there are distinct differences between the ionospheric structures of reconnection predicted by the antiparallel and component hypotheses. A non-zero B_y component of the IMF causes the antiparallel region at the magnetopause to split into two high-latitude regions, which diverge further from the subsolar point as the B_y component becomes more dominant (*Luhmann et al., 1984*). Two separate merging lines in each hemisphere are the outcome of mapping the two reconnection sites to the ionosphere. Some observational support for this hypothesis comes from the ionospheric flow measurements of *Chisham et al, (2003)*.

2.1.2 Reconnection under northward IMF conditions

Reconnection under northward IMF, occurring at high-latitudes tailward of the cusp, has received less attention in the literature in comparison with equatorial reconnection for southward IMF. In this case, the merging is expected to move from low latitudes to high latitudes (as illustrated in Figure 2.3). It is found that during intervals with northward IMF, Dungey-cycle flow and substorm activity are reduced (e.g. *Fairfield and Cahill, 1966; Reiff et al., 1981*). During northward IMF, the ionospheric convection is much more structured, the polar cap is smaller, and compared to the case of southward IMF, velocities are normally of smaller magnitude. The bottom panel in Figure 2.1 illustrates the convection flow pattern during northward IMF, the panel at the bottom center showing the flow pattern for a purely northward IMF. As the reconnection is possible only between the IMF and the open field lines of the magnetotail, this results in a four cell ionospheric convection pattern for northward IMF. The bottom right and left panels of Figure 2.1 illustrate the effect of different orientation of the B_y components of the IMF. As can be seen in the figure, changing B_y creates asymmetry in the dawn-dusk direction. It is usually thought that the low latitude cells are formed due to the viscous interaction (*Axford and Hines, 1961*), and the high latitude cells are due to reconnection.

Dungey (1963) proposed that whenever the Interplanetary Magnetic Field (IMF) is purely northward, the geomagnetic field of a completely closed model magnetosphere and the IMF become antiparallel and merge tailward of the cusp on field lines that form the tail lobes. Later studies suggested that reconnection between the IMF and open tail lobe magnetic field does not change the total amount of open flux in the magnetosphere as reconnection happens on already open field lines and no open flux will be produced or destroyed (e.g., *Russell, 1972; Cowley, 1981; Reiff and Burch, 1985; Cowley and Lockwood, 1992*).

Using a 3D global MHD simulation of the solar wind interaction with the Earth's magnetosphere for strictly northward IMF, *Berchem et al.* (1995) discovered that most of the field lines sunward of the reconnection site became

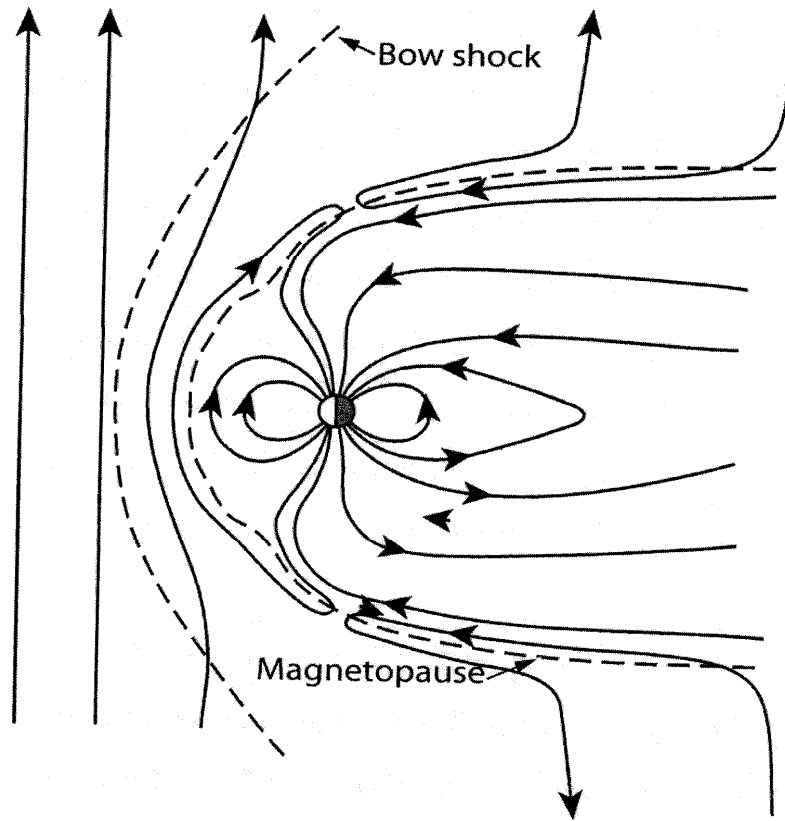


Figure 2.3 View of the magnetosphere in the noon-midnight meridian during northward IMF in which “two-lobe” reconnection in both northern and southern hemispheres closes open flux (from *Grocott, 2002*)

closed through a symmetrical reconnection process happening in both hemispheres, while the lobe field lines tailward of the reconnection site became unattached causing an erosion of the plasma mantle. *Richard et al.* (1994) claimed that the dominant mechanism of magnetosheath plasma entry into the magnetosphere was convection on reconnected field lines. They also found that for northward IMF, particles entered the magnetosphere when the field lines on which they were convecting became closed by cusp reconnection, forming the closed low latitude boundary layer.

IMF northward conditions lead to a range of interesting phenomena, some of which are the centre points of this thesis and will be discussed in the following section.

2.2 IMF northward related phenomena

As mentioned earlier on in this section, the dynamics of the Earth's coupled magnetosphere-ionosphere system is largely influence by the orientation of the IMF. More accurately, it depends primarily on the strength and orientation of the transverse GSM y and z components of the field. Despite a wealth of information on IMF southward related phenomena, there are still undiscovered areas when it comes to phenomena occurring under northward IMF condition. A few examples of such phenomena are lobe reconnection, which happens at very high latitude at the dayside, magnetospheric substorms, tail reconnection during IMF northward non-substorm intervals (TRINNI) which occurs at the nightside, and transpolar arc, details of which are given below.

2.2.1 Lobe reconnection

Lobe reconnection is expected to occur under northward IMF ($B_z > 0$) (e.g. *Dungey*, 1963; *Russell*, 1972; *Reiff and Burch*, 1985; *Milan et al.*, 2000). Reconnection of magnetic flux tubes which extend into the tail lobes results in

open flux closure in and field line contraction back towards the Earth. Lobe reconnection can take place in just one hemisphere (Fig. 2.4a) or in both hemispheres (Fig. 2.4b). Figure 2.4 illustrates two cross sections of the Earth's magnetosphere in the noon-midnight meridian. In (a) the IMF is northward with a significant B_y component which causes the single lobe reconnection occurring at the same time, but independently, in both hemispheres. The newly reconnected field lines have one footprint in one hemisphere, either south or north, and the other end draped around the subsolar magnetopause and into the IMF. As a consequence of the flow of the solar wind and the magnetic pressure on the twisted field lines, sunward flow is produced at around noon magnetic local time (MLT), the field lines then slide into the magnetic lobe creating two "reverse" convection cells at the dayside (Fig. 2.4c). There is no sign of any changes in the size of the polar cap as no new flux is added or removed from the polar cap but being "stirred" (Crooker, 1992). Ground based observations and low altitude orbiting satellites have observed a decrease in the energy of the precipitating magnetosheath particles in the cusp with decreasing magnetic latitude (Cowley and Lockwood, 1992, and references therein; Ruohoniemi and Greenwald, 2005, and references therein; Chisham *et al.*, 2004 and references therein).

2.2.2 Dual lobe reconnection (DLR)

In 1963, Dungey proposed the concept of Dual Lobe Reconnection (DLR) for the first time. Since then, there have been a few studies on this subject but not as much attention has been given to the DLR as to single lobe reconnection. However, some studies such as the works of Milan *et al.* (2000) and Øieroset *et al.*, 2005 have contributed to the greater understanding of DLR process. In their work, they study the effects of the IMF orientation on the location of the lobe reconnection and the nature of the ionospheric flow associated with it respectively.

The IMF B_y component plays a very important role in the displacement of the lobe reconnection site in both hemispheres. In the case of a non-zero B_y , this

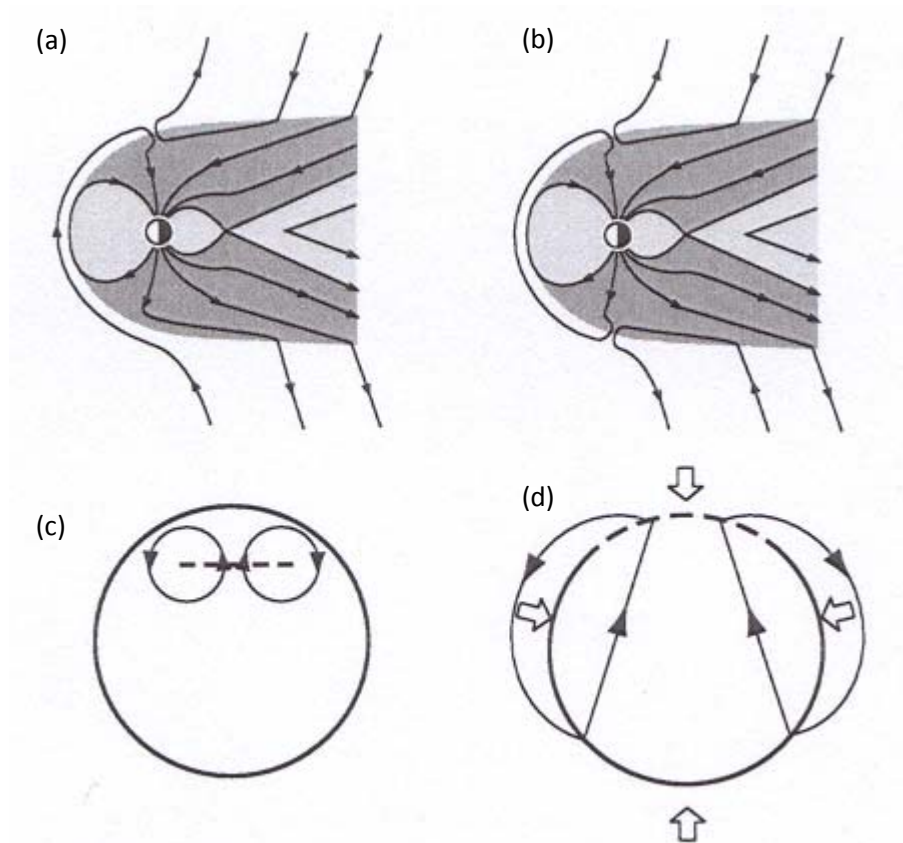


Figure 2.4 Cross sections of the Earth's magnetosphere in the GSM X-Z plane and ionospheric convection patterns where arrowed lines show flow streamlines and the large arrows illustrates contraction of the polar cap for the case (a & c) IMF $B_z > 0$ nT, and (b & d) IMF $B_z > 0$ nT, $B_y = 0$ nT. The arrowed solid lines indicate the magnetic field lines during (a) single lobe reconnection and (b) dual lobe reconnection (From *Imber et al.*, 2006).

displacement means that in the North and South hemispheres, different interplanetary magnetic field lines are reconnected independent of each other, this process being referred to as single lobe reconnection occurring in the two hemispheres (*Huang et al.*, 2000, *Milan et al.*, 2000).

Occurrence of lobe reconnection on the same magnetic field lines at both hemispheres simultaneously (Fig. 2.4b), can be interpreted as the formation of the low latitude boundary layer during northward IMF (*Song and Russell*, 1992). During this mechanism, tail magnetic flux is converted into new dayside closed magnetic flux (*Rieff and Burch*, 1985) and a cold and dense plasma sheet can be formed as a consequence (e.g. *Øieroset et al.*, 2005, and references therein). As can be seen from Fig. 2.4d, the polar cap gets contracted due to the ionospheric flow traversing sunward across the dayside open/closed field line boundary. This would end in the creation of poleward flows around adiaroic (impassable) sections of the open/closed field line boundary, away from the merging gap. The newly closed magnetic field lines then get pushed towards the tail by solar wind pressure.

Signatures of DLR are also detectable in measurements made by ground based instruments. Recently a study of the ionospheric signatures of the DLR was made by *Imber et al.* (2006) when they described the first attempt to identify the signature of dual lobe reconnection from the ionospheric flow measurements. They demonstrated the effects of dual lobe reconnection on ionospheric convection and showed that the total flux crossing the open/closed field line boundary is relatively small during the DLR process. A study of the ionospheric convection in the Northern Hemisphere measured by high frequency radars was presented by *Marcucci et al.* (2008). They showed that simultaneous reconnection poleward of both the northern and southern cusps occurs at a variable rate on the dusk part of the magnetosphere when the IMF clock angle is small.

2.2.3 Substorms in the magnetosphere

Coupling of the magnetosphere and ionosphere has always been a very interesting phenomenon to study as it provides vital information on the reconnection process both at the dayside and at the nightside. So far in this chapter, a brief introduction to the reconnection process at the dayside has been given. A further aspect of magnetosphere-ionosphere coupling is the occurrence of reconnection in the magnetotail. One of the most interesting nightside phenomena is the build-up of flux in the tail, followed by an explosive release of magnetospheric energy, known as magnetic substorm. Discovery of magnetic substorms goes back to nearly 40 years ago, when they were mainly an observational phenomenon.

When the IMF turns southward, the interplanetary and terrestrial magnetic field lines reconnect at the nightside magnetopause. Magnetic substorm happens when the rate of reconnection at the dayside magnetopause exceeds that in the tail. The open flux which is then added into the tail lobe then begins to build up, forcing the system to go through a typical evolution on a 1-2 hour timescale (known as substorm) which occur six times a day, on the average (Akasofu, 1968). There are three substorm phases (shown in Fig. 2.5), which make up the substorm cycle, a) growth, b) expansion, and c) recovery.

The storage of some of the energy transferred to the Earth's magnetotail forms the first of the three phases of the substorm, the "growth" phase. The energy in the tail then gets released when the field lines in the inner magnetosphere relax from their stretched, tail-like configuration and snap back into a more dipolar configuration. This phase is known as the expansion phase, the cause of which is yet an unknown issue. During this phase, charged particles in the plasma sheet get energized and injected into the inner magnetosphere. The magnetosphere returns to its quiet state at the final stage, what is called the "recovery phase" of the substorm.

One of the main substorm features in the ionosphere is caused by earthwards accelerating influx of particles from the tail, which produces the

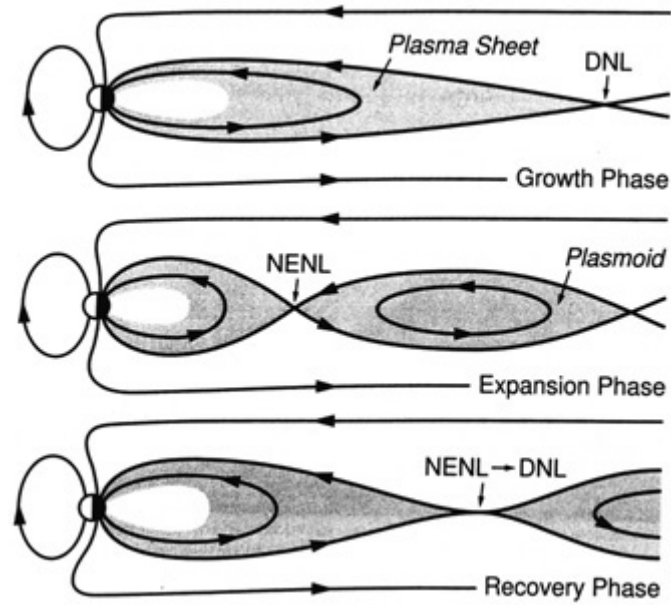


Figure 2.5 Schematic of three stages of substorm development illustrating substorm features in the noon-midnight meridian plane of the magnetosphere (*W. Baumjohan and R.A. Treumann, Basic Space Plasma Physics, 1996*).

NENL: *Near Earth Neutral Line*

DNL: *Deep-tail Neutral Line*

auroral brightening. The auroral behaviour during substorms was first described by *Akasofu* (1964) using arrays of all-sky cameras allocated around the auroral oval. Looking down on the North Pole, with noon at the right and dusk to the left, Figure 2.6 illustrates the development of an auroral substorm in three different substorm phases from left to right: growth, expansion, and recovery phases. At the growth phase, as can be seen from Fig. 2.6, there is a quiet state without much brightening happening in the auroral oval. At the expansion phase however, a bright bulge of auroral disturbance is observed in a form of a sudden brightening in most of the midnight sector expanding dawn-duskward. This period usually lasts about 30-50 minutes. At the final phase, the auroral activity fades out and the magnetosphere relaxes back to its pre-substorm state.

Despite a wealth of knowledge on understanding of substorm phenomenology, there are still unanswered issues, such as “what causes substorm onset?”.

In 2007, NASA launched a fleet of five satellites called THEMIS, the Time History of Events and Macroscale Interactions during Substorms. This ongoing mission should solve the unanswered question of what triggers geomagnetic substorms. These five identical probes will line up along the sun-Earth line and collect coordinated measurements every four days. This way they will be able to observe nearly more than 30 substorms during the two-year mission. The measurements from this constellation of satellites will then enable scientists to have an inclusive view of the substorm phenomena from Earth's upper atmosphere indicating where and when each substorm begins. Figure 2.7 illustrates a cross-section of the magnetosphere in the noon-midnight meridian, using circled numbers 1-3 to indicate the Earth's postulated sequential stages of substorm activity, and five different colored dots (P1-5) to show the location of the satellites in the magnetotail.

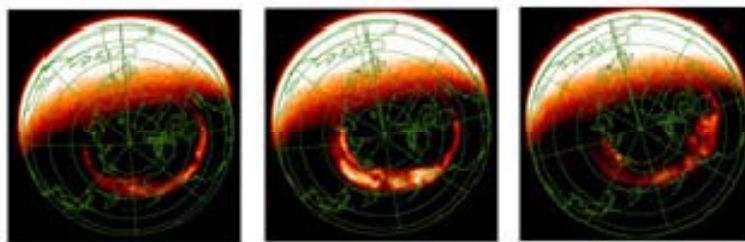


Figure 2.6 Three stages of Substorm development in the ionosphere. From left to right: Growth, expansion, and recovery phases. (*W. Baumjohan and R.A. Treumann, Basic Space Plasma Physics, 1996*).

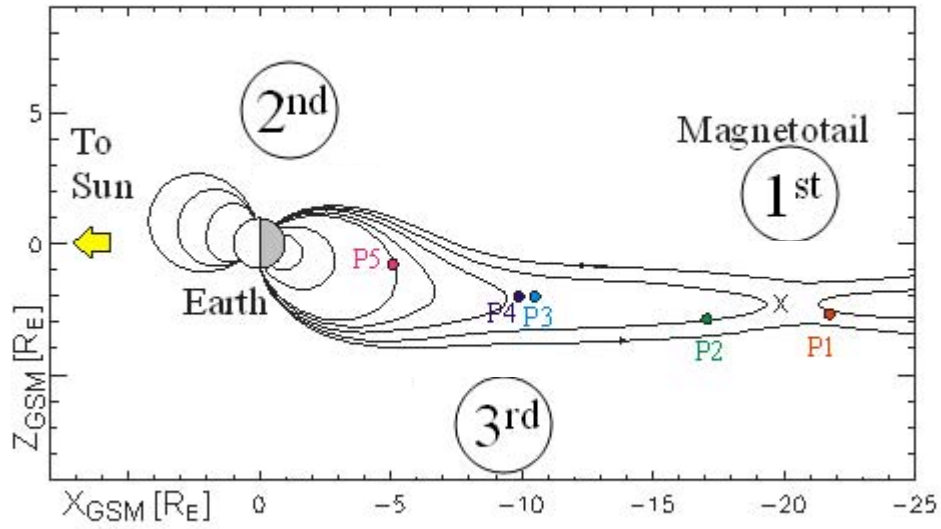


Figure 2.7 cross-section of the magnetosphere in the noon-midnight meridian, using circled numbers 1-3 to indicate the 3 substorm process, and five different colored dots (P1-5) to show the location of the satellites in the magnetotail (Courtesy of NASA).

2.2.4 Tail reconnection during IMF northward non-substorm intervals

As previously mentioned in section 2.2.2, during northward IMF, dayside reconnection can occur poleward of the cusps. In the case of purely northward IMF, reconnection happens between the Earth's open magnetic field lines and the IMF, which leads to generation of lobe cell convection in the ionosphere and magnetosphere (*Reiff and Burch, 1985*). When the B_y component of the IMF is non-zero, reconnection can happen between the Earth's closed magnetic field lines and the IMF on the equatorward side of the cusp (e.g. *Nishida et al., 1998*). This process creates merging-cell convection and is responsible for producing the flow bursts magnitude of which were measured by *Senior et al., (2002)* and *Grocott et al. (2003)*. The particular phenomena discussed in detail by them were bursts of fast ($\sim 1000 \text{ ms}^{-1}$) westward auroral zone flow in the nightside ionosphere. These observations were made during extended intervals of modest dayside driving associated with a northward IMF. The flow bursts were assumed to be associated with the episodic reconnection in the distant magnetotail as there were no signs of substorm activity registered by spacecrafts. These bursts of "tail reconnection during IMF northward non-substorm intervals" were then named TRINNIs by *Grocott et al. in 2005*. An interesting example of TRINNI like flows is given in Fig. 2.8. This figure illustrates three consecutive snapshots of the ionospheric convection map, showing streamlines and vectors of the nightside ionospheric flows derived from high frequency radar measurements for 12th of March 2002. These data are shown on geomagnetic latitude-MLT grids, with midnight at the bottom and dusk to the left. The colour bars indicate the magnitude of the flow vectors, and the red arrows show the TRINNIs.

In the opposite hemisphere, however, the newly B_y -dependent east-west flows downstream of the reconnection site go to the opposite direction. This can be caused by the Svalgaard-Mansurov effect (*Svalgaard, 1973*). As mentioned above, this effect suggests the opposite directed flows in the opposite hemispheres

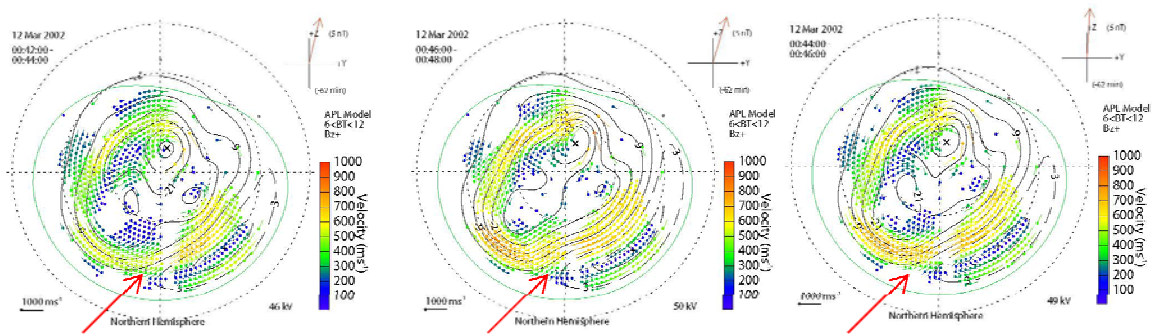


Figure 2.8 Three consecutive snapshots of the ionospheric convection map, showing streamlines and vectors of the nightside ionospheric flows derived from high frequency radar measurements for 12th of March 2002. These data are shown on geomagnetic latitude-MLT grids, with midnight at the bottom and dusk to the left. The colour bars indicate the magnitude of the flow vectors, and the red arrows show the TRINNIIs.

are associated with newly-opened flux tubes, poleward of the open-closed field-line boundary, that are being pulled sideways by the field tension force. As a result of this tension force, open field lines convect tailward and reconnect in the twisted neutral sheet. This procedure generates asymmetric merging cells in the ionosphere (*Grocott et al.*, 2005).

Figure 2.9 illustrates a schematic representation of the “TRINNI” field aligned topology. The convection streamlines for the Northern and Southern Hemisphere are shown using the black and grey solid arrow curves respectively for the case of positive IMF B_y (The opposite is true for the negative B_y). The straight lines indicate the tail field lines, which connect the two hemispheres via the reconnection line. Twisted closed flux tubes are produced as a result of magnetic reconnection happening between the field lines mentioned above (shown in panel b). Panel b demonstrates two corresponding views towards the Earth from the tail under the 2 IMF B_y orientation conditions. The dashed lines show the twisted neutral sheet and field lines marked by the letter B indicate the newly reconnected field lines. The thick back arrowed curves show the closed flux tubes being untwisted in the ionosphere. This figure also shows that the bursts are not necessary geomagnetically conjugate in each hemisphere.

Being a relatively newly identified phenomenon, TRINNIs have not been studied in more than a few cases. A detailed study of TRINNIs will be presented in chapters 4 and 6, in order to investigate their origin and conjugacy.

2.2.5 The transpolar arc

Using the global imaging instrument onboard the Dynamics Explorer 1 spacecraft, *Frank et al.* (1982, 1986) first reported transpolar aurora from space, i.e. a long-lived auroral structure extending across the complete polar region, with both ends connecting to the auroral oval, resembling a Greek letter “ θ ” (therefore they are also known as theta aurora). The first visual observations of such features, however, were by the British Antarctic Expedition during the austral winter of 1908 (*Mawson*, 1916). When the theta aurora is viewed from high-

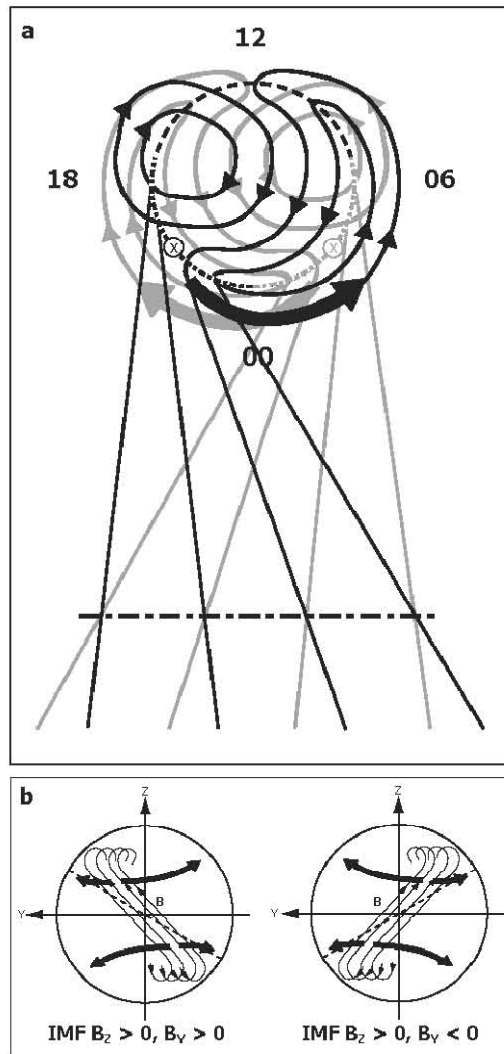


Figure 2.9 A view of the northern polar cap from above the Earth, showing the open-closed field line boundary using a dashed circle. Dungey-cycle twin convection cells are shown as the solid black/grey arrowed curves for the simultaneous flow in the Northern/Southern Hemisphere respectively (*Grocott et al., 2004*)

altitude satellites, the bar in the letter theta appears to be aligned with the Sun, stretching across the entire polar cap, and these arcs are therefore known as transpolar arcs (An example of which is shown in Fig. 2.10). Transpolar arcs are thought to be the optical manifestation of particle precipitation on closed field lines (*Frank et al.*, 1982, 1986; *Zhu et al.*, 1997). However, other observations, which demonstrate the occurrence of polar rain electrons and relativistic electrons adjacent to and outside of polar cap arc, suggest the arcs are on open field lines, (*Hardy et al.*, 1982; *Hardy*, 1984; *Gussenhoven and Mullen*, 1989).

In 1993, Zhu et al. introduced the very first time-dependent theoretical model displaying the features of temporal evolution and fine spatial structures of transpolar arcs. They developed a quantitative time-dependent model in which the electrodynamics of transpolar arcs are treated self-consistently in the frame of the coupled magnetosphere-ionosphere system. Figure 2.11 is a schematic diagram showing the Magnetosphere-ionosphere framework for a transpolar arc model. Initially, a magnetosphere shear flow carried by Alfvén waves propagates toward the ionosphere. The downward propagating Alfvén waves are partially reflected from the ionosphere and then bounce around between the ionosphere and magnetosphere. The features of wave reflections depend on the conditions in the ionosphere and magnetosphere. The propagating Alfvén waves carry both upward and downward field-aligned currents. The precipitating electrons associated with upward field-aligned currents increase the conductivity in the ionosphere. The changed ionospheric conductivity launches a secondary Alfvén wave toward the magnetosphere. The whole process is transient during which all physical quantities in the ionosphere change self-consistently in time and transpolar arcs develop. Because of the finite conductivity in the ionosphere, the temporal changes of Alfvén waves in the coupled magnetosphere-ionosphere system diminish with time, and the whole magnetosphere-ionosphere system, as well as the development of transpolar arcs, eventually approaches an asymptotic steady state. At this steady state, the electric field in the ionosphere remains constant in time because there is no further change of the wave field along magnetic field lines, and a constant Poynting flux carried by Alfvén waves feed the constant

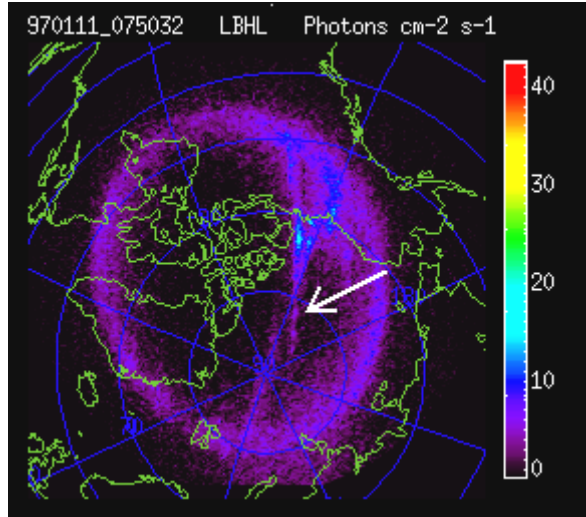


Figure 2.10 A transpolar arc is visible in this UVI image of the aurora on Jan. 11, 1997, at 07:50:32 UT. *Credit: NASA/Marshall Space Flight Center.*

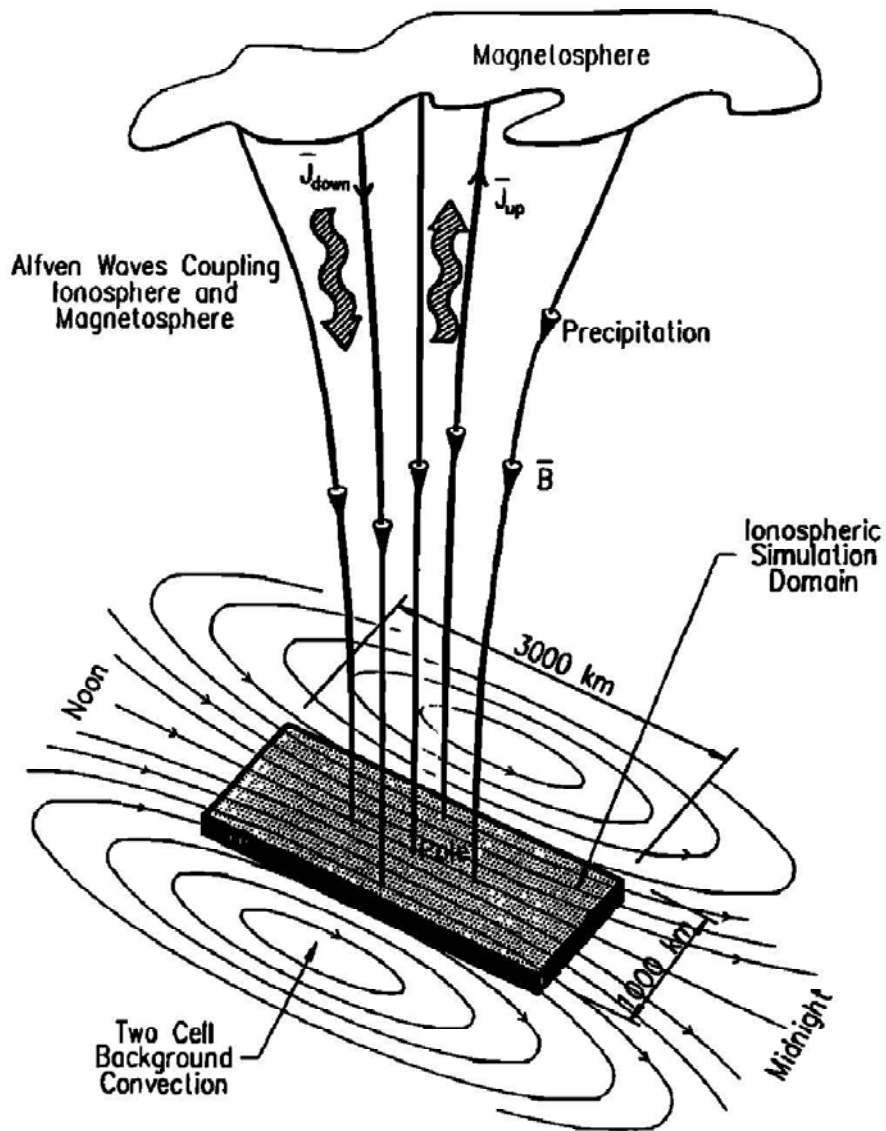


Figure 2.11 A schematic diagram showing the geophysical framework of the transpolar arc model. The background ionosphere convection is for illustrative purposes and not necessarily a two-cell convection (After *Zhu et al., 1993*).

energy dissipation in the ionosphere. The enhancement of the ionospheric conductivity in the model is assumed to be caused mainly by the precipitating electrons associated with the upward field-aligned currents. Maximum flexibility is given to the inputs of the model, which allows the model either to simulate transpolar arcs under different conditions or to test various theoretical hypotheses.

Developing such a quantitative model, provided some interesting results such as follows:

1. In a self-consistent development of transpolar arcs, an initial single-arc precipitation pattern splits into multiple arcs. This result suggests that the observed multiple transpolar arcs might not be due to any multiple structures in the magnetospheric source region, but instead, such a multiple feature is internally organized in the dynamical process of the transpolar arcs determined by the whole magnetospheric-ionospheric system.

2. Strong downward currents can develop near the most intense upward currents and form pair structures of field-aligned currents in transpolar arcs.

3. While transpolar arcs are developing, the associated current system tends to become further localized, and at steady state the current system in the narrow regions around the arcs is locally self-closed.

A recent study (*Eriksson et al., 2005*) looks at some of the above issues using a different model. They suggest that the apparent continuous band of the transpolar arc may be considered as two separate entities, one on the dayside and one on the nightside, driven by two different physical processes. The dayside part of the transpolar arc is associated with sunward lobe convection and an upward northward IMF B_z current. Examining a case study, they illustrated that the dayside part of the duskside transpolar arc formed due to quasi-continuous merging between the IMF and the lobe magnetic field tailward of the cusp. Using Magneto Hydro Dynamic (MHD) simulation, they suggested that their case study is indeed the case with northward IMF B_z (NBZ) type opposite field aligned currents being generation on either side of a lobe reconnection site at $(X, Y, Z)_{GSM} = (-4.67, 5.38, 10.19)$ RE. The nightside part of the arc, however, generally tailward of the dawn-dusk meridian is stagnant or antisunward flow and the

upward FAC region of Harang discontinuity. This region is associated with the shear zone where the eastward electrojet, equatorward of the shear, and the westward electrojet, poleward of the shear, meet. Figure 2.12 (a, b, and c) illustrates seven magnetic field lines, which are traced from seven (x_0, y_0, z_0) locations in the proximity of the enhanced sunward MHD flows at 0240 UT on 16th of December 2001. All field lines also pass near $(X, Y, Z)_{\text{GSM}}=(-4.67, 5.38, 10.19) R_E$ which is the approximate location of a lobe reconnection site between the draper IMF and the tail lobe field. These figures illustrate the resulting flux tubes from three different perspectives at 0240 UT. One field line is closed and appears to be anchored near the merging regions in both hemispheres. Four of the field lines are open and connected to the northern hemisphere polar cap at one end with the other end being connected to the draped IMF. One field line has recently become disconnected from the Earth and another is a typical IMF field lines. One of these open field lines is not yet affected by this merging site, however, and may be considered as an old field line previously opened by merging on the dayside magnetopause (Figs. 2.12a and b).

High latitude lobe reconnection may generate sunward flows typically during sub-Alfvénic magnetosheath conditions (e.g. *Matsuoka et al.*, 1996; *Phan et al.*, 2003) due to a sunward directed $\mathbf{j} \times \mathbf{B}$ force that initially acts to pull the kinked magnetic field sunward. Figure 2.11d suggests that the simulated sunward flow is indeed driven by such $\mathbf{j} \times \mathbf{B}$ forces. A major part of this process occurs on the earthward side of magnetopause. Arrows illustrate the velocity component in the XZ_{GSM} plane at $Y=2.1 R_E$ and the X_{GSM} component of the $\mathbf{j} \times \mathbf{B}$ force is colour-coded from blue (tailward) to red (sunward). The topology of the magnetic field is also illustrated with open, closed, and IMF fields indicated in black, red, and blue, respectively.

The work presented in chapters 4 and 5 of this thesis attempts to elucidate this subject, by making a detailed analysis of these auroral features, which are excited in association with different nightside reconnections. Given below is a brief summary of current understanding on transpolar arc phenomenology.

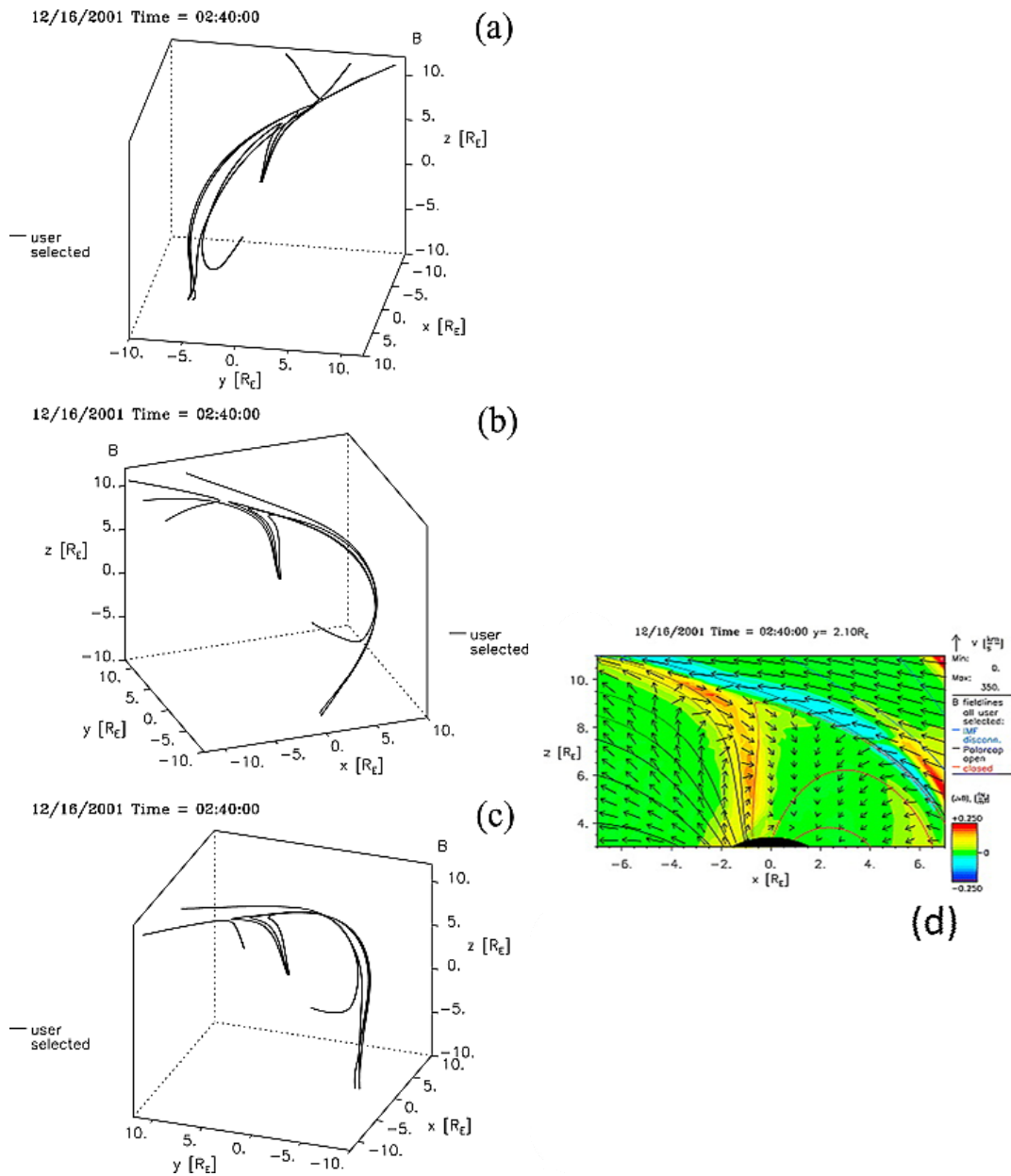


Figure 2.12 (a,b, and c) Seven magnetic field lines are traced from seven (x_0, y_0, z_0) locations in the proximity of the enhanced sunward MHD flows at 0240 UT. All field lines also pass near $(X, Y, Z)_{GSM} = (-4.67, 5.38, 10.19)R_E$ which is the approximate location of a lobe reconnection site between the draped IMF and the tail lobe field, (d) MHD simulation results of the magnetic field topology, velocity, and the $\mathbf{j} \times \mathbf{B}$ force near the lobe reconnection site are shown projected into the XZ_{GSM} plane at $Y=2.1R_E$. Vector field shows the projected velocity and the background color indicates the $(\mathbf{j} \times \mathbf{B})_x$ component (After Eriksson *et al.*, 2005).

2.2.5.1 Formation and dynamics of transpolar arcs

Many studies have been undertaken recently to explain the formation and dynamic characteristics of the transpolar arcs. Previous studies (*Cumnock et al.*, 1997; *Kullen et al.*, 2002 and references therein) have indicated that a majority of transpolar arcs appear during northward IMF, a strong IMF magnitude, and high solar wind speed.

In 2005, *Milan et al.* presented a case study in which they showed a transpolar arc forming as a result of TRINNI happening in the Northern Hemisphere. According to their findings, the occurrence of the TRINNI could lead to a build up of closed flux, which is unable to convect normally in the return flow regions due to competition between the conjugate hemispheres, resulting in tongues of closed flux protruding from the plasma sheet (shown in Figure 2.13).

Their observation suggests that in the presence of a transpolar arc the polar cap is partitioned into two compartments dawnward and duskward of the arc. Division of the polar cap into two compartments of open flux partitioned by the transpolar arc under northward IMF conditions was also suggested by (*Frank et al.*, 1986; *Huang et al.*, 1987; *Zhu et al.*, 1997; *Frey*, 2007), in which case the polar cap will contain two regions of open flux, which map to a bifurcated tail lobe. It should be possible for changes in the size of each compartment to occur through the reconnection process under different IMF conditions, which can transfer open flux from one compartment to the other. The subsequent expansion of one compartment and correspondingly deflation of the other can lead to the motion of the arc (*Milan et al.*, 2005). Figure 2.14 illustrates this motion caused by expansion of the polar cap. This theoretical model was used in the work of *Goudarzi et al.* (2008) which will be discussed thoroughly in chapter 4.

It has been shown that the y-component of the IMF controls the (dawn-dusk) motion of transpolar arcs. After being formed, transpolar arcs can move slowly across the polar cap in the direction of the new IMF By component in the Northern hemisphere (*Frank et al.*, 1986; *Huang et al.*, 1989; *Valladares et al.*, 1994) and in the opposite direction in the Southern Hemisphere (*Craven et al.*,

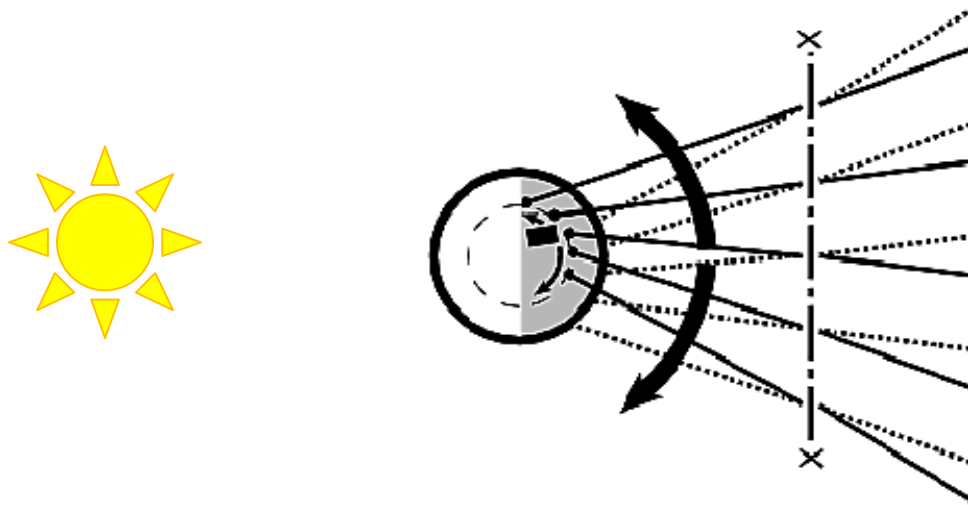


Figure 2.13 Schematic diagrams indicating the field topologies in the magnetotail after reconnection for $B_y < 0$. Dashed circle indicates the polar cap, and solid (dotted) lines represent nightside field lines for the Northern and (Southern) Hemisphere. Convection return flows in the equatorial plane of the tail and in the ionosphere are shown using arrows. (Adapted from *Milan et al.*, 2005)

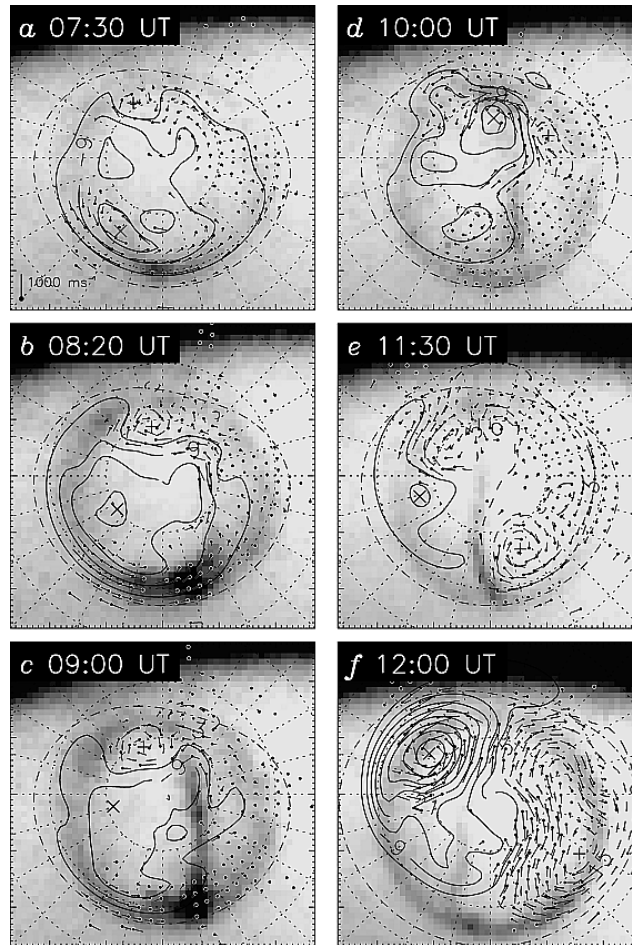


Figure 2.14 Ionospheric convection maps measured by high frequency radars with superimposed IMAGE FUV auroral data with noon at the top and dusk to the left. Displacement of the transpolar arc caused by expansion of the polar cap is illustrated using 6 snapshots (After *Milan et al.*, 2005).

1991).

Transpolar arcs appear in many different shapes (*Kullen et al.*, 2002). There are some transpolar arcs which are dynamic and move towards either the dusk or dawn side of the oval, while other kinds, such as oval-aligned transpolar arcs, stay on the side of the polar cap where they initially form (*Valladares et al.*, 1994). Both of these kinds, either dynamic or quasi-steady transpolar arcs, appear to be produced at the poleward edge of the duskside (dawnside) auroral oval for positive (negative) IMF B_y in the Northern Hemisphere. A few studies have shown that theta aurora can coexist in both hemispheres, with one being the mirror image of the other (*Craven et al.*, 1986; *Craven et al.*, 1991; *Craven and Frank*, 1991; *McEwen and Zhang*, 2000). However, another investigation showed cases when the transpolar arc was observed in only one hemisphere and was absent in the other (*Ostgaard et al.*, 2003).

2.2.5.2 Particle precipitations associated with transpolar arcs

The observation of both the electron and proton aurora consequently improves the understanding of the magnetospheric phenomena and their diversity. TPAs are known to be associated with both ion and electron precipitation where the ion precipitation is spread across the arc and electron precipitation is more structured (*Frank et al.*, 1986; *Cumnock et al.*, 2002). The precipitating electrons in the theta arcs are associated with electric fields (*Frank et al.*, 1986) probably resulting from shear flows at the convection reversal boundary (*Cumnock et al.*, 2002). Particle characteristics (spectra and ion composition) observed in the arcs indicate that the theta auroras are created on closed field lines (*Peterson and Shelley*, 1984; *Frank et al.*, 1986) as predicated by models (*Reiff and Burch*, 1985; *Chang et al.*, 1998).

The topology of the field lines in a transpolar arc is another widely studied subject. Some early studies suggested that the field lines threading the transpolar arcs were closed through the plasma sheet or the plasma sheet boundary layer (*Peterson and Shelley*, 1984; and *Frank et al.*, 1986). Using DE1 high-altitude

plasma instrument (HAPI) electron and ion data, *Menietti and Burch* (1987) discovered that some of TPAs occur on closed field lines with particle signatures and plasma parameters similar to those of the magnetospheric boundary plasma sheet. In 1988, *Frank and Craven* showed that large-scale TPAs lie on closed field lines. In 1997, *Zhu et al.* claimed that the open-closed field line issue of the transpolar arcs is still controversial. However, in 1991, it was suggested by *Meng and Mauk* that the controversy about the origin of particles in polar arcs probably appeared because of the different natures of the transpolar arcs, which were studied by different authors, and that large-scale polar arcs probably lie on closed field lines while small scale arcs lie on open field lines.

Using DMSP-F6 data, *Makita et al.* (1991) determined the energy of the precipitating electrons in transpolar arcs, which is a few keV, and protons have a high energy component above 10 keV. Transpolar auroral particles were measured by *Cumnock et al.*, (2000, 2002) with ion fluxes ranging from a fraction of mW/m^2 up to $\sim 1 \text{ mW/m}^2$ and a typical average energy of $\sim 0.5 \text{ keV}$ (An example is given in Figure 2.15). In general, typical particle energies associated with transpolar arcs are slightly lower than in the main oval (*Zhu et al.*, 1997).

In chapter 5, particle precipitation during transpolar arc events are studied in the arc itself as well as in the main oval. In particular, observations performed by NOAA satellites and DMSP spacecraft will be looked into in order to investigate the origin of the particles precipitating into the Earth's upper atmosphere. Finding out whether these particles are located on open or closed field lines, will help scientists to gain a better understanding of the origin of the transpolar arcs.

2.3 Field aligned currents

The Field Aligned Currents (FACs) play a very important role in coupling energy and momentum to the polar region of the upper atmosphere by transmitting stress between the solar wind and magnetosphere to the ionosphere

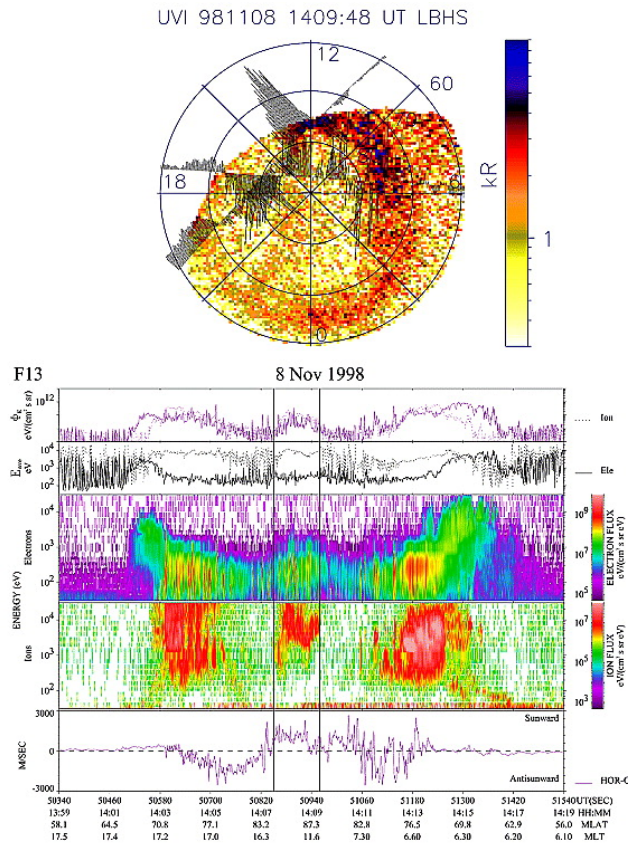


Figure 2.15 Data shown are from a low orbiting satellite passing in the Northern Hemisphere (1217–1241 UT) that occurs during the UVI data period collected by Polar UV imager. At the top are the horizontal plasma flows of the two satellites, perpendicular to the satellite track plotted over a UV image. (bottom) A spectrogram includes, from top to bottom, (1) electron and ion integral energy flux, (2) electron and ion average energy, (3) precipitating electron spectrogram, (4) precipitating ion spectrogram, and (5) cross-track horizontal plasma drift. In Figure 1 (bottom) vertical lines mark the times when one of the satellites reaches highest magnetic latitudes (*Cummock et al.*, 2002).

(Cowley, 2000). This interaction delivers up to 10^{12} W to the thermosphere during geomagnetic storms (e.g. *Monreal Mac-Mahon and Gonzalez, 1997*), creates an enormous global electrical circuit that carries current and causes the aurora, heats the polar atmosphere, and drives neutral winds (*Richmond and Thayer, 2000*). The FACs are typically located at magnetic latitudes between 65° and 75° . The distribution of the large-scale field-aligned currents, like ionospheric convection patterns is strongly dependent on the magnitude and direction of the IMF, the solar wind speed and density, and the ionospheric conductivity (*Iijima and Porterman, 1976a; Iijima and Porterman, 1978; Weimer, 2001; Papitashvili et al., 2002*). Although there has been a lot of work done on the basic configuration of FACs, there are still unanswered questions regarding their variability particularly during geomagnetic storms activities.

The Birkeland current signatures are rather straightforward to detect as they are typically 100s of nT measured at low earth orbit. The large-scale system of FACs was first detected as “transverse magnetic disturbances” by the low altitude polar-orbiting satellite 1963 38C (*Zmuda et al., 1966*), although their signature were not identified as the effect of FACs straight away. A year later *Cummings and Dessler (1967)* found a link with the current system, which had first been introduced by *Birkeland* sixty years earlier (*Birkeland, 1908*). Using data collected over a period of 16 months, *Cummings and Dessler* measured the average configuration of the Birkeland currents by magnetic field measurements from the low Earth orbiting TRIAD satellite. Figure 2.16 shows a basic model of the FAC system, which is illustrated by the large-scale distribution of current flow direction pattern, measured from data collected from 439 passes of TRIAD during geomagnetically less active conditions (*Iijima and Potemra, 1976b*). They identified the global statistical pattern of field-aligned currents which are composed of two contiguous rings, the equatorward region 2 system at lower latitude and the region 1 system immediately poleward of it at higher latitude. The low-latitude currents (region-2), are mainly due to pressure gradients in the inner magnetosphere and maps into the Central Plasma Sheet (CPS). Region-1 currents, which maps in the Plasma Sheet Boundary (PSB), flow at the interface between

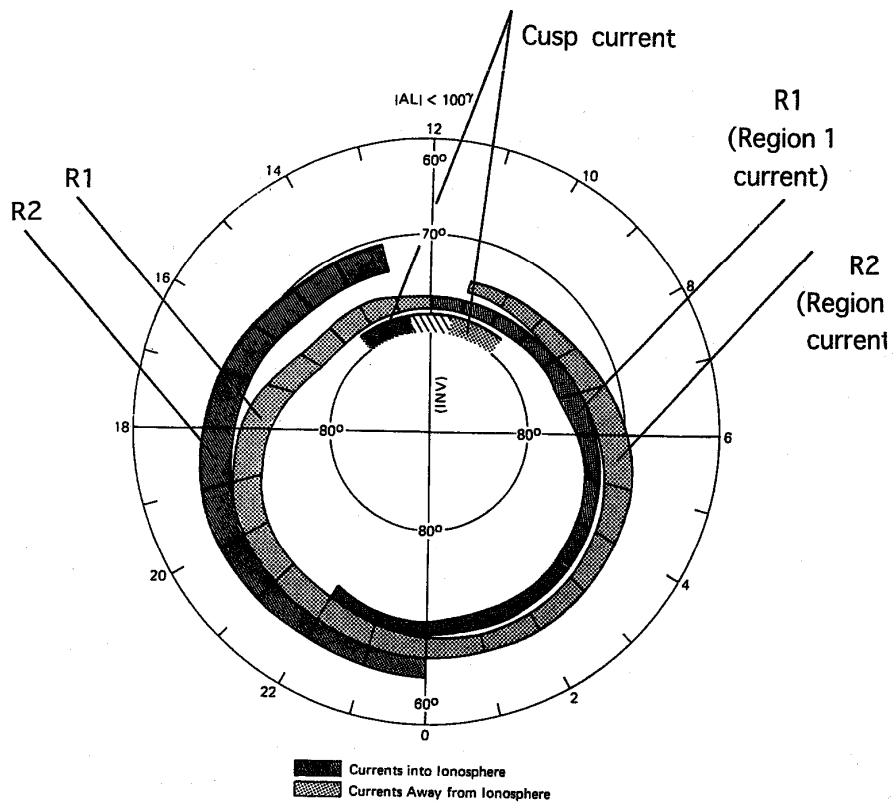


Figure 2.16 A basic model of the FAC system, which is illustrated by the large-scale distribution of flow direction pattern, measured from data collected from 439 passes of TRIAD during geomagnetic less active conditions (after *Iijma and Potemra, 1976b*).

open and closed field lines, are due to the interaction between the solar wind and the magnetosphere (*Klumpar, 1979; Sugiura et al., 1984; Yamauchi et al., 1998*).

Figure 2.17 illustrates the general auroral zone current circuit, in which can be seen the magnetospheric partial ring current flowing in the nightside inner plasma sheet region (*Cowley, 2000*). The current then closes in the ionosphere through region 2 FACs, north-south Pedersen currents across the auroral zone ionosphere, and then out as region 1 currents flowing in the outer layer of the plasma sheet to the magnetopause, and closing in the magnetosheath plasma. Poynting flux is being fed into both the dissipative ionospheric Pedersen currents, and into the energy stored in the compressed and heated hot magnetospheric plasma by the magnetosheath “generator” in the steady state, in the absence of which, the circuit could be powered by the decay of the tail magnetic flux which threads through it.

Birkeland currents and magnetic perturbations are related via Ampere’s law, $\nabla \times \mathbf{B} = \mu_0 \mathbf{J}$, where at low altitude \mathbf{J} is field aligned current. Since the Earth has a curl free magnetic field, it is more helpful to deal only with the magnetic perturbations from the main field, $\Delta \mathbf{B}$. The Iridium system satellites, which are three axes stabilized and nadir pointing, are able to detect the magnetic perturbations from the Birkeland currents. What make the data from the Iridium data set favorable for measuring a statistical description of the Birkeland currents are: a) the ability to yield a two-dimensional distribution every hour which makes it possible to identify intervals with stable currents, b) the large size of the data set, makes it possible to choose a small division of the data for analysis and still have enough data to yield statically significant results (*Anderson et al., 2006*). The in-situ observations made by the Ørsted and DMSP satellites have been used to verify the accuracy of the Iridium large-scale fits of the magnetic perturbations (*Korth et al., 2004; Waters et al., 2004; Korth et al., 2005*). These studies illustrate the importance of the value of multi-satellite observations for characterizing FACs.

The existence of upward and downward current sheet pairs was shown in the past using observation of field-aligned currents associated with TPAs.

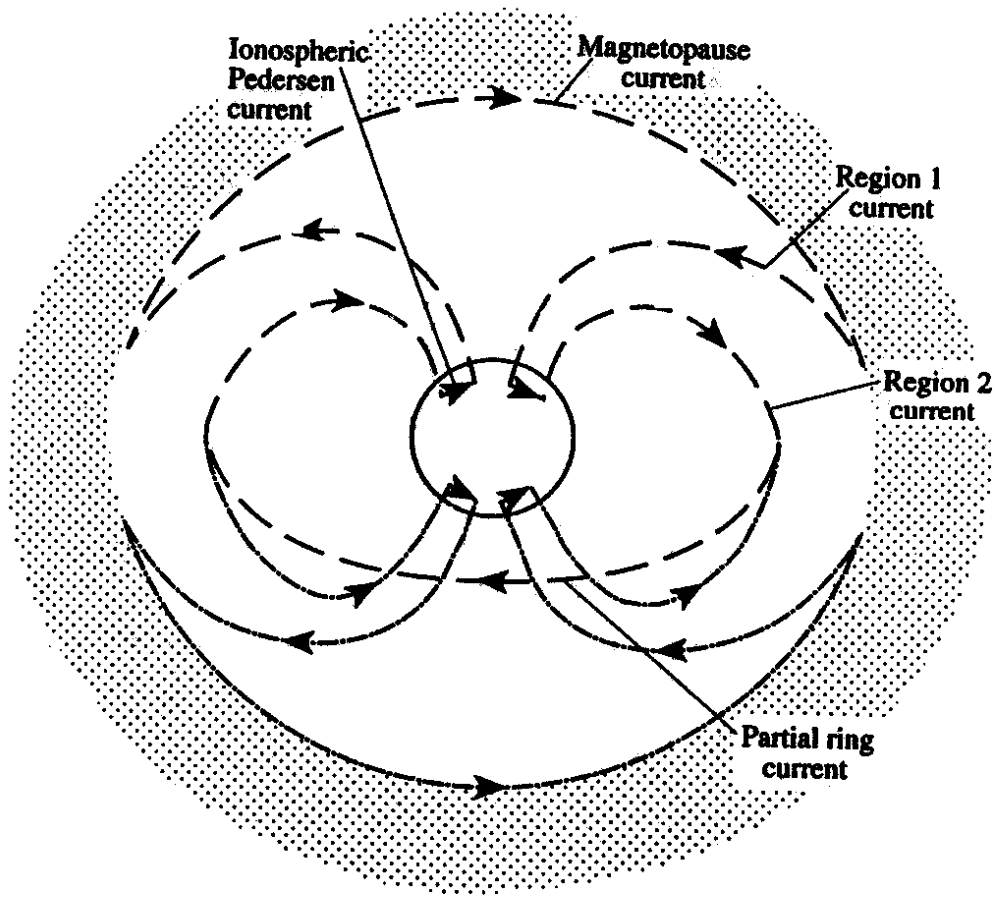


Figure 2.17 General auroral zone current circuit schematic of the Earth, looking from the tail, showing both the northern (dashed lines) and southern (dot-dashed lines) branches of the circuit (after Cowley, 2000)

Marklund and *Blomberg* (1991) carried out a model study of the relationship between the large scale convection pattern and the transpolar arc associated field-aligned currents. They modeled cases with locally balanced upward and downward arc currents, as well as the case of a single upward and downward current associated with the arc but not locally balanced. With locally balanced current the effect on the convection pattern is localized, whereas an unbalanced arc current system leads to a modification of the convection pattern on the global scale. Satellites have observed all three current configurations (e.g. *Frank et al.*, 1986; *Menietti and Burch*, 1987; *Marklund*, 1993; *Blomberg and Cumnock*, 2004). In addition, as the IMF becomes more northward, both the region 1 to Region 2 and the NBZ to region 1 current ratios increase (e.g. *Blomberg and Marklund*, 1993).

Chapter 4 will look into the field-aligned current patterns using large-scale fits of the magnetic perturbations from Iridium satellite constellation, in order to investigate a variety of field-aligned current configurations associated with the changing global aurora.

2.4 Summary

This chapter has provided a background on the nature of the solar-terrestrial environment, Earth's magnetosphere and its interaction with the interplanetary magnetic field. It has also provided an overview of various effects of the reconnection under different IMF orientations on the magnetosphere. The transpolar arc which is an example of a phenomenon that occurs predominantly during northward IMF has been reviewed. The final part of this chapter discussed the formation and dynamics of this unique phenomenon and introduced field aligned current system which later on would contribute to this study of the origin of the transpolar arc.

Chapter 3

Instrumentation and experimental techniques

This thesis employs a number of different data sources. In particular, the SuperDARN radar network is used to measure the ionospheric convection flow. In addition the ACE spacecraft is used to determine the relevant upstream IMF conditions, while polar orbiting DMSP spacecraft and NOAA satellites are used to investigate the characteristics of precipitating particles. The Iridium system satellites were used to measure the field aligned currents. Finally, to examine the auroral configuration, the Wideband Imaging Camera (WIC) aboard the IMAGE spacecraft has been used. These systems are now described in more detail.

3.1 The Super Dual Auroral Radar Network

The 20 high frequency (HF) coherent radars which form the Super Dual Auroral Radar Network cover a large part of the northern and southern auroral ovals (*Greenwald et al., 1995; Chisham et al., 2007*). These radars are designed to employ backscatter from high-latitude field-aligned ionospheric plasma density irregularities (radar aurora) as a trace of the bulk plasma motion under the influence of the convection electric field, and hence as a diagnostic tool for the investigation of large-scale magnetospheric-ionospheric coupling. In 1983, the Goose Bay HF radar was the first SuperDARN radar to be deployed, and followed the development of several paired VHF radar systems including the Scandinavian Twin Auroral Radar Experiment (STARE) (*Greenwald et al., 1978*), the Sweden And Britain Radar Experiment (SABRE) (*Nielsen et al., 1983*), and the Bistatic Auroral Radar System (BARS) (*McNamara et al., 1983*). Following the successful operation of the Goose Bay radar, the growth of SuperDARN took place over the decade starting in 1994 resulting in the current 20 operational radars.

Some of the basic ideas regarding the usage of coherent backscatter radars in observing the ionosphere are discussed below, including a more detailed description of the SuperDARN radars.

3.1.1 The SuperDARN radars

As has been said before, SuperDARN is an international collaborative network of HF radars which monitors ionospheric plasma convection over the majority of the northern and southern polar regions. SuperDARN is currently comprised of 14 operational radars in the Northern Hemisphere and 6 radars in the southern hemisphere. The locations of the radars currently in operation are shown in figure 3.1. The radars normally sound 16 beams to form a full 52° azimuthal scan. During the standard operating mode each of the radars performs a full scan every two minutes (or one minute), with a dwell time of 7 seconds (or 3 seconds) per beam. Each beam is typically divided into 75 range gates, of 45 km in length in the standard common mode, in which the distance to the first gate is 180 km. In the fast common mode of operation a complete scan happens every minute. In addition to the common and fast common modes of operation, the schedule includes discretionary and special time to test and run alternative operating modes. The radars can operate in the HF band between 8 MHz and 20 MHz.

Most of the radars also have, separated by typically 100 m from the main array and parallel to it, a four-antenna interferometer array that is used to make vertical angle-of-arrival measurements. By measuring the phase difference between the antenna arrays it is possible to deduce the elevation angle of arrival of the incoming radio waves. This is important for identifying the HF propagation mode.

3.1.2 Nature of coherent backscatter

In this section we discuss the scattering mechanisms that cause radars to receive echoes from the ionosphere.

(a)



(b)



Figure 3.1 The SuperDARN fields of view in (a) the northern and (b) the southern hemispheres (geographic co-ordinates).

Backscatter of the radar radio wave, k_r , occurs from ionospheric irregularities with wave vectors, k , which satisfy the Bragg condition $k = \pm 2k_r$. The field-aligned nature of the irregularities ($k \perp B$, where B is the magnetic field) requires that the radar wave vector is orthogonal to the local magnetic field ($k_r \perp B$) at the point of scatter for the return wave vector to be incident on the radar and coherent backscatter to be observed. The advantage of HF radars over VHF radars, which were previously employed for convection studies (e.g. *Greenwald et al.*, 1978; *Nielsen et al.*, 1983a), is their ability to achieve the orthogonality condition with the magnetic field in the F region as well as the E region due to the refractive nature of radio wave propagation in the 3 MHz to 30 MHz frequency band (for a full discussion of HF propagation see *Davies*, (1990)).

Figure 3.2 illustrates some of the possible propagation modes by which backscatter information can be returned to an HF radar located near auroral latitudes and pointing poleward. Backscatter originates where k_r approaches orthogonality with the magnetic field B , in the case of ionospheric backscatter, or from the ground. The nomenclature for HF propagation was originally developed for point to point communications between ground stations and hence whole hops (propagation from ground to ionospheric reflection point and back to ground) are labeled with integer number and a letter denoting the reflecting layer, e.g. 1F denotes 1 reflection from the ionosphere to ground and back. Ground backscatter from this point of ground incidence is then termed 1F backscatter. As ionospheric backscatter originates between points of ground incidence it is labeled as integer and-a-half. At a ground incidence some power is scattered back along the direction of propagation, and some is reflected forward into a second hop, allowing, for instance, $1\frac{1}{2}$ F ionospheric backscatter and 2F ground backscatter to be observed at further ranges. More comprehensive nomenclature has been introduced (*Davies*, 1967) to describe some regions of backscatter, for instance the F-E / mode; in this system the $1\frac{1}{2}$ F mode is termed the F-F/mode. (Note that in summer months the F region can separate into the F1 and F2 layers, allowing propagation by, for instance, the 1F1 and 1F2 modes.) Three example rays are illustrated in figure 3.2, and it is possible that all three or a combination of them

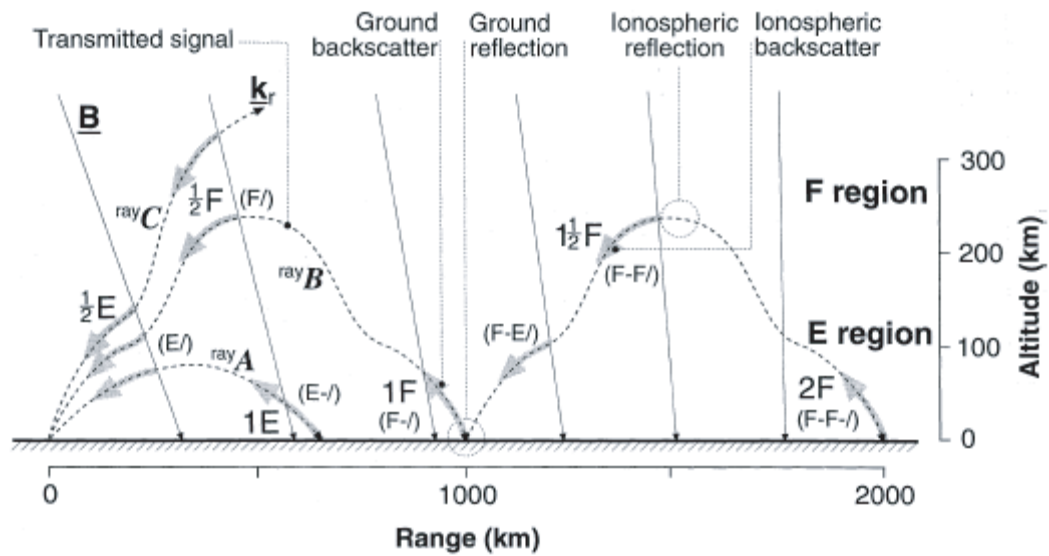


Figure 3.2 A schematic diagram of some of the possible propagation modes and regions from which backscatter can occur. Ranges and altitudes are approximate and depend on ionospheric conditions. Three rays are illustrated: *A* E region mode; *B* F region mode producing far-range as well as near-range backscatter; *C* a ray that penetrates the ionosphere (from *Milan et al.*, 1997).

can propagate simultaneously depending on the ionospheric electron density distribution with altitude and range. The ranges indicated are also dependent on the ambient ionospheric conditions. Ray A has a low elevation angle and backscatters and reflects in the E region; multiple hops are also possible here. Ray B has a higher elevation angle and reflects in the F region, producing backscatter in both the E and F regions. Ray C has the highest elevation angle and ionospheric refraction is insufficient to produce reflection, so the ray penetrates the ionosphere. In this case, though, ionospheric backscatter can be observed in the E and F regions ($\frac{1}{2}$ E and $\frac{1}{2}$ F modes), no ground backscatter (1F or 2F) or far range ionospheric backscatter ($1\frac{1}{2}$ F) is produced. The refraction effects in the ionosphere lead to a much larger viewing area at HF than can be achieved with VHF auroral radars, for which only the $\frac{1}{2}$ E mode is possible.

Plasma drift velocity along the beam, backscattered power and spectral width of the signal are the three principal parameters which the radars measure. These three parameters are determined using the complex autocorrelation function (ACF) of the received signal, which is achieved by utilizing a multi-pulse transmission sequence. The radars transmit a seven-pulse sequence common mode of operation. The pulses are separated by integral multiples of the unit pulse separation time. During the common mode of operation the radars transmit their seven-pulse pattern (0, 9, 12, 20, 22, 26, 27) during a 100 ms transmission window. The radars switch to receiver mode after each pulse is transmitted and the return signal is sampled periodically and processed in order to produce the ACF for each range, each a function of the lag time. The multi-pulse sequence is usually repeated 70 times at each beam position for a 7 s dwell time and the 70 resulting ACFs are integrated and averaged to increase the signal to noise ratio.

Analysis of the auto-correlation function of the returned signals yields backscatter Doppler spectra, from which can be derived the spectral characteristics of power, line-of-sight (l-o-s) Doppler velocity, v_{los} , and spectral width, Δv (Hanuise *et al.*, 1993). The Doppler velocity gives an estimate of the radar l-o-s component of the plasma convection velocity (Nielsen and Schlegel, 1983; Villain *et al.*, 1985; Ruohoniemi *et al.*, 1987), and hence two radars with

overlapping field-of-view, such as CUTLASS (*Lester et al.*, 2004), can create vector maps of convection flow across large regions of the high-latitude ionosphere (*Nielsen et al.*, 1983b). For this reason SuperDARN radars are generally deployed in pairs, so as to give as wide vector coverage of the auroral and polar cap region as possible (*Milan et al.*, 1997).

3.1.3 The map potential model

As has been said before, the SuperDARN HF radars provide l-o-s velocity measurements of ionospheric convection flow over the polar regions of the northern and southern hemispheres. Although measurements of l-o-s velocity can provide us with valuable information on the motion of the plasma, it is more useful to know the full vector velocity if a true picture of the convection pattern is to be derived. A number of techniques have been developed to obtain 2-D plasma flow vectors from these l-o-s observations, such as the “merging” technique which is assumed to be the most accurate method of deriving local flow vectors from l-o-s velocities. This technique allows 2-D vectors to be determined where there are simultaneous co-located l-o-s measurements within the fields of view of a radar pair. As there are not many overlapping l-o-s velocities, the area over which the convection pattern can be imaged is relatively small (e.g. see, figure 3.3(c) compared with figure 3.3 (b)). In an effort to improve the coverage availability, the “Map Potential” model was developed by *Ruohoniemi and Baker* (1998). As merged vectors can not be measured due to poor coverage from one radar of a pair, multiple l-o-s velocities serve to constrain the possibilities for the large scale convection pattern, which can be measured using mathematical fitting procedures that will be discussed below.

Initially the l-o-s velocity data are filtered to remove data with error estimates greater than 200 m s^{-1} and also ground-scatter. The smoothed velocities are then mapped onto a polar grid (e.g. Fig. 3.3(a)). These gridded data from each radar are then used to estimate a best-fit solution for the electrostatic potential, which is expressed in spherical harmonics up to an order specified by the user.

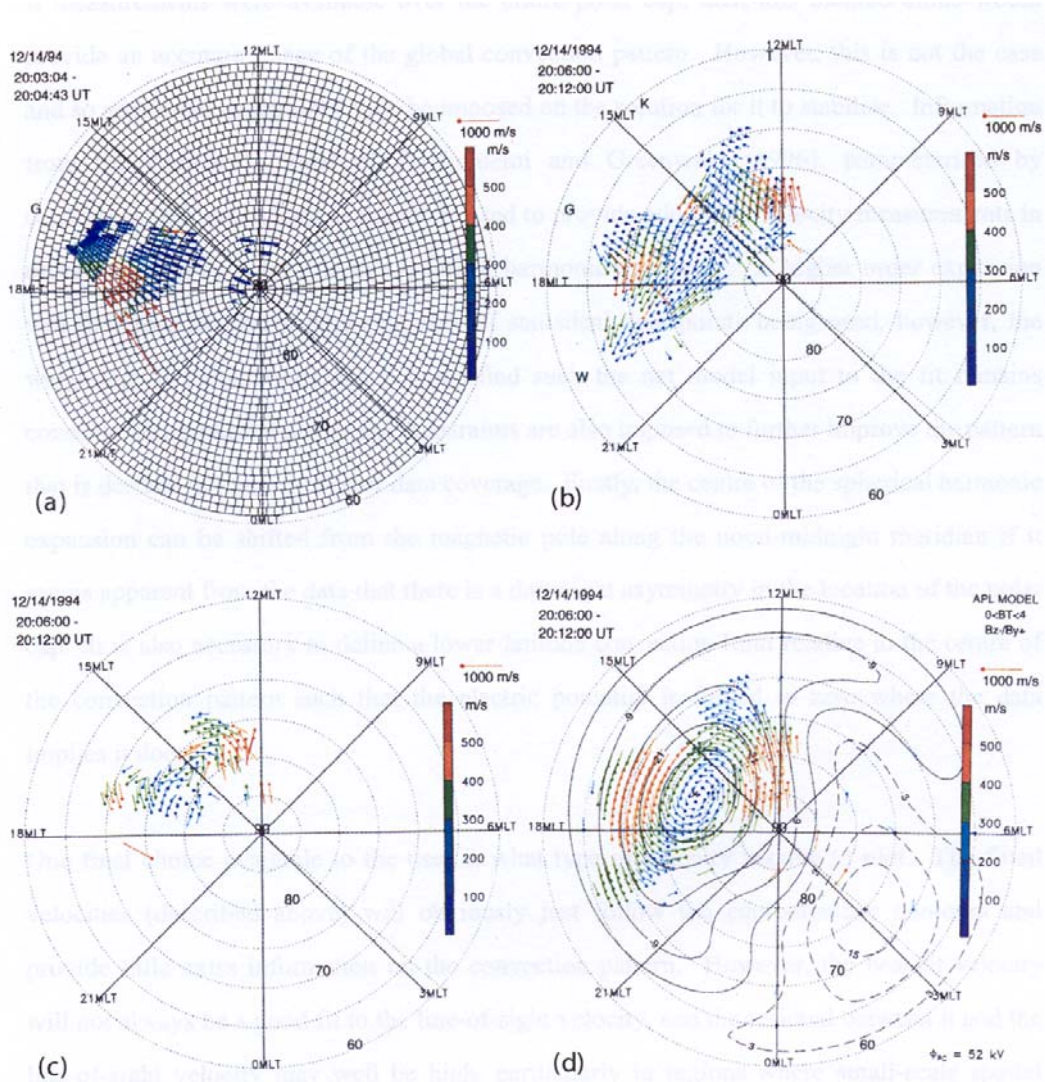


Figure 3.3 Exemplar SuperDARN data after various levels of analysis. (a) Filtered, averaged, line-of-sight velocity data from the Goose Bay radar, shown on the global grid used for spatially averaging the data. (b) The average line-of-sight velocity data from four of the northern hemisphere SuperDARN radars (indicated by their letter codes, listed in table 3.1). (c) Convection velocity vectors obtained by merging the overlapping line-of-sight velocity values in (b). (d) Solution for the global convection pattern obtained by fitting the line-of-sight velocity data in (b) and data from a statistical convection model to a 4th order expansion of the electrostatic potential in spherical harmonics; the streamlines are equipotentials of the ionospheric electric field shown every 6 kV (from *Grocott, 2002*).

The electrostatic potential on the grid is related to the convection electric field by $\mathbf{E} = -\nabla\varphi$, which is related to the velocity via the following equation:

$$\mathbf{V}_D = \frac{\mathbf{E} \times \mathbf{B}}{B^2} \quad (3.1)$$

where B is the local magnetic field.

Minimizing the residual between the l-o-s velocity and the projection of the fitted velocity onto the l-o-s direction then provide us with the fitted velocity. The plasma streamlines of the modeled convection pattern (e.g. Fig. 3.3(d)) are then represented by the equipotentials of the best-fit solution.

Availability of velocity measurements over the entire polar cap would enable this method to provide us with a highly accurate image of the global convection pattern. However, this is not usually the case and we must impose more on the solution for it to stabilize. Additional velocity measurements are provided by information from the statistical model of *Ruohoniemi and Greenwald (1996)*, in order to constrain each term in the spherical harmonic expansion. A larger number of statistical data points are needed for higher order expansions, though, the weight of these can be adjusted such that the net model input to the fit remains constant. Also, there are a number of additional constraints which are imposed to further improve the pattern that is driven in areas with poor data coverage. In areas with a large amount of radar data (e.g. afternoon cell in fig 3.3d) there can be a high degree of confidence regarding the large scale pattern and the potential associated with that cell, whereas in areas with no radar data (e.g. morning cell in fig 3.3d) the flow pattern is entirely determined by the statistical model which makes it difficult to reach any conclusions based on the configuration of the cell. If the data shows a day-night asymmetry in the polar cap region, the center of the spherical harmonic expansion can be shifted from the magnetic pole along the noon-midnight meridian. We also need to define a lower-latitude convection limit relative to the centre of the convection pattern such that the electric potential is forced to zero at the equatorward boundary of the convection pattern.

Finally, there is an opportunity of choosing the type of velocity vectors which the user is going to use to plot the data. There are two types of velocity

vectors available in this software: the fitted vectors and the “true” vectors. The fitted velocities (described above) will follow the equipotentials contours and provide little extra information on the convection pattern. However, the best-fit velocity will not always be a good fit to the l-o-s velocity, and the residual between it and the l-o-s velocity may well be high, particularly in regions where small-scale spatial structures have not been defined by the fit. It is therefore often useful to plot what are called “true” vectors. These vectors are resolved using the l-o-s velocity and the tangential component of the fitted velocity. This ensures that nothing of the original data is lost, in contrast to relying purely on the best-fit result (*Grocott, 2002*).

3.2 ACE spacecraft

Launched in August 1997 aboard a Delta II rocket, the ACE (Advanced Composition Explorer) spacecraft provides us with a comprehensive analysis of the upstream solar wind and IMF. ACE was designed by the John Hopkins University Applied Physics Laboratory (JHU/APL). It is located near the L1 Lagrangian point, some 221 RE upstream of the Earth, close to the Sun-Earth line. This spacecraft accommodates a total of ten instruments, nine scientific instruments for the primary mission and one engineering instrument for a secondary mission (*Chiu et al., 1998*). Upstream solar wind and IMF conditions during the intervals, which will be discussed in chapter 4, were measured using the Magnetic Field Experiment (MAG) (16-s), and the Solar Wind Electron, Proton, and Alpha Monitor (SWEPAM) (64-s) instruments (*McComas et al., 1998; Smith et al., 1998; Stone et al., 1998*). The ACE/MAG instrument is a twin triaxial fluxgate magnetometer system, which can measure the local interplanetary magnetic field (IMF) direction and magnitude and establish the large scale structure and fluctuation characteristics of the IMF at 1 AU upstream of Earth as a function of time throughout the mission. ACE/SWEPAM measures the solar wind plasma electron and ion fluxes (rates of particle flow) as functions of direction

and energy using ion and electron sensors. Both sensors use electrostatic analyzers with a fan-shape field-of-view. These data provide detailed knowledge of the solar wind conditions and internal state every minute.

ACE data corresponds to a distance of 1.5 million kilometers from Earth. Thus, whenever the ACE spacecraft observes features in the solar wind they haven't yet arrived at the near-Earth space environment. Hence a time delay needs to be considered between ACE and all phenomena which may result on Earth. In order to estimate the time delay in our studies we have used the method of *Khan and Cowley* (1999), and include the propagation time in the solar wind upstream of bow shock, the frozen-in transit time across the subsolar magnetosheath, and the Alfvénic propagation time along open field lines from the subsolar magnetopause to the ionosphere.

3.3 DMSP auroral particle instruments

The first Defense Meteorological Satellite Program (DMSP) spacecraft was launched in January 1965. The spacecraft are in near-polar and circular orbits at an altitude of 835 to 850 km to provide data for the specification of terrestrial weather and the near Earth space environment. The orbital inclinations of these spacecraft are 96 degrees. One of the space environment sensors which have been flown on DMSP F12, F13, and F14 spacecraft is the SSJ/4 (*Hardy et al.*, 1984), designed to measure the flux of precipitating electrons and ions with energies between 30 eV and 30 keV. This instrument is an electrostatic analyzer and observes only highly field-aligned particles well within the loss cone. The special sensor for ions, electrons, and scintillation (SSIES) (*Rich and Hairston*, 1994) provides measurements of the horizontal plasma flow and ion density at a rate of 6 samples per second.

3.4 Imaging ultraviolet aurora

Magnetospheric studies can provide us with a better understanding of how charged particles, magnetic fields, and electric fields interact with each other. Such studies also provide us with information regarding how these interactions are affected by external influences, such as the solar wind and its magnetic field, which can lead to a variety of phenomena including the aurora. Examining the global aurora can also provide information on the dynamic of magnetospheric regions. It has been almost 50 years since the first in situ measurements of magnetospheric particles and fields were made and there have been many missions, which have subsequently made such measurements. However, the IMAGE spacecraft is the first space mission to observe the magnetosphere by remote sensing techniques only (*Mende et al.*, 2000a).

The IMAGE satellite instrument complement includes three Far Ultraviolet (FUV) instruments, the Wideband Imaging Camera (WIC) which provides broad band ultraviolet images of the aurora for maximum spatial and temporal resolution, the Spectrographic Imager (SI) which images different types of aurora, and the Geo which observes the distribution of the geocoronal emission. In this thesis, only data from the WIC have been used.

WIC is used primarily to image the total intensity of the aurora in a wavelength region most representative of the aurora source and least contaminated by dayglow. With a sufficient resolution to resolve auroras on a scale of 1 to 2 latitude degrees, WIC covers the entire polar regions from spacecraft apogee, which makes it a good instrument to study the global aurora (*Mende et al.*, 2000b).

The instrument is sensitive in the spectral region from 140-190 nm. Mounted on the rotating IMAGE spacecraft, the WIC views radially outward and has a field of view of 17° in the direction which is parallel to the spacecraft spin axis. Its field of view is 30° in the direction perpendicular to the spin axis, although only a $17^\circ \times 17^\circ$ image of the Earth is recorded.

3.5 The Iridium satellite constellation

Orbiting at low Earth altitude, the Iridium system consists of ~70 satellites, each of which carries a 48nT resolution engineering magnetometer as part of the attitude determination system which is adequate to detect large scale Field Aligned Current (FAC) (*Anderson et al.*, 2000). Iridium satellites have polar orbits at 780 km altitude, in six equally spaced orbit planes with at least eleven satellites in each plane, which have an ~2 hour MLT spacing. Johns Hopkins University Applied Physics Laboratory (JHU/APL), has developed techniques to process Iridium magnetic field data and obtain global maps of magnetic perturbations due to FACs in both hemispheres on time scales of a few hours or less. The magnetometers are sampled 11 times per second for use on board, but saved at lower resolution for telemetry to the ground, typically one data sample every 200 seconds although higher sampling rates are used intermittently. One of the advantages of having multiple satellites in each orbit plane is to overcome the coarse time sampling on individual satellites. Even so, the time sampling determines the effective time resolution of the system for specifying the global current system. In order to generate maps of the global magnetic perturbation (ΔB) pattern, the satellite locations and cross track perturbations are transformed to Altitude Adjusted Corrected Geomagnetic (AACGM) coordinates (*Baker and Wing*, 1989). Then a coordinate system centered on the statistically averaged auroral zone center is defined, displaced 3.1° toward midnight (*Holzworth and Meng*, 1975). In this auroral centered system longitude is divided into 16, 30° wide sectors with centers spaced 15° , giving a resolution of ~2 hours. All cross track ΔB values are then accumulated in each sector to give a latitude profile of ΔB by averaging the data in 2° bins shifted by 1° of latitude.

In order to check the accuracy of the Iridium data set (intensity and location of the FACs), supplementary corroboration is needed. Some of the checks of the Iridium system data are imaging of auroral UV and visible

emissions, and convection electric fields obtained from ground based radars, examples of which will be explained in more detail in chapter 4.

3.5.1 FACs from the Iridium satellite constellation

The large-scale distribution of the global FACs can be measured directly from the magnetometer data with a resolution determined by the 30 longitude spacing between orbit planes (*Waters et al.*, 2001).

Engineering magnetometer data have been recorded on a non-interference basis for scientific use from all ~70 satellites distributed since February 18, 1999 (*Anderson et al.*, 2000). Although the Iridium system magnetometers are digitized with a low resolution of 48 nT, they are adequate to sense FAC signatures. In order to be able to use the data from so many satellites for analytical purposes, the processing has been automated. The primary step is to transform the model magnetic field IGRF-1995, into the satellite coordinate system and take it out of the observations. A matrix is then derived from the residuals of all the three components which are correlated with the main field. This matrix corrects for cross-talk, departures of sensor orientation from the assumed body coordinates, set field offsets, and increases drift. As the final step, periods longer than 26 minutes which correspond to 1/4 orbit, are high pass filtered by zeroing the Fourier coefficients. This latter process will eradicate extensive period residuals, attributed mainly to errors in the model field. By applying the filter to intervals of data when time resolution was high enough to determine noticeably the FACs on a single pass, the filter period cutoff was selected, and in order to measure when the filter started to twist the polar cap signature, shorter filter periods are used progressively. The next step is to distinguish physical signals from noise. In order to do that, the distribution of the absolute values of final residuals is constructed and the noise level assessed from the medium of this distribution.

One of the interesting points, which came out of the work of *Anderson et al.* (2000), was the mirror effect of the perturbations measured in opposite hemispheres. The perturbations mentioned above, were measured using the

satellite track and the net perturbation over the polar cap region 1/2 perturbation (Iijima *et al.*, 1982). According to some investigations (Erlandson *et al.*, 1988; Watanabe *et al.*, 1996), the data collected from the Iridium satellites, demonstrate negligible substantiation for a third current sheet, as the satellite track is roughly dawn-dusk so the Region 0 system is not expected to add extensively to the signals. East-west magnetic perturbation maps are shown in Figure 3.4, where figure 3.4.a indicates the perturbation pattern resulting from idealized concentric cylindrical distributions of region 1/2 current. The colors blue and red represent eastward and westward perturbation respectively and the little solid arrows indicate the sense of magnetic perturbation vectors. Figures 3.4.b and c, show perturbation maps for the northern and southern hemispheres (The southern hemisphere map is viewed looking down from the north through the Earth) accordingly which are derived from Iridium magnetometer data, for a three hour interval. Gray dots indicate satellite locations for which magnetometer readings are available. These perturbation maps are simplified as they do not contain Region 0 or Harang discontinuity currents, although on the other hand, they do indicate the basic perturbation pattern one expects to find, that is eastward at dusk, westward at dawn and sunward over the polar cap. In order to produce these global perturbation patterns, the satellite location and cross track perturbations are transformed to Altitude Adjusted Corrected Geomagnetic (AACGM) coordinates. Then a coordinate system will be defined centered on a statistically average auroral zone center, displaced 3.1° toward midnight (Holzworth and Meng, 1975) Longitude is divided into $16 \times 30^\circ$ wide sectors with centers spaced 15° , giving a resolution of ~ 2 hours. All cross track ΔB values are then added up to give a latitude profile of ΔB by averaging the data in 2° bins shifted by 1° . In order to work out the average, the values are weight by a cosine taper that goes to zero at the edge of the longitude sector, $\cos(\pi(\lambda_0 - \lambda_i)/2\Delta\lambda)$ where λ_0 is the center longitude of the sector, λ_i is the longitude of the measurement and $\Delta\lambda$ is the sector longitude half width (15°). The data are also weighted by the dot product of unit vectors in the cross track and azimuth directions, as the cross track and

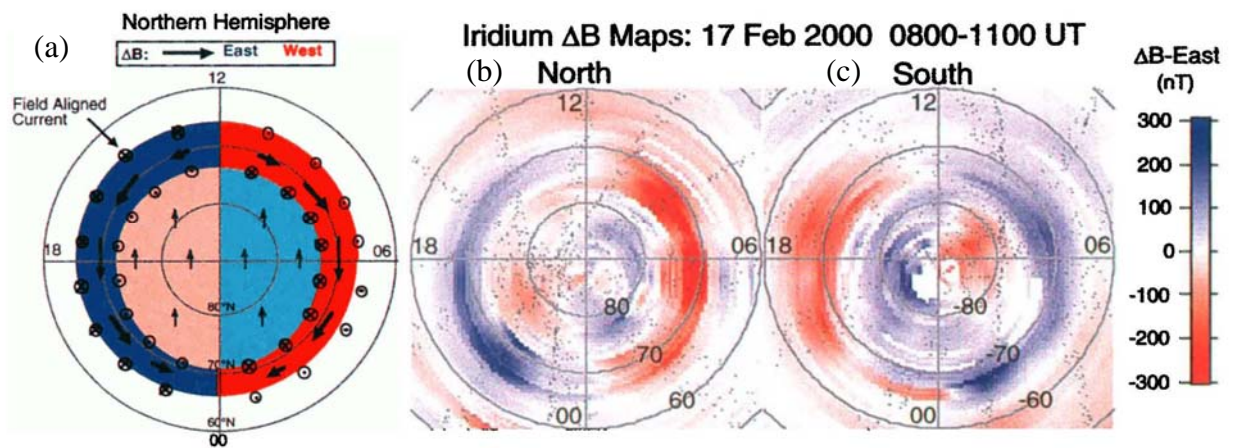


Figure 3.4 Illustrates East-west magnetic perturbation maps from the northern and southern hemispheres from 0800-1100 UT from 17 February, 2000 and an idealized Region 1/2 perturbation pattern (after *Anderson et al.*, 2000)

magnetic azimuth directions are not identical. At the final stage the east-west average ΔB is then mapped back to AACGM coordinates (*Anderson et al.*, 2000).

3.6 NOAA satellites

The National Oceanic and Atmosphere Administration Polar Orbiting Environmental Satellites (NOAA/POES) circle the Earth and provide global information from 870 km above the Earth providing daily global coverage, with morning and afternoon orbits that deliver global data, for improvement of weather forecasting.

These satellites carry a number of monitors, which detect the precipitation of energetic ions and electrons into the atmosphere and the particle radiation environment at the altitude of the satellite (*Evans and Greer*, 2000).

3.7 Summary

In this chapter we have described the instruments which have been employed in the collection of data used in this thesis. In the next 3 chapters we discuss the use of these instrument in various studies such as measurement of ionospheric convection velocities by the SuperDARN HF coherent radars which can provide information on the large-scale convection pattern over most of the northern (and some of the southern) hemisphere polar ionosphere. The ability of combining the convection patterns with the measurements of the magnetic field in the magnetosphere and in upstream interplanetary space, makes SuperDARN a unique tool in the investigation of solar wind-magnetosphere-ionosphere interactions. The work discussed in the next chapter employs these data resources in studying the dynamics and formation of transpolar arcs.

Chapter 4

Multi-instrument observation of a transpolar arc in the Northern Hemisphere

4.1 Introduction

Previous chapters have described the solar-terrestrial environment and reviewed more recent work and demonstrated the importance of understanding the transpolar arc formation and dynamics, which are currently of considerable interest. In this chapter we present a case study of a transpolar arc, discuss its formation and the motion caused by changes in the distribution of open flux with the polar cap as it is affected by dayside reconnection.

The transpolar arc of interest was imaged by the Imager for Magnetopause-to-Aurora Global Exploration IMAGE FUV/Wide-band Imaging Camera (WIC) instrument (*Mende et al.*, 2000a, 2000b), during a 3-h interval on 5 February 2002, detail of which is fully explained in section 4.2. Observations indicate that a burst of reconnection in the geomagnetic tail, which was not associated with a substorm, was responsible for the formation of the arc. The arc initially formed across the central polar cap, extending from near midnight to noon such that the polar cap was approximately divided in half. The subsequent motion of the arc was controlled by the amount of open flux being added to the dawn sector polar cap from a magnetopause reconnection site on the post-noon side of the magnetosphere. The dayside reconnection happened during a period when the IMF B_y component was dominant, although the B_z component initially remained positive, and resulted in strong westward azimuthal flows in the noon sector. The arc continued to move towards the duskside auroral oval after the IMF B_z turned

Chapter 4: Multi-instrument observations of a transpolar arc in the Northern Hemisphere

southward. A keogram of the FUV/WIC auroral observations along the dawn-dusk meridian provides further evidence of the expansion and contraction of the polar cap during the period in which different IMF orientations occurred. Furthermore, section 4.3 compares images from IMAGE and ionospheric convection flow from SuperDARN measurements. Vortical convection flows occurred exactly at the time and location of the formation of the transpolar arc as it moved across the polar cap. Section 4.4 will supplement the observations shown in sections 4.1-3 with particle precipitation data from DMSP spacecraft, in order to investigate the magnetospheric origin of precipitating particles associated with the TPA. Although there has been a lot of work published on transpolar arcs (TPAs), there are still unanswered questions concerning the magnetospheric source regions and the electrodynamic involved in the initial appearance of the oval-aligned transpolar arc, such as the relation between the transpolar arc, field-aligned current (FAC) sheets, and the overall convection pattern.

In section 4.5, we examine the FAC systems associated with the transpolar arc of interest. In this element of the study three different data sets, the FAC obtained from Iridium magnetic field data, auroral emissions observed by the IMAGE spacecraft, and the curl of the ionospheric flow velocity measured by the SuperDARN radars are compared.

Section 4.5 begins with a brief explanation of how the FAC data are obtained from the Iridium satellite magnetic field data (fully described in chapter 3). Section 4.6 discusses the observation presented in the present chapter, in order to identify features associated with the transpolar arcs. The observations are then compared with the theoretical model developed by *Milan et al.* (2005) to explain the formation of the arc through reconnection in the tail as well as the subsequent motion of the arc in response to dayside reconnection. This chapter is based upon the work in *Goudarzi et al.* (2008).

4.2 Event Overview

4.2.1 Interplanetary magnetic field data

In Figure 4.1 we show upstream solar wind and interplanetary magnetic field (IMF) conditions during the interval of interest, 0800-1300 UT on 5 February 2002, measured using the SWEFAM and MAG instruments, respectively, on the Advanced Composition Explorer (ACE) satellite (*McComas et al.*, 1998; *Smith et al.*, 1998; *Stone et al.*, 1998). ACE orbits the L1 Lagrangian point at approximately $X \approx 234 R_E$ (Earth Radii) sunward of the Earth. IMF GSM components are plotted as a function of corrected universal time (UT plus the estimated propagation time from the satellite to GSM $X=0$) which for this interval has been calculated as 69 minutes using the method of *Khan and Cowley* (1999). The time period during which the transpolar arc was observed within the polar cap is highlighted in grey in Figure 4.1.

The IMF was associated with an away sector Parker spiral magnetic field ($B_x < 0$); the total field magnitude was large ($B \sim 16$ nT). The B_x component was negative throughout the whole interval. The B_z component was positive for an hour and forty five minutes before it turned negative at approximately 09:40 UT. The B_y component was quite variable and changed its direction several times before the arc appeared, which caused the variation in the IMF clock angle before 09:40 UT. As indicated in Figure 4.1 (highlighted section), the arc persisted for a period of three hours. There was a sudden change in B_z from being strongly negative to strongly positive right after the arc disappeared. This sudden change was also observed in the B_y behaviour, as it increased from zero to positive. The solar wind dynamic pressure (Fig. 4.1, bottom panel) reached a maximum of 9.5 nPa at about 11:00 UT and after that reduced to approximately 3 nPa.

05 Feb 2002

Ace IMF data

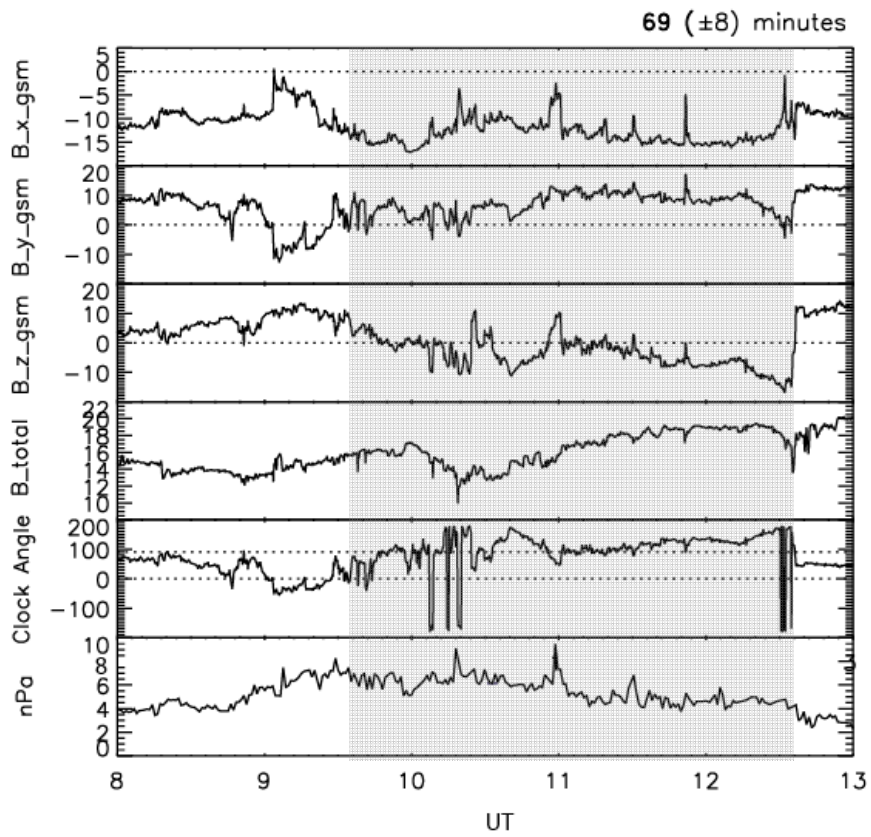


Figure 4.1 The interplanetary magnetic field components, B_x , B_y , and B_z in GSM coordinates along with the corresponding clock angle and solar wind dynamic pressure, measured by the ACE spacecraft. The measurement was made during a 5-h interval on 5 February 2002. Highlighted in grey is the period when the transpolar arc was observed.

4.2.2. IMAGE FUV data

The Far Ultraviolet (FUV) imaging system onboard the IMAGE spacecraft provides global images of the aurora. IMAGE was launched on March 25, 2000 into an elliptical polar orbit with an apogee altitude of 7.2 Earth radii and the perigee altitude of 1000km. The initial apogee was at 40 degrees north latitude. The Wideband Imaging Camera (WIC) experiment is one of three detectors installed on the FUV instrument (*Mende et al.*, 2000a, 2000b). The WIC camera is designed to image the whole Earth and the auroral oval from satellite distances greater than 4 R_E to the centre of the Earth.

A sequence of auroral images taken by FUV/WIC on 5 February 2002 during the development of the transpolar arc is presented in Figures 4.2a-4.2f. Each panel is presented in a magnetic latitude and MLT coordinate system, with local noon at the top and dusk to the left. Dayglow in the sunlit hemisphere is apparent at the top of each panel 4.2a-4.2d. In this sequence the transpolar arc is first apparent at about 09:03 UT (Figure 4.2b), starting to appear at the point where the aurora is brightest in the premidnight sector. Around 09:43 UT (Figure 4.2c) the complete transpolar arc can be observed to lie in the centre of the polar cap, slightly displaced to the dusk (dawn) side on the nightside (dayside). The transpolar arc exists within the polar cap for the next three hours. At 09:54 UT (Figure 4.2d), the width of the arc has slightly increased and stays like this for approximately 20 minutes before the arc starts to thin again. Another noticeable point in this figure, is the large burst of dayside aurora slightly equatorward of the main oval, which we assume is caused by the dayglow. As can be seen from figure 4.2, the dayglow intensity is variable which might be due to the variation in the strength of the magnetic field (Figure 4.1).

At 11:10 UT (Figure 4.2e), the arc slowly moves towards dusk. The arc continues its duskward motion and by 12:32 UT (Figure 4.2f), has moved across the polar region and appears to have merged with the duskward auroral oval. Prior to 10:00 UT the auroral oval remains relatively uniform in size, although, by

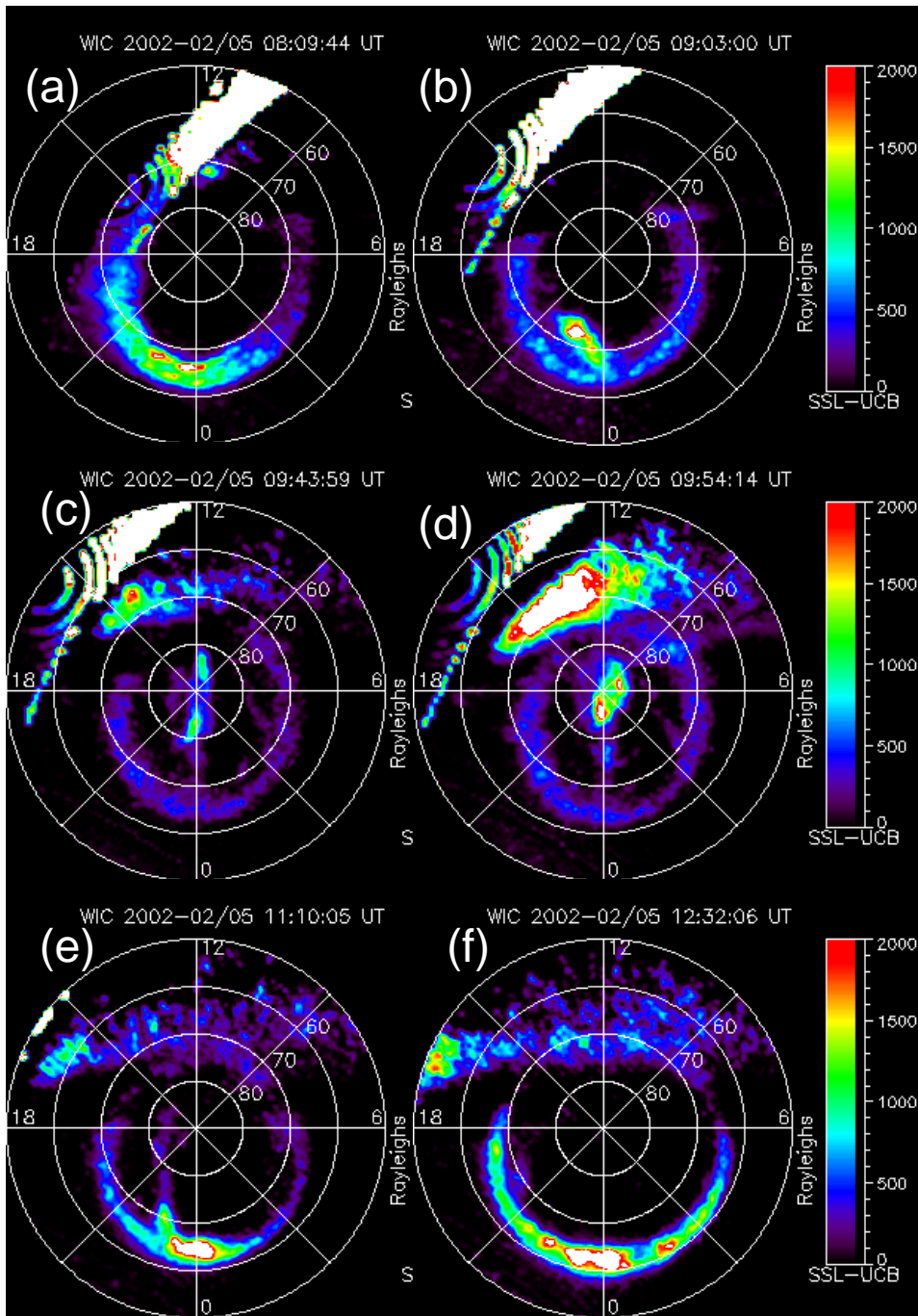


Figure 4.2 On 5 February 2002, the Imager for magnetopause-to-Aurora Global Exploration (IMAGE) FUV/Wide-band Imaging Camera (WIC) instrument provides images of the auroral configuration in the Northern Hemisphere. The data are plotted in magnetic latitude and magnetic local time, with noon toward the top and dusk to the left of each panel.

Chapter 4: Multi-instrument observations of a transpolar arc in the Northern Hemisphere

11:10 UT (Figure 4.2e) and especially by 12:32 UT (Figure 4.2f), the auroral oval has expanded to lower latitude.

The top panel of Figure 4.3 is a keogram of FUV/WIC auroral observations along the dawn-dusk meridian. The motion of the transpolar arc described above and the auroral oval is clearer in this Figure. The lower three panels of this figure are the three components of the IMF from the ACE spacecraft repeated from Figure 4.1. In Figure 4.3a the auroral oval is visible in both dusk and dawn sectors, and after 09:30 UT, the transpolar arc is also visible in the middle of the oval. From this observation it is also clear that the auroral oval starts shrinking at about 08:55 UT when the IMF becomes strongly northward. The process goes on until 10:00 UT when B_z becomes southward, and the polar cap starts to expand again, moving the auroral oval to lower latitudes. At about 09:36 UT a thick region of auroral luminosity is observed in the centre of the polar cap, the transpolar arc, which gets thinner as it travels towards dusk throughout the interval.

Using the technique described by *Milan et al.* (2003), and *Milan* (2004a, 2004b), we determined the open flux contained within the magnetosphere from the size of the polar cap in the auroral measurements, and the variation in this as a function of time. In his calculation, *Milan* (2004b), illustrated that the rate of change of open flux in the magnetosphere is determined by the competition between the rates of dayside and nightside reconnection. In order to describe the above statement, he used Faraday's law:

$$\frac{d}{dt} \int_{PC} \mathbf{B} \cdot d\mathbf{s} = \frac{dF_{PC}}{dt} = \phi_D - \phi_N \quad (4.1)$$

where \mathbf{B} is the magnetic field strength at ionospheric altitudes, F_{PC} is the flux contained in the polar cap, and ϕ_D and ϕ_N are the rate (voltages) of creation and destruction of open flux at the low-latitude dayside magnetopause and in the magnetotail, respectively (e.g. *Siscoe and Huang*, 1985; *Holzer et al.*, 1986; *Lockwood and Freeman*, 1989; *Lockwood*, 1991). If the polar cap remains

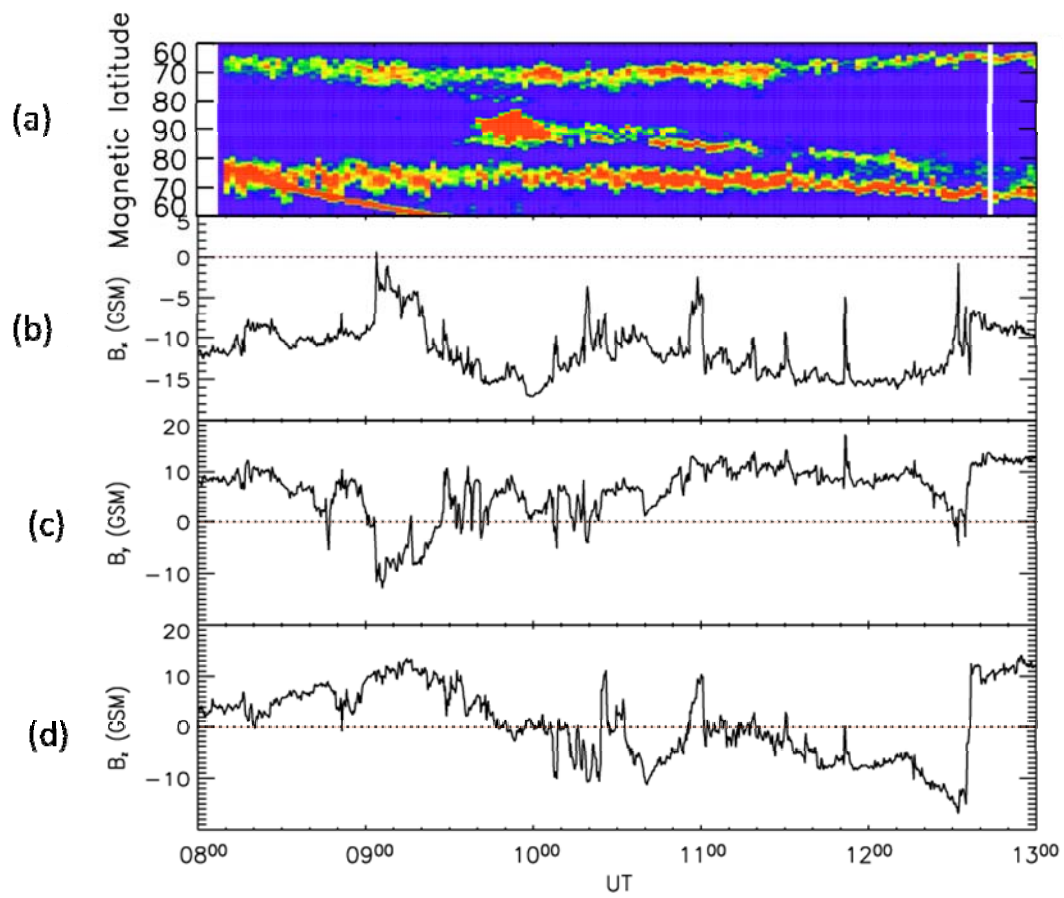


Figure 4.3 (a) Keogram presentation of the transpolar arc observed by the IMAGE FUV/WIC along the dusk-dawn meridian. (b, c, and d) IMF information from the ACE satellite.

approximately circular, then the rate of antisunward flux transport across this dawn-dusk meridian has been discussed by *Lockwood* (1991) and *Lockwood and Cowley* (1992) to be given by

$$\phi_{PC} = \frac{1}{2}(\phi_D - \phi_N) + \phi_V \quad (4.2)$$

Lockwood and Cowley (1992) included the voltage associated with a viscous interaction as $\phi_V=0$. In 2004, *Milan et al.* measured ϕ_D and ϕ_N from observations of the polar ionosphere, and used this to determine ϕ_{PC} (*Milan et al., 2004b*).

As was mentioned above, we used the same method in order to calculate the flux content of the polar cap. The total open flux together with the total open flux in each of the two sections of the polar cap, i.e. dawn and dusk sector is presented in Figure 4.4a, Figure 4.4b shows the rate of change of polar cap area (the difference between dayside and nightside reconnection rate) averaged over specific intervals and Figure 4.4c shows the IMF clock angle. These observations will be discussed in more detail in section 4.4.1.

4.3 *Ground-based SuperDARN convection*

Figure 4.5 shows the ionospheric convection measurements made by the SuperDARN radars, superimposed on the IMAGE auroral observations, which were shown in Figure 4.2. In order to produce the convection maps, we used 2-min averages of line-of-sight Doppler velocity observations made by eight Northern Hemisphere radars, from which the convection maps were derived using the technique of *Ruohoniemi and Baker* (1998). In Figure 4.5 each map shows the “true” vectors determined by the SuperDARN global convection mapping, colour coded by their magnitude. The black curves represent equipotentials of the convection electric field with little crosses denoting the centres of the convection cells.

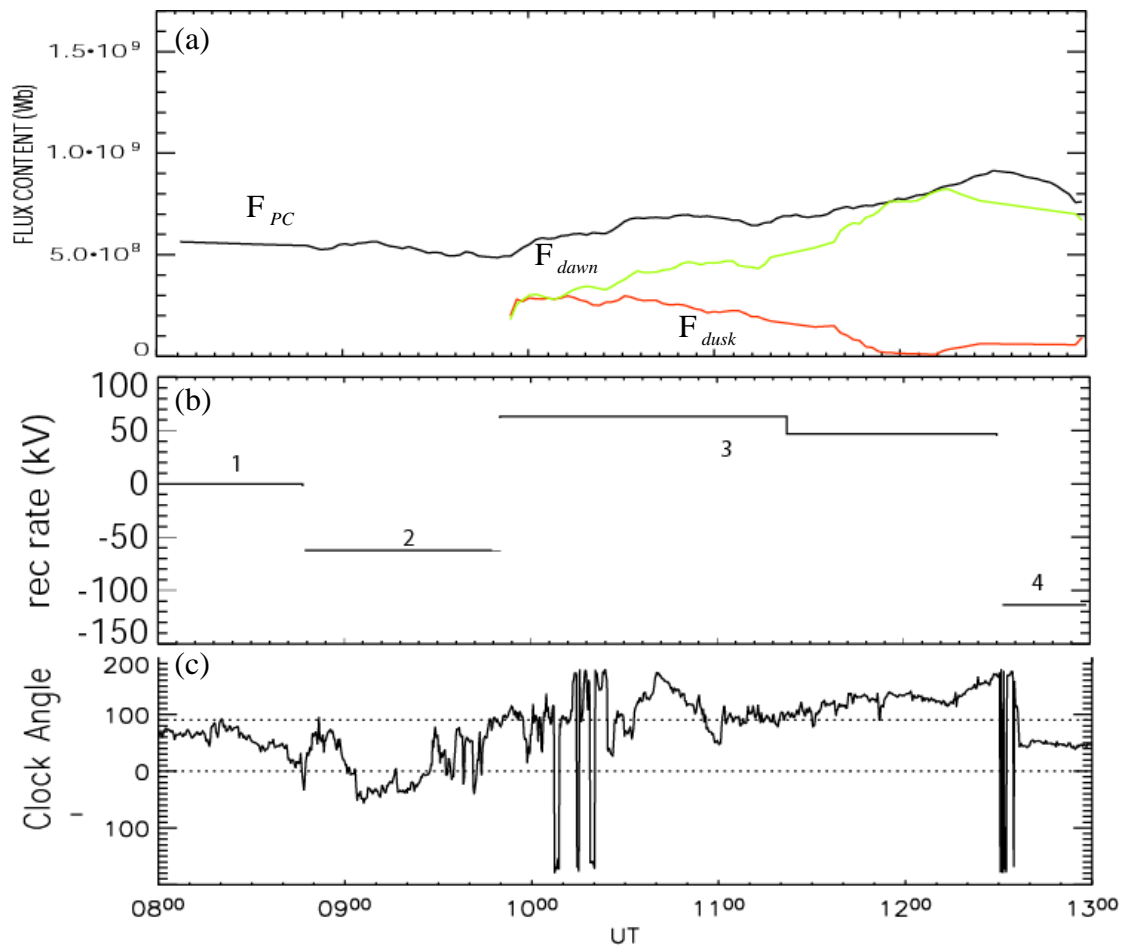


Figure 4.4 (a) Total polar cap flux (black curve), and flux contained downward (green curve) and duskward (red curve) of the transpolar arc, determined from the auroral observations. (b) Reconnection rates derived from the changes in polar cap flux (see text for more details). (c) IMF B_z component.

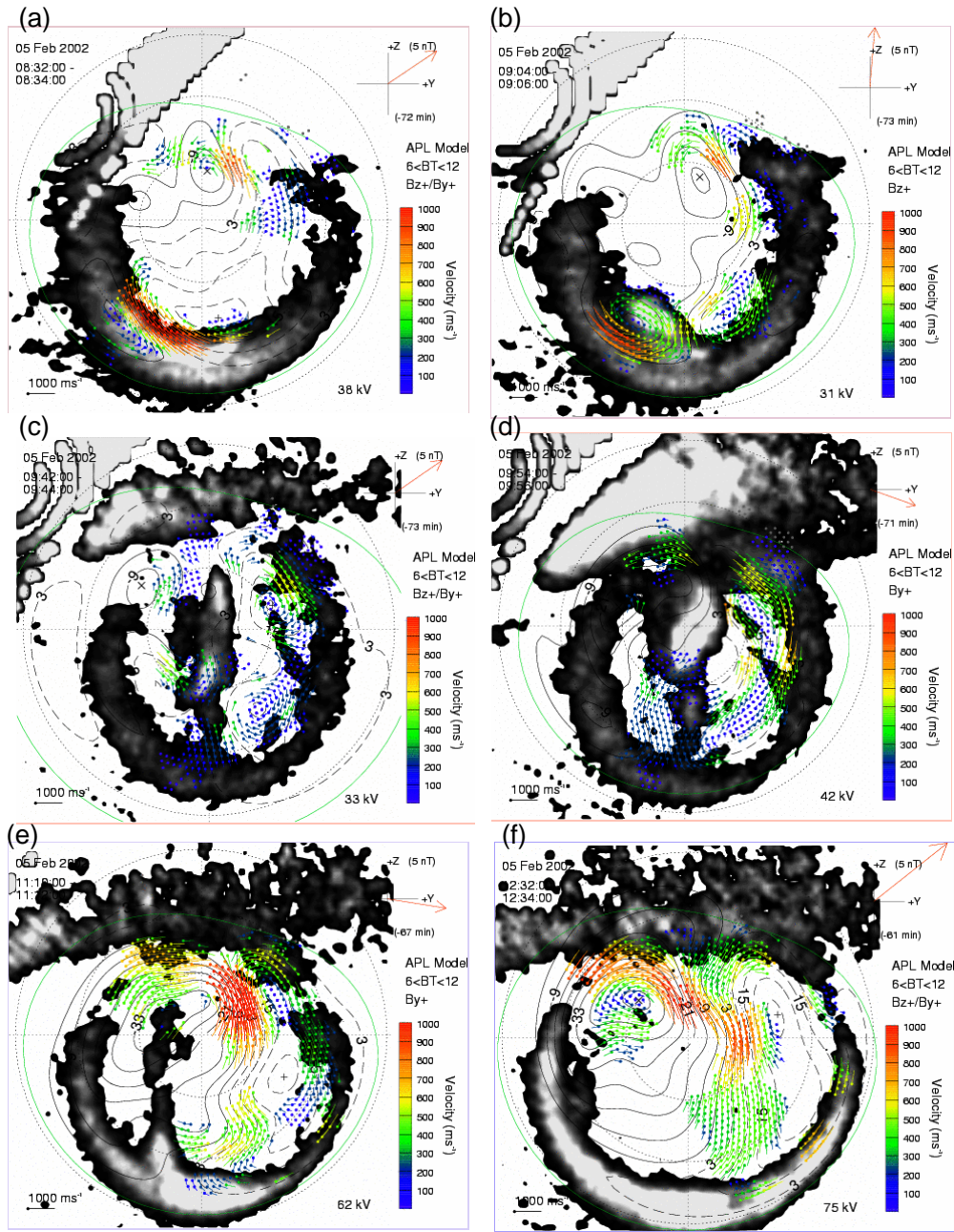


Figure 4.5 SuperDARN convection maps with superimposed IMAGE FUV auroral data.

Chapter 4: Multi-instrument observations of a transpolar arc in the Northern Hemisphere

Figure 4.5a, shows convection typical of positive B_y and B_z conditions. In this figure which is from 08:32 UT there are some sunward flows in the post noon sector indicative of reconnection at the tail lobe. There are two cells which are not symmetrical and slightly biased toward dawn, as a consequence of the IMF $B_y > 0$, (e.g., *Russell, 1972; Cowley, 1981; Reiff and Burch, 1985; Cowley and Lockwood, 1992; Huang et al, 2000; Milan et al., 2000; Chisham et al., 2004*). The bright spot in the premidnight sectors is associated with relatively strong eastward flows, similar to these reported by *Senior et al. (2002), Grocott et al. (2003, 2004)*, and *Walker et al. (1998)*. Such flows are usually observed during episodes of magnetotail reconnection happening during extended intervals of northward IMF but with no evidence of substorm activity. These have been termed TRINNIIs “tail reconnection during IMF-northward, nonsubstorm intervals”, by *Milan et al. (2005)*.

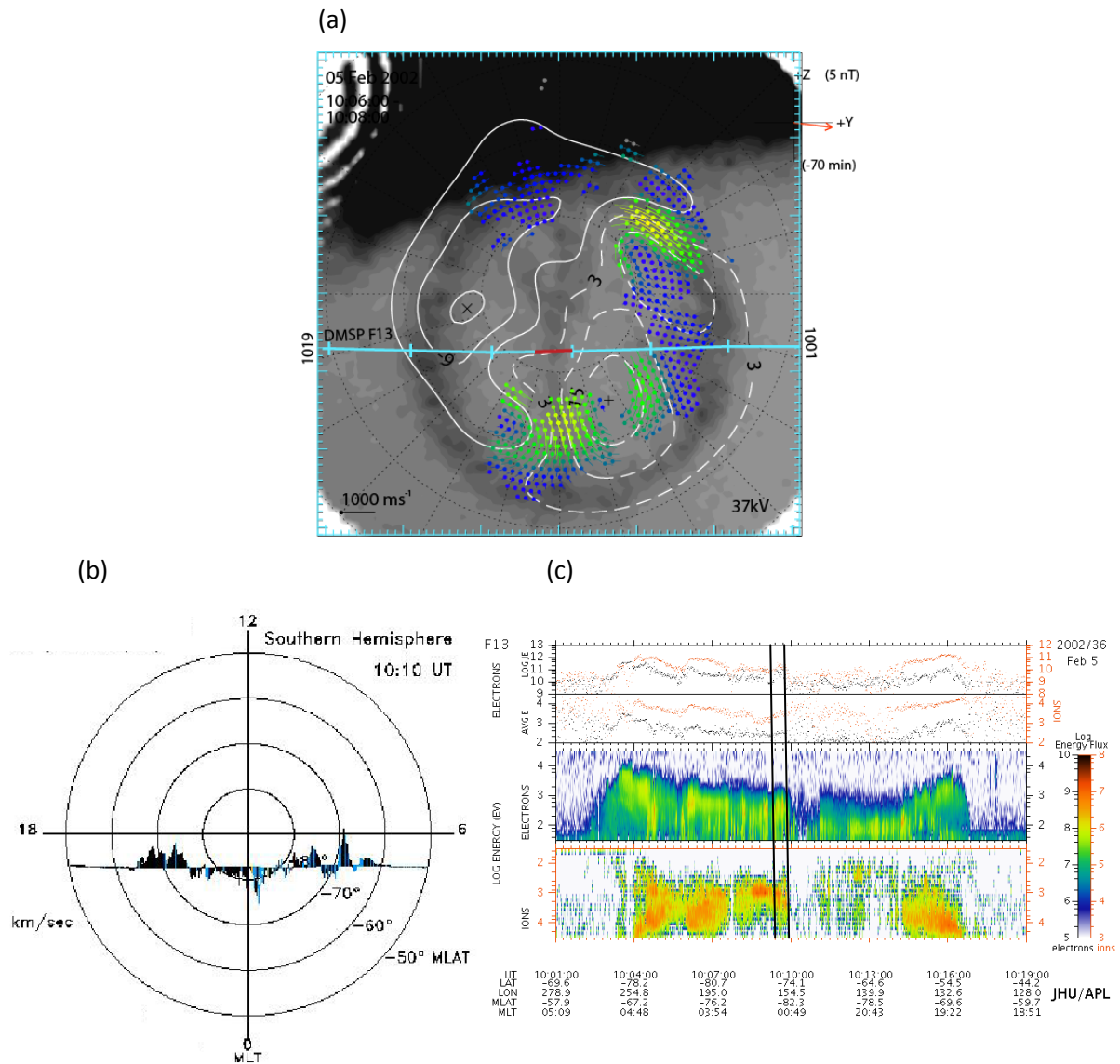
In Figure 4.5b there is a vortical flow pattern (anti-sunward flows at higher latitude and sunward flows at lower latitudes) coincident with the brightening in the nightside aurora, which seems to be the origin of the transpolar arc. These vortical flows last for 22 minutes and vanish right after the change in direction of B_y to negative while B_z is still positive. There are also some very strong flows at the dayside in the prenoon lobe convection cell. At the time the transpolar arc becomes fully formed (Figure 4.5c) the flows seem to be weaker at both dayside and nightside. The auroral oval appears to be displaced toward dawn as B_y is still positive. At 09:54 UT (Figure 4.5d), the y-component of the IMF is strongly positive, and that is when the width of the arc starts to increase and this process goes on for 12 minutes. From about 10:32 UT the IMF turns southward again, and that is when very strong anti sunward flows in the prenoon and sunward flows in the postnoon convection cells are observed typical of dayside low latitude reconnection. However, the flows in the dawn-sector polar cap are much stronger than the flows in the dusk sector indicating that new open flux is accumulating on the dawn side of the transpolar arc, which may explain why the arc is getting pushed toward dusk as newly opened magnetic flux is moved towards the dawn sector as can be seen in Figure 4.5e. This accumulation of open

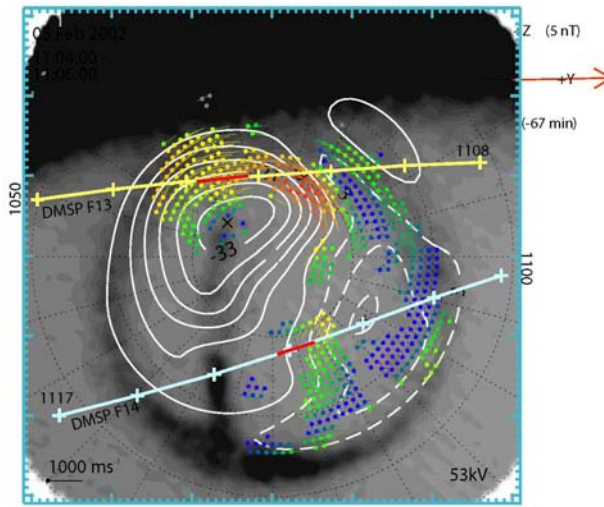
flux is also associated with the expansion of the auroral oval to lower latitudes. Figure 4.5f shows the auroral oval has expanded to lower latitudes by the time the IMF turns northward again after an hour of being southward. From the evidence given it seems that the motion of the arc is governed by the direction of the B_y and B_z components of the IMF. This motion will be discussed in more detail in section 4.4.2.

4.4 Particle precipitation overview

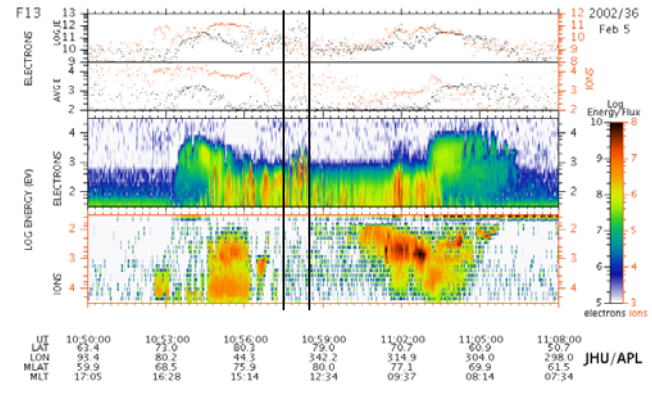
TPAs are associated with both ion and electron precipitation where the ion precipitation is spread across the arc and electron precipitation is more structured (*Frank et al.*, 1986; *Cumnock et al.*, 2002). The precipitating particle signature associated with theta aurora may also occur as an isolated region (of particles associated with the plasma sheet). The TPA, surrounded by particles normally associated with the polar cap, may map to a bifurcated magnetotail (*Frank et al.*, 1982, 1986; *Bythrow et al.*, 1985; *Hoffman et al.*, 1985). In this section, the ionospheric signatures of TPA of interest are studied using the particle precipitation data from DMSP.

Figures 4.6 and 4.7 illustrate the ionospheric footprint of DMSP satellite tracks as they passed the polar regions in the Northern and Southern Hemispheres, shown by yellow and light blue solid lines respectively. The tracks have been overlaid onto the corresponding FUV maps in the Northern Hemisphere only, due to lack of FUV data in the Southern Hemisphere. Combination of particle precipitation and auroral emission data provides a better understanding of the formation and dynamics of the TPA. By overlaying the satellite tracks, which passed the southern polar region on the FUV data in the Northern Hemisphere, one can compare the particle precipitation into the atmosphere in the Southern Hemisphere at the presence of the TPAs in the Northern Hemisphere. Although this is not the ideal scenario, this method can provide vital information regarding the conjugacy of the TPAs.

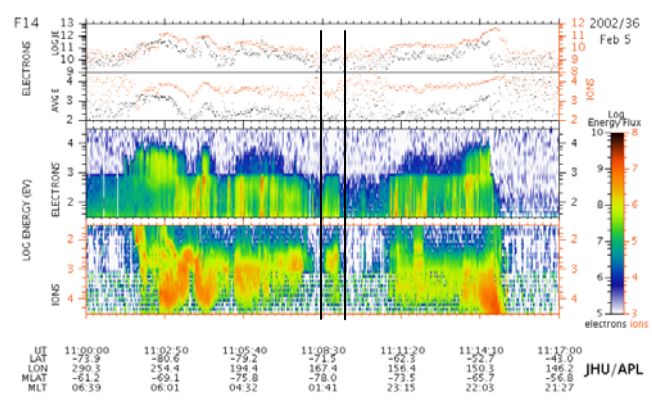




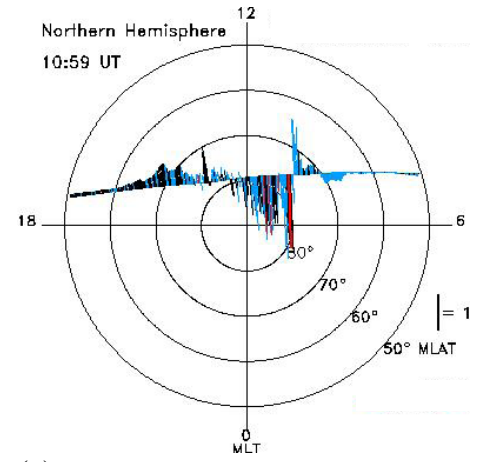
(a)



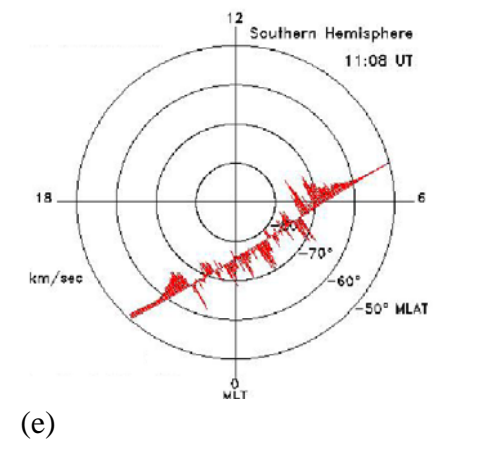
(b)



(d)



(c)



(e)

Figure 4.7 Data shown from DMSP F13 pass in the Northern Hemisphere and DMSP F14 in the Southern Hemisphere on 05 February 2002 (10:50-11:08 UT and 11:00-11:17 UT) that occurs during the FUV data period.

Chapter 4: Multi-instrument observations of a transpolar arc in the Northern Hemisphere

Figure 4.6a illustrates the DMSP F13 satellite track plotted over a FUV rendered over the 10:06-10:08 UT SuperDARN equipotential contours (Ruohoniemi and Baker, 1998) taken at the time DMSP F13 is at highest magnetic latitudes. The DMSP satellite track with horizontal plasma flows, perpendicular to the satellite track is shown in figure 4.6b. Figure 4.6c shows the F13 spectrogram includes, from top to bottom, (1) electron and ion integral energy flux, (2) electron and ion average energy, (3) precipitating electron spectrogram, and (4) precipitating ion spectrogram.

Figure 4.6a displays the 1001-1019 UT, interval of the global SuperDARN convection pattern (Ruohoniemi and Baker, 1998). The equipotential contours confirm an antisunward $\mathbf{E} \times \mathbf{B}$ drift over the TPA at this time. The drift information from DMSP F13 which is crossing the southern polar cap at this time shows antisunward flows in the southern hemisphere around midnight MLT which is expected as the IMF is positive B_y dominant. The DMSP F13 spectrogram shows an expanded oval, therefore it is very hard to distinguish the TPA signatures. However, the region marked by black solid lines indicates an increase in the ion energy flux for a short period in the post-midnight sector. Although, it is quite impossible to spot any special features, which would be associated with the TPA, there are large amounts of energetic protons (~ 1 keV) in the polar cap which raises an interesting topic to investigate.

At around 1100 UT, there are DMSP satellite passes over the northern and southern polar cap (Fig. 4.7a), tracks of which are overlaid on top of the 1050-1108 UT convection map. The ionospheric flows illustrated in the convection map, confirms the sunward, antisunward, and again sunward drifts shown in DMSP F13 pass (Figure 4.7c). The DMSP F13 spectrogram (Figure 4.7b) indicates an increase in the electron energy and flux at around 79° and 1400 MLT (shown by black solid lines in Figure 4.7b). This region is surrounded by regions void of ions and filled with energetic electrons. In the Southern Hemisphere, however, the spectrogram shows extended duskside and dawnside auroral ovals. In the middle of the oval observed, there is a region of high energetic ions disconnected from both sides of the oval, which can be associated with the TPA

in the Southern Hemisphere. The estimated location of the TPA in the Southern Hemisphere seems to be parallel to the TPA in the Northern Hemisphere with a 180° counterclockwise rotation, as it is found to locate in the post-midnight sector. Yet again another example of highly energetic ions are observed in the satellite data at the nightside (Figure 4.7d).

4.5 Field Aligned Current (FAC) observations

As previously mentioned in chapter 2, the distribution of the large-scale field-aligned currents, like ionospheric convection patterns, is strongly dependent on the magnitude and direction of the IMF. *Anderson et al.* (2006) presented a statistical analysis, the results of which illustrated that a direct correspondence between the Birkeland currents and the solar wind dynamo, and in particular that the most poleward currents, are intimately linked with magnetopause reconnection, regardless of the IMF orientation. Figure 4.8 presents the statistical distributions of the large-scale Birkeland currents under different IMF conditions derived by *Anderson et al.* (2006). These maps are obtained from an analysis of 3138 one-hour snapshots of global distributions observed by Iridium. The 8 panels are arranged according to the IMF direction projected in the Y-Z GSM plane, as indicated by the central diagram. The double line arrow in each panel shows the inferred direction of flow implied by the most poleward currents (*Anderson et al.*, 2006). What makes their statistical model appealing is its agreement with the theoretical and simulation results for convection driven by magnetopause reconnection (e.g., *Cowley et al.*, 1991). The convection patterns of *Cowley et al.* (1991) could be reproduced by assuming that the ionospheric electric field \mathbf{E} points from regions of downward FAC to regions of upward FAC and that convection velocities are given by $\mathbf{V} = \frac{\mathbf{E} \times \mathbf{B}}{B^2}$ where \mathbf{B} points downwards. The inferred most poleward flows are anti-sunward for southward IMF and sunward for northward IMF. For positive (negative) IMF B_y , the flows are directed toward dawn (dusk) and rotate progressively from anti-sunward to sunward as the IMF

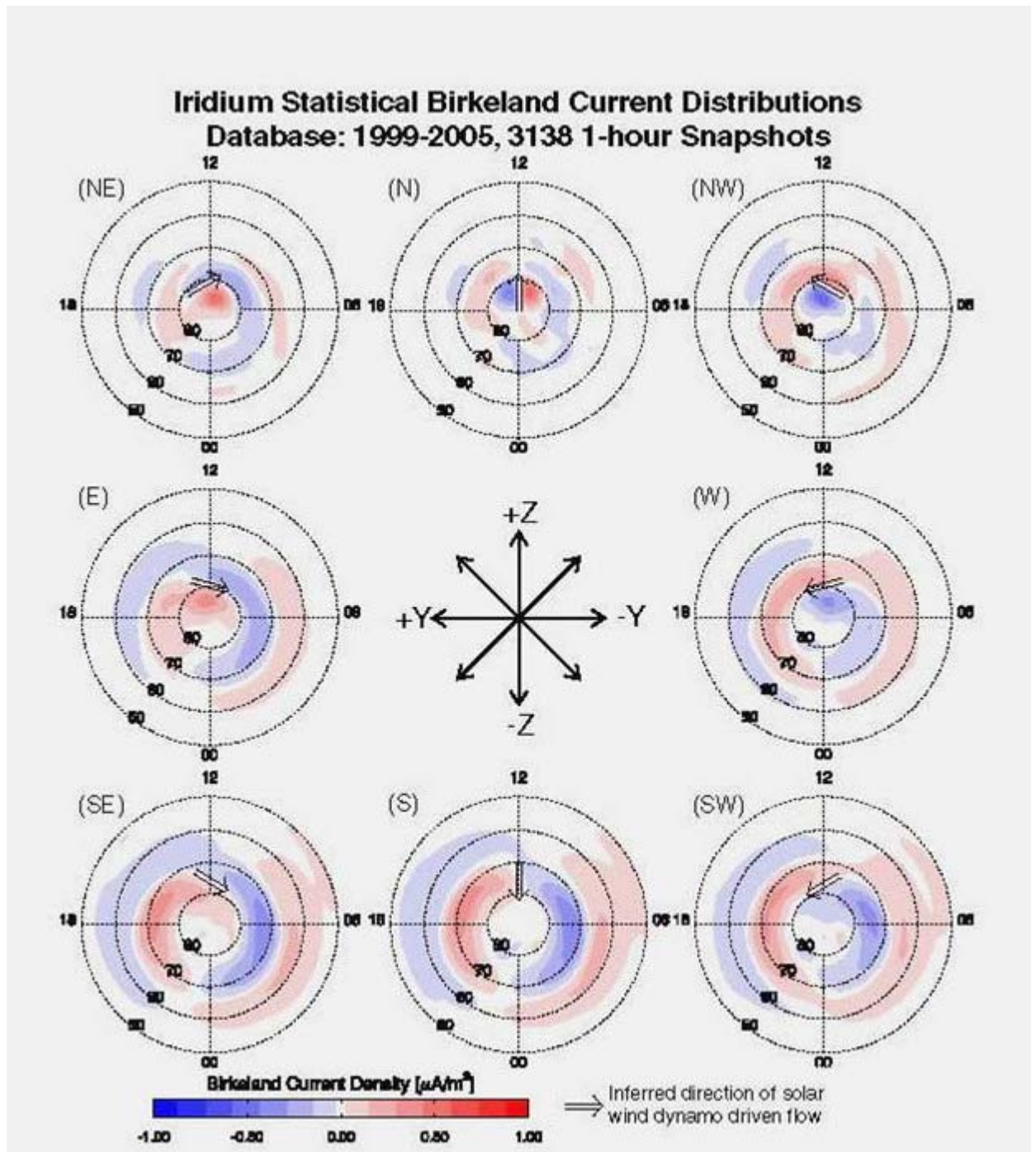


Figure 4.8 Indicates the statistical distributions of the large-scale Birkeland currents under different IMF conditions (after *Anderson et al.*, 2006).

turns northward.

Study of the global distribution of the Birkeland currents could have significant implications for understanding convection and energy deposition in the polar ionosphere. To this end, we examine in detail the FAC patterns observed by Iridium and deduced from SuperDARN convection measurements for the case study presented earlier on in this chapter.

4.5.1 Data and observations

Since the discovery of transpolar arcs, it has been suggested that the transpolar arc is a region that coincides with sunward convection, closed field lines and precipitating electrons of plasma sheet origin (e.g. *Peterson and Shelley*, 1984; *Frank et al.*, 1986). However, other observations, which demonstrate the occurrence of polar rain electrons, suggested the arcs are on open field lines, (*Hardy et al.*, 1982; *Hardy*, 1984; *Gussenhoven and Mullen*, 1989). Recent studies (e.g. *Milan et al.*, 2005; *Goudarzi et al.*, 2008) illustrate that transpolar arcs can form in regions where closed field lines are accumulated in return flows caught by opposing tension between the opposite hemispheres.

With so many different theories and explanations concerning the formation and dynamic characteristics of the transpolar arcs, it is crucial to find a new way to put these different theories to a test. One way of investigating whether transpolar arcs form on closed or open field lines, is to look at convection flows measured by SuperDARN radars to investigate whether the arcs are associated with shear flows driven by converging electric fields, which would be characteristic of open field line generation theories.

Examining the ionospheric convection maps provided by radar data is a good way of looking for shear flows. However, it is necessary to mention that occasionally the SuperDARN radars suffer from a lack of echoes either due to the absence of ionospheric irregularities or because of strong HF radio wave absorption in the ionosphere, which sometimes makes the observations uncertain. Therefore, in order to determine the conditions more accurately, we compare three

Chapter 4: Multi-instrument observations of a transpolar arc in the Northern Hemisphere

datasets from ground and space based instruments: the auroral images examined earlier on in this chapter along with the FAC distribution derived globally from both, SuperDARN HF radars and the constellation of Iridium satellites. Description of how FACs can be driven from Iridium satellite constellations was given in chapter 3. The FAC maps measured by SuperDARN radars are implied by the curl of the velocity field (derived from the electric potential) and has been determined using the technique described by *McWilliams et al.*, (2001) (after *Freeman et al.*, 1990; *Sofko et al.*, 1995). Below, we describe the method under which FACs are estimated.

According to *Sofko et al.* (1995), SuperDARN measurements of ionospheric convection can be used to directly estimate the FAC per unit Pedersen conductance. The FAC density at ionospheric altitudes can be written explicitly as:

$$J_I = [\Sigma_p \mathbf{B} \cdot (\nabla \times \mathbf{v})] + [(\mathbf{v} \times \mathbf{B}) \cdot \nabla \Sigma_p + (Bv) \cdot \nabla \Sigma_H] \quad (4.3)$$

where \mathbf{v} is the ionospheric plasma convection velocity, B is the geomagnetic field, Σ_p and Σ_H are the height-integrated Pedersen and Hall conductances, respectively. In relation to the SuperDARN co-ordinate convention, a positive FAC is radially out of the ionosphere, nearly anti-parallel to the magnetic field in the Northern Hemisphere. The SuperDARN coordinate (z direction is radially out of the ionosphere) convention, in our dataset, implies that an upward vorticity corresponds to a downward FAC and vice versa.

Conductivity estimates from the aurora are not 100% accurate as they can only be determined for specific spectral emission frequencies, therefore models are not accurate enough to correspond to minute by minute radar scans of the plasma convection. As a result, one cannot integrate up through the ionosphere to estimate the total conductance (*Germany et al.*, 1994). We note that the vorticity is in fact normalised by the Pedersen conductance and does not provide a direct measure of the FAC.

4.5.1.1 Comparison of auroral images and field-aligned currents

As explained earlier in this chapter, one of the best ways of studying the nature of the TPAs is to use the FAC maps to look for any features associated with the formation or motion of the TPAs. In order to compare the location of the TPA of interest with the FAC maps driven from SuperDARN convection measurements, we overlaid the outer boundary of the aurora emissions on the FAC maps (Figs. 4.9 and 4.10). In Fig. 4.9, the magnetospheric FAC per unit Pedersen conductance, $\mathbf{B} \cdot (\nabla \times \mathbf{v})$, derived from the map potential equipotential contours are presented along with the poleward and equatorward boundary of the aurora emission (solid black curves) for (a) 08:32 UT, (b) 09:04 UT, (c) 09:42 UT, (d) 09:54 UT, (e) 11:10, (f) 12:32 UT. These are the times presented in the convection and aurora comparison in Fig. 4.5. Negative vorticity (into the ionosphere) corresponds to a positive FAC component out of the ionosphere (red), and a positive vorticity (out of the ionosphere) corresponds to a negative FAC component into the ionosphere (blue). In the premidnight sector (Figs. 4.9a&b), large bands of upward FAC is estimated from the map potential model which agree extremely well with the morphology of the FUV aurora outer boundaries of which are presented using black curves. The observed bands of upward FAC co-locate with bands of bright aurora, which is produced primarily by precipitating electrons, which can give rise to the aurora, as was seen by the IMAGE WIC camera.

Figures 4.9c&d illustrate the FAC maps for the time when the TPA is fully formed. The regions of upward FACs are co-located with the TPA, which again is an indicator of precipitating electrons that caused the luminosity in the polar cap. However, it is necessary at this stage to mention that due to lack of backscatter at very high latitudes in the SuperDARN radar data, some of the FAC estimates at these latitudes are not constrained by data but by the map potential model.

The sense of ionospheric plasma vorticity in the noon sector is downward, implying an upward magnetospheric FAC (Figs 4.9a, b, and c). Appearance of

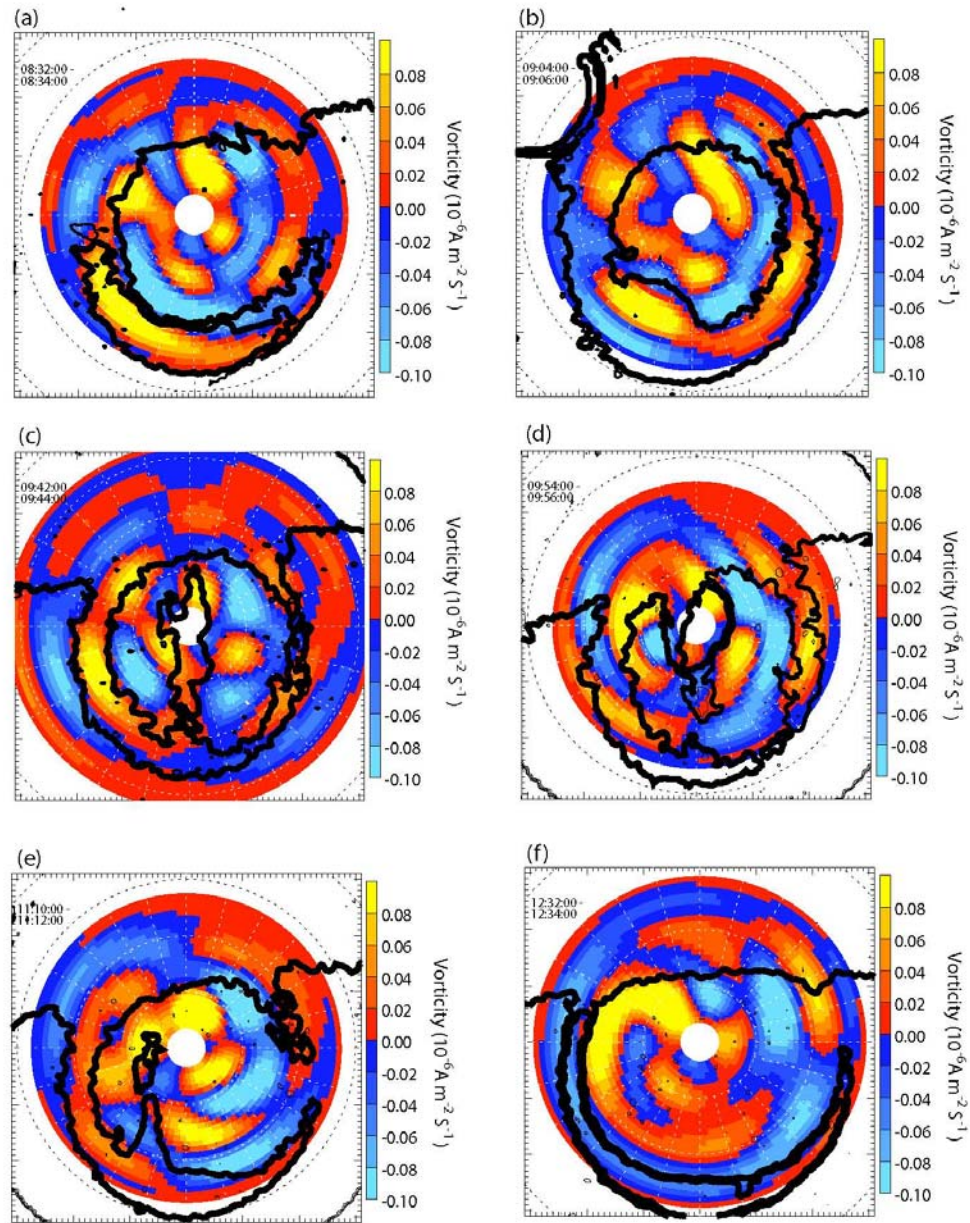


Figure 4.9 The outer boundary of the aurora emission overlaid on the FAC estimate per unit Pedersen conductance $B.(\nabla \times v)(\mu A m^{-2} S^{-1})$ obtained from the map potential contours for the scans starting at (a) 08:32 UT, (b) 09:04 UT, (c) 09:42 UT, (d) 09:54, (e) 11:10 UT, and (f) 12:32 UT. The FAC direction is defined according to the SuperDARN coordinates convention, where z is radially out of the ionosphere. Negative vorticity (into the ionosphere) corresponds to a positive FAC component (red), and positive vorticity (out of the ionosphere) corresponds to a negative FAC component (blue).

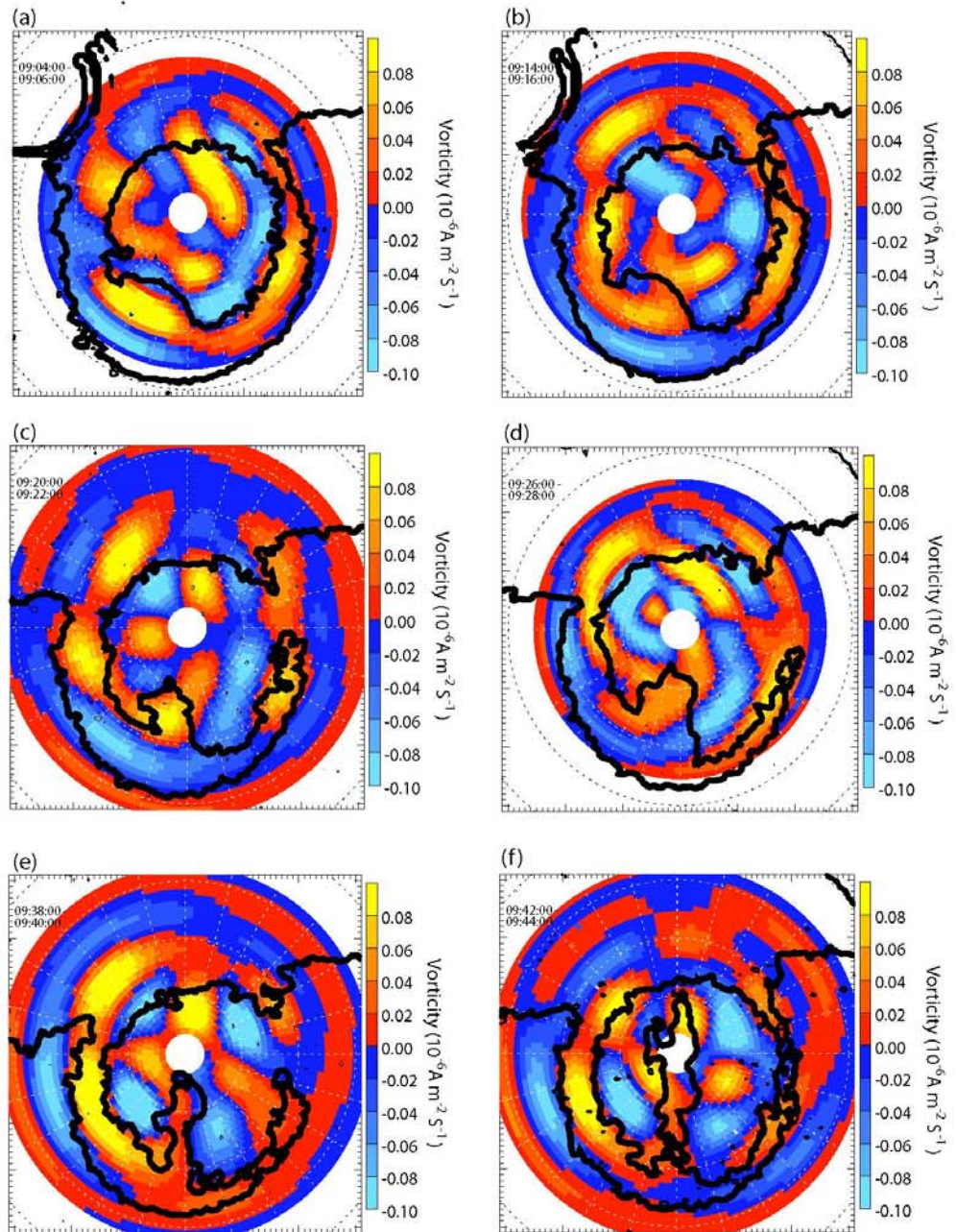


Figure 4.10 The outer boundary of the aurora emission overlaid on the FAC estimates obtained from the map potential contours for the scans starting at (a) 09:04 UT, (b) 09:14 UT, (c) 09:20 UT, (d) 09:26, (e) 09:38 UT, and (f) 09:42 UT.

Chapter 4: Multi-instrument observations of a transpolar arc in the Northern Hemisphere

such upward FACs in the noon sector which progress to the prenoon sector as time passes, indicates the addition of upward vorticity to the dawn compartment of the polar cap that causes the polar cap to expand to lower latitude resulting the duskward motion of the TPA (Figs 4.9c and d).

In order to investigate whether there are any FAC features associated with the formation of the TPA, we present six snapshots of FAC maps (same format as Fig. 4.9). Overlaid on these maps are the outer boundaries of the auroral emissions, shown as black solid curves (Fig. 4.10a-f). As can be seen from these maps, the arc forms in the premidnight sector and gradually propagates in a dawnward direction towards the center of the polar cap. By the time the TPA is fully formed (Fig. 4.10f), the position at which the TPA joins the main auroral oval has been displaced from 2300 MLT to midnight. It is to note the steady formation of a region of upward FACs, as the TPA develops (Fig. 4.10b-f).

In order to investigate the relationship between the FACs and formation of the TPA of interest, more data from both space and ground based instruments have been examined in the next two sections.

4.5.1.2 Comparison of averaged auroral images and field-aligned currents

In order to compare the auroral emissions with the Birkeland currents, one-hour averages of the WIC images were constructed from ~30 snapshots taken approximately two minutes apart, each of which is registered in magnetic latitude and local time. Figures 4.11 to 4.14 illustrate averaged FACs obtained from Iridium data superimposed on the corresponding averaged IMAGE WIC observations. The snapshots were taken between 08:00 UT and 13:00 UT on 05 February 2002. The UT times on the plots corresponds to the time at the centre of the data collection interval. The images presented in these plots are 10 minutes apart, but each is the average of one hour (a sliding average).

Since the same data grid has been used as that for the SuperDARN data, the FAC data have been truncated to not go beyond the SuperDARN data boundary. It

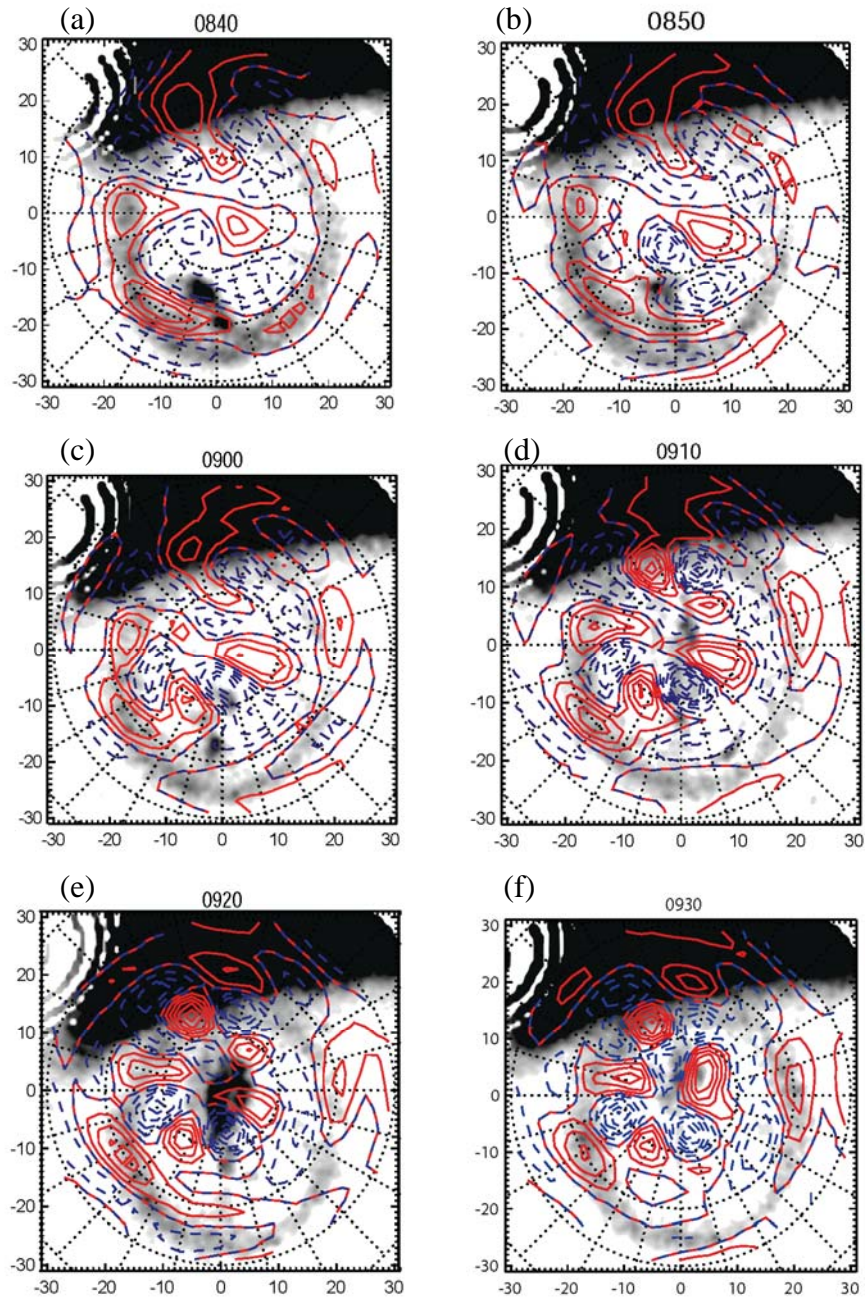


Figure 4.11 Illustrates averaged field-aligned currents for the Northern Hemisphere obtained from Iridium data superimposed on the corresponding one-hour averaged WIC aurora emission observations on 5 February 2002. The format for all patterns is magnetic latitude versus MLT with magnetic noon directed toward the top and minimum latitude at 60° . Upward and downward FACs are shown in red and blue, respectively.

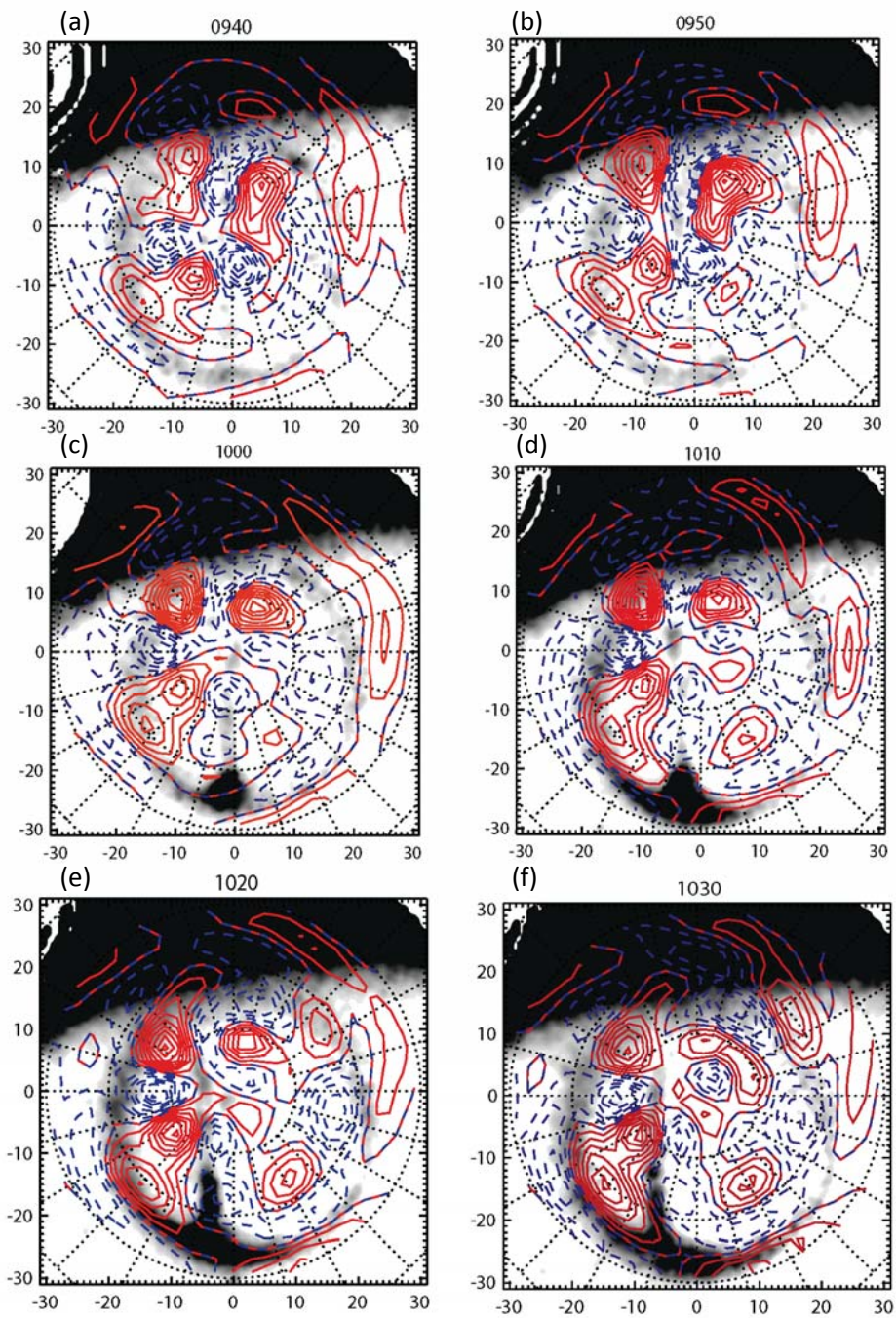


Figure 4.12 Superimposed averaged FACs on the averaged auroral emissions measured on the 5 February 2002 (same format as Figure 4.11).

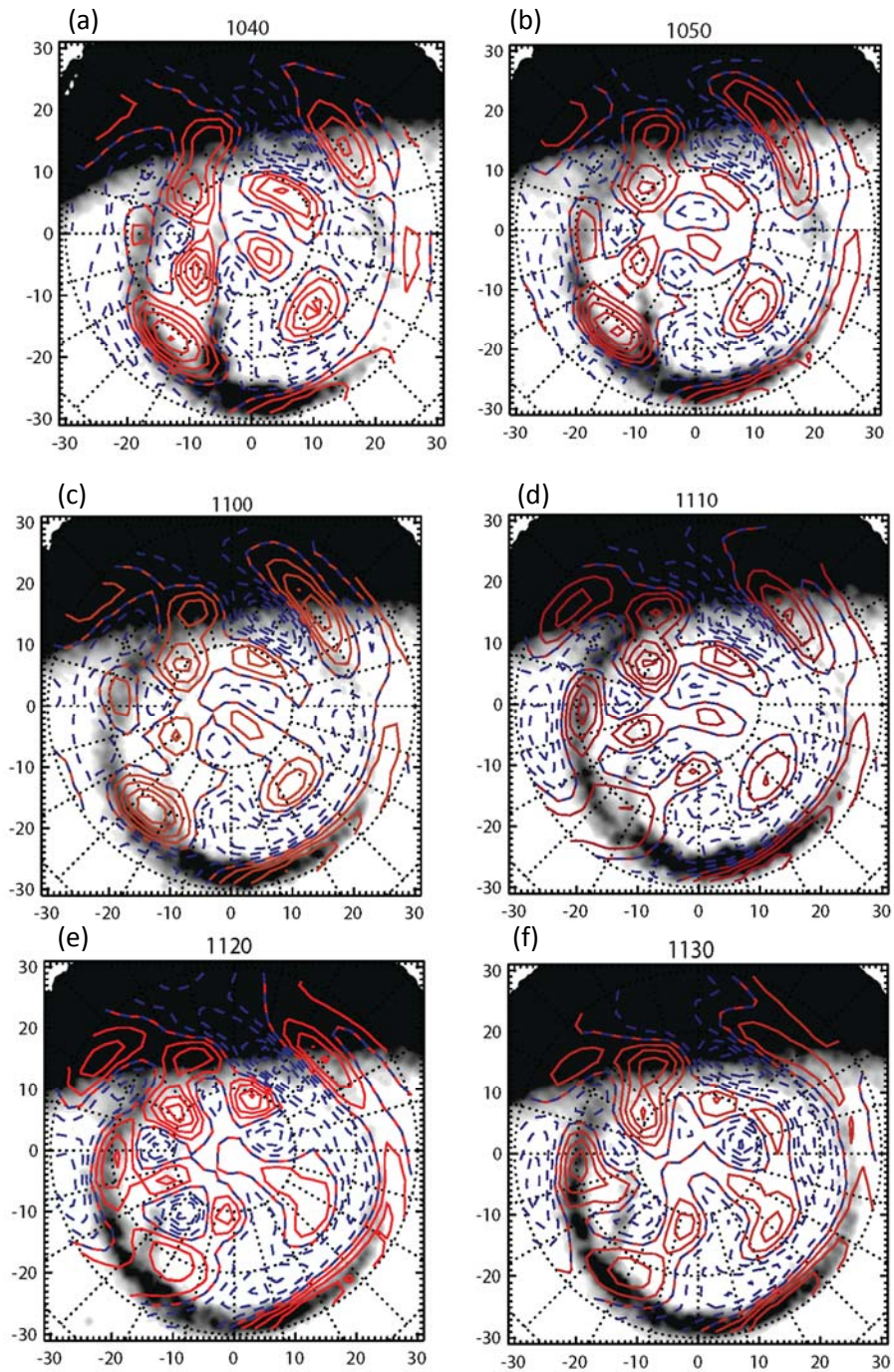


Figure 4.13 Superimposed averaged FACs on the averaged auroral emissions measured on the 5 February 2002 (same format as Figure 4.11).

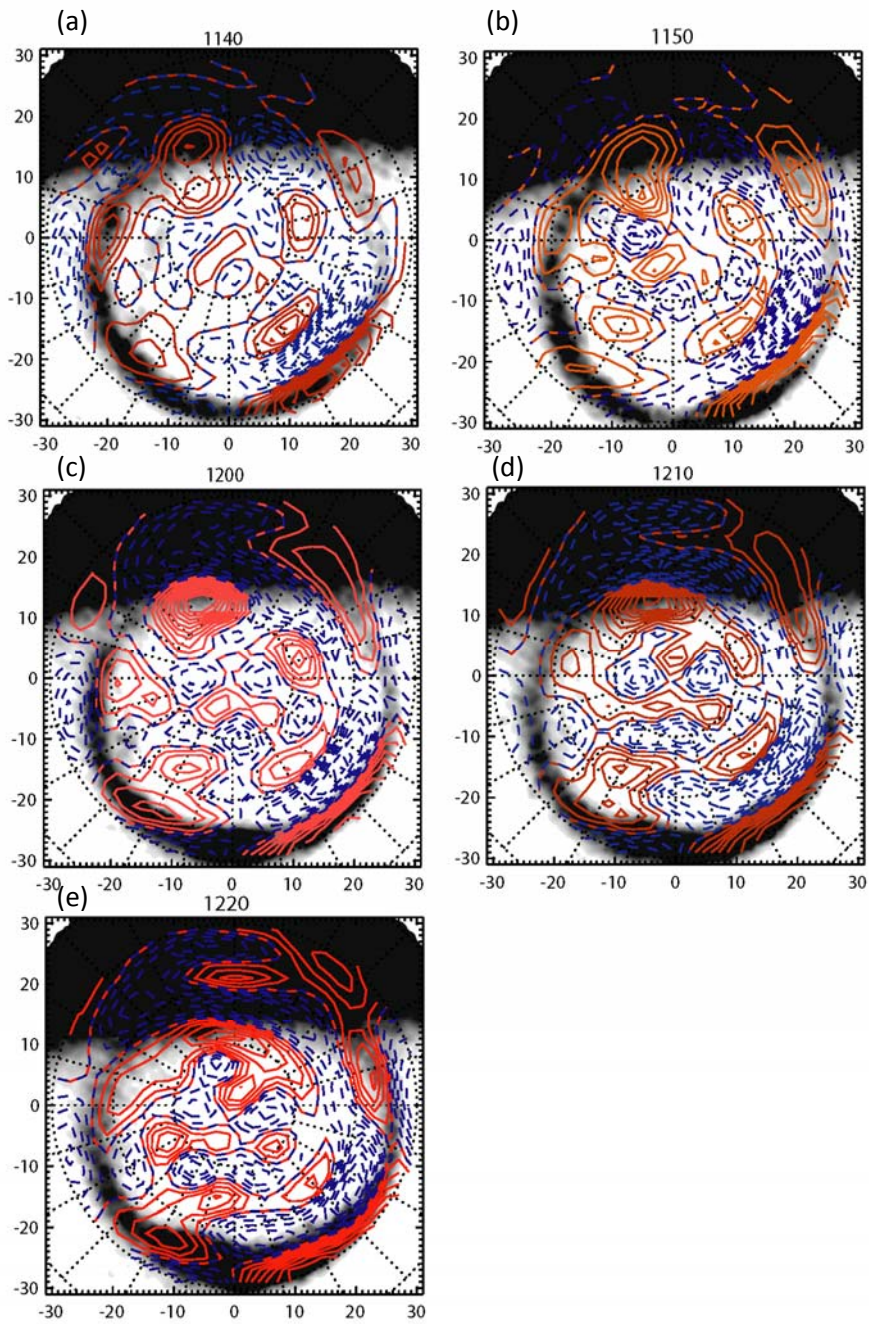


Figure 4.14 Superimposed averaged FACs on the averaged auroral emissions measured on the 5 February 2002 (same format as Figure 4.11).

also means that the FAC data is on a very fine spatial grid (the SuperDARN electric field grid). This does not reflect the spatial resolution of the FAC data (or the SuperDARN data) which is set by the order of the data fit. In order to produce the FACs for the date of interest the available DMSP (F13 and F15) and Ørsted magnetometer data are used along with the Iridium data. To plot each of the field-aligned current density average maps presented in Figures 4.11-4.14, a 1-hour data collection interval was used, with downward and upward FACs represented by the colours blue dashed and red solid lines, respectively. FACs are presented in μAm^{-2} radially outward from Earth.

However, caution must be taken when analysing this dataset, as there is a difference between averaging of the FACs and averaging of the auroral intensity. Averaging small scale FACs over an hour under stable IMF conditions is more reliable as the result might reflect the true current system. Whereas, if the currents are not stable (due to various reasons, IMF condition being one of them), then they are more likely to average out, or possibly give unstructured results. Auroral luminosity, on the other hand, will just be smeared over a larger spatial scale.

The first plot in Fig. 4.11 shows a region of upward FAC in the pre-midnight sector at $\sim 70^\circ$ of latitude, which is associated with the auroral oval. Between 20 MLT and 03 MLT, across the midnight sector, is a pair of FACs, one upward poleward of 65° magnetic latitude and one downward equatorward of this. This current pair is consistent with eastward azimuthal ionospheric flow, the TRINNI event described in the previous chapter. This FAC pair persists until about 0900 UT.

There is evidence for the onset of the TPA in this image (Fig. 4.11a) in the form of a bright auroral spot poleward of the upward FAC and apparently coincident with a downward FAC near 75° latitude and 23 MLT. The TPA eventually extends towards the dayside oval, forming a theta aurora, the origin of which is still in between a region of upward and downward current at about 2300 MLT (Fig. 4.11c). At 0930 UT (Fig. 4.11f), 0940 and 0950 UT (Fig. 4.12a), the nightside part of the TPA fades out, which is most likely due to low luminosity at the nightside.

Chapter 4: Multi-instrument observations of a transpolar arc in the Northern Hemisphere

In the third plot of Figure 4.12 (1000 UT), the complete TPA is visible again. Examination of these and subsequent figures of the FAC systems as the TPA moves duskward before merging with the oval, suggest that there is no consistent FAC feature associated with the TPA. Had the TPA formed on open field lines, it was expected an upward FAC would be associated with the TPA and move with it.

4.5.1.3 Comparison of averaged ionospheric flows with FACs measured from two different sources

In order to have a comparison between the FAC measurements from the ground based instrument and the FAC measurements from the spacecraft, two sets of FAC measurements are shown in the second and third columns of Figure 4.15.

Figure 4.15 shows the averaged SuperDARN convection maps and the derived equipotential contours produced over the IMAGE WIC observations (first column), averaged FACs obtained from Iridium data superimposed on the corresponding averaged IMAGE WIC observations (second column), and averaged FACs measured by SuperDARN radars with fitted potential contours overlaid (third column) for three selected times.

Each of the averaged SuperDARN convection maps overlaid on averaged auroral emissions (shown in the first column of Fig. 4.15) are driven using a data set of velocity measurements collected with the northern SuperDARN radars over an hour.

These FAC patterns are shown in the third column of Figure 4.15 illustrate the magnetospheric FAC per unit Pedersen conductance, $B \cdot (\nabla \times v)$, derived from the averaged map potential equipotential contours, along with the potential contours from which they were derived for (c) 0800-0900 UT, (f) 0900-1000 UT, (i) 1000-1100 UT. The positive vorticities (red/yellow) correspond to upward field aligned current, and negative vorticities (blue) to downward field aligned current.

Figure 4.15a shows the arc at the very early stage when it was forming in

Chapter 4: Multi-instrument observations of a transpolar arc in the Northern Hemisphere

the nightside oval. Ionospheric flows show a set of relatively fast azimuthal flows at very high latitudes ($\sim 73^\circ$) in the pre-midnight and postmidnight sector. Very fast ($\sim 900 \text{ ms}^{-1}$) flows at high latitude in the dayside pre-noon sector are due to the reconnection process happening under IMF northward and B_y dominant condition at the dayside magnetopause.

In the three top panels there is broad consistency between the location of the nightside auroral oval and regions of upward FACs derived from both Iridium and SuperDARN observations. There is almost no consistency between FACs derived by the two methods at higher latitudes.

Figure 4.15d shows the TPA after nearly two hours when it is fully formed and slightly displaced towards dusk. The averaged ionospheric flows at the dayside, show antisunward flows, which are being added to the dusk compartment of the polar cap, expanding the auroral oval to lower latitude. Westward flows at the west side of the TPA create upward FACs which are visible in Figures 4.15e & f in forms of red bulges in the premidnight sector at about 70° of latitude.

Figure 4.15g shows the position of the TPA after another hour when the very strong ionospheric flows have caused more expansion in the auroral oval and pushed the TPA towards dusk. The very strong westward flows at high latitudes at the dayside create upward FACs, which are shown in both FAC data sets by red/yellow vorticities. Again, there is broad consistency between the large-scale FAC patterns at auroral latitudes, derived by the two methods, but within the polar cap, there are large discrepancies.

4.6 Discussion

The above description indicates several important elements to discuss. These are the dynamics of the polar cap and variation of the flux content within the polar cap, the dynamics of the transpolar arc and the relationship to the IMF, the formation region of the arc and relation to reconnection in the tail, and finally evidence of field-aligned currents in polar cap arcs. Each of these points is now considered separately in the following discussion.

4.6.1 Variation of the polar cap flux content

In order to look at the dynamics of the polar cap, we first return to the IMF in more detail (Fig. 4.1). At the start of the interval, B_z is quite weak while B_y is strongly positive. As can be seen from Figure 4.3a, the transpolar arc divides the polar cap into two separate sectors, dusk and dawn, both of which contain a certain amount of flux. The flux quantity for both the dawn and dusk sector is determined and shown in figure 4.4a by green and red curves, respectively, along with the total flux content of the polar cap (black curve). In order to study the effects of IMF orientations on the flux contents of the polar cap we have divided the data set into four intervals. As demonstrated in Figure 4.4a, the total flux content of the polar cap remains constant at about 0.5 GWb between 0800 and 0850 UT, when the IMF is northward, which suggests three possible scenarios during these positive B_z conditions; i) either there is no reconnection ongoing at the magnetopause and in the tail, ii) the amount of flux being produced by dayside and nightside reconnection are exactly balanced, iii) lobe reconnection is occurring but not changing the amount of flux. Examining the snapshots in this case study shows that under strong positive B_y component, low latitude reconnection occurs which then adds newly open flux to the polar cap (*Goudarzi, 2008*). Therefore closure of flux caused by TRINNIs at the nightside would make up for the amount of flux that was added to the polar cap due to low latitude reconnection at the dayside, which is why the total flux content of the polar cap remains constant for this period. This result is consistent with the previous suggestions made by (*Grocott et al. 2003, 2004*), where two case studies were investigated, in both of which estimation of the changes in open flux presented during highly distorted B_y dominant IMF condition, indicated approximately balanced dayside and nightside reconnection at rates of $\sim 30\text{-}35$ kV. After 09:00 UT B_z becomes strongly positive and dominates the B_y component. It is after this that at the poleward edge of the premidnight aurora an auroral brightening occurs in association with vortical plasma flows (Figure 4.5b).

Chapter 4: Multi-instrument observations of a transpolar arc in the Northern Hemisphere

Events termed TRINNIs are an important component of the magnetic flux transfer process within the magnetosphere (*Grocott et al.* 2003, 2004) and these are indicative of magnetic flux closure in the nightside. Data from the LANL geosynchronous satellites confirms the absence of any substorm activity in the interval of interest. Absence of substorm activity until near 12:30 UT is also confirmed by WIC observations. Due to the closure of the open flux in the magnetotail during the TRINNI event, there is a slight decrease in the open flux content of the magnetosphere of approximately 0.2 GWb which leads to a decrease in the size of the polar cap (Figure 4.4). This observation is yet again in agreement with the suggestions made by (*Grocott et al.* 2003), where they indicate that in one example, where the flow reversal boundary was well observed, a small ($\sim 1^\circ$) contraction of the polar cap boundary occurred. The time-average rate of flux change from 08:30 UT to 09:30 UT indicates a nightside reconnection rate of ~ 51 kV, that is consistent with the values *Grocott et al.* suggested in 2003 for the nightside reconnection rate which was elevated typically to values ~ 45 -60 kV. As there is no evidence of low latitude reconnection at the dayside therefore, the total reconnection rate is dominated by the nightside reconnection and is defined as a negative rate in figure 4.4 as the polar cap is shrinking.

From about 09:55 UT until 12:35 UT the IMF turns more southward. During this period, the flux content of the polar cap increases to nearly 1 GWb implying a time averaged reconnection rate of approximately 70 kV throughout this interval, although the rate is slightly smaller in the second part of the interval. The southward turning of the IMF at around 09:55 UT causes low-latitude reconnection between closed terrestrial field lines and the IMF which leads to the addition of new flux from one compartment to the other as shown in Figure 4.5e and 4.5f. This effect is much clearer in Figure 4.4a where the flux content of each compartment is shown for dawn sector (green curve) and dusk sector (red curve). Finally at the end of the interval, at 12:35 UT the IMF turns northward again at which time the flux content of the polar cap decreases. This decrease is a result of the substorm associated reconnection of open flux in the magnetotail which

Chapter 4: Multi-instrument observations of a transpolar arc in the Northern Hemisphere

started shortly after 12:30 UT; an auroral brightening is seen in Figure 4.2e-4.2f. The reconnection rate changes to -110 kV. The dynamics of the polar cap during this interval and the subsequent motion of the auroral oval, therefore, are controlled by reconnection processes in both the tail and at the dayside magnetopause. In this interval reconnection in the tail occurs first during a period when there was no substorm activity and then later as a result of substorm activity following a period of southward IMF. The reconnection potential associated with the substorm is of order twice that associated with the TRINNI. These findings are consistent with the theoretical model suggested by *Milan et al. (2005)*, as they speculate that the arc is formed by a burst of nonsubstorm nightside reconnection and that its consequent motion is controlled predominantly by the rate of reconnection happening at the dayside and nightside.

4.6.2 Formation and motion of the transpolar arc

At about 09:00 UT the transpolar arc forms at the poleward edge of the auroral oval, existence of which was also confirmed by the DMSP particle precipitation data (Sec. 4.4). This brightening is coincident with vortical flows shown in Figure 4.5b. This brightening occurs slightly poleward of the TRINNI and the flow does appear to change from azimuthal to vortical.

Milan et al. (2005) surmised that during TRINNIs, reconnection of the magnetic field lines in the tail creates new closed field lines which are not contained in the meridian plane of the tail, but connected to the dawn and dusk ionospheres in opposite hemispheres. Under normal circumstances when a tail reconnection X-line forms, the resulting closed field lines are contained in meridian planes, and as they contract and convect around the Earth toward the dayside, they generate dawnward and duskward return flow in the nightside ionosphere symmetrically about the noon-midnight meridian (Figure 4.16b and 4.16c). The topology associated with the TRINNI however, results in strong westward flow across the midnight meridian in the case of $B_y < 0$, in the midnight sector of the Northern Hemisphere ionosphere. The Southern Hemisphere end of

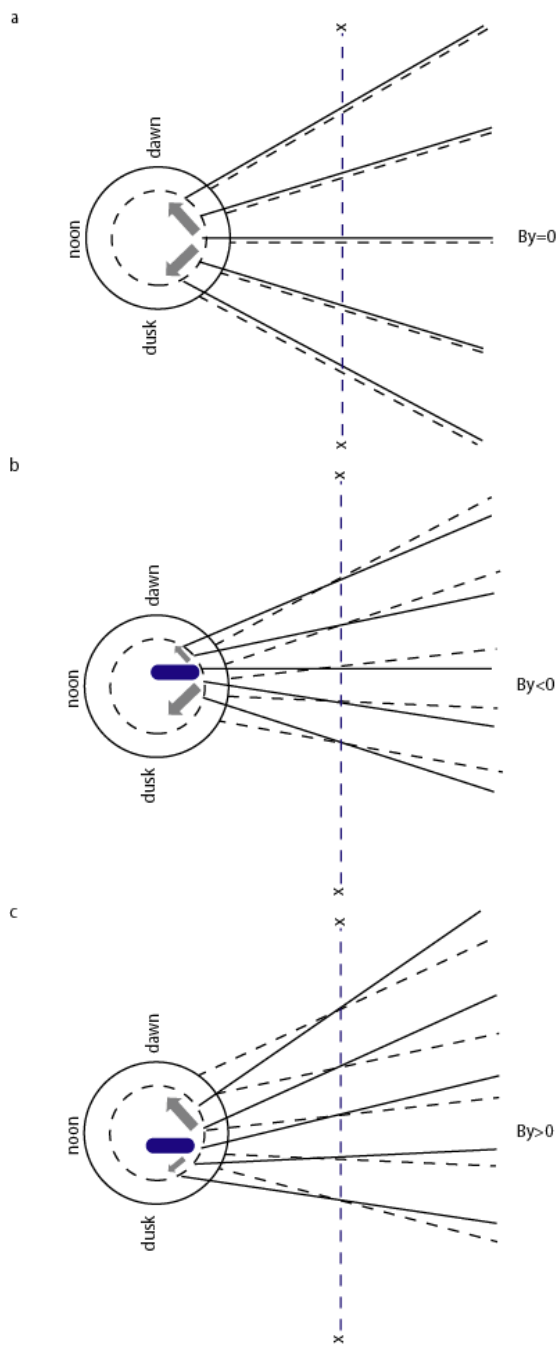


Figure 4.16 Schematic diagrams to show the field topologies in the magnetotail after reconnection for (a) IMF $B_y=0$ (b) $B_y<0$ and (c) $B_y>0$. Dashed circle indicates the polar cap, and solid (dashed) lines represent nightside field lines for the Northern and (Southern) Hemisphere, Convection return flows in the equatorial plane of the tail and in the ionosphere are shown using arrows. In Fig. 6b and c, opposing forces in the Northern Hemisphere and Southern Hemisphere result in the formation of transpolar arcs shown with blue rectangles (based on Fig. 6, Milan et al., 2005).

Chapter 4: Multi-instrument observations of a transpolar arc in the Northern Hemisphere

the field lines map to the dusk sector ionosphere and need only convect slowly in the return flow. Correspondingly, in the dawn sector of the Northern Hemisphere, slow or stagnant eastward return flow is expected as the southern hemisphere ends of these field lines attempt to catch up with the vigorous eastward flow in the midnight sector. However, the field line that maps to the noon-midnight meridian in the equatorial plane faces competition between the Northern and Southern hemispheres, as both ends of this field line cannot simply convect sunward in the return flow region as is the case in simpler field geometries.

However in this case study, the transpolar arc forms during $B_y > 0$, and when the opposite direction of the ionospheric flows is observed, again as predicted by *Milan et al.* (2005). In this case study the transpolar arc is formed in the region where closed field lines are accumulated in return flows stymied by opposing tension between the opposite hemispheres. This region corresponds to the western end of a strong eastward convection jet for IMF $B_y > 0$ (Figure 4.16c).

During the formation of the transpolar arc, the y-component of the IMF is positive and larger in magnitude than the B_z component which remains mainly positive. Two convection cells are formed with one larger than the other, “orange” and “banana” shaped cells which are slightly biased toward dawn. From about 09:55 UT the polar cap expands implying dayside reconnection dominates over nightside reconnection at this time. During this time the flow at the dayside is strongly azimuthal due to the large B_y component with the flow going from post noon to pre-noon (e.g. Figure 4.5e). In the theoretical model proposed by *Milan et al.* (2005), the arc motion was governed by siphoning open flux from one side of the arc to the other by lobe reconnection. In the present case the mechanism is similar, i.e. motion being caused by a redistribution of open flux. However the redistribution is caused by addition and subsequent accumulation of open flux on one side of the arc only by B_y dominated low latitude reconnection at the dayside magnetopause. In this case, the dayside reconnection adds open flux to the dawn cell of the polar cap, inflating the dawn sector polar cap and also causing the polar cap to expand.

Chapter 4: Multi-instrument observations of a transpolar arc in the Northern Hemisphere

Although this theoretical model sounds completely reasonable for the formation of the transpolar arc, there seems to be another phenomenon which is associated with the formation of the transpolar arc in this interval and that is the vortical flow at the westward edge of the nightside auroral oval. These vortical flows seem to be located close to the origin of the transpolar arc and they accompany the arc all the way into the polar cap and disappear as soon as the arc forms completely (Figure 4.17, red ovals). *Eriksson et al.* (2005) observed a clockwise lobe convection vortex at the dayside part of a transpolar arc which was associated with upward field aligned current sheet. They proposed that as the quasi-continuous lobe reconnection sustains the dayside oval-aligned transpolar arc, the transpolar arc of interest lies on open field lines, which is in disagreement with our proposed model. Considering all the evidence given earlier we can conclude that the transpolar arc of interest is one continuous band which lies on closed field lines. This, however, is not in agreement with the theoretical model proposed by (*Eriksson et al.*, 2005) on the formation of transpolar arc, as their theoretical model suggested a division in the oval-aligned transpolar arcs into two separate entities, one on the dayside and one nightside, driven by two different physical processes. *Eriksson et al.*, (2005) also suggested as a consequence that there would be strong shear in the plasma flow associated with the transpolar arc. However, the ionospheric flow measured by the SuperDARN radars in this case study demonstrates no shear in the plasma flow at the location of the transpolar arc. Thus, we conclude that the transpolar arc lies on closed field lines.

4.6.3 Evidence of field-aligned currents in polar cap arcs

Studying auroral emissions provides a way to assess both the magnetosphere-ionosphere interaction as well as the particle precipitation input due to different phenomena happening in the Earth's space environment. In this section, the auroral emissions as observed by IMAGE FUV/WIC are discussed in terms of the Birkeland currents and in some cases the ionospheric flows derived from Iridium and SuperDARN. One of the interesting ways of investigating the

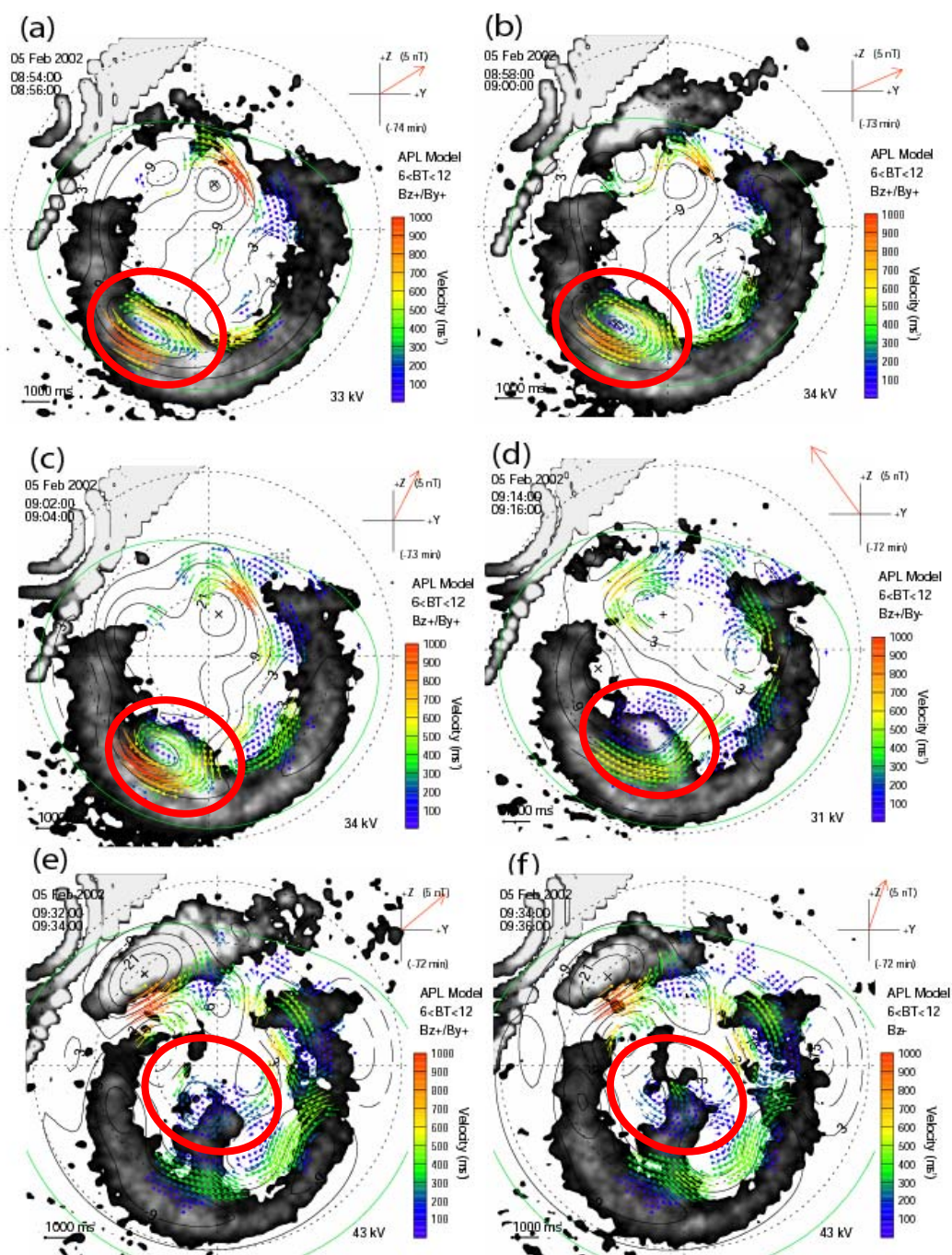


Figure 4.17 SuperDARN convection maps with superimposed IMAGE FUV auroral data. Marked with red ovals are locations of the vortical flows.

Chapter 4: Multi-instrument observations of a transpolar arc in the Northern Hemisphere

nature of the transpolar arcs is looking for various features in field-aligned current patterns and their associated large-scale convection map. Evidence of field-aligned currents in polar cap arcs has been found in various observations in the past.

Burke et al. (1982) claimed that the TPAs in the polar cap are associated with upward field-aligned currents, based on simultaneous electric, magnetic field, and electron flux measurements from three dawn-dusk passes of the S3-2 satellites. *Chiu* (1989) proposed a model in which TPAs are yet again assumed to be on open field lines, and the formation of the arcs is shown to be caused by a current response to mesoscale velocity shear structures in the ionosphere that are not matched in the magnetosphere. As was mentioned previously in chapter 2, *Zhu et al.* (1993a) proposed yet another theoretical model in which they claimed that the development of TPAs starts with a magnetospheric plasma shear flow moving earthward along either open or closed field lines.

Since then, the controversy regarding the magnetospheric origin of the TPA has persisted until this date when different theoretical models are proposed to explain the nature of the TPAs.

As was mentioned in chapter 2, in 1991, *Marklund and Blomberg* conducted a model study of the correlation between the large-scale convection patterns and the transpolar arcs associated field-aligned currents. They claimed that there are three current configurations associated with the TPAs. They suggested that as a result of locally unbalanced currents, the convection pattern can become modified on the global scale. Some other studies detected all three current configurations mentioned above in their observations (e.g. *Frank et al.*, 1986; *Menietti and Burch*, 1987; *Marklund et al.*, 1991; *Obera et al.*, 1993; *Blomberg and Marklund*, 1993; *Blomberg and Cumnock*, 2004).

Very often, the field-aligned current sheets associated with polar cap arcs have been associated with multiple pair structures (e.g. *Valladares and Carlson*, 1991; *Berg et al.*, 1994). They reported numerous cases where the occurrence of 4 to 5 pairs of current sheets associated with TPAs were detected.

Chapter 4: Multi-instrument observations of a transpolar arc in the Northern Hemisphere

In 2004, *Cumnock et al.* reconstructed the ionospheric electrodynamical state associated with the evolution of theta aurora originating from both the dawn and dusk sides of the auroral oval. In the cases they examined, the TPA current configuration consists of a pair of upward and downward FACs with the upward current on the dawnside. The TPA moves with the convection cell as it evolves which is an indicator of the TPA being a global phenomenon. Figure 4.18 illustrates on the left, modelled field-aligned current patterns for each of the DMSP passes on 8 November 1998; and on the right, the electrostatic potential patterns generated by the model. Upward and downward currents are shown in red and blue, respectively, positive potentials are shown in blue and negative in red. The black line denotes zero potential. At very high latitudes in the convection, cells shown in first and third plots are not symmetrical. This means there is either an upward or downward current, but not both. In the second plot, however, both upward and downward currents exist. In their observations, the TPA is embedded in the dawnward field-aligned current and even during its evolution, it is collocated with the same part of the plasma flow pattern. The duskside originating arc is collocated with the duskward portion of the high-latitude sunward flow region, even as this region moves dawnward. They suggested that due to the large-scale nature of the convection cell associated with TPAs, they are a global phenomenon rather than a localized feature moving across the high-latitude region.

As fully described in chapter 2, *Eriksson et al.* (2005) proposed an electrodynamic scenario for a particular TPA, using a set of observations and the supporting MHD simulations. They claimed that the apparent continuous band of the duskside TPA is divided into one dayside and one nightside entity that may be driven by two seemingly independent physical processes. They identify the high latitude dayside branch of the double-TPA with an upward FAC near the center of this evolving clockwise lobe cell. The nightside part of the TPA generally tailward of the dawn-dusk meridian is related to an upward FAC associated either with clockwise convection cells or the velocity shear zone of the Harang discontinuity (e.g. *Koskinen and Pulkkinen*, 1995).

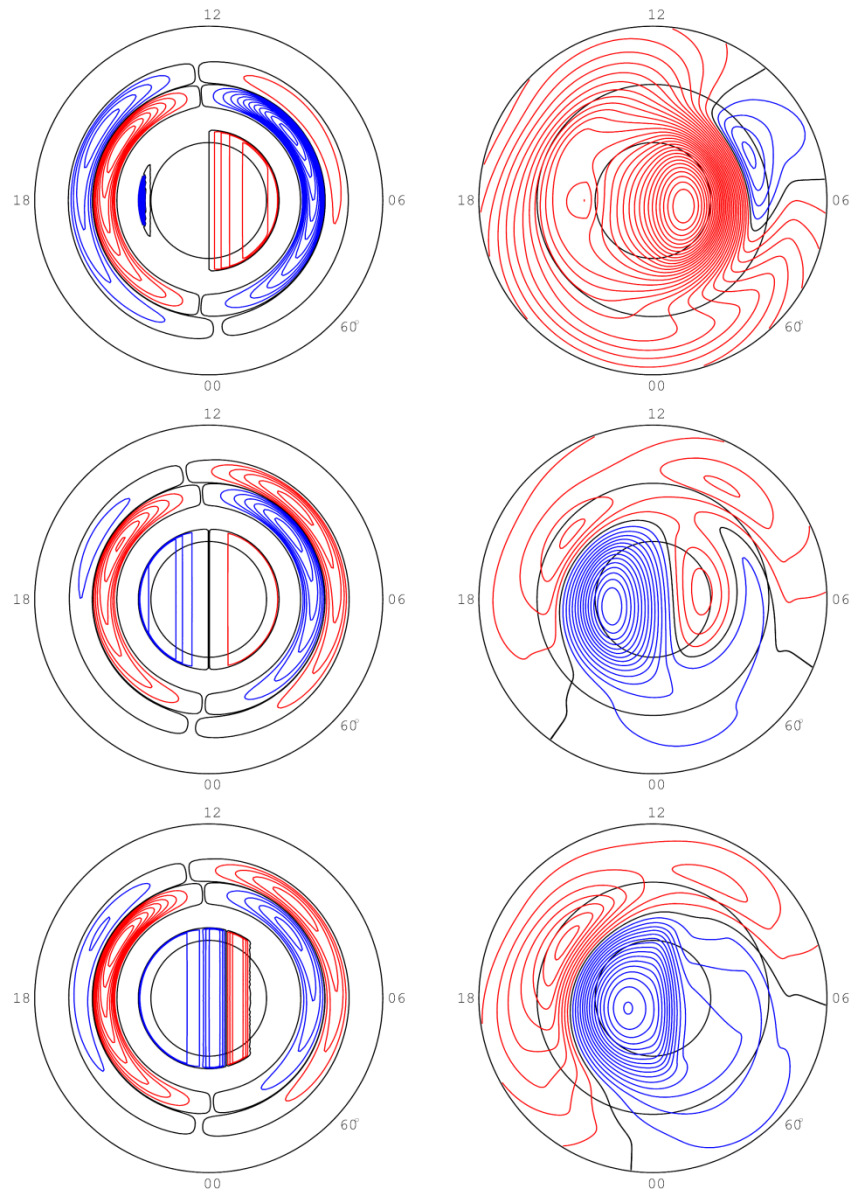


Figure 4.18 Illustrates on the left, modelled field-aligned current patterns ($0.1 \mu\text{A}/\text{m}^2$ contour separation) for each of the DMSP passes on 8 November 1998; and on the right, the electrostatic potential patterns (3 kV contour separation) generated by the model. Upward and downward FACs are shown in red and blue, respectively; positive potentials are shown in blue and negative in red. The black line denotes zero potential (From *Cumnock et al.*, 2004).

Chapter 4: Multi-instrument observations of a transpolar arc in the Northern Hemisphere

However, our observations (Fig. 4.15), show a lack of association between the TPA and upward FAC regions associated with the shear flow, do not support the scenario outlined by *Eriksson et al.* (2005).

Comparing the observations presented in figures 4.9-4.14, with the statistical distributions of the large-scale Birkeland currents introduced by *Anderson et al.* 2006 (Fig. 4.8), there is a clear agreement between the FAC patterns in our dataset and the Iridium statistical Birkeland current distributions at low latitudes ($\sim 70^\circ$).

There is an interesting point in the first few plots in Fig. 4.11, and that is the continuous presence of upward FACs at the nightside. These flows are associated with downward flows crossing the midnight sector and are evidence for the important role TRINNIs play in the formation of the TPA. Additional patches of upward currents observed at high latitudes ($\sim 80^\circ$ between 0800 and 1600 MLT) can be associated with the high latitude lobe reconnection (i.e. Fig. 4.12a-d). Although at lower latitudes upward field aligned current is coincident with the main auroral oval emissions, there are no features seen in the FAC data, which can be associated with the TPA, apart from the initial onset region.

Comparing the location of the TPA with the averaged FAC patterns (Fig. 4.11-14), one can see that in none does TPA lie consistently in a region of upward FAC region, which can be due to the averaging process that compromises the accuracy. Although it is necessary to mention that the nightside end of the TPA at the very beginning stage of formation (first plot of Fig. 4.11) seems to be connected to the nightside auroral oval, which is in the upward FAC region.

Figure 4.11a shows a localized region of intense emissions in the midnight sector, which can be associated with the origin of the transpolar arc. At lower latitude (about 70°), the auroral emissions are coincident with the upward current derived from Iridium. Continuous flowing of the currents in and out of the ionosphere results in the production of the auroral ovals (*Iijima and Potemra*, 1976). These currents are known to be driven by continuous interaction between the IMF and the Earth's magnetic field. The auroral ovals coincide with the upward FAC regions where electrons flow into the ionosphere. Collision of these

Chapter 4: Multi-instrument observations of a transpolar arc in the Northern Hemisphere

penetrating electrons into the ionosphere results in transferring ionospheric particles into energetically excited states that may be deexcited by emission of characteristic photons, which generates the aurora. Figure 4.15 illustrates the upward field aligned currents, which are responsible for the production of the aurora.

An interesting phenomenon little studied in the past is the presence of vortical flows prior to the formation of the TPA (as was discussed earlier). Understanding the origin of the vortex mentioned above can contribute to a better understanding of the various phenomena occurring in the magnetosphere prior and during the formation of the TPAs (which can be an interesting subject to pursue in the future). An averaged convection map is given in Fig. 4.15a which shows the resulting potential pattern, solid and dashed contours for negative and positive potentials, respectively. The formation of a vortex in the pre-midnight sector is clearly visible as strong upward current in Fig. 4.15c. From then on, as was mentioned earlier on in the current chapter, the vortex mentioned above, travels into the polar cap along with the TPA. Unfortunately, as mentioned before, the FAC from the Iridium constellation patterns are averaged over an hour, they are not reliable sources to study this rare phenomenon in more detail. Nevertheless, the reasonable stability of the IMF may have lead to a better comparison of observations. Another interesting example of vortical flows at the presence of the TPA is given in chapter 5.

4.7 Summary

In this chapter we have presented, a detailed multi-instrument study of a transpolar arc in the Northern Hemisphere under different IMF orientations. *Milan et al* (2005) suggested that the motion of the arc can be controlled by various factors such as reconnection processes and the IMF orientations. In their theoretical model, a case study was presented where due to different IMF conditions, different types of reconnection occurred (e.g. high- and low-latitude reconnection) resulting in motion of the arc and makes the arc to move. What

Chapter 4: Multi-instrument observations of a transpolar arc in the Northern Hemisphere

makes our results noteworthy is the variable IMF orientations and visible effects of this variation on the formation and dynamics of the transpolar arc.

The summary of this study is as follows:

The formation of the transpolar arc is initiated by reconnection of magnetic flux in the tail which also forms the fast azimuthal flow (TRINNI) across magnetic midnight.

Some nightside vortical flows seem also to be associated with the origin of the arc and accompany the arc into the polar cap.

Subsequent motion of the arc is caused by both the redistribution of open flux in the magnetotail lobes, as well as the addition of newly open flux added by low latitude reconnection.

No apparent flow shear is associated with the transpolar arc within the polar cap.

Existence of the TPA of interest was confirmed in both northern and southern hemispheres by the particle precipitation data from DMSP spacecraft, suggesting that TPA of interest is a global phenomenon.

In this chapter, we have also brought together three major data sets, which give a good overview of the conditions in the ionosphere and near magnetosphere during a TPA event on 5 February 2002. Many interesting findings have been presented as well as showing more evidence for the mechanism responsible for the formation and dynamics of the TPA of interest. The averaged locations of the upward and downward FACs at high latitudes over an hour are constrained using the global distribution of Birkeland currents measured by Iridium satellite constellation and also the curl of velocity measured by SuperDARN radars. The averaged ionospheric convection patterns illustrate the strength and directions of the ionospheric flows prior to and during the formation of the TPA over the course of one hour. The comparison between the three was used to investigate the formation process as well as the dynamics of the transpolar arc and look at the corresponding field-aligned current patterns to find any relevant features.

Chapter 4: Multi-instrument observations of a transpolar arc in the Northern Hemisphere

This chapter has also given an overview of the work, which has been done on the large scale FACs and presented observation of the current systems along with the convection maps and auroral images. Comparison of FUV and FAC data illustrates that the location of transpolar arc does not correlate with any organized Birkeland currents obtained from Iridium satellite magnetic data.

Simultaneous occurrence of the upward FACs with the vortical flows at the nightside and the TRINNI type flows during the interval of interest, is an indicator of precipitating electrons, which are responsible for the formation of the TPA. The existence of upward FACs prior to the formation of the TPA, confirms the results presented in this chapter regarding the formation mechanism of the TPA.

To summarise, the work presented in this chapter, indicates a consistency with the model for transpolar arc formation proposed by *Milan et al.*, (2005) which places the arc on closed magnetic field lines. Further examples are investigated and discussed in chapter 5 to demonstrate that this model can explain transpolar arc formation and dynamics under a variety of conditions.

Chapter 5

Five further transpolar arc studies

5.1 Introduction

Chapter 4 has presented observations of a dynamic transpolar arc (TPA), discussed the formation and dynamics of the TPA, the effects of variable IMF orientations on its motion, and investigated the associated FAC systems. This case study is an interesting example of a TPA, which indicates a consistency with the model for TPA formation proposed by *Milan et al. (2005)*. Their model suggested that reconnection of magnetic flux in the tail initiates the formation of the TPA, and that the subsequent motion of the arc is caused by either the redistribution of open flux in the magnetotail lobes, or the addition of newly open flux added by low latitude reconnection. This chapter aims to contribute to the discussion of these issues through five further examples, in order to investigate the validity of the conclusions from the case study presented in chapter 4.

The process by which these events were chosen is explained in detail in the next section. Although, ideally, one would wish to study more events in order to provide a statistical analysis of the observed behaviour, the six events presented in this thesis represent the only conjunctions identified with SuperDARN radar data of sufficient quality to adequately investigate the models proposed so far.

Section 5.2 will present the details of another five case studies. These details include upstream interplanetary conditions for the new case studies, characteristics of the ionospheric flow in the presence of the TPAs, and the particle precipitation data from DMSP and NOAA satellites in some cases in both hemispheres in order to provide a greater understanding of the origin of the transpolar arcs.

5.2 Event selection

TPAs were initially identified in the IMAGE/FUV data by visual inspection. Figure 5.1 presents a typical example of a TPA seen in IMAGE/FUV data. These images were taken by the FUV/WIC instrument onboard the IMAGE spacecraft between 0900 UT and 1530 UT on 5 February 2002, the interval discussed in chapter 4. Lighter shades indicate brighter aurora, and dayglow is evident at the top of each image. Red arrows show the TPA in this sequence which is located mainly in the premidnight sector.

The intervals selected for this survey of TPAs were taken from images similar to those in Figure 5.1, collected between the years 2000 and 2004. TPAs were chosen simply based on an initial visual inspection of the tongue of auroral luminosity in the middle of the polar cap in the auroral emission data. This preliminary survey revealed 157 intervals with TPAs visible within the polar cap.

The ionospheric convection measurements made by SuperDARN for each of the intervals was then investigated to find cases with sufficient radar coverage, as they are good sources of gaining a better understanding of the nature of the TPAs. As previously mentioned in chapter 3, where radar coverage is not sufficient, the map potential fit is constrained by the inclusion of vectors from a statistical model of convection, parameterized by upstream IMF conditions (*Ruohoniemi and Baker, 1998*). Therefore, intervals where flow measurements were available in the local time sector where the TPAs formed were identified. Of the original 157 events, 5 with concurrent radar data were chosen (in addition to the one interval which was thoroughly discussed in chapter 4).

Intervals of interest occurred on, 25th November 2001 (TPA1), 2nd March 2002 (TPA2), 04th March 2002 (TPA3), 11th March 2002 (TPA4), 12th March 2002 (TPA5), each of which has remarkable points, which will be explained in detail in the next few sections. A few facts such as the start and end time of appearance of the TPAs in each event are listed in Table 5.1. The start and end times shown in Table 5.1, are simply estimated by registering the time when the TPAs appear and disappear in images captured by the IMAGE FUV/WIC. Therefore, it does not necessarily indicate the actual birth and decay time of the

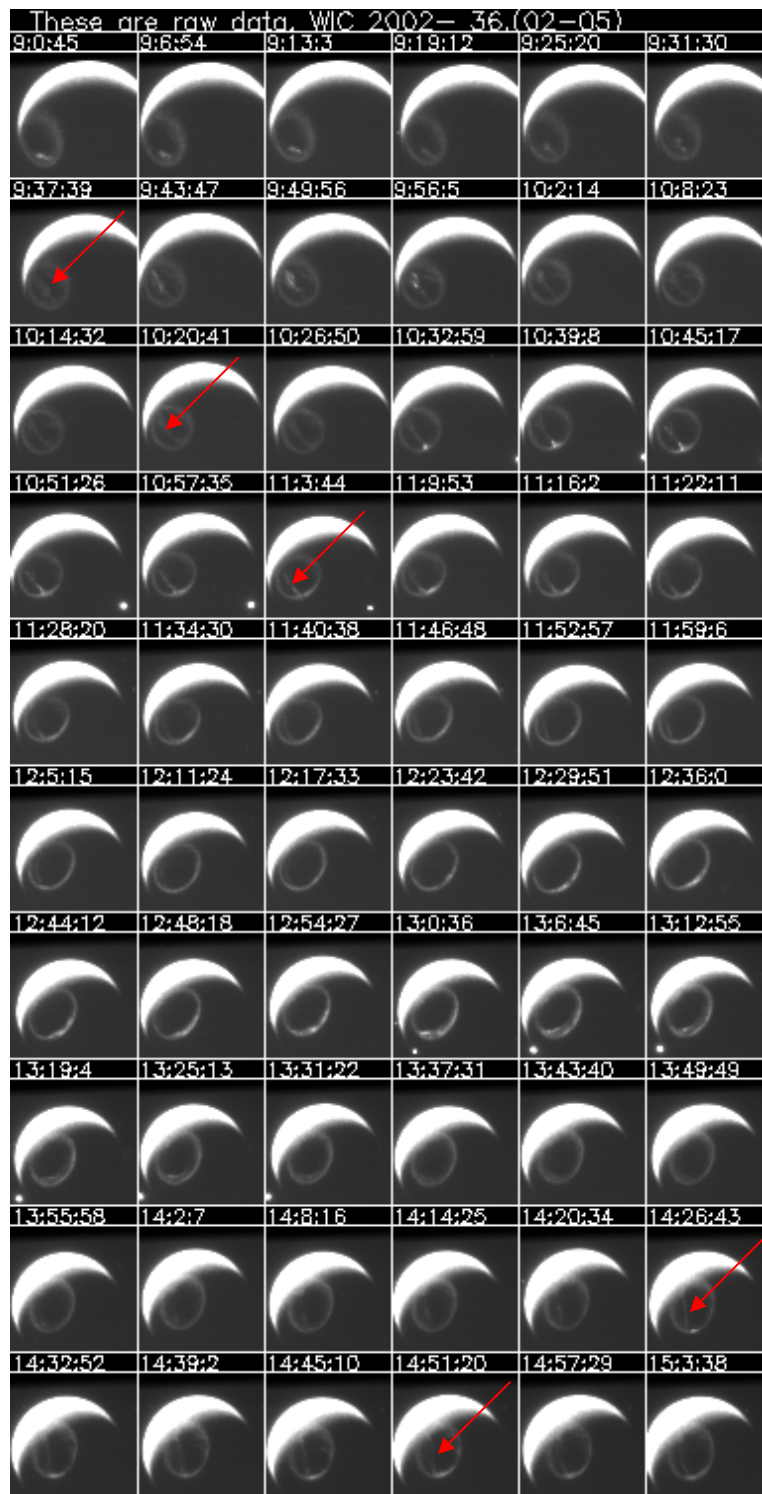


Figure 5.1 Selected snapshots of IMAGE/FUV data captured by Wideband Imaging Camera between 0900 UT and 1530 UT on 5 February 2002. Tongue of auroral luminosity emanating from the nightside auroral oval also known as transpolar arcs are visible within the polar cap the location of which is shown using red arrows.

Date	TPA event		Time	
		Code	Start	End
25 November 2001		TPA1	00:28 UT	09:30 UT
02 March	2002	TPA2	11:00 UT	16:00 UT
04 March	2002	TPA3	05:00 UT	11:30 UT
11 March	2002	TPA4	19:00 UT	24:00 UT
12 March	2002	TPA5	00:00 UT	04:00 UT

Table 5.1 The start and end time of the appearance of the TPAs in 5 selected events. These times were estimated by registering the time when the TPAs appear and disappear in images captured by the IMAGE FUV/WIC.

TPAs.

In the next few sections of this chapter, details of the five different case studies will be discussed from a phenomenological point of view. We introduce the TPAs and look at their motions using keograms of the IMAGE FUV/WIC auroral observations along the dawn-dusk meridian, discuss the IMF condition, and highlight a number of interesting points for each interval including ionospheric flow behaviours and particle precipitation data.

5.2.1 TPA1: 25th November 2001

The first selected interval was 25th of November 2001. As was mentioned previously in section 4.2.2, one of useful ways to investigate the location and dynamics of TPAs, the auroral ovals and their relationship with the IMF, is to produce a keogram of the IMAGE FUV/WIC auroral observations along the dawn-dusk meridian (dawn at the top and dusk at the bottom). One such keogram is presented in Figure 5.2a for 0000-1000 UT on 25th November 2001. The red arrow indicates the transpolar arc. It is necessary to mention that there are some factors, which can reduce the reliability of keograms. These factors include the appearance of the strong dayglow at the dayside, technical problems with the instrument, and lack of auroral emission, each of which will appear in the detailed explanations of the case studies in this chapter. Upstream solar wind and IMF conditions are shown in figures 5.2b-g; (b) B_x , (c) B_y , (d) B_z , (e) B_{total} , (f) clock angle, and (g) solar wind dynamic pressure.

In this example due to the spacecraft orbit there is a lack of auroral emission data from IMAGE FUV dataset prior to and at the time of the formation of the first TPA, "TPA1" (25th November 2001). It is, therefore difficult to investigate the origin of TPA1 due to this data gap, although the dynamics can be investigated. The TPA1 is visible for most of the interval 0100-1000 UT although it varies significantly in brightness, becoming subvisual on a couple of occasions during the period of observation. This might be caused by lack of luminosity in the IMAGE data or simply be due to the nature of the arc itself. From this observation, it is also clear that the duskside auroral oval and TPA1 are rather

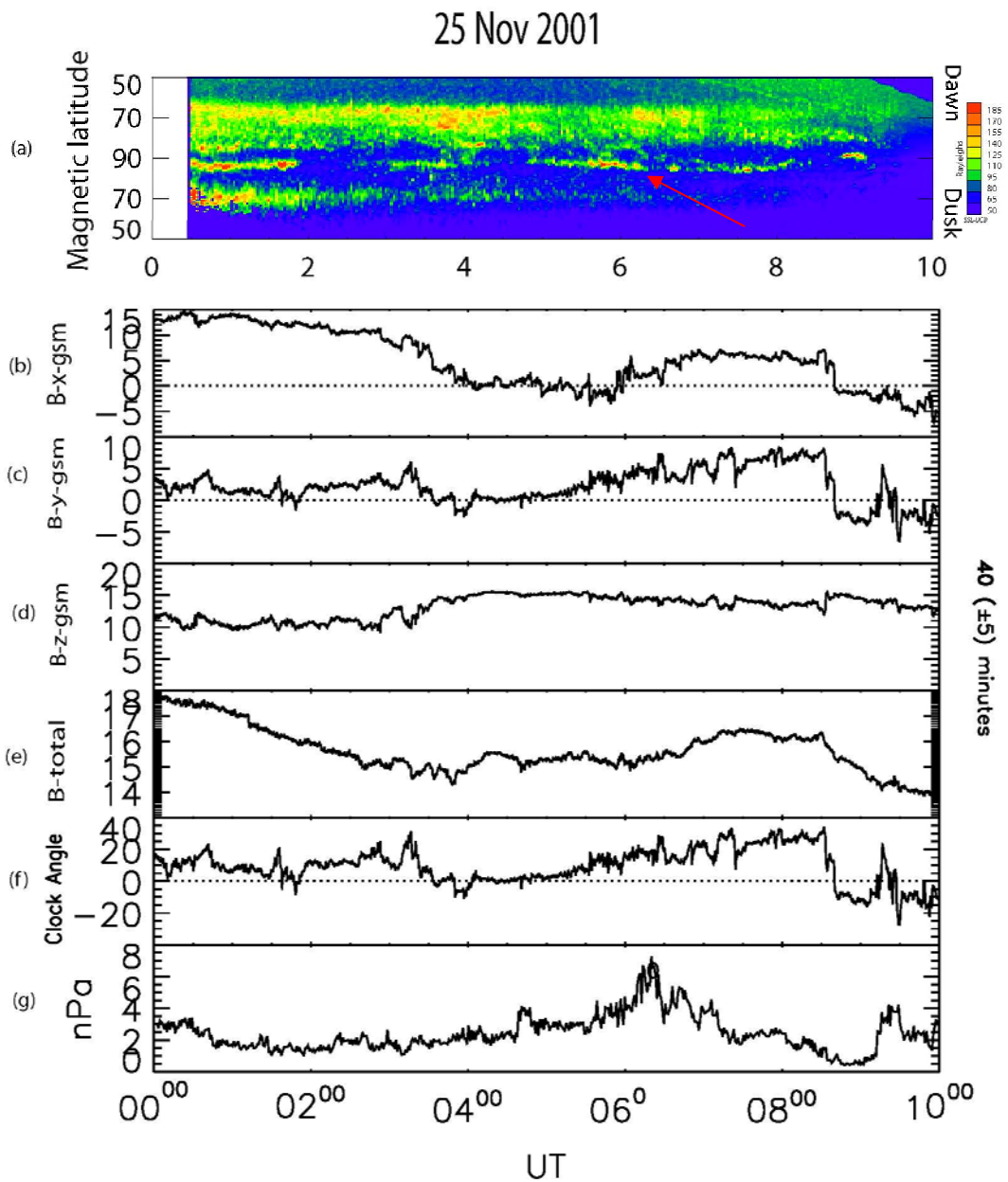


Figure 5.2 (a) Keogram presentation of the transpolar arc observed by the IMAGE FUV/WIC along the dusk-dawn meridian, (b-f) IMF information, and (g) Solar wind dynamic pressure measured by the ACE satellite.

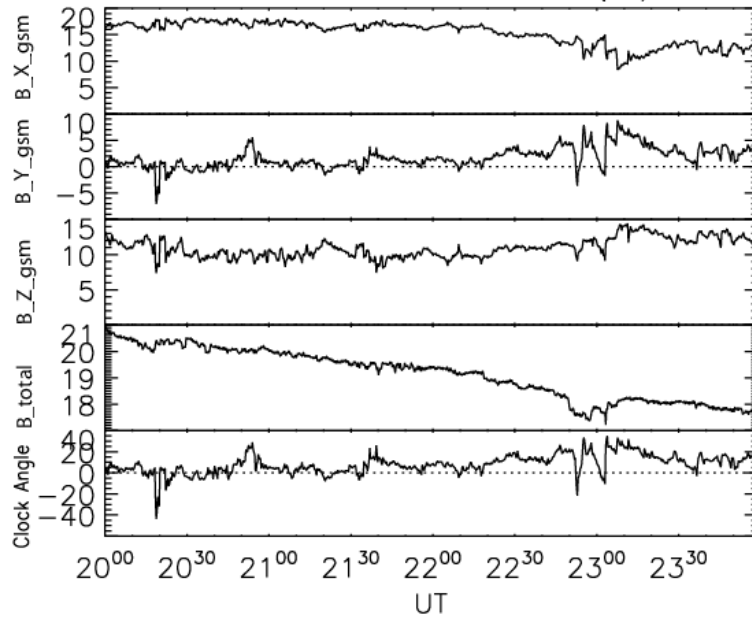
dynamic. Although the arc loses its luminosity for short periods of time, it stays close to 90° latitude for the first 2 hours and then moves slightly dawnward in association with a poleward motion of the dusk side auroral oval until around 0500 UT. A slight duskward movement starts to happen after 0500 UT, which carries on until 0800 UT. At about 0939 UT TPA1 starts to fade again.

As can be seen from the keogram data (Fig. 5.2a), the IMAGE FUV data starts at around 0030 UT. The TPA1 lies right in the middle of polar cap ($\sim 90^\circ$ latitude), for the first 90 minutes, which is due to the steady state of IMF components during that time period. After 0200 UT, TPA1 disappears from IMAGE FUV data for around 40 minutes and appears again at around 0240 UT. Throughout this time period the IMF B_y component is smaller than either IMF B_z or IMF B_x (Fig. 5.2b-d). Between 0400 and 0500 UT the B_y and B_x components become close to zero and the IMF is purely northward. At the start of this interval there is no visible TPA but it does re-appear at 0430 UT. After 0500 UT the IMF B_y component is increasing, which can explain the duskward motion of the TPA1 while the duskside part of the oval is still moving poleward. By the end of the interval, the TPA starts to move towards dawn. Dawnward motion of the TPA1 seems to be related to the change in the direction of the IMF B_y component (Fig. 5.2c).

Figure 5.3 illustrates B_x , B_y , and B_z interplanetary magnetic field components in GSM coordinates. These components were measured by the magnetometer on board the ACE spacecraft, along with the corresponding clock angle, for interval on 24 November 2001. The extra set of IMF data for 24th November is presented in order to study the IMF condition prior to the appearance of TPA1 after midnight of the 24th. The regions highlighted in grey in each of the Figures 5.3 are when the TPAs were observed in IMAGE data (which will be presented below). The data have been time lagged by the time indicated on the top right of the plot to account for the propagation delay from ACE located near the L1 Lagrangian point to the magnetopause and the subsequent propagation of information to the ionosphere using the method of *Khan and Cowley* (1999). The variations in the relative magnitude of the two components of the IMF (B_y and B_z) are reflected in the IMF clock angle, which is measured from 0° (equivalent to

24 Nov 2001

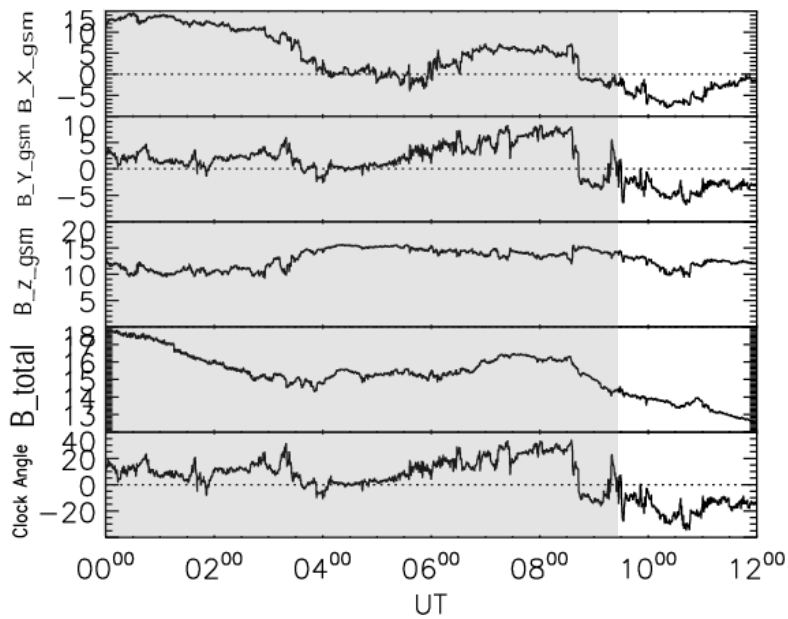
Ace IMF data 36 (± 2) minutes



(a)

25 Nov 2001

Ace IMF data 43 (± 8) minutes



(b)

Figure 5.3 GSM B_x , B_y , and B_z interplanetary magnetic field components, along with the corresponding clock angle, measured during a 16 hour interval on (a)24, and (b)25 November 2001 by the ACE spacecraft.

due northward IMF) through 90° (positive B_y).

As was fully described in chapter 2, one of the conditions under which the TPAs are expected to occur, is when the IMF has a significant northward component (*Frank et al., 1982, 1986; Zhu et al., 1997*). As can be seen from figure 5.3, the B_z component of the IMF is northward prior to and during the whole of the interval. This is in agreement with the association of the TPA with northward IMF (*Lassen and Danielsen, 1978; Burke et al., 1982; Carlson et al., 1988; Valladares et al., 1994*).

The B_y component of the IMF varies from zero to as much as 8 nT, but mainly stays positive. Prior to the formation of TPA1, the B_y component of the IMF is close to zero for a long time except for a short period between 2250-2320 UT on the 24th of November when it increases slightly and after that goes back to being weak again.

In order to highlight a few interesting ionospheric flow characteristics during the formation and motion of the TPA, we look at the auroral emission data from IMAGE spacecraft with superimposed SuperDARN convection maps. Figure 5.4 illustrates five selected snapshots of the location of the TPA1 and associated ionospheric flows during the course of 8 hours. Fig. 5.4a shows the full TPA1 at the beginning of the interval, which lies in the dusk sector of the polar cap under positive B_y , as expected. At about 0643 UT the TPA disappears for a short period of time and Fig. 5.4b shows the auroral oval in the absence of TPA1 11 minutes after this disappearance some 14 minutes later, centred on 70° of latitude, cross midnight azimuthal flows can be seen which are similar to a TRINNI although initially these flows are weaker than those typically seen in a TRINNI (Figure 5.4c). At about 0757 UT, a burst occurs in the auroral emission in the midnight sector (very bright spot in Fig. 5.4e) which eventually causes the TPA to collapse into the nightside of the auroral oval and fades. Unfortunately, the auroral emission data is lost by the end of the interval, making it impossible to investigate how the TPA fades.

Chapter 4 introduced the occurrence of vortical flows prior to the formation of the TPA. More studies of vortical type flows are necessary in order to elucidate a link between the formation of the TPAs and occurrence of vortical flows at the

TPA 1: 25 November 2001

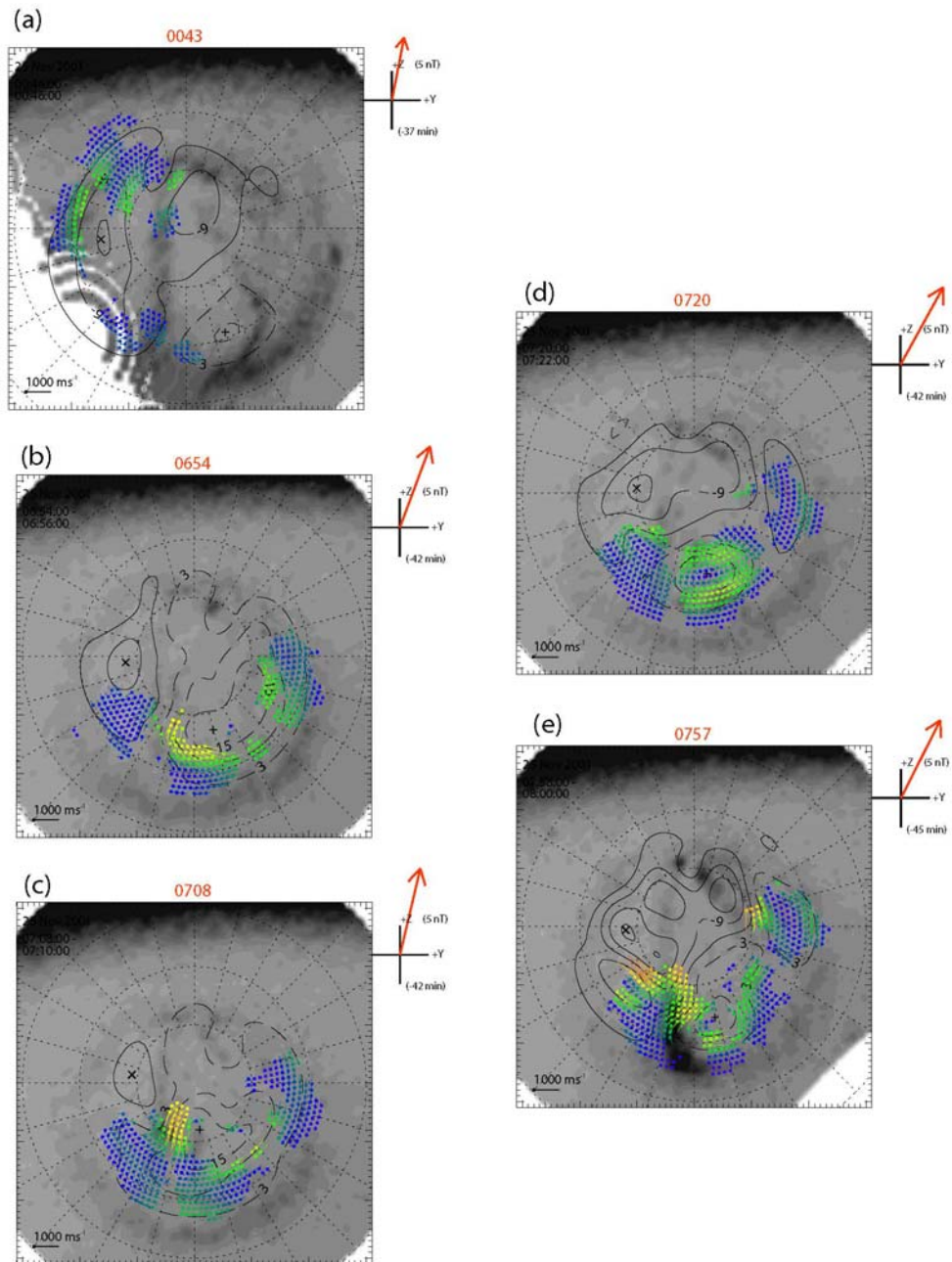


Figure 5.4 (a-e) Five auroral snapshots with SuperDARN estimates of the simultaneous ionospheric convection overlaid.

nightside end of the TPAs. Figure 5.5 presents another example of vortical flows which are followed by a TRINNI during TPA1. Five auroral snapshots with SuperDARN estimates of the simultaneous ionospheric convection overlaid, are illustrated in Fig. 5.5. Red ovals indicate the location of the vortices at the nightside, and red arrows show the TRINNI type flows. At about 0523 UT on 25th November 2001 (Fig. 5.5a), a vortex starts forming at very high latitude (about 75°, 0030 MLT) on the east side of the TPA. The vortical flows are still evident at 0526 UT (Fig. 5.5b) but have been replaced the TRINNI flows at the bottom of the TPA at 0530 UT (Fig. 5.5c). The TRINNI type flows for this interval are shown in Figs. 5.5d and e, as fast cross midnight azimuthal flows at around 75° of latitude.

Figure 5.6(a) shows the DMSP F15 satellite track for 25th November 2001, overlaid on the corresponding FUV and map potential data provided by IMAGE/WIC and SuperDARN radars respectively at the central time of the DMSP pass. The data shown occur during nearly due northward IMF with a weak positive B_y (indicated by the arrow in the top right of Fig. 5.6a). Figure 5.6(c) illustrates the DMSP F15 satellite particle precipitation data when the satellite is at the highest latitudes. Figure 5.6c presents, from top to bottom (1) electron and ion integral energy flux, black and red respectively (2) electron and ion average energy, black and red respectively (3) precipitating electron spectrogram, and (4) precipitating ion spectrogram, with energy increasing downward.

DMSP 15 observed the centre of an inverted V electron precipitation region at 03:22:20 UT that generates a visual polar arc shown in Figure 5.6a. The unique inverted-V type structure of auroral electron precipitating fluxes is known for the presence of a maximum (peak) in energy spectrum such that in the satellite frame the spectral maximum first increases to a maximum energy and then decreases, following an “inverted-V” type variation in energy. Before the inverted V signatures there were few precipitating electrons and no ions. After the inverted V, however, there are structured electrons at energies less than 1 keV and ions above 1 keV. These particle signatures occur on the dayside of TPA1. The ionospheric flow measured by DMSP F15 drift information (Fig. 5.6b) suggest that the arc appeared on the poleward side of distinct antisunward and sunward

TPA 1: 25 November 2001

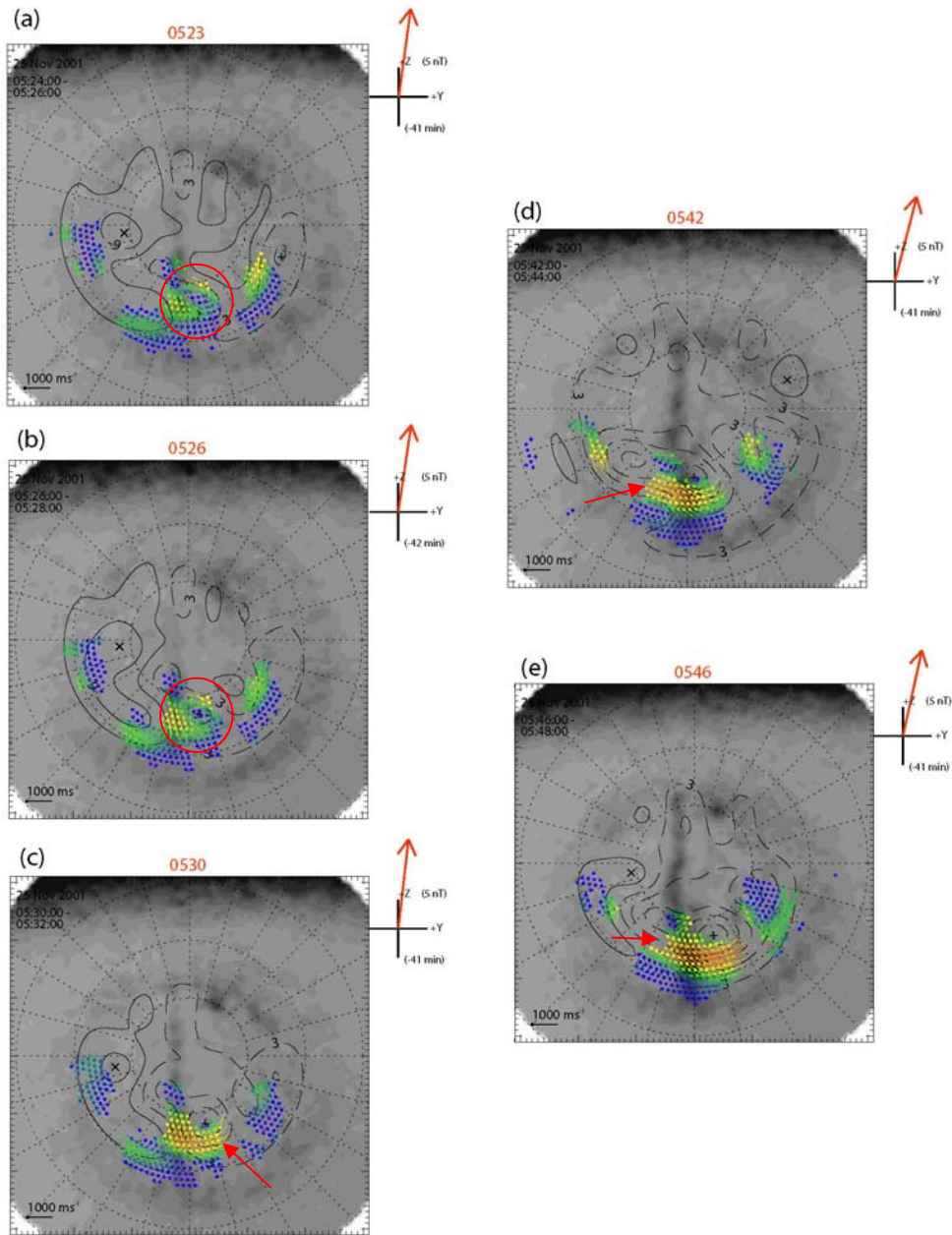
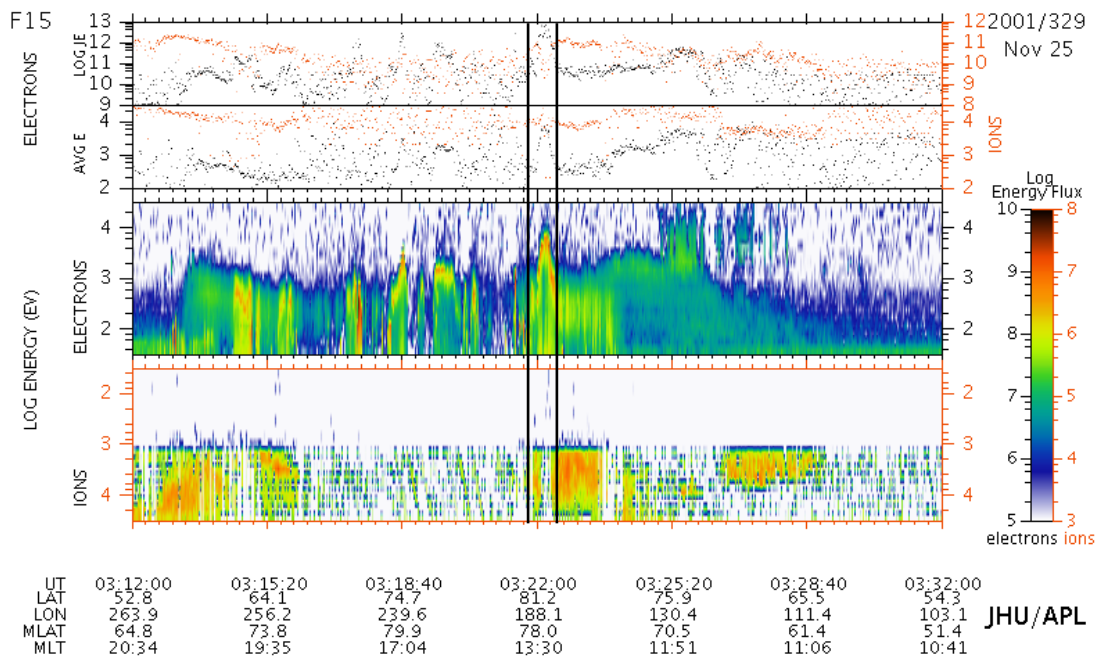
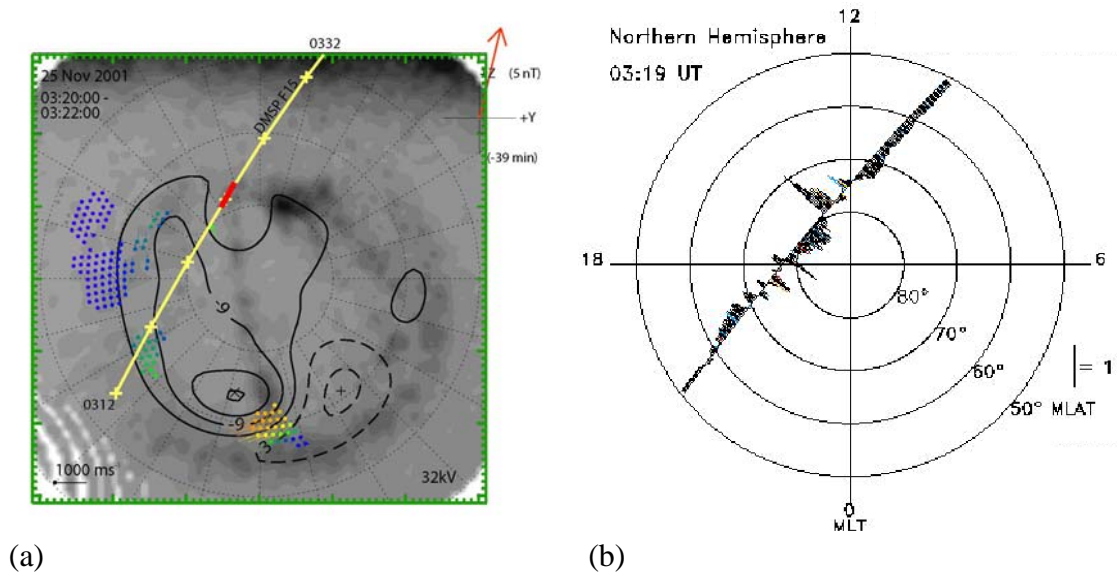


Figure 5.5 (a-e) Five auroral snapshots with SuperDARN estimates of the simultaneous ionospheric convection overlaid. Red oval indicating the location of the vortices at the nightside, and red arrows showing the TRINNI type flows.

TPA1: 25 November 2001



(c) **Figure 5.6** Data shown from the DMSP pass on 25 November 2001 (03:12-03:32 UT) that occurs during the IMAGE FUV data period. (a) At the top is the F15 satellite track plotted over a FUV rendered over the 0320-0322 UT SuperDARN equipotential contours (*Ruohoniemi and Baker, 1998*) taken at the time F15 is at highest magnetic latitudes. (b) The same satellite track with horizontal plasma flows, perpendicular to the satellite track. (c) The F15 spectrogram includes, from top to bottom, (1) electron and ion integral energy flux, (2) electron and ion average energy, (3) precipitating electron spectrogram, and (4) precipitating ion spectrogram.

flow channels, which can be indicators of upward FAC. The DMSP F15 spectrogram shows an extended dawnside oval, and IMAGE FUV indicates an expanded oval. DMSP data show that at the highest latitude portion of the duskside oval (at about 80 deg magnetic latitude (MLAT)) the electron and the ion spectra are those of a transpolar arc, but the energy flux is more typical of the oval and average energy is increasing. These arc signatures (between the black solid lines) are collocated with the duskside of the high-latitude sunward flow region. Poleward of the high-latitude arc signature is a spatially broad region of open field lines identified by polar rain in the electron data and a lack of ion precipitation at ~ 0316-0332 UT.

5.2.2 TPA2: 2nd March 2002

The Second interval was during 2nd of March 2002. TPA2 was visible in the IMAGE data for approximately 5 hours. However, it is difficult to estimate how long TPA2 existed, precisely, as the dayglow reduces the visibility of TPA2 and the auroral oval by the end of the interval. In this case study, the auroral oval stays at 70° latitude throughout the whole interval (Fig. 5.7a, same format as Fig. 5.2a). The structure of TPA2 and its motion is also shown in Fig. 5.7a, where the duskward motion of the arc after 1200 UT is clear.

During this interval, the IMF is variable, both in direction and strength. For the first 3 hours of the interval IMF B_z component decreases until it reaches zero at around 1030 UT. The IMF B_y component, however, goes through a sudden change in direction from negative to positive just before 1100 UT. Although a duskward motion is observed for TPA2 from the time it appears in the data until 1230 UT, this motion is perhaps most rapid after the IMF turned from $B_y < 0$ to $B_y > 0$ for the second time at around 1130 UT (Fig. 5.7c). The location of TPA2 is steady (~ 90°) for the rest of the interval when the IMF B_z component is strongly positive (just before 1300 UT) and dominant and IMF B_y component is decreasing slowly. A few interesting points regarding this interval are given below.

Figure 5.8(a-e) illustrates five snapshots of the Northern Hemisphere auroral configuration by (IMAGE) FUV/WIC instrument, presented in a magnetic

02 Mar 2002

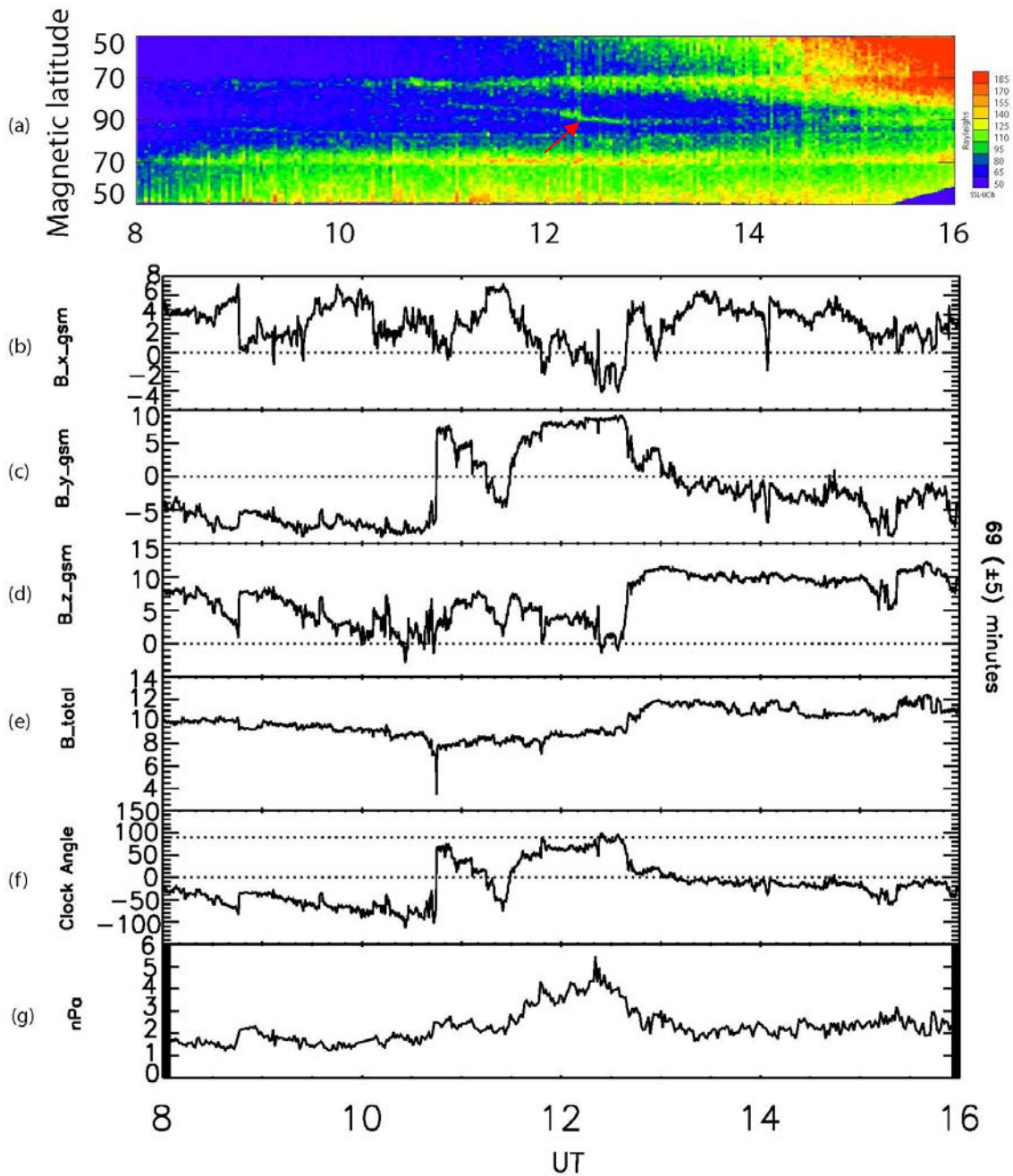


Figure 5.7 (a) Keogram presentation of the transpolar arc observed by the IMAGE FUV/WIC along the dusk-dawn meridian (b-g) IMF information measured by the ACE satellite.

TPA2: 02 March 2002

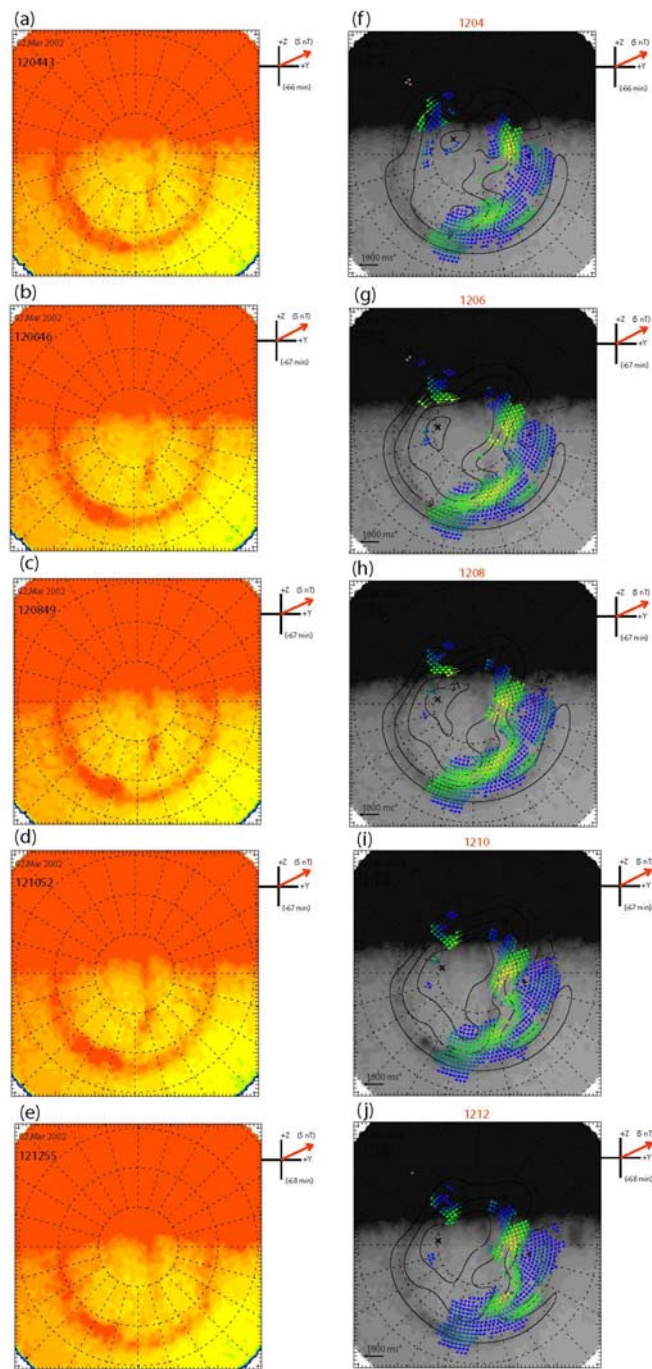


Figure 5.8 (a-e) Five snapshots of the Northern Hemisphere auroral configuration by the IMAGE FUV/WIC instrument, presented in a magnetic latitude and magnetic local time frame, with noon towards the top of each panel. (f-j) Five auroral snapshots of figures 5.8(a-e), with SuperDARN estimates of the simultaneous ionospheric convection overlaid. Vectors indicate the location of convection measurements.

latitude and magnetic local time frame, with noon towards the top of each panel. The second column of Fig. 5.8(f-j), presents the five auroral snapshots of figures 5.8(a-e), with SuperDARN estimates of the simultaneous ionospheric convection overlaid. Vectors indicate the location of convection measurements. What is noticeable in these figures (5.8a-e), are the motions of the dayside and nightside parts of the TPA, which appear to be independent from each other. As can be seen from Figures 5.8(f-j), there are dawnward flows at the post-noon sector (starting from 1530 MLT) flowing into the dawn compartment.

Another example of the displacement of the arc caused by motion of the ionospheric flows is given in Figure 5.9. This figure shows two snapshots of the arc at 1302 UT and 1424 UT. During this time the arc moved from near midnight to 22 MLT. This displacement seems to be caused by the redistribution of flux in the polar cap. What makes these sets of plots more interesting, is the IMF condition between 1302 and 1424 UT when the arc was displaced by nearly 2 hours of MLT on the nightside. The IMF is northward for the duration of this interval. On the dayside (Fig. 5.9c-e) there is evidence for sunward flows near noon indicating that the flow is being driven by lobe reconnection. As predicted by *Milan et al.* (2005), for the case of $B_z \text{ \& } B_y \geq 0$; $|B_y| < B_z$, plasma and flux is stirred within the polar cap, pushing the arc towards dusk.

Figure 5.10 shows particle precipitation data from DMSP F13 and NOAA 16, which were crossing the Northern polar cap when DMSP F14 was passing the southern polar cap, tracks of which are demonstrated in Fig. 5.10b by blue line (Southern Hemisphere pass) and yellow lines (Northern Hemisphere pass). Cross track plasma drift data from DMSP F13 (Fig. 5.10d) illustrates sunward flows in the postnoon sector and antisunward flows in the prenoon sector. Comparing the SuperDARN ionospheric flows at the dayside (shown in Fig. 5.10b) with the horizontal plasma flow data provided by DMSP F13, there is an agreement between the two regarding the direction of the flows. Signatures of the TPA are yet again observed in the DMSP F13 spectrogram (Fig. 5.10c). A region of high energy electrons at the highest latitude ($\sim 82^\circ$ and ~ 1300 MLT) being surrounded by regions void of ions and lower energy electrons, can be interpreted as the signatures of the TPA in the spectrogram data. At around the same

TPA2: 02 March 2002

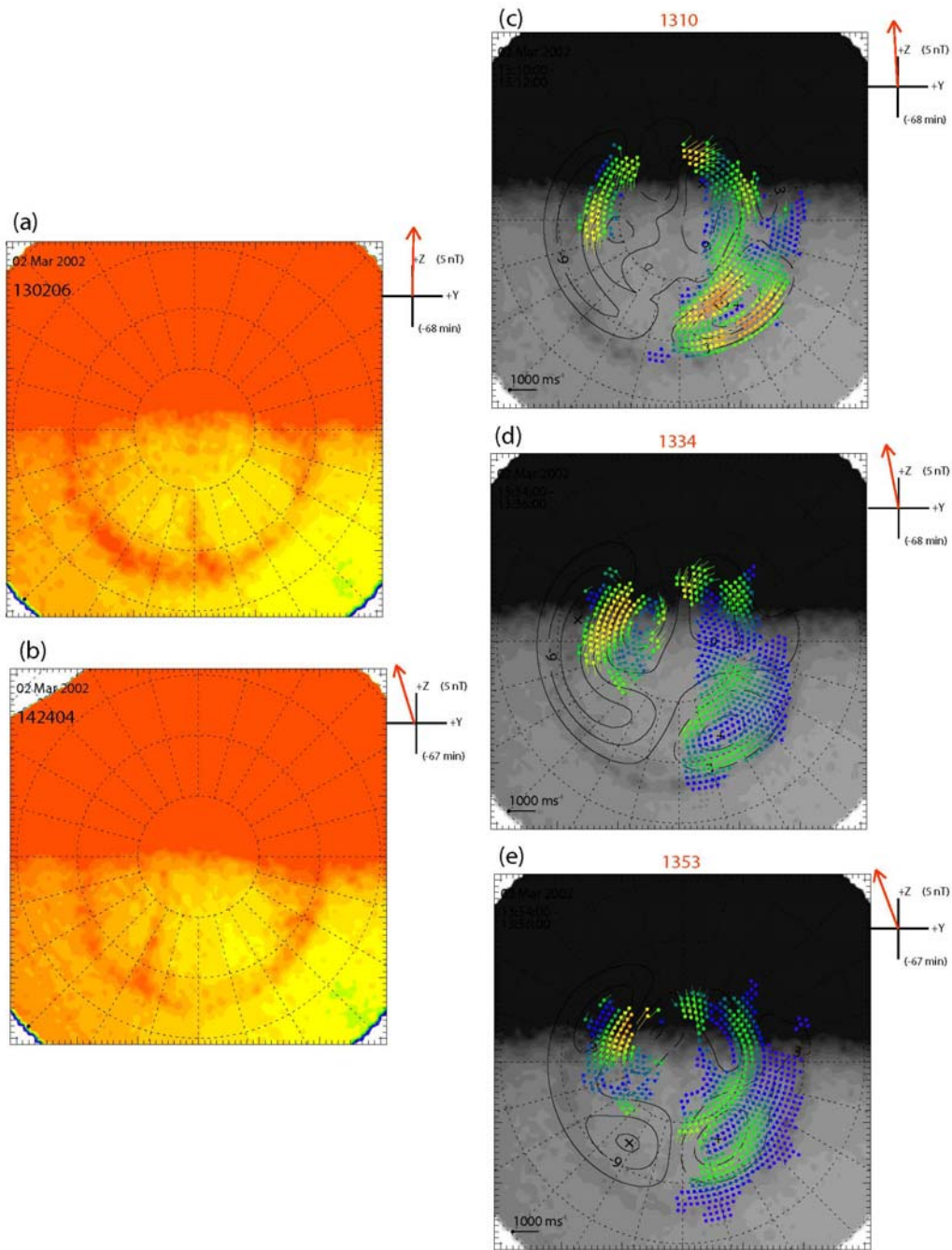
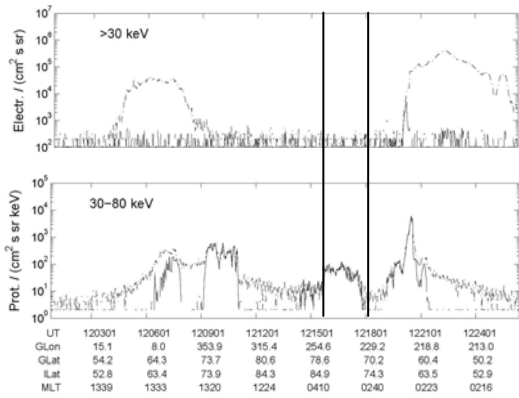
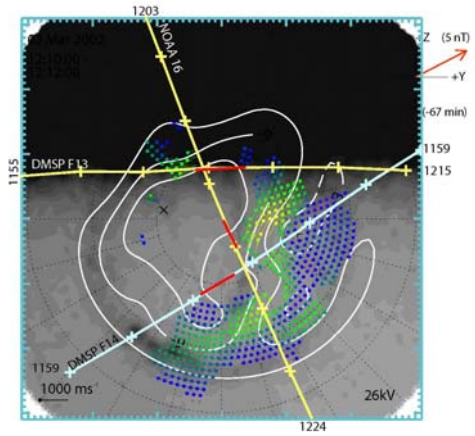


Figure 5.9 (a & b) Two snapshots of the Northern Hemisphere auroral configuration (c-e) Three auroral snapshots, with SuperDARN estimates of the simultaneous ionospheric convection overlaid. Vectors indicate the location of convection measurements.

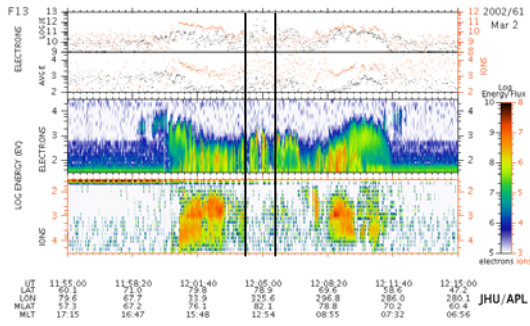
TPA2: 2 March 2002



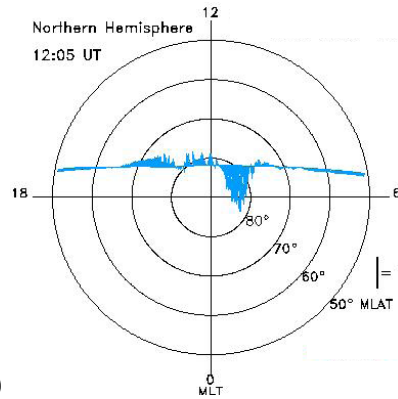
(a)



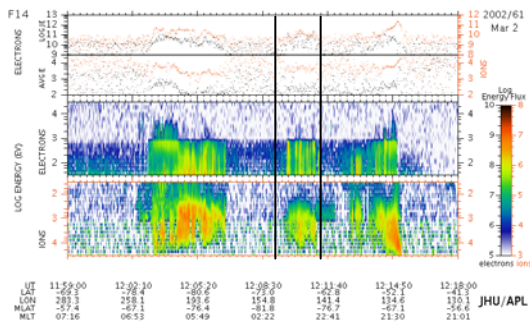
(b)



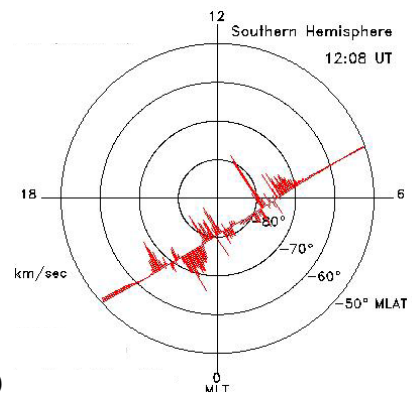
(c)



(d)



(e)



(f)

Figure 5.10 Data shown from DMSP F13 and NOAA 16 pass in the Northern Hemisphere and DMSP F14 in the Southern Hemisphere on 02 March 2002 that occurs during the FUV data period.

universal time, NOAA 16 is crossing the northern polar cap when the satellite identifies a region of highly energetic ions at the nightside at around 80° and 0200 MLT. Spectrogram data from DMSP F14 pass in the Southern Hemisphere identifies a region of precipitating electrons and ions surrounded by regions of void in both ions and electrons. This southern hemisphere pass suggests that there may be some degrees of conjugacy in the observations of particle signatures and the TPA (Figure 5.10e).

5.2.3 TPA3: 4th March 2002

The third interval happened on 4th of March 2002. It is difficult to estimate how long TPA3 (is shown using a red arrow) lasted for, as the first hours of IMAGE FUV data are again missing as a result of the spacecraft orbit. Another TPA is observed in the keogram data (shown using a yellow arrow). The second TPA is located in the dawn region and exhibits a duskward motion throughout the interval.

As can be seen in the keogram of the third case study (Fig. 5.11a), the equatorward edge of the auroral oval is located at 65° latitude at the beginning of the interval and slowly goes up to 70° latitude by 1000 UT and thereafter moves towards lower latitude again by the end of the interval (Fig. 5.11a). It is difficult to judge when exactly the TPA forms as it gradually forms out of the duskside auroral oval and moves towards the centre of the polar cap by 0600 UT (Fig 5.11a). Right after the TPA reaches the highest latitude ($\sim 90^\circ$), it starts to move back towards dusk. This motion continues until 1000 UT when the TPA becomes dynamically stable and stays at $\sim 70^\circ$ latitude until 1200 UT.

The variable IMF for this interval (Fig. 5.11b,c, and d) makes it rather difficult to see the effects of changes in the IMF on the formation and dynamics of TPA3. Although the strength of the IMF B_y component varies dramatically throughout the interval it mainly stays positive. After 0600 UT when both IMF B_z and B_y components become rather weak the TPA starts to move towards dusk. At around 0800 UT when the IMF becomes mainly B_y dominant, the TPA stays at the same location until the end of the interval when again due to loss of data it is

04 Mar 2002

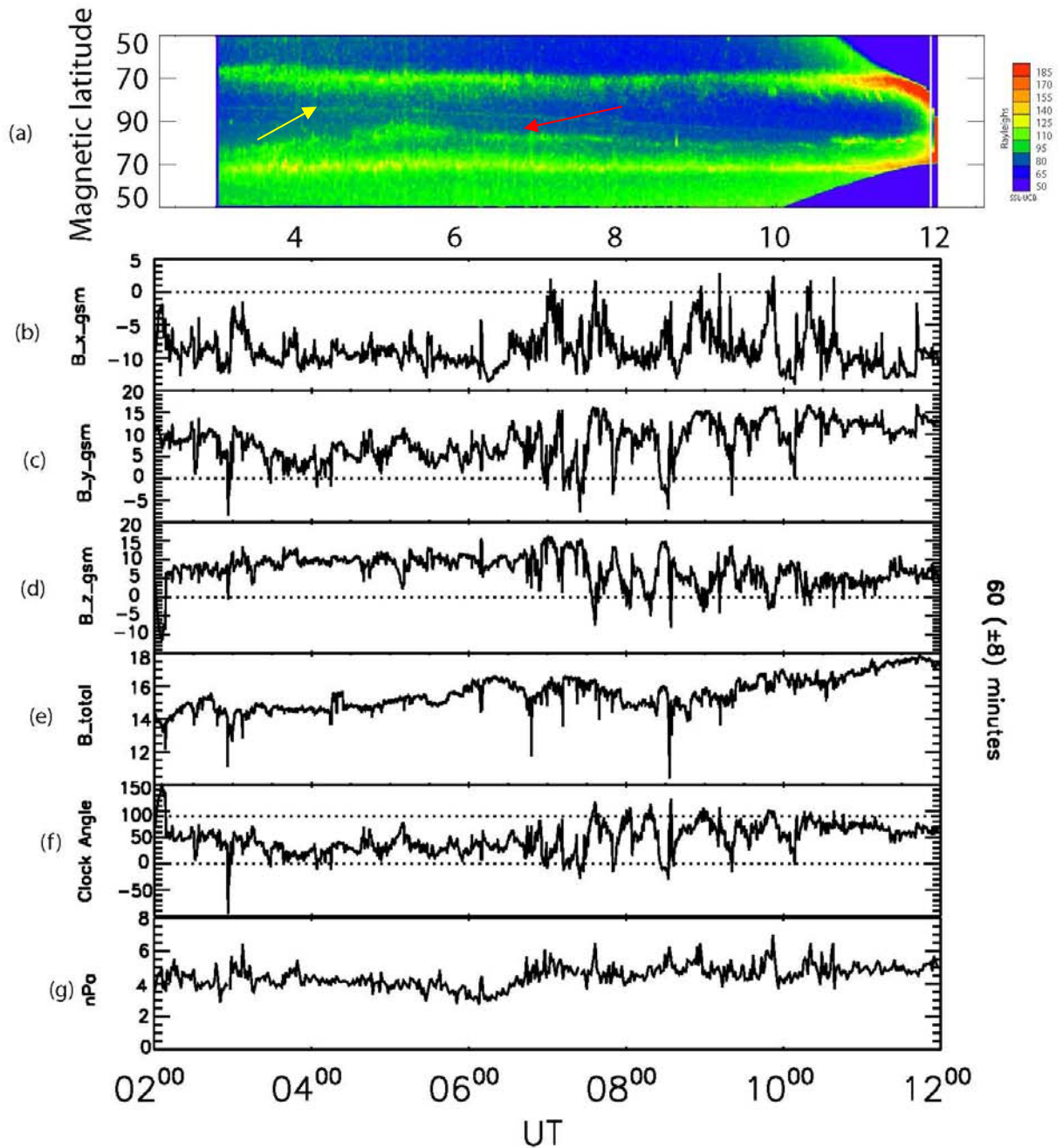


Figure 5.11 (a) Keogram presentation of the transpolar arc observed by the IMAGE FUV/WIC along the dusk-dawn meridian (b-g) IMF information measured by the ACE satellite.

impossible to track the TPA motion.

Figure 5.12 shows the first set of examples of the motion of TPA3 using three snapshots of the auroral emission for three different locations of the TPA, along with three snapshots of the ionospheric flows overlaid on the auroral emission data from the same times, in order to show what is causing certain movements of the TPA. As can be seen in Figures 5.12a-c, TPA3 extends across the polar cap on the duskside. The arc then starts to move towards dusk (Fig. 5.12c) and eventually merges with duskside auroral oval. Looking at the ionospheric flows (Fig. 5.12d-f) provides the answers as to why the TPA is being pushed towards dusk. As the IMF is northward with its B_y component being dominant and strongly positive, high-latitude reconnection can siphon open flux from one region to the other (*Milan et al.*, 2005). Figure 5.12d-f are just three snapshots of many examples of the ionospheric flow behaviour towards the end of interval. These snapshots illustrate the dawnward motion of ionospheric flows at the dayside which carries newly created open flux from the dayside into the dawn compartment of the polar cap (*Goudarzi et al.*, 2008), or moves open flux from the duskside to the dawnside (*Milan et al.*, 2005). This redistribution of flux causes the motion of the TPA towards dusk.

Occurrence of a second arc in the post midnight sector is yet another point which makes this case study particularly interesting. Figures 5.13a, b, and c show the gradual appearance and decay of this second arc (Black arrow indicates the first TPA, blue arrows indicate the second TPA). Figures 5.13d and e show some of the ionospheric flow behaviour prior to the appearance of the second TPA. The second TPA seems to be locally stable, which is probably due to the steady IMF conditions during its existence. The second TPA starts to fade away at around 0814 (Figure 5.13c), following a long period when the IMF had been strongly B_y dominant. The direction of the IMF causes the reconnection to happen in the post noon sector, leading to an inflation of the dawnside compartment of the polar cap, as magnetic flux moves there. As a consequence, the post midnight sector of the auroral oval moves to the lower latitudes. This motion seems to be the reason for the disappearance of the second TPA.

TPA3: 04 March 2002

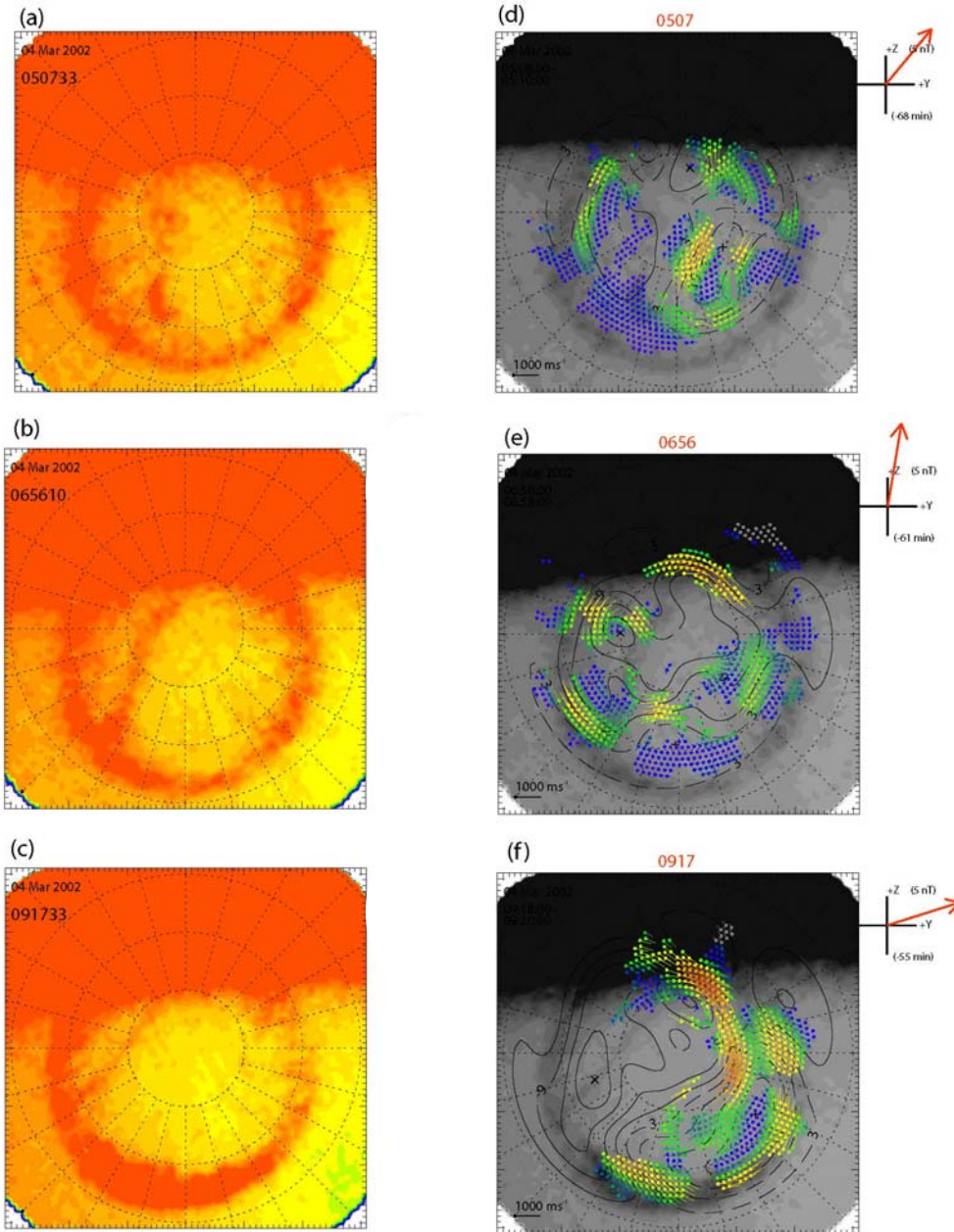


Figure 5.12 (a-c) Three snapshots of the Northern Hemisphere auroral configuration. (d-f) Three auroral snapshots, with SuperDARN estimates of the simultaneous ionospheric convection overlaid. Vectors indicate the location of convection measurements.

TPA3: 04 March 2002

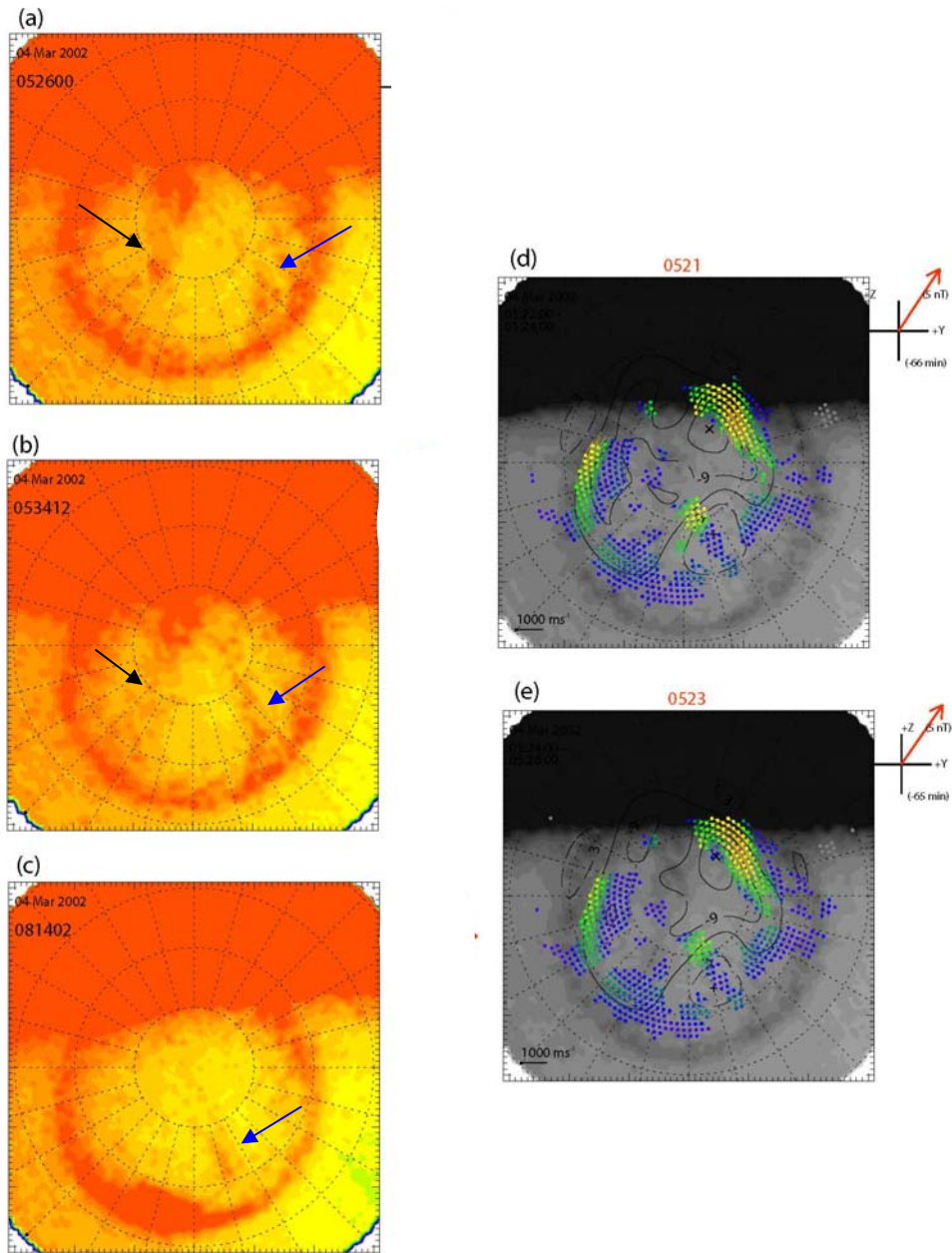


Figure 5.13 (a-c) Three snapshots of the Northern Hemisphere auroral configuration. (d-e) Two auroral snapshots, with SuperDARN estimates of the simultaneous ionospheric convection overlaid. Vectors indicate the location of convection measurements.

5.2.4 TPA4: 11th March 2002

The fourth interval happened on 11th of March 2002. What makes this interval noticeable is that TPA4 is part of a long lasting TPA, the second part of which happened on 12th of March 2002, and which will be discussed in the next section.

One of the difficulties we face here is that tracking the motion of TPA4 from looking at the keogram alone is rather difficult due to the very strong dayglow. As can be seen from Fig. 5.14a, the dusk part of the auroral oval is not clearly visible due to the strong dayglow, whereas the dawnside auroral oval seems to be steady and located at 70° latitude. Auroral emission data captured by the IMAGE spacecraft show slight movement of TPAs towards dawn at around 2124 UT. This dawnward motion is associated with the dawnward turning of the B_y after 2100 UT (Fig. 5.14c). In order to show this displacement, two selected snapshots of the Northern Hemisphere auroral configuration are shown in figure 5.15a & b. Figures 5.15c-e illustrate the corresponding convection maps for three selected times. As can be seen from 5.15a & b, the arc has moves from just before 2400 MLT to 0200 MLT within 4hours. This dawnward motion can be explained by investigating the ionospheric flow characteristics, three selected examples of which are given in Figs. 5.15d & e. According to the convection maps presented in Figs. 5.15d & e, high latitude reconnection in the dawn compartment of the polar cap is responsible for transferring plasma and flux from dawn to dusk compartment of the oval, causing the TPA to move dawnward.

At about 2303 UT the B_y turns positive (Fig 5.15e), creating dawnward flows at the dayside. This change in the direction of the ionospheric flows would cause a change in the direction of the motion of the TPA. This motion, however, is an immediate but a very slow one, the effect of which is visible after approximately an hour and will be discussed in the next case study.

Figure 5.16 illustrates DMSP F15 satellite pass on 11 March 2002. By comparing the IMAGE data with the azimuthal flow data from DMSP F15, it is obvious that the arc is collocated with the duskside of the high-latitude sunward flow region. The spectrogram shows either an unusual broad arc (from 193724-

11 Mar 2002

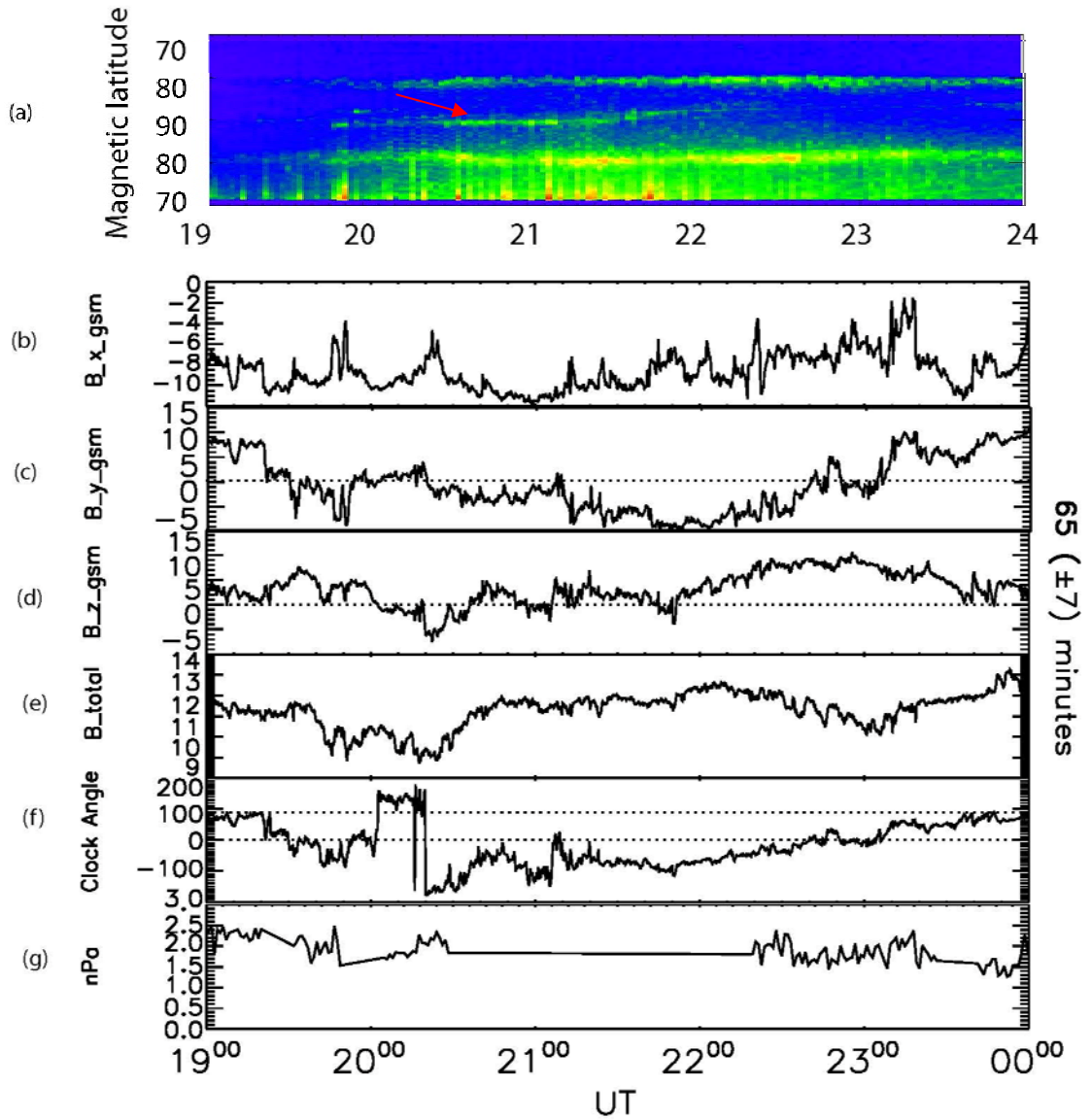


Figure 5.14 (a) Keogram presentation of the transpolar arc observed by the IMAGE FUV/WIC along the dusk-dawn meridian (b-g) IMF information measured by the ACE satellite.

TPA4: 11 March 2002

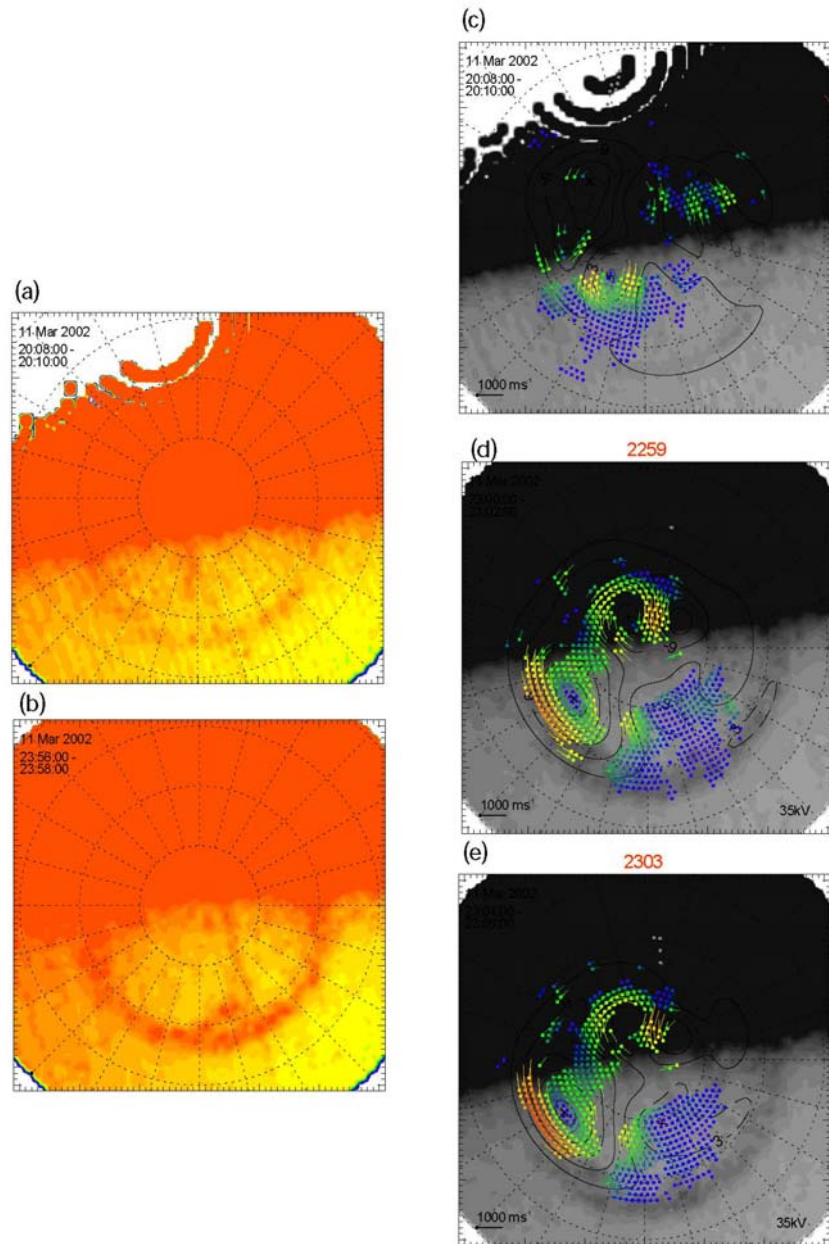


Figure 5.15 (a-c) Three snapshots of the Northern Hemisphere auroral configuration. (d-f) Three auroral snapshots, with SuperDARN estimates of the simultaneous ionospheric convection overlaid. Vectors indicate the location of convection measurements.

TPA4: 11 March 2002

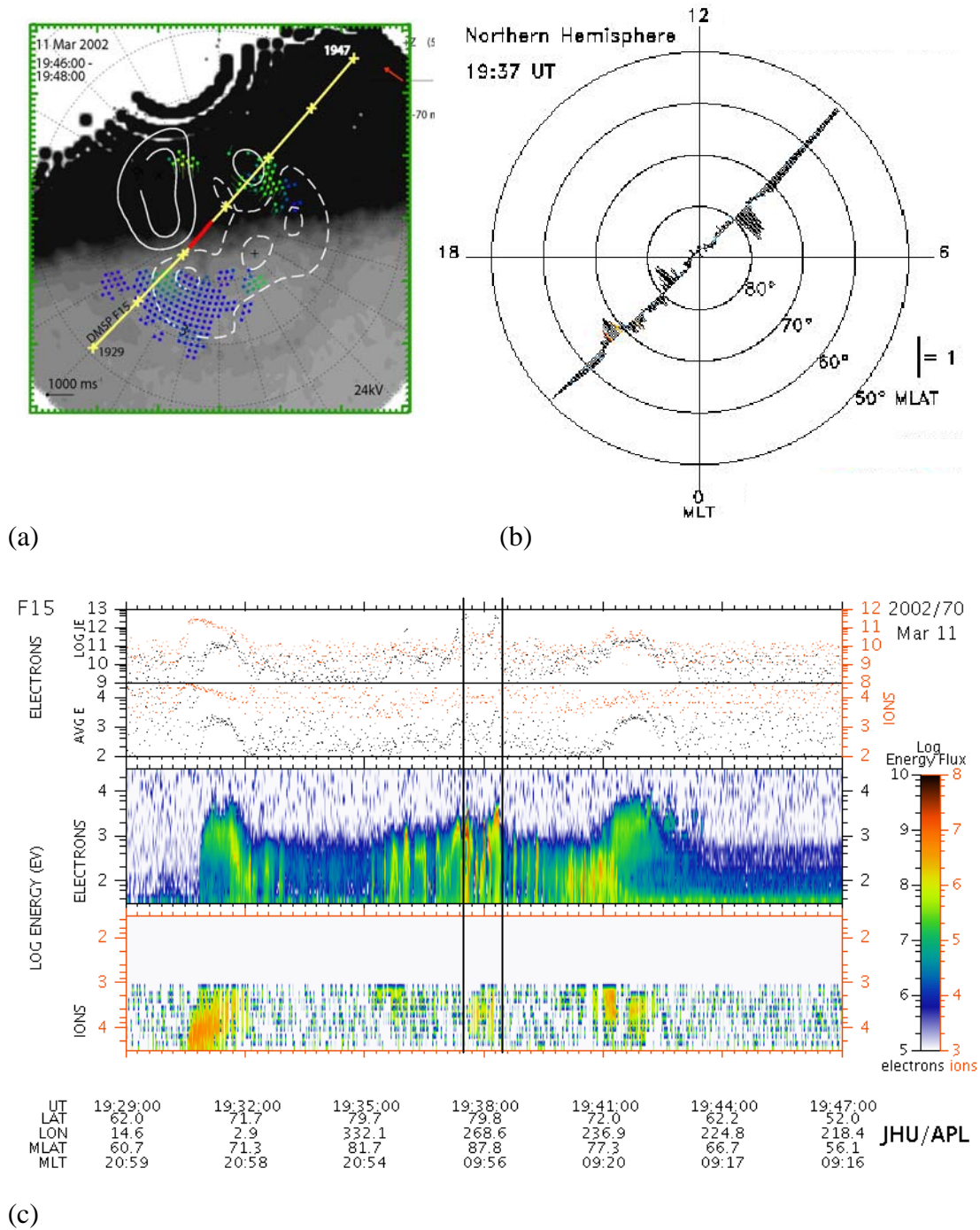


Figure 5.16 Data shown from DMSP F15 pass on 11 March 2002 (19:29-19:47 UT) that occurs during the FUV data period.

193820 UT) or double arc is associated the TPA seen in the FUV image. The particle precipitation consists mainly of an electron signature and ion signature (energy flux) usually associated with the auroral oval (closed field lines) which is between the poleward part of the boundary plasma sheet (BPS) and a region (prior to the appearance of the TPA) which can be identified as a mantle population on the basis of low-energy 1 keV ion precipitation (*Newell et al.*, 1991). This is consistent with the clear spatial separation of the higher energy flux associated with the TPA from the associated with the auroral oval.

At about 2010 UT, on the same date, there are two satellite passes (NOAA 15 and DMSP F13), both of which reach high magnetic latitudes where they capture signatures of the TPA (Figure 5.17c-d). Figure 5.17b indicates the DMSP F13 plasma flows. However the data are flagged as undetermined for this interval and therefore one must be careful about the accuracy of this dataset. On the duskside of the dawn-dusk meridian large antisunward and sunward flows are seen in Figure 5.17b. Comparing these flows with the convection map in Figure 5.17a, it is obvious that the flows are indicators of a clockwise convection cell. On the satellite track, there are two more sets of sunward and antisunward flows, which again indicate the presence of clockwise convection cells. A signature of the transpolar arc is observed in both satellite dataset at around 88° latitude where the TPA is located on the duskside of the noon-midnight meridian. The arc is collocated with the duskside of the high-latitude sunward flow region. The NOAA 15 spectrogram shows a peak in 30-80 keV ions (marked by a black arrow in Fig. 5.17c) and no particular signature of the arc in the > 30 keV energy electrons at the highest latitude. The DMSP F13 spectrogram, however, shows an electron and ion signature which is typical of the auroral oval (closed field lines) which is surrounded by regions void of ions and filled with polar rain electrons (associated with open field lines). This is consistent with the clear spatial separation of the higher energy flux associated with the TPA from that associated with the auroral oval.

Figure 5.18 illustrates another two satellite crossings of the northern polar cap. At the time of the observations shown in Fig. 5.18, both IMF B_z and B_y have changed their directions from being negative and positive to positive and

TPA4: 11 March 2002

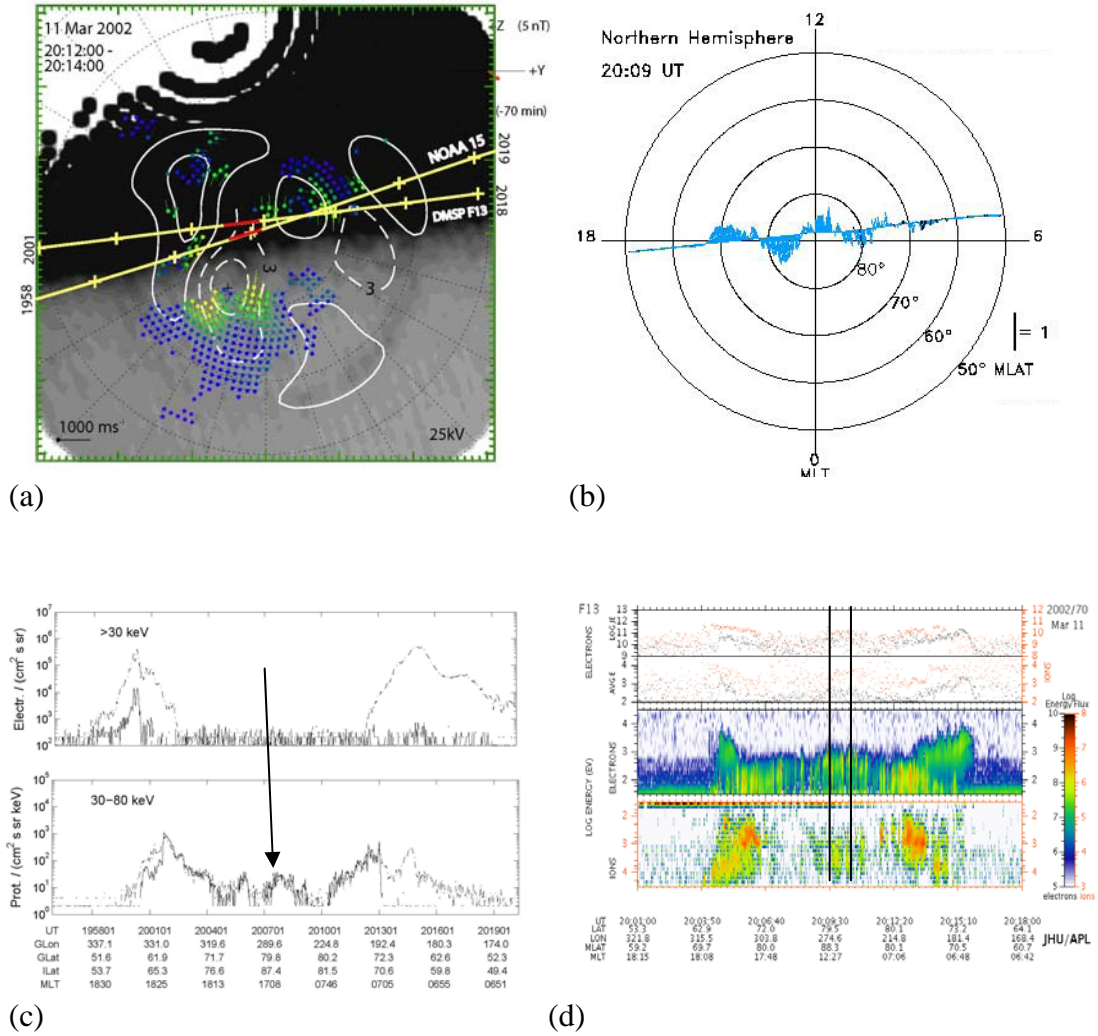


Figure 5.17 Data shown from NOAA 15 and DMSP F13 pass on 11 March 2002 (19:58-2019 UT & 20:01-2018 UT) that occurs during the FUV data period.

TPA4: 11 March 2002

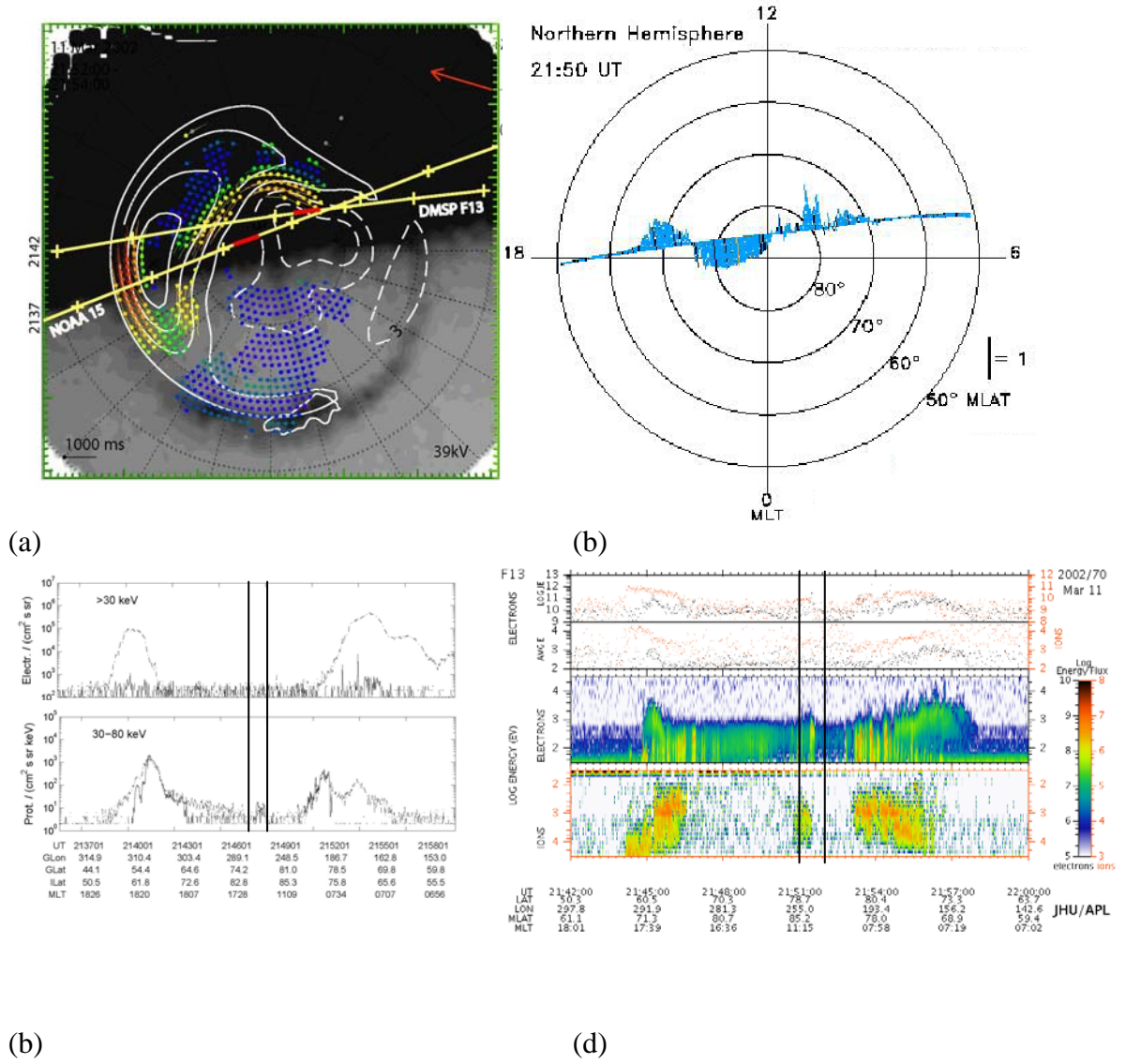


Figure 5.18 Data shown from NOAA 15 and DMSP F13 pass on 11 March 2002 (2137-2158 UT & 2142-2200 UT) that occurs during the FUV data period.

negative respectively. Similar conditions for the DMSP F13 plasma flow figure applies for this set of observations as the previous one where the data is flagged as undetermined. Again at the duskside of the noon-midnight meridian, there are strong sunward and antisunward flows which are associated with the clockwise convection cell. As the B_y component of the IMF is positive and dominant, appearance of clockwise convection cells can be explained by low latitude reconnection process happening at the duskside of the oval. Once again, the NOAA 15 spectrogram shows a small peak in high energy ions but no particular signature of the arc in the high-energy electrons at the highest latitude. The DMSP F13 spectrogram shows a concentrated presence of electron and ion signatures, which are typical of the auroral oval and is surrounded by regions void of ions and filled with polar rain electrons. This is yet again consistent with the clear spatial separation of the higher energy flux associated with the TPA from that associated with the auroral oval.

Finally, the last set of data belongs to a conjugate observation of the particle precipitation data from DMSP F14 in the Northern Hemisphere, NOAA 15 and DMSP F13 in the Southern Hemisphere (Fig. 5.19). The region between the solid black lines (Fig. 5.19b) indicates a region of highly energetic ions and electrons, which is surrounded by void of ions and filled with polar rain electrons. Unfortunately, due to loss of data prior to 2056 UT, it is difficult to see the duskside oval boundary in the spectrogram data. At around the same universal time, satellites NOAA 15 and DMSP F13 are crossing the southern polar cap. It is interesting to compare the open/closed field line boundary location in both data sets and find the agreement in both satellite data regarding the location of the auroral oval. However, the signatures of the TPA are not very clear from the spectrogram data. This might be due to the fact that the satellites are crossing the polar cap at very high-latitudes ($\sim 85^\circ +$). Comparison of the ionospheric flows (Fig. 5.19a) with cross track plasma drift data from DMSP F13 (Fig. 5.19e), shows an agreement regarding the direction of the ionospheric flows.

TPA4: 11 March 2002

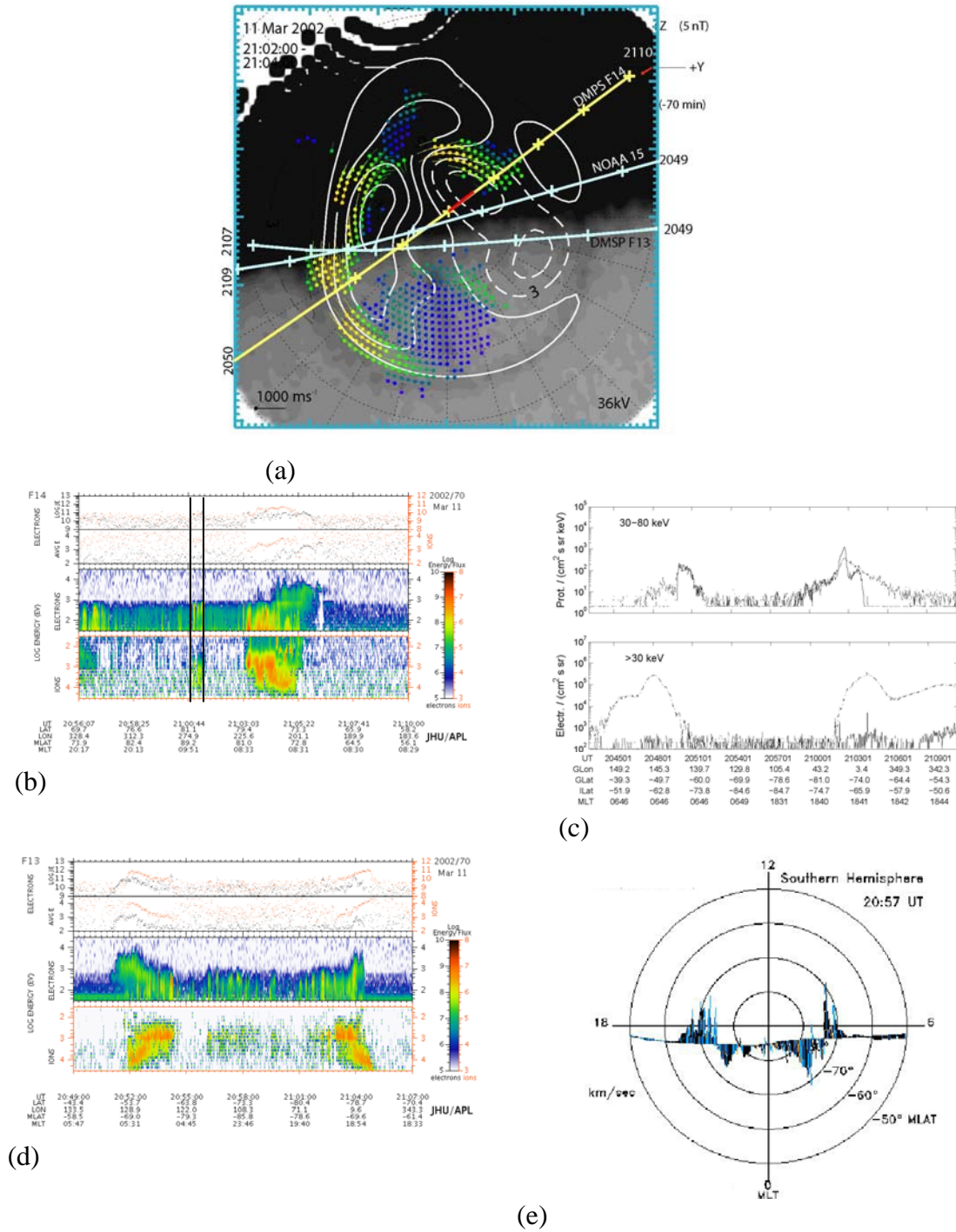


Figure 5.19 Data shown from DMSP F14 and NOAA 15 pass in the Northern Hemisphere and DMSP F13 in the Southern Hemisphere on 11 March 2002 that occurs during the FUV data period.

5.2.5 TPA5: 12th March 2002

The last interval is 12th of March 2002. As mentioned above, this interval is the second part of a long lasting TPA, which started on the 11th of March 2002.

Figure 5.20a, illustrates the motion of TPA5 in dusk-dawn meridian. In this keogram the auroral oval in the dawn and dusk sectors are located near 70° latitude throughout the interval of observation. Continuing its motion from the previous day, TPA5 changes its direction from dawnward to duskward. A steady duskward motion of the TPA starts at 90° latitude at 0000 UT and carries on for the next couple of hours when it reaches 80° at around 0430 UT.

The IMF B_y and B_z components stay mainly positive during the 5th interval (Fig. 5.20c and d respectively). Duskward motion of this TPA is visible and seems to be associated with the positive IMF B_y component. The TPA is visible from the beginning of the day at 0002 UT, as it was formed on the previous day (discussed above). Due to the B_y component of the IMF being strongly positive, the reconnection seems to be happening at the dayside, at very high-latitude, creating dawnward flows. Figure 5.21 illustrates the motion of the arc, starting from 2356 UT on the previous day after the B_y component of the IMF turned positive. As mentioned previously, when B_y changes its position from positive to negative, it is expected that the arc moves to the opposite direction which will happen immediately but slowly. Figures 5.21a, b, and c, show this motion over the course of an hour. In order to have a better understanding of this motion, Figures 5.21d, e, and f, present the ionospheric convection for three time slots shown in Figures 5.21a, b, and c, to show the cause of this westward motion. All three latter figures show strong dawnward flows, transferring the flux from the dusk to the dawn compartment, making the nightside auroral oval expand to lower latitude and causes the TPA to move towards dusk.

During the course of the same interval on 12th March 2002, the TPA keeps moving duskward, a motion for which the positive B_y component of the IMF seems to be responsible. Figure 5.22 shows a series of ionospheric convection maps overlaid on the auroral emissions to illustrate the ionospheric flows causing this motion. As can be seen in these plots, a positive B_y component of the IMF is

12 Mar 2002

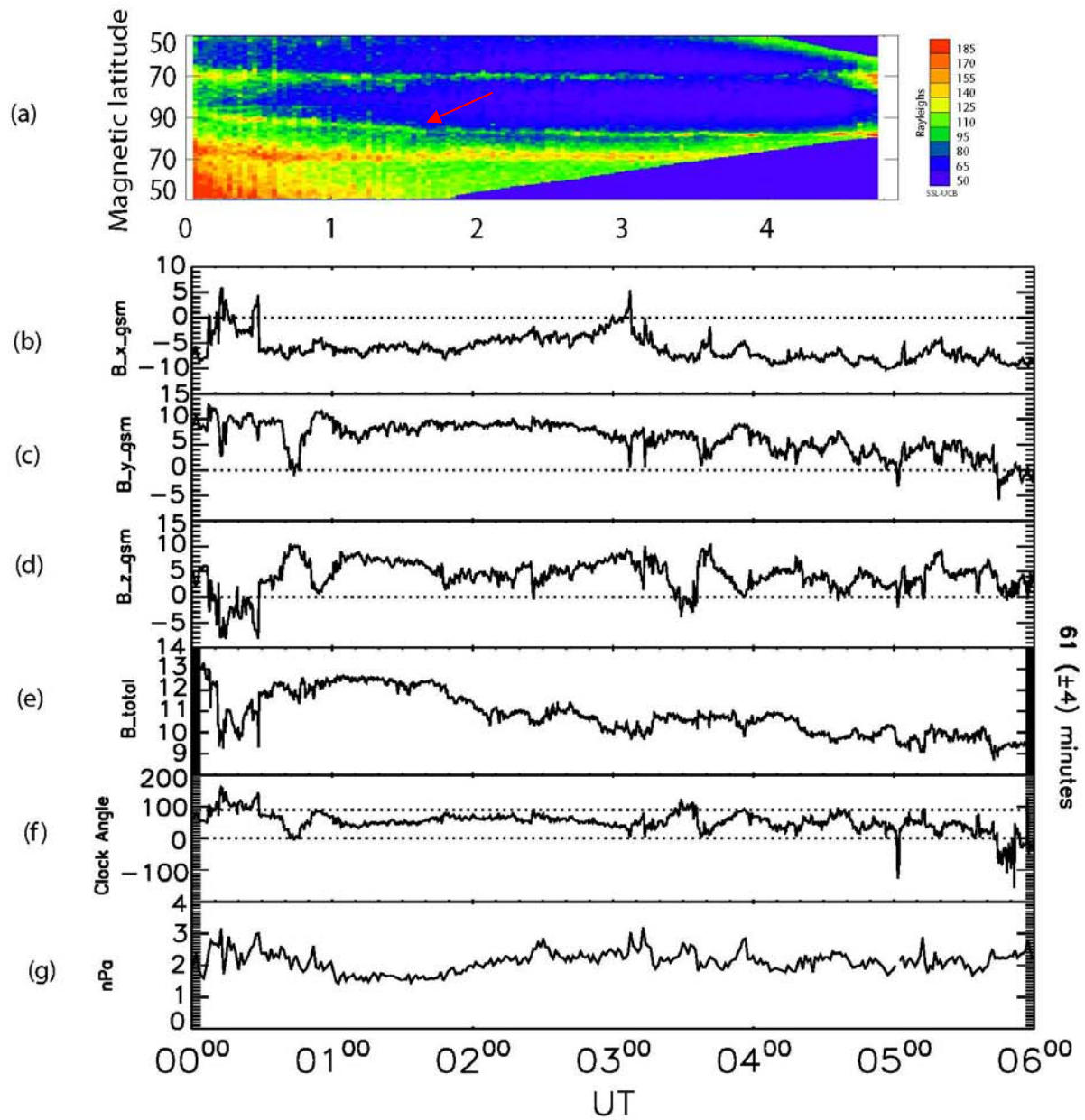


Figure 5.20 (a) Keogram presentation of the transpolar arc observed by the IMAGE FUV/WIC along the dusk-dawn meridian (b-g) IMF information measured by the ACE satellite.

TPA5: 12 March 2002

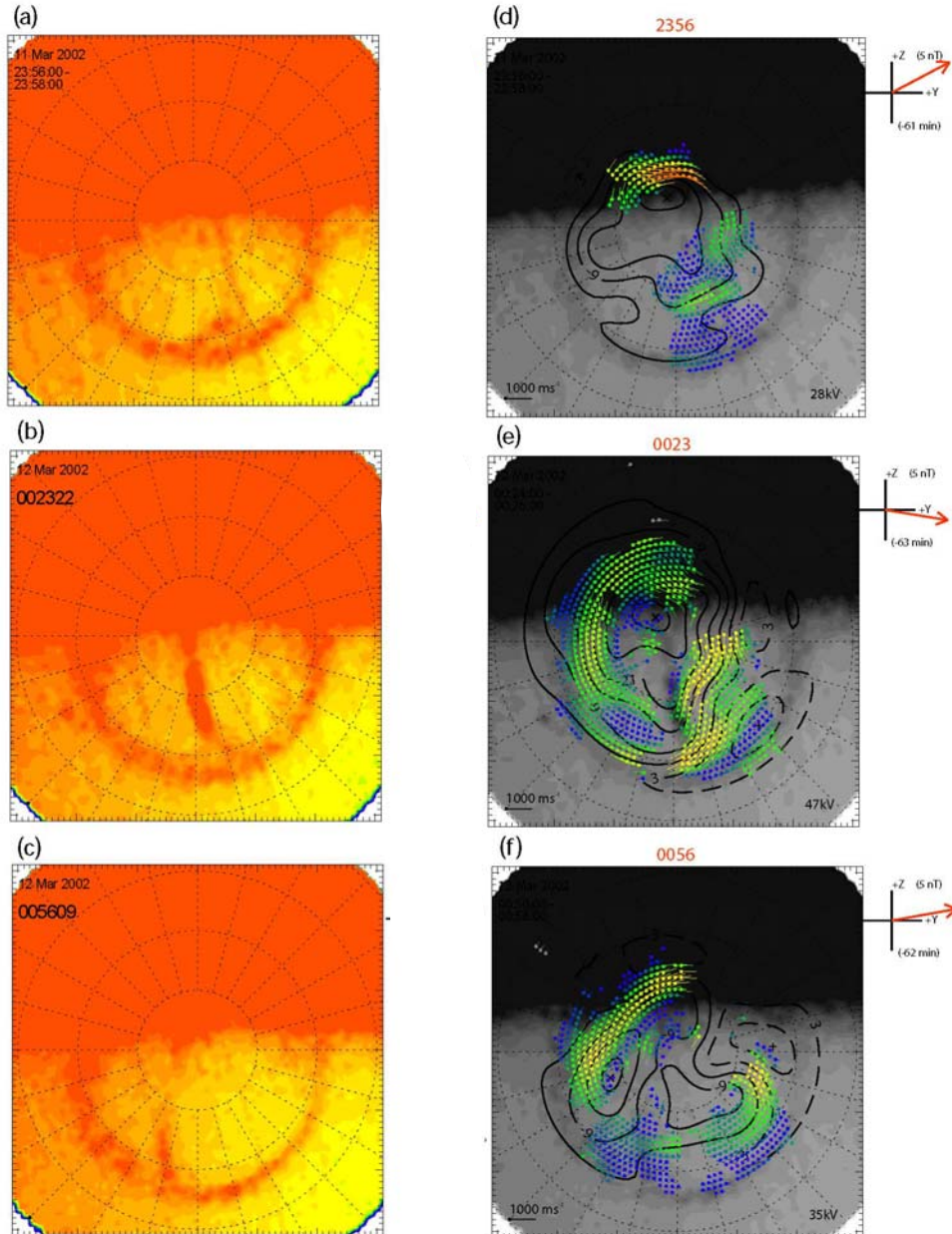


Figure 5.21 (a-c) Three snapshots of the Northern Hemisphere auroral configuration. (d-f) Three auroral snapshots, with SuperDARN estimates of the simultaneous ionospheric convection overlaid for three time slots shown in figures 5.21a-c. Vectors indicate the location of convection measurements.

TPA5: 12 March 2002

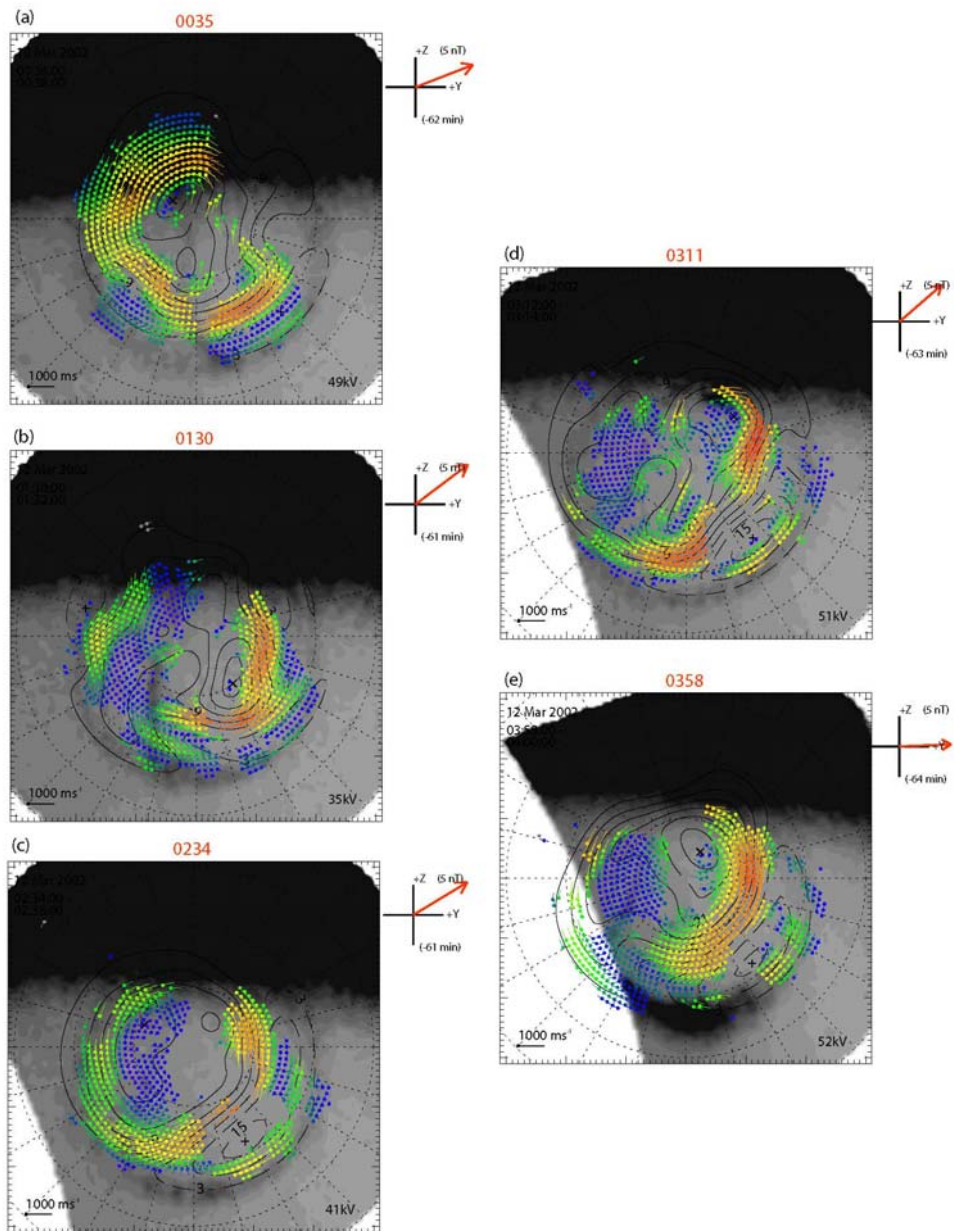


Figure 5.22 (a-e) Five auroral snapshots, with SuperDARN estimates of the simultaneous ionospheric convection overlaid. Vectors indicate the location of convection measurements.

causing high-latitude reconnection. From this process, plasma and flux is stirred and transferred from the dusk to dawn cell, causing the dusk compartment to contract and the dawn compartment to expand (*Milan et al.*, 2005). As a result of this the TPA moves towards dusk.

An example of the build-up of closed flux at the nightside, pushing the arc into the polar cap, occurred on the 11th & 12th March 2002. A set of snapshots are presented in Figure 5.23, where rather strong sunward flows are visible at high-latitude. These flows are located at the exact same location that the arc is which can only prove the point that the arc forms as a result of closed flux emanating from the nightside auroral oval (*Frank et al.*, 1986; *Huang et al.*, 1987; *Zhu et al.*, 1997; *Milan et al.*, 2005). Based on some observations, it has been suggested that the large-scale convection on one side of the shear flow associated with TPAs can be stagnant or reverse to the sunward direction (*Carlson et al.*, 1984; *Mende et al.*, 1988). TPAs with mesoscale sunward flows were reported using DE satellite measurements (*Frank et al.*, 1986). They found that for bright TPAs the convection within the arcs is sunward while the background convection outside the arcs is antisunward.

Fig. 5.24 illustrates an observation of TRINNIIs. Figure 5.24a shows dawnward TRINNI like flows at lower latitudes ($\sim 66^\circ$) in the Northern Hemisphere, the origin of which corresponds to the nightside end of the TPA just before 2300 MLT. Figures 5.24b,c show another two examples of these cross midnight azimuthal flows at 0139 and 0141 UT.

TPAs 5 & 6: 11 & 12 March 2002

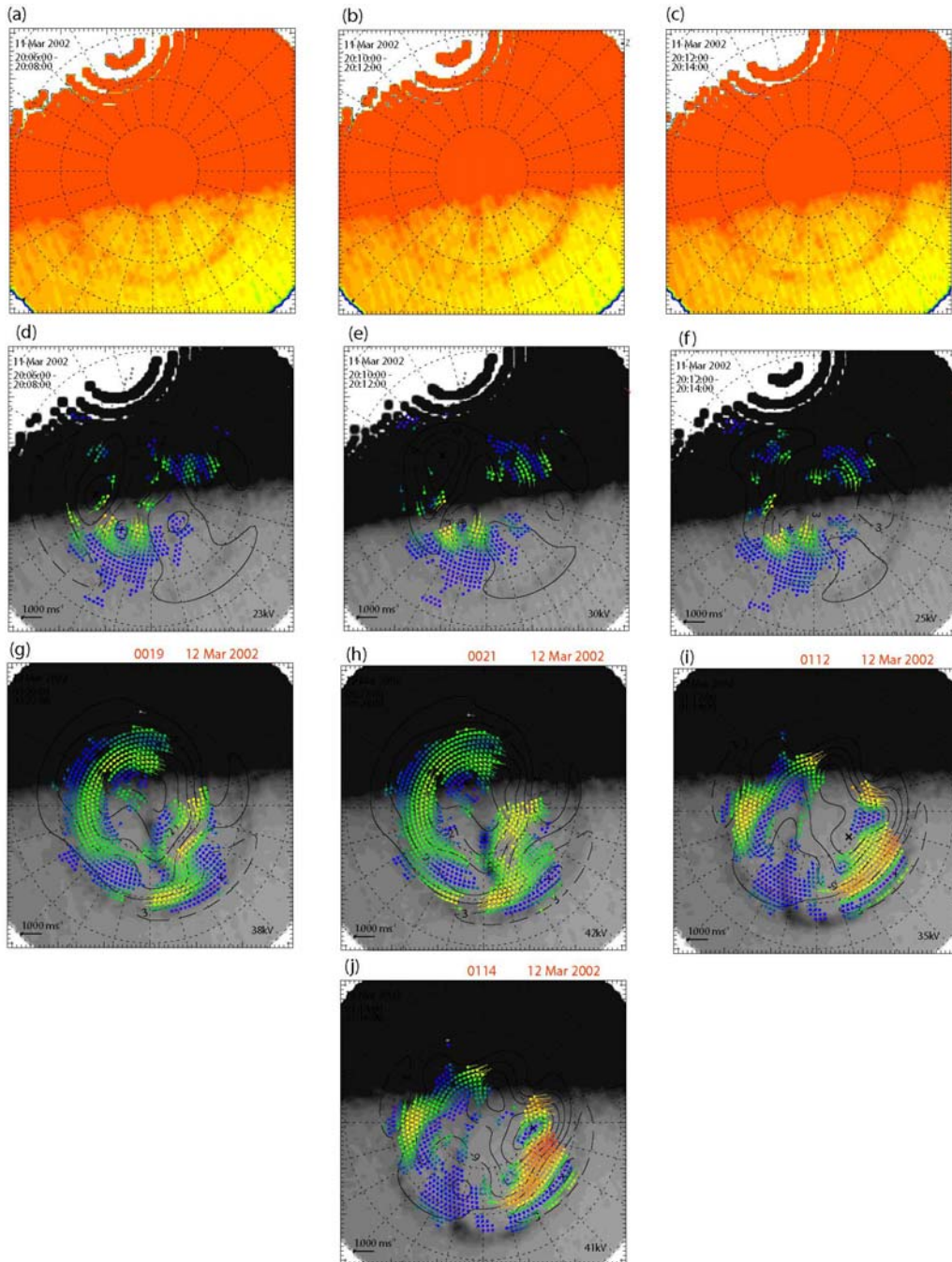


Figure 5.23 (a-c) Three snapshots of the Northern Hemisphere auroral configuration for 11th March 2002. (d-f) Three auroral snapshots of figures 5.23a-c, with SuperDARN estimates of the simultaneous ionospheric convection measurements. (g-j) Four snapshots of Northern Hemisphere auroral configuration with SuperDARN estimates of the simultaneous ionospheric convection measurements for 12th March 2002.

TPA5: 12 March 2002

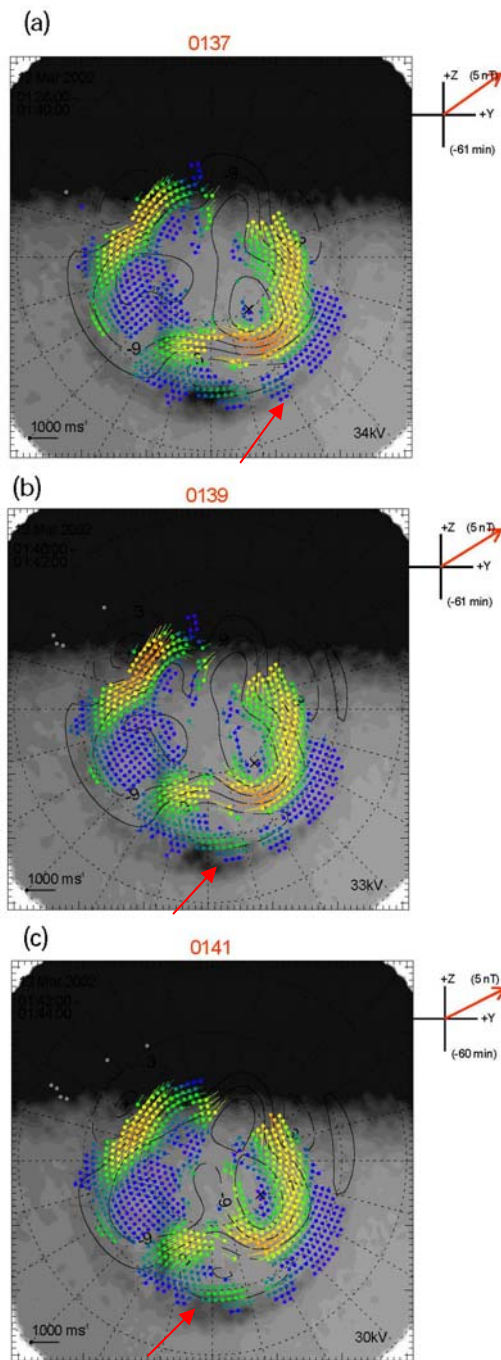


Figure 5.24 (a-c) Three auroral snapshots of the Northern hemisphere polar cap, with SuperDARN estimates of the simultaneous ionospheric convection overlaid. Vectors indicate the location of convection measurements. Red arrows indicating the TRINNI type flows.

5.3 Discussion

The above descriptions point out a number of important elements to discuss. These are the IMF conditions and its effects on where the TPAs form, the motion of the TPA and the relationship to the IMF, the characteristics of the ionospheric flows in the presence of TPAs and their effects on the dynamics of the TPAs, the observation of TRINNI type flows and vortical flows associated with TPA, and finally particle precipitation observation in the vicinity of the TPA. These points are considered in the following discussion.

5.3.1 IMF effects

Section 5.2 gave a few examples of different ionospheric flow behaviour some of which were discussed in the literature in the past. Detailed study of the IMF showed a consistency between the case studies presented in this chapter and the predictions made by *Frank et al.* (1982, 1986), and *Zhu et al.* (1997), as they predicted that one of the conditions under which the TPA is expected to occur is when the IMF has a significant northward component. Although the statistical correlations of polar cap features with the IMF B_y component are not as clear as those for B_z component, there has been a considerable amount of work done on the effects of the B_y component on the formation and dynamics of the TPAs. In some studies, there were no associations found between the IMF B_y and the distribution of TPAs (*Lassen and Danielsen, 1978; Rairden and Mende, 1989; Valladares et al., 1994*), although, in some other studies there are clear relationships between the IMF B_y and formation of the TPA (*Gussenhoven, 1982; Elphinstone et al., 1990; Makita et al., 1991; Kullen et al., 2002; Milan et al., 2005; Goudarzi et al., 2008*). In 1990, *Elphinstone et al.* proposed that B_y positive implies high-latitude TPAs in the dusk sector, while negative B_y results in dawn sector TPAs. Our auroral emission data provided by keograms presented earlier in section 5.2, are in agreement with *Elphinstone et al.* (1990). Locations of the TPAs at the beginning of every one of the case studies presented in this chapter seem to have a direct relationship with the orientation of the IMF B_y .

However, our observations are not in agreement with the theoretical model proposed by *Makita et al.* (1991), as they claimed that the TPAs appear in the morning sector for IMF $B_y < 0$ and in the evening sector for IMF $B_y > 0$. Although origins of some of the TPAs are not clear due to the lack of data, for those for which the data is available, it seems that locations of the TPAs depend on the IMF B_y orientation.

Dynamics of all the five TPAs studied in this chapter are consistent with the theoretical model suggested by *Milan et al.* (2005). Comparing the keograms of the TPA1-5 with the IMF conditions, we observed that the changes in the IMF B_y and B_z directions have direct effects on the motion of the TPAs. However, the TPAs are not expected to move immediately, but changes in the IMF orientation affect the reconnection site, which then affects the motion of the ionospheric flows causing the TPAs to move.

5.3.2 Effects of ionospheric flows on the dynamics of TPAs

In the previous sections there have been cases where studying the dynamics and decay of the TPAs is difficult due to the absence of data in the IMAGE datasets. In the absence of the FUV data for the beginning and end of the interval in the IMAGE dataset, we relied on the ionospheric flow data by looking at the convection patterns derived from SuperDARN radar data to have a better understanding of the nature of the TPA. Ionospheric convection flows measured by the SuperDARN radars provided interesting information on flows around the locations of the TPAs. A number of interesting observations are given below.

Vortical flows at the nightside end of a TPA were first mentioned in chapter 4 (*Goudarzi et al.*, 2008). The search for vortical flows in the presence of TPAs was carried on in chapter 5 with further five case studies. Another type of interesting vortical flows were observed during the second interval (Fig. 5.5). What makes these vortices even more unusual than the previous ones discussed in this thesis, is the effect they have on the motion of the lower part of the TPA. The vortices shown using red ovals form on the dawnside of the TPAs when the B_y component of the IMF starts to get stronger. As the TRINNI-related flows get

stronger at about 0542 UT, the TPA moves towards dawn (Fig. 5.5e), but by 0546 UT has returned to its original location. The appearance of vortical flows in the nightside, in the vicinity of TPAs is an unusual phenomenon which was also discussed in the previous case study in chapter 4. There has been no mention of such flows in the previous studies of the TPAs, which leaves numerous unanswered questions regarding the origin of these vortices. However, these vortical flows appear at the nightside in the midnight sector, under northward IMF condition, and prior to the formation of TRINNIIs.

As mentioned in chapter 2, there have been numerous hypotheses proposing different models to explain the dynamics of the TPA. *Milan et al.* (2005) suggested that the motion and location of the formation of TPAs are controlled by the IMF B_y orientation. Other modelling studies (*Kullen and Janhunen, 2004; Naehr and Toffoletto, 2004*) provided results which are consistent with the subsequent motion of the nightside section of TPA1 across the polar cap under the assumption that a bifurcated nightside polar cap corresponds to a TPA.

The difference in the dynamics of the dayside and nightside part of the TPA (presented in Fig. 5.8) is another interesting outcome of one of the case studies (TPA2). Considering the theory of *Milan et al.* (2005), one might expect to see the arc moving towards dusk, but by looking at the position of the arc in figures 5.8 (a-e), it is obvious that the dayside part of the TPA is not moving, whereas the nightside part is being pushed towards the west by westward ionospheric flows. Division of the TPA was suggested by *Eriksson et al.* in 2005 who proposed that the dayside part of the TPA generally corresponds to the sunward flows on the duskward side of the lobe convection cell (e.g. *Burch et al., 1985*). These lobe cells flows are occasionally enhanced above 1000 m/s. The nightside portion of the TPA, however, generally spans the region on its equatorward side consistent with the velocity shear zone of the Harang Discontinuity (HD) in agreement with *Nielsen et al.* (1990).

Studying the ionospheric flows during each interval demonstrated the location of the reconnection site, addition, removal, and redistribution of flux have direct effects on the dynamics of the TPA (*Milan et al., 2005; Goudarzi et al.,*

2008). Figure 5.25 illustrates the motion of the TPA caused by ionospheric convection flow predicted by the theoretical model suggested by *Milan et al.*, 2005 for the cases of (a) B_z and (b) B_y dominant.

Several good examples of the effects of the ionospheric flows on the dynamics of the TPAs are discussed in this chapter. A number of interesting casdes are highlighted below:

- The tilt in the nightside part of TPA2 (Fig. 5.8a-e) is caused by westward flows originating in the dawn compartment of the polar cap.
- Duskward motion of TPA2 (Fig. 5.9) after 1300 UT is caused by redistribution of open flux within the polar cap when the IMF is dominantly northward.
- Duskward motion of TPA3 (Fig. 5.12) is caused by addition of newly opened flux (produced by high latitude reconnection in the post noon sector) from dusk to dawn compartment.
- Motion of the second arc during the third interval (Fig. 5.13a-c) towards midnight sector, is caused by strong antisunward/westward flows in the dawn compartment.
- Fig. 5.21 illustrates one the best examples of the effects of the ionospheric flows on the dynamics of TPA. As can be seen from Figs. 5.21d-f, removal of flux from dusk compartment and addition of these flux to the dawn compartment is causing the nightside polar cap to move to the lower latitude and therefore pushing TPA5 towards dusk. This continuous motion is illustrated in Fig. 5.22.

The observations summarised above are consistent with *Milan et al.* (2005) theoretical model, which show that dynamics of TPAs depend of types of reconnection and dynamics of the ionospheric flows.

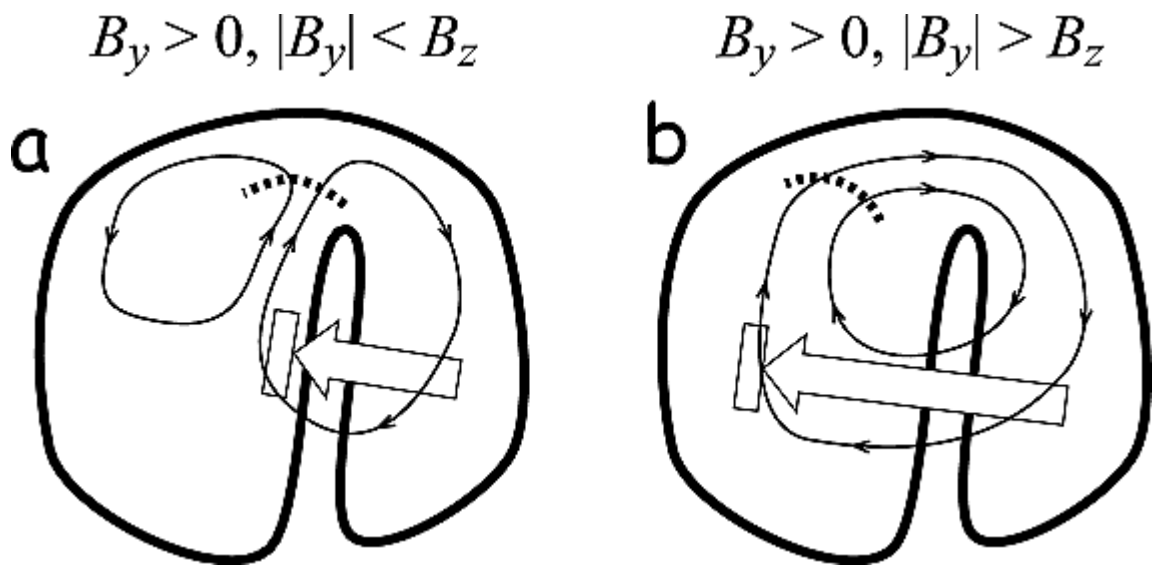


Figure 5.25 Ionospheric convection patterns for northward IMF, for the cases (a) $|B_y| < B_z$ and (b) $|B_y| > B_z$. The patterns shown above are appropriate for $B_y > 0$; for $B_y < 0$ the patterns would be a mirror image about the noon-midnight meridian. Large arrows show the direction and maximum extend of the TPA motion in response to the convection flow. In Figure 5.25a, if the TPA was located in the duck sector, motion would be dawnward toward the noon-midnight meridian. In Figure 5.25b, motion is duskward, irrespective of the location of the TPA (after Milan *et al.*, 2005).

5.3.3 Observation of TRINNIs associated with TPA

As mentioned in chapter 2, following the work of *Nishida et al.* (1998), *Grocott et al.* (2004) suggested that the ionospheric signatures of a TRINNI were caused by the reconfiguration of an asymmetric tail resulting from prolonged dayside reconnection between terrestrial field lines and a B_y -dominant IMF. By the time tail field lines reconnected some distance downtail, they would have ionospheric footprints, which were significantly displaced in azimuth in opposite hemispheres. Therefore, the coincident Southern Hemisphere flows similarly take the form of high-speed bursts. It is also suggested that these Southern Hemisphere counterparts have the opposite east-west flow asymmetry, both in the location of the flows out of the polar cap, and in the direction of the return flows. In other words, northern B_y -positive bursts resemble southern B_y -negative bursts, and vice-versa.

In 2005, *Milan et al.* suggested that the occurrence of the TRINNI and the formation of the TPA are linked. They speculated that the strong dawn/duskward flows crossing the midnight sector azimuthally are the result of the dawn-dusk forces exerted on newly opened field lines by the B_y orientation. Newly closed field lines are created as the reconnection keeps happening in the tail. The newly closed field lines are not contained in the meridional planes but they straddle the noon-midnight meridian plane of the tail, connecting the dawn and dusk sectors in opposite hemispheres. The opposing forces in opposite hemispheres results in the formation of a TPA.

Whilst TRINNIs are extremely important phenomena for understanding the origin of the TPAs (*Milan et al.*, 2005, *Goudarzi et al.*, 2008), very little is understood about them and their driving mechanism. A noticeable flow behaviour in Figure 5.4c is that the TRINNI type flows in the premidnight sector originates from 2130 MLT whereas the nightside end of the TPA was located at 2330 MLT. This appears inconsistent with the theoretical model *Milan et al.* (2005), as the location of the TPA at the nightside was not similar to the location of the start of the TRINNI. This has opened a new horizon for further TRINNI studies.

Two other interesting examples of TRINNI type flows is given in Figures

5.5 and 5.24. What makes the TRINNI interesting during the first interval, is the occurrence of vortical flows prior to the formation of the TRINNI (fig. 5.5). The same phenomenon was observed in the previous case study, which was described in chapter 4. However, there is one main difference and that is: in the case study presented in chapter 4, the vortical flow and TRINNI were formed prior to the formation of the TPA, whereas in this case, the vortical flow and TRINNI type flows are seen ~ 5 hours after TPA1 was observed in the FUV data. Although, as the arcs disappears just after 0400 UT, it is possible that these observed vortical and TRINNI type flows are the cause of the reproduction of the arc at around 0530 UT.

TRINNI type flows illustrated in Fig. 5.24 are one of the interesting examples of TRINNIs where the TRINNI is still happening after the arc has been formed for approximately 5 hours. Presence of TRINNIs in this case can confirm that not only TRINNIs seem to be responsible for the formation of the arc but also they can play an important role in development and continuation of the TPA.

5.3.4 Particle precipitation overview

Based on interhemispheric observations of the TPAs, it has been suggested that TPAs can be present in both hemispheres, simultaneously (*Mizera et al.*, 1987; *Obara et al.*, 1988; *Craven et al.*, 1991). This suggestion was based either on the similarity of the electron spectra of narrow precipitation structures observed simultaneously in the polar regions of both hemispheres, or on a comparison of simultaneous images of the northern and southern polar caps from the Viking and DE satellites which was first done by *Craven et al.* in 1991. In their findings, the TPA observations coincided with abrupt changes in all IMF components. The two polar arcs were found to be parallel with a 180° counterclockwise rotation and they move in opposite directions. However, it should be noted that all these reported conjugate TPAs were theta auroras. There have been no reports of conjugacy with regard to small-scale isolated TPAs, which are more common. This can suggest two scenarios: 1) it is difficult to make simultaneous comparisons of small-scale isolated polar cap arcs in the two

hemispheres, 2) there is no conjugacy for small-scale isolated polar cap arcs and that they are either on open field lines or the arcs in different hemispheres have dramatically different magnetospheric source regions. *Østgaard et al.*, 2003, presented two events where both polar caps were observed and a theta aurora was seen in one hemisphere, but not in the other. They suggested that the B_x component of the IMF plays a very important role in controlling the position of the lobe reconnection, eventually producing the shear flow in just one hemisphere, which would lead the production of the TPA, or alternatively as an additional effect, the theta aurora may be suppressed in one hemisphere due to different exposure to solar EUV radiation. The implications of the conjugacy observations for the magnetospheric source regions of polar cap arcs are very interesting topics for further TPA studies.

In this chapter, two examples of interhemispheric observation of the TPAs are presented. Unfortunately due to lack of FUV data in the Southern Hemisphere, only the auroral emissions in the Northern Hemisphere are shown. DMSP and NOAA satellite passes over the northern and southern polar caps are overlaid on northern auroral emissions to investigate the particle precipitation measurements in both hemispheres at the presence of TPAs.

Following the discussion from section 5.2.1, we use particle precipitation data to investigate whether the dayside part of TPA1 lies on closed or open field lines. As can be seen in Fig. 5.6a, DMSP F15 passes the post noon sector of the polar cap. Although a satellite pass over the dayside part of the TPA would be ideal, one must depend on the available observations. As explained above at around 0322 UT, a sudden increase in the electron energy flux right before the satellite reaches the dayside auroral oval, can be associated with the TPA (Fig. 5.6c). The spectrogram data shown in Fig. 5.6c therefore suggests that the dayside part of TPA1 is associated with closed field lines, which then rules out the theoretical model suggested by *Eriksson et al.*, 2005 regarding the TPAs being divided into two dayside and nightside features.

Comparing these findings with the data set which was previously discussed in section 5.2.2 regarding the motion of the TPA within the auroral oval (Fig. 5.10), it is obvious that from the particle precipitation data one can see

the signatures of higher energy flux associated with the auroral oval (closed field lines). Therefore, by having the moving end of the TPA at the nightside due to the westwards ionospheric flows and particle signatures of the closed field lines at the dayside TPA, one can conclude that there are enough evidences to support that the TPA of interest lies on closed field lines.

5.4 Summary

The combination of space-based optical observations with the continuous monitoring of the ionospheric convection flows supplied by ground based instruments leads to a huge increase of our understanding of previously known localized aurora, its formation, and its dynamics. In this chapter, the ionospheric electrodynamical state associated with formation and dynamics of the TPA originating from both the dawn and the dusk sides of the auroral oval was studied for another 5 unique TPAs.

Like most TPA cases studied in the past, the IMF is northward at least for part of the time for all 6 case studies presented in this thesis. By looking into the dynamics of the TPAs presented in this thesis, it is confirmed that in nearly every case, the reconnection process plays a very important role in the motion of the arc. Therefore, the B_y and B_z components of the IMF become very important factors in the dynamics of the TPAs as they control the location of the ongoing reconnection. Dawnside (Dusk side) formation of the TPA and duskward (dawnward) motion occurs when B_y changes from negative to positive (positive to negative). During the evolution the TPA is embedded in a negative (positive) potential cell (or local minimum/maximum) (*Cumnock et al., 2004; Milan et al., 2005; Goudarzi et al., 2008*).

Using ground based instruments (SuperDARN radars) to study TPAs is a new method, which only recently is being used by scientists (i.e. *Eriksson et al., 2005; Milan et al., 2005, Goudarzi et al., 2008*). By examining characteristics of the ionospheric flows in the presence of the TPAs, many different phenomena were observed which would agree and disagree with various hypothesis proposed so far regarding the formation and dynamics of the TPA. A few

examples are: sunward flows at high-latitude, and signatures of TRINNIs. By observing the sunward flows at the same location that the arc exists, one can conclude that the TPA embedded in the same region of sunward flow (and electrostatic potential), moves with the convection cell as it evolves. This indicates that the TPA lies on closed field lines and is a global phenomenon (*Cumnock and Blomberg, 2004*).

The appearance of TRINNIs at the nightside end of the TPAs is yet again further evidence for the TPA being a global phenomenon. Being a young topic in the TPA studies, it is crucial to investigate as many examples as possible in order to find out whether there is a link between TRINNI occurrence and transpolar arc formation. The TRINNI, which was observed in the Northern Hemisphere and presented in this chapter, is consistent with the theoretical model proposed by *Milan et al. (2005)*. These TRINNI type flows form at the nightside end of TPA and form at dawn for $B_y < 0$ and dusk for $B_y > 0$ in the Northern Hemisphere and in some cases vice versa in the Southern Hemisphere (previously reported by *Kullen et al., 2002*).

Examining the ionospheric flows indicated that there was no apparent flow shear associated with the TPA within the polar cap, which would be expected if the arc was associated with an upward field aligned current on open field lines.

An interhemispheric study of the particle precipitation data indicates that there is evidence which supports the fact that TPA lie on closed field lines, as the particles shown in the spectrogram seems to be more typical of those located on closed field lines. In most cases, there are certain features, which can be interpreted as signatures of TPAs in the opposite hemisphere, which agree with the fact that the TPAs are global phenomena.

Appearance of high energetic ions ($\sim 30\text{-}80$ keV) at the nightside in NOAA data is a very interesting new finding. Investigating the origin of these particles will help us to better understand particle precipitation data associated with TPAs.

Overall, the results explained above, have demonstrated that there is enough evidence to prove that the TPAs presented in this chapter are not isolated physical phenomena in the polar near-Earth space, but are closely connected to many other plasma processes in the solar-terrestrial environment. Processes such as poleward

Chapter 5: Five further transpolar arc studies

motion of the newly formed tongue of closed field lines at the nightside, which seem to be responsible for the formation of TPAs, are consistent with the TPAs being associated with closed field lines.

Chapter 6

Summary and Future Work

6.1 Motivation

One of the most fascinating phenomenon in astrophysical plasma known to scientists is magnetic reconnection. This process occurs within the terrestrial magnetosphere, making it straightforward to study. Magnetic reconnection is known to be responsible for much of the energy input into the Earth's upper atmosphere. As a consequence of reconnection between the solar wind and the geomagnetic field, conditions enable energetic particles to precipitate into the Earth's upper atmosphere. As a result of this interaction, the atoms and molecules are driven to excited states and, during the subsequent de-excitation, photons are emitted, creating one of the most spectacular phenomena in the Earth's environment, "The Aurora".

Since the 1980s, scientists have come up with controversial explanations and theoretical models in order to explain the magnetospheric source regions for TPAs. Up to the present, various types of TPAs have been introduced with unique characteristics and magnetospheric source regions. Understanding the magnetic source regions of TPAs can be especially interesting for magnetospheric physicists as it provides vital information regarding the coupling between the magnetosphere and ionosphere.

6.2 Summary of Results

The research presented in this thesis has been concerned with the ionospheric convection flow and particle precipitation associated with the formation and dynamics of TPAs. These studies have made use of data from a variety of ground and space based instruments. The data sets which were examined in detail are images of far ultraviolet aurora from the wideband imaging camera on board of the IMAGE spacecraft. In addition to this, the ionospheric plasma convection patterns obtained from the global-scale SuperDARN HF radars provided essential information regarding the solar wind-magnetosphere-ionosphere coupling and the displacement of magnetic flux at high latitudes. Particle precipitation data measured by low-orbiting spacecrafts such as DMSP and NOAA added important information regarding the particle energy fluxes of the TPAs, which is central to the investigating of the formation and dynamics of TPAs.

As mentioned earlier, previous studies have mainly suggested two hypotheses for the formation of TPAs: 1) TPAs lie on open magnetic field lines (*Hardy et al.*, 1982; *Hardy*, 1984; *Gussenhoven and Mullen*, 1989); and 2) TPAs lie on closed magnetic field lines (*Frank et al.*, 1982, 1986; *Zhu et al.*, 1997; *Milan et al.*, 2005). The initial study, which was presented in Chapter 4 and published in *Goudarzi et al.*, 2008, detailed a multi-instrument study of a unique TPA observed in the northern hemisphere during an interval of variable IMF. Although the IMF is northward prior to the formation of the TPA, it changes its orientation after the TPA is formed and the effects of these changes in the IMF orientation are quite visible in the motion of the TPA. Ionospheric convection flows were examined prior to and during the formation of the TPA and a very strong link was found between the two different types of flows (TRINNIs and vortices) and the formation of the TPA. The appearance of TRINNI type flows prior to the formation of the TPA was first suggested by *Milan et al.*(2005) as one of the main factors which play a very important role in the formation of the TPA.

Chapter 6: Summary and Future Work

Another interesting phenomenon observed in the case study mentioned above is the formation of vortical flow in the pre-midnight sector which seem to be associated with the origin of the TPA and accompanies the arc into the polar cap. This unique phenomenon had not been observed in previous studies which makes it an interesting new subject related to the formation of the TPA. The ionospheric convection patterns showed outstanding results as they illustrated that the subsequent motion of the TPA is controlled by the transport of open flux from one side of the TPA to the other as a result of reconnection between the IMF and the geomagnetic field at the low-latitude dayside magnetopause. This was yet another observation which confirmed the theoretical model suggested by *Milan et al.* (2005).

Another interesting point, which came out of the ionospheric convection map patterns, was the absence of flow shear associated with the TPA. Looking more precisely for shear flow brought us to a thorough investigation of the field-aligned current during this event and presented in chapter 4. Using three major data sets, we investigated the conditions in the ionosphere and near magnetosphere during the TPA of interest. Comparison of auroral emission and field-aligned current data illustrates that the location of the TPA discussed in chapter 4, does not correlate with any organized Birkeland currents. Signatures of TRINNIs appear in the field-aligned current maps as upward FACs at the midnight sector.

In order to contribute to the issues which came out of the case study examined in chapter 4, five further examples were selected and discussed in chapter 6. The investigation of the new case studies was enhanced by including the particle precipitation data in the vicinity of the TPAs. The observations illustrated that particle precipitation associated with the TPAs behaves as if located on closed field lines. These results yet again confirm the theory of TPAs lying on closed field lines. In most of the interhemispheric observation of TPAs using particle precipitation data, there are certain features in the spectrogram data, which can be interpreted as the signatures of TPAs in the opposite hemisphere which can only prove that TPAs are a global phenomenon.

Detailed investigation of the ionospheric convection flows measured during each of the 5 case studies, revealed numerous facts, which confirmed the results derived from the case study presented in chapter 4. Facts such as the occurrence of TRINNI prior to the appearance of the TPA, and redistribution of the magnetic flux causing the TPAs to move east-west ward, which confirms the theoretical model proposed by *Milan et al. (2005)*.

6.3 Future Directions

Although considerable progress has been made in over thirty years of studying TPAs, for example the formation of TPAs under northward IMF is now well accepted, a number of significant issues remain. Some of these relate to the mechanism under which TPAs form and move as the magnetospheric source region of TPAs is the main missing piece of the TPA formation puzzle. Others relate to the ionospheric convection flow behaviour prior to and during the presence of TPAs. Detailed studies of 6 TPAs in this thesis, summarized above, highlight the existence of further unanswered questions, and point the way towards several future studies. The sections below consider some of the next steps that now need to be taken to gain a better understanding of the nature of TPAs.

6.3.1 IMF B_x effects of TPAs

As has already been discussed in previous chapters, the majority of the TPAs occur during intervals of northward IMF conditions. Much work has been done during the past couple of years on investigating the effects of IMF B_y component on the formation and dynamics of TPAs. As a result of which a link was discovered between the direction of IMF B_y and the location of the formation of TPAs (*Elphinstone et al., 1990*). Fairly recently, another effect of IMF B_y component was discussed in the work of *Milan et al. (2005)*, where they illustrated a case study in which the dusk-dawn motion of the TPAs was highly dependent on IMF B_y orientation. However, in some cases, it has been suggested

that no correlation exists between IMF B_y component and the local time distribution of TPAs (*Rairdren and Mende, 1989*).

A similar controversy exists in the study of the effects of the IMF B_x component. However, some hypothesis suggest that there is a B_x dependence for the occurrence of polar cap arcs, and they found that more TPAs occurred during the period of negative B_x (*Lassen and Danielsen, 1978*). Effects of B_x on the rate of the lobe reconnection, has also been discussed in the literature as it affects the motion of TPAs in opposite hemispheres. A preliminary search in the IMF data for each of the 6 intervals have shown that the IMF B_x component is negative during most of the intervals discussed in this thesis. However, a more detailed study on the effects of IMF B_x on the redistributing of the magnetic flux within the polar cap is required.

6.3.2 Detailed study of vortical flows at the nightside

The appearance of vortical flows at the nightside in the vicinity of the TPA, is a very interesting point which came out the case study presented in chapter 4. The most remarkable issue discovered regarding the motion of the vortex mentioned above, was that it accompanied the head of the TPA while it was forming and moving poleward. Another example of these vortical flows is given in chapter 5, although the latter example is more stationary and does not move along with the TPA.

As there has been no mention of such flows in the literature, detailed examination of more examples of such flows in the presence of TPAs, can contribute a great deal to have a better understanding of the ionospheric flow responses to the formation and dynamics of TPAs.

6.3.3 Statistical study of TRINNIs associated with TPAs

Milan et al. (2005) first introduced a link between the appearance of cross midnight fast azimuthal flows (known as TRINNIs) and the formation of TPAs. A few examples presented in this thesis, confirmed the theoretical model suggested by *Milan et al.* (2005), however, more examples are needed to investigate whether occurrence of TRINNIs are essential for the formation of TPAs. Therefore, a statistical study of TRINNIs during TPA events can help to increase our knowledge regarding the formation mechanism of TPAs.

Another interesting phenomenon discovered in this thesis was a unique form of interhemispheric TRINNI. TRINNIs are traditionally known to be global phenomena, an example showed in chapter 5, illustrated a TRINNI, which looked quite different from the model proposed by *Grocott et al.* (2005), as the fast flows were moving towards the same direction in opposite hemispheres. More interhemispheric observations of TRINNIs is necessary to investigate different types of magnetotail related reconnection and various phenomena associated with them.

Although detailed study of 6 TPAs presented in this thesis has contributed to a greater understanding of the nature of transpolar arcs, it also brought out a number of new lines of enquiry which may beneficially be pursued in future work.

Bibliography

Akasofu, S. -I., The development of the auroral substorm, *Planet. Space Sci.* 12, 273-282, 1964.

Akasofu, S.-I., *Polar and Magnetospheric Substorms*, Reidel, Dordrecht, 1968.

Alfvén and Fälthammar, H. Alfvén and C-G. Fälthammar , *Cosmical Electrodynamics*. In: (2nd ed.), *Oxford at the Clarendon Press* (1963), p. 195 Section 5.5.3, 1963.

Anderson, B. J., K. Takahashi, and B. A. Toth, Sensing global Birkeland currents with Iridium engineering magnetometer data, *Geophys. Res. Lett.*, 27, 4045–4048, 2000.

Anderson, B. J. H. Korth, C. L. Waters, D. L. Green, and P. Stauning, Statistical Birkeland current distributions from magnetic field observations by the Iridium constellation, *Ann. Geophys.*, 26, 671–687, 2008.

Axford, W.I. and C.O. Hines, A unifying theory of high-latitude geophysical phenomena, *Can. J. Phys.*, 39, 1433-1464, 1961.

Baumjohann, W., and R. A. Treumann, *Basic Space Plasma Physics*, Imperial Coll. Press, London, 1997.

Berchem, J., J. Raeder, M. Ashourabdalla, Magnetic-flux ropes at the high-latitude magnetopause, *Geophys. Res., Lett.*, 22, (10): 1189-1192, 1995.

Berg, G. A., M. C. Kelley, M. Mendillo, R. Doe, J. Vickrey, C. Kletzing, F. Primdahl, and K. D. Baker, Formation and eruption of sun-aligned arcs at the polar cap-auroral oval boundary, *J. Geophys. Res.* 99, 17577, 1994.

Biermann, L., and A. Schlüter, Cosmic Radiation and Cosmic Magnetic Fields. II. Origin of Cosmic Magnetic Fields, *Phys. Rev.*, 82, 863, 1951.

Birkeland, K., *The Norwegian Aurora Polaris Expedition, 1902-1903*, vol. 1, Sec.1, Christiania (Oslo): H. Aschehoug & Co., pp. 1-315, 1908.

Blomberg L. G. and G. T. Marklund, High-latitude electrodynamic and aurorae during northward IMF, in: *Auroral Plasma Dynamics*, *Geophys. Monogr. Ser.*, 80, edited by R. L. Lysak, 55-68, AGU, Washington, D. C., 1993.

Blomberg, L. G., and J. A. Cumnock, Electrodynamic of transpolar aurorae,

Bibliography

Adv. Space Res., Volume 36, Issue 10, p. 1785-1790, 2004.

Burch, J.L., P.H. Reiff, J.D. Menietti, R.A. Heelis, W.B. Hanson, S.D. Shawhan, E.G. Shelley, M. Sugiura, D.R. Weimer, J.D. Winningham, IMF By dependent plasma flow and Birkeland currents in the dayside magnetosphere 1. Dynamics Explorer Observations *J. Geophys. Res.*, 90, No. A2, 1577-1593, 1985.

Burke, W. J., M. S. Gussenhoven, M. C. Kelley, D. A. Hardy, and F. J. Rich, Electric and magnetic characteristics of discrete arcs in the polar cap, *J. Geophys. Res.* 87, 2431, 1982.

Bythrow, P. F., W. J. Burke, T. A. Potemra, L. J. Zanetti, and A. T. Y. Lui, Ionospheric evidence for irregular reconnection and turbulent plasma flows in the magnetotail during periods of northward interplanetary magnetic field, *J. Geophys. Res.*, 90, 5319, 1985.

Carlson, H. C. Jr, V. B. Wickwar, E. J. Weber, J. Buchau, J. G. Moore, and W. Whiting, Plasma characteristics of polar cap F-layer arcs, *Geophys. Res. Lett.* 1, 895. 1984.

Carlson, H. C. R A. Heelis, E. J. Weber, and J. R. Shaber, Coherent mesoscale convection patterns during northward interplanetary magnetic field, *J. Geophys. Res.* 93, 14501, 1988.

Chang, S. -W., et al., A comparison of a model for the theta aurora with observations from Polar, Wind and SuperDARN, *J. Geophys. Res.*, 103, 17, 367-17,390, 1998.

Chapman, S. and V.C.A. Ferraro, A new theory of magnetic storms, *Terrest. Magnetism Atoms. Elec.*, 36, 171, 1931.

Chisham, G., M. P. Freeman, M. Pinnock, and I.J. Coleman, Measuring the reconnection rate in the dayside ionosphere during an interval of due northward IMF, *Geophysical Research Abstracts*, Vol. 5, 03529, 2003.

Chisham, G., M. P. Freeman, T. Sotirelis, A statistical comparison of SuperDARN spectral width boundaries and DMSP particle precipitation boundaries in the nightside ionosphere, *Geophysical Research Letters*, Vol. 31, L02804, doi:10.1029/2003GL019074, 2004

Chisham, G., M. Lester, S. E. Milan, M. P. Freeman, W. A. Bristow, A. Grocott, K. A. McWilliams, J. M. Ruohoniemi, T. K. Yeoman, P. L. Dyson, R. A. Greenwald, T. Kikuchi, M. Pinnock, J. P. S. Rash, N. Sato, G. J. Sofko, J.-P. Villain and A. D. M. Walker, A decade of the Super Dual Auroral Radar

Bibliography

Network (SuperDARN): scientific achievements, new techniques and future directions, *Surv. Geophys.*, 28, 33–109, doi:10.1007/s10712-007-9017-8 2007.

Chiu, Y. T. Formation of polar cap arcs configurations. *Geophys. Res. Lett.* 16, 743. 1989.

Chiu, M. C., U. I. Von-Mehlem, C. E. Willey, T. M. Betenbaugh, J. J. Maynard, J. A. Krein, R. F. Conde, W. T. Gray, J. W. Hunt Jr., L.E. Mosher, M.G. McCullough, P.E. Panneton, J.P. Staiger and E.H. Rodberg, ACE Spacecraft, *Space Science Reviews*, V. 86, Issue 1/4, P. 257-284, 1998.

Cowley, S. W. H. Magnetospheric asymmetries associated with the Y-component of the IMF, *Planet. Space Sci.*, 29, 79, 1981.

Cowley, S. W. H., Morelli, J. P., and Lockwood, M.: Dependence of convective flows and particle precipitation in the high latitude dayside ionosphere on the X- and Y -components of the interplanetary magnetic field, *J. Geophys. Res.*, 96, 5557–5564, 1991.

Cowley, S. W. H., and M. Lockwood, Excitation and decay of solar wind-driven flows in the magnetosphere-ionosphere system, *Ann. Geophysicae*, 10, 103, 1992.

Craven, J. D., L. A. Frank, C. T. Russell, E. J. Smith, and R. P. Lepping, Global auroral responses to magnetospheric compressions by shocks in the solar wind: Two case studies, in *Solar Wind-Magnetosphere Coupling*, ed. by Y. Kamide and J. A. Slavin, pp. 377-380, Terra Scientific Publ. Co., Tokyo, 1986.

Craven, J. D., and L. A. Frank, Diagnosis of auroral dynamics using global auroral imaging with emphasis on large-scale evolution, in *Auroral Physics*, pp. 273-288, ed. by C.-I. Meng, M. J. Rycroft and L. A. Frank, Cambridge University Press, Cambridge (English), 1991.

Craven, J. D., J. S. Murphree, L. A. Frank, and L. L. Cogger, Simultaneous optical observations of transpolar arc in the two polar caps, *Geophys. Res. Lett.*, 18, 2297, 1991.

Crooker N. U. Reverse convection, *J. Geophys. Res.*, 97, 19,363-19,372, 1992.

Cummings, W. D., and A. J. Dessler, Field-aligned currents in the magnetosphere, *J. Geophys. Res.*, 72, 1007, 1967.

Cumnock, J. A., J. R. Sharber, R. A. Heelis, M. R. Hairston, and J. D. Craven, Evolution of the global aurora during positive IMF Bz and varying IMF By

Bibliography

conditions, *J. Geophys. Res.*, 102, 17, 489, 1997.

Cumnock, J. A., J. R. Sharber, R. A. Heelis, L. G. Blomberg, G. A. German, J. F. Spann, and W. R. Coley, Interplanetary magnetic field control of theta aurora development, *J. Geophys. Res.*, 107(A7), 1108, doi:10.1029/2001JA009126, 2000.

Cumnock, J. A., J. R. Sharber, R. A. Heelis, L. G. Blomberg, G. A. Germany, J. F. Spann, and W. R. Coley, Interplanetary magnetic field control of theta aurora development, *J. Geophys. Res.*, 107(A7), 1108, doi: 10.1029/2001JA009126, 2002.

Cumnock, L. A., and L. G. Blomberg, transpolar arc evolution and associated potential patterns, *Ann. Geophys.*, 22, 1213, 2004.

Davies, K., *Ionosphere Radio*, Peter Peregrinus Ltd., London, 1990.

Dungey, J. W., Interplanetary magnetic field and the auroral zones, *Phys. Rev. Lett.* 6, 47, 1961.

Dungey, J. W., The structure of the exosphere, or adventures in velocity space, in *Geophysics: The Earth's environment*, edited by C. DeWitt, J. Hieblot, and A. Lebeau, pp. 503-550, Gordon and Breach, Newrk, N. J., 1963.

Elphinstone, R. D., K. Jankowska, J. S. Murphree, and L. L. Cogger, The configuration of the auroral distribution for interplanetary magnetic field Bz northward, 1, IMF Bx and By dependencies as observed by the Viking satellite, *J. Geophys. Res.*, 95, 5791, 1990.

Erickson, G. M., R. W. Spiro, and R. A. Wolf, The physics of the Harang discontinuity, *J. Geophys. Res.*, 96, 1633, 1991.

Eriksson, S., J. B. H. Baker, S. M. Petrinec, H. Wang, F. J. Rich, M. Kuznetsova, M. W. Dunlop, H. Reme, R. A. Greenwald, H. U. Frey, H. Luhr, R. E. Egun, A. Balogh, and C. W. Carlson, On the generation of enhanced sunward convection and transpolar aurora in the high-latitude ionospheric by magnetic merging, *J. Geophys. Res.*, 110(A11), 218, doi: 10.1029/2005JA011149, 2005.

Erlandson, R. E., L. J. Zanetti, T. A. Potemra, and P. F. Bythrow, IMF By dependence of Region 1 Birkeland currents near noon, *J. Geophys. Res.*, 93, 9804, 1988.

Etemadi, A., S. W. H. Cowley, M. Lockwood, B. J. I. Bromage, D. M. Willis, and H. Lühr, The dependence of high-latitude dayside ionospheric flows on the north-south component of the IMF: A high-time resolution correlation analysis using EISCAT "Polar" and AMPTE UKS and IRM data, *Planet. Space Sci.*, 36, 471, 1988.

Bibliography

Evans, D. S., and M. S. Greer, Polar orbiting environmental satellite space environment monitor, 2, Instrument descriptions and archive data documentation, NOAA Tech. Memo. OAR SEC-93, Natl. *Oceanic and Atmos. Admin.*, Boulder, Colo., 2000

Fairfield, D.H., and L. J. Cahill, Transition region magnetic field and polar magnetic disturbance, *Journal of Geophysical Research*, Vol. 71, p. 155, 1966.

Frank, L. A., J. D. Craven, J. L. Burch, and J. D. Winningham, Polar view of the Earth's aurora with dynamic explorer, *Geophys. Res. Lett.*, 9, 1001, 1982.

Frank, L. A., J. D. Craven, D. A. Gurnett, S. D. Shawhan, D. R. Weimer, The theta aurora, *J. Geophys. Res.*, 91, 3177, 1986.

Frank, L. A., and J. D. Craven, Imaging results from Dynamics Explorer 1, *Rev. Geophys.*, 26, 249, 1988.

Freeman, M. P., C. J. Farrugia, S. W. H. Cowley, M. Lockwood and A. Etemadi, The response of the magnetosphere-ionosphere system to solar wind dynamic pressure variations, *Proc. Chapman Conf. Magnetic Flux Rapes*, pp 611, 1990.

Frey, K. E., J. W. McClelland, R. M. Holmes, and L. C. Smith, Impacts of climate warming and permafrost thaw on the riverine transport of nitrogen and phosphorus to the Kara Sea, *J. Geophys. Res.*, 112, G04S58, doi:10.1029/2006JG000369, 2007.

Germany, G. A., Torr, M. R., Torr, D. G., and Richards, P. G., Use of FUV auroral emissions as diagnostic indicators, *J. Geophys. Res.*, 99, 383-388, 1994.

Goudarzi A., M. Lester, S. E. Milan, and H. U. Frey, Multi-instrumentation observations of a transpolar arc in the northern hemisphere, *Ann. Geophys.*, 26, 201-210, 2008.

Greenwald, R. A., W. Weiss, E. Nielsen, N. R. Thomson, STARE: A new radar aurora backscatter experiment in northern Scandinavian, *Radio Sci.*, 13, 1021-1039, 1978.

Greenwald, R. A., K. B. Baker, J. R. Dudeney, M. Pinnock, T. B. Jones, E. C. Thomas, J. -P. Villain, J.-C. Cerisier, C. Senior, C. Hanuise, R. D. Hunsucker, G. Sofko, J. Koehler, E. Nielsen, R. Pellinen, A. D. M. Walker, N. Sato, and H. Yamagishi, DARN/SuperDARN: A global view of the dynamics of high-latitude convection, *Space Sci. Rev.*, 71, 761, 1995.

Greenwald, R. A. J. M. Ruohoniemi, W. A. Bristow, G. J. Sofko, J. -P. Villian, A. Huuskinen, S. Kokubun, and L. A. Frank, Mesoscale dayside convection

Bibliography

vortices and their relation to substorm phase, *J. Geophys. Res.*, 101, 21, 697-713, 1996.

Grocott, A. Radar Observations of Convection in the Nightside High-Latitude Ionosphere, PhD Thesis, University of Leicester, U.K., 2002.

Grocott, A., S. W. H. Cowley, and J. B. Sigwarth, Ionospheric flow during extended intervals of the northward but By-dominated IMF, *Ann. Geophys.*, 21, 509-538, 2003.

Grocott, A. S. V. Badman, S. W. H. Cowley, T. K. Yeoman, and P. J. Cripps, The influence of IMF By on the nature of the nightside high-latitude ionospheric flow during intervals of positive IMF Bz, *Ann. Geophys.*, 22, 1755-1764, 2004.

Grocott, A., T. K. Yeoman, S. E. Milan, S. W. H. Cowley: Interhemispheric observations of the ionospheric signature of tail reconnection during IMF-northward non-substorm intervals, *Ann. Geophys.*, 23, 1763-1770, 2005.

Gussenhoven, M. S., Extremely high-latitude auroras, *J. Geophys. Res.*, 87, 2401, 1982.

Gussenhoven, M. S., and E. G. Mullen, Simultaneous relativistic electron and auroral particle access to the polar caps during interplanetary magnetic field Bz northward: A scenario for an open field line source of auroral particles, *J. Geophys. Res.*, 94, 17,121, 1989.

Hanuise, C., J. P. Villain, D. Gresillon, B. Cabrit, R.V. Greenwald, and K. B. Baker, Interpretation of HF radar ionospheric Doppler spectra by collective wave scattering theory, *Ann. Geophysicae*, 11, 29-39, 1993.

Hardy D. A., W. J. Burke and M. S. Gussenhoven, DMSP optical and electron measurements in the vicinity of polar cap arcs. *J. Geophys. Res.* 87, 2413, 1982.

Hardy, D.A., L.K. Schmitt, M.S. Gussenhoven, F.J. Marshall, H.C. Yeh, T.L. Shumaker, A. Hube, and J. Pantazis, Precipitating electron and ion detectors (SSJ/4) for the block 5D/Flights 6-10 DMSP satellites: Calibration and data presentation, *Rep. AFGL-TR-84-0317*, Air Force Geophys. Lab., Hanscom Air Force Base, Mass., 1984.

Hoffman, R. A., R. A. Heelis, and J. S. Prasad, A sun-aligned arc observed by DMSP and AE-C. *J. Geophys. Res.* 90, 9697, 1985.

Holzer, R. E., McPherron, R. L., and Hardy, D. A.: A quantitative empirical model of the magnetospheric flux transfer process, *J. Geophys. Res.*, 91, 3287-3293, 1986.

Bibliography

Holzworth, R. H., and C. -I. Meng, Mathematical representation of the auroral oval, *Geophys. Res. Lett.*, 2, 377,-380, 1975.

Huang, C. Y., L. A. Frank, W. K. Peterson, D. L. William, W. Lennartsson, D. G. Mitchell, R. C. Elphic, and C. T. Russell, Filamentary structures in the magnetotail lobes, *J. Geophys. Res.*, 92, 2349-2363, 1987.

Huang, C. Y., J. D. Craven, and L. A. Frank (1989), Simultaneous observations of a theta aurora and associated magnetotail plasma, *J. Geophys. Res.*, 94, 10, 137, 1989.

Huang, C. Y., G. J. Sofko, A. V. Koustov, D. A. Andre, J. M. Ruohoniemi, R. A. Greenwald, and M. R. Hairston, Evolution of ionospheric multicell convection during northward interplanetary magnetic field with $|B_z/B_y| > 1$, *J. Geophys. Res.*, 105, 27,095-27,107, 2000.

Iijima, T. and T. A. Potemra, The amplitude distribution of field-aligned currents at northern high latitudes observed by TRAUD, *J. Geophys. Res.*, 81, 2165, 1976a.

Iijima T. and T. A. Potemra, Field-aligned currents in the dayside cusp observed by Traid, *J. Geophys. Res.*, 81, 5971, 1976b.

Iijima, T.; Fujii, R.; Potemra, T. A.; Saflekos, N. A., Field-aligned currents in the south polar cusp and their relationship to the interplanetary magnetic field, *Journal of Geophysical Research*, vol. 83, Dec. 1, 1978, p. 5595-5603. Navy-NSF-supported research, 1978.

Iijima, T., and T.A. Potemra, The relationship between interplanetary quantities and Birkeland current densities, *Geophys. Res. Lett.*, 9, 442-445, 1982.

Imber, S.M., S. E. Milan, B. Hurbert, The auroral and ionospheric flow signatures of dual lobe reconnection: *Ann. Geophys*, 24, 3115-3129, 2006.

Khan, H., and S.W.H. Cowley, observations of the response time of high latitude ionospheric convection to variations in the interplanetary magnetic field using EISCAT and IMP-8 data, *Ann. Geophysicae*, 17, 1306, 1999.

Kivelson, M.G., and C.T. Russel, *Introduction to Space Physics*, Cambridge University Press, 1995.

Klumpar, D. M., Relationships between auroral particle distributions and magnetic field perturbation associated with field-aligned currents, *J. Geophys. Res.*, 84, 6524-6532, 1979.

Bibliography

Korth, H., B. J. Anderson, H. U. Frey, T. J. Immel, and S. B. Mende, Conditions governing localized high-latitude dayside aurora, *Geophys. Res. Lett.*, 31, L04806, doi:10.1029/2003GL018911, 2004.

Korth, H., B. J. Anderson, H. U. Frey, and C. L. Waters, High latitude electromagnetic and particle energy flux during an event with sustained strongly northward IMF, *Ann. Geophys.*, 23, 1295-1310, 2005.

Koskinen, H. E. J., and T. I. Pulkkinen, Midnight velocity shear zone and the concept of Harang discontinuity, *J. Geophys. Res.*, 100, 9539, 1995.

Kullen, A., The connection between transpolar arcs and magnetotail rotation, *Geophys. Res. Lett.*, 27, 73, 2000.

Kullen, A., and P. Janhunen, Relation of polar auroral arcs to magnetotail twisting and IMF rotation: A systematic MHD simulation study, *Ann Geophys.*, 22, 951-970, 2004.

Lassen, K., and C. Danielsen, Quiet time pattern of auroral arcs for different directions of the interplanetary magnetic field in the yz-plane, *J. Geophys. Res.*, 83, 5277, 1978.

Lester, M., P. J. Chapman, S. W. H. Cowley, S. J. Crooks, J. A. Davies, P. Hamadyk, K. A. McWilliams, S. E. Milan, M. J. Parsons, D. B. Payne, E. C. Thomas, J. D. Thornhill, N. M. Wade, T. K. Yeoman, and R. J. Barnes, Stereo CUTLASS - A new capability for the SuperDARN HF radars, *Ann. Geophys.*, 22, 459-473, 2004.

Lockwood, M., and Freeman, M. P.: Recent ionospheric observations relating to solar wind-magnetosphere coupling, *Phil. Trans. R. Soc. A.*, 328, 93, 1989.

Lockwood, M., Flux transfer events at the dayside magnetopause: transient reconnection or magnetosheat pressure pulses?, *J. Geophys. Res.*, 96, 5497-5509, 1991.

Luhmann, J. G., R. J. Walker, C. T. Russell, N. U. Crooker, J. R. Spreiter, S. S. Stahara, Patterns of potential magnetic field merging sites on the dayside magnetopause, *J. Geophys. Res.*, 89, 1739, 1984.

MacMahon, M. R., and W. D. Gonzalez, Energetics during the main phase of geomagnetic superstorms, *J. Geophys. Res.*, 102, 14,199-14,207, 1997.

Makita, K., C. I. Meng, and S. I. Akasofu, Transpolar auroras, their particle precipitation, and IMF By component, *J. Geophys. Res.*, 96, 14,085, 1991.

Marcucci, M. F., I. Coco, D. Ambrosino, E. Amata, S. E. Milan, M. B.

Bibliography

Bavassano Cattaneo, A. Retinò, Extended SuperDARN and IMAGE observations for northward IMF: Evidence for dual lobe reconnection, *J. Geophys. Res.*, VOL. 113, A02204, doi:10.1029/2007JA012466, 2008.

Marklund, G. T. and L. G. Blomberg, On the influence of localized electric fields and field-aligned currents associated with polar arcs on the global potential distribution, *J. Geophys. Res.*, 96, 13, 977, 1991.

Marklund, G. T., L. G. Blomberg, J. S. Murphree, R. D. Elphinstone, L. J. Zanetti, R. E. Erlandson, I. Sandahl, O. de la Beaujardiere, H. Opgenoorth, F. J. Rich, On the electrodynamical state of the auroral ionosphere during northward IMF: A transpolar arc case study, *J. Geophys. Res.*, 96, 9567, 1991.

Marklund, G. T., Viking investigations of auroral electrodynamical parameters, *J. Geophys. Res.*, 98, 1691, 1993

Matsuoka, A., K. Tsuruda, H. Hayakawa, T. Mukai, and A. Nishida, Electric field structure and ion precipitation in the polar region associated with northward interplanetary magnetic field, *J. Geophys. Res.*, 101, 10,711, 1996.

Mawson, D., Auroral observations at the Cape Royds Station, Antarctica. *Proc. Roy. Soc. S. Aust.* XL, 151, 1916.

McComas, D.J., S.J. Bame, P. Barker, W.C. Feldman, J.L. Phillips, P. Riley, and J.W. Griffiee, Solar Wind Proton Alpha Monitor (SWEPAM) for the Advance Composition Explorer, *Space Sci. Rev.*, 86, 563, 1998.

McEwen, D. J., and Y. Zhang, A continuous view of the dawn-dusk polar cap, *Geophys. Res. Lett.*, 27, 477, 2000.

McNamara, A.G., D.R. McDiarmid, G.J. Sofko, J.A. Koehler, P.A. Forsyth, and D.R. Moorcroft, BARS - A dual bistatic auroral radar system for the study of electric field in the Canadian sector of the auroral zone, *Adv. Space Res.*, 2, 145-148, 1983.

McWilliams, K.A., Ionospheric Signatures of Dayside Reconnection Processes, PhD Thesis, University of Leicester, U.K., 2001.

McWilliams, K.A., T.K. Yeoman, and S.W.H. Cowley, The dayside ultraviolet aurora and convection responses to a southward turning of the interplanetary magnetic field, *Ann. Geophysicae*, 19, 707-721, 2001.

Mende, S. B., J. H. Doolittle, R. M. Robinson, and R. R. Vondark, plasma drifts associated with a system of sun-aligned arcs in the polar cap, *J. Geophys. Res.* 93, 256, 1988.

Bibliography

Mende, S. B., H. Heetderks, H. U. Frey, M. Lampton, S. P. Geller, R. Abiad, O. H. W. Siegmund, A. S. Trensins, J. Spann, H. Dougani, S. A. Fuselier, A. L. Magoncelli, M. B. Bumala, S. Murphree, and T. Trondsen, Far ultraviolet imaging from the IMAGE spacecraft. 2. Wideband FUV imaging, *Space Sci. Rev.*, 91, 271–285, 2000a.

Mende, S. B., H. Heetderks, H. U. Frey, M. Lampton, S. P. Geller, S. Habraken, E. Renotte, C. Jamar, P. Rochus, J. Spann, S. A. Fuselier, J. –C. Gerard, R. Gladstone, S. Murphree, and L. Cogger, Far ultraviolet imaging from the IMAGE spacecraft. 1. System design, *Space Sci. Rev.*, 91, 243–270, 2000b.

Meng, C. –I., and B. H. Mauk, Global aurora morphology, *U.S. Natl. Rep. Int. Union Geod. Geophys. 1987-1990, Rev. Geophys.*, 29, 1028, 1991.

Menietti J. D., and J. L. Burch, DE 1 observations of theta aurora plasma source regions and Birkeland current charge carries, *J. Geophys. Res.* 92, 7503, 1987

Milan, S.E., T.K. Yeoman, M. Lester, E.C. Thomas, and T.B. Jones, Initial backscatter occurrence statistics from the CUTLASS HF radars, *Ann. Geophysicae*, 15, 703, 1997.

Milan, S. E., M. Lester, S. W. H. Cowley, and M. Brittnacher, Dayside convection and auroral morphology during an interval of northward interplanetary magnetic field, *Ann. Geophys.*, 18, 436, 2000.

Milan, S. E., Lester, M., Cowley, S. W. H., Oksavik, K., Brittnacher, M., Greenwald, R. A., Sofko, G., and Villain, J.-P.: Variations in polar cap area during two substorm cycles, *Ann. Geophysicae*, 21, 1121, 2003.

Milan, S. E., S. W. H. Cowley, M. Lester, D. M. Wright, J. A. Slavin, M. Fillinghim, C. W. Carlson, and H. J. Singer, Response of the magnetotail to changes in the open flux content of the magnetosphere, *J. Geophys. Res.*, 109, A04220, doi: 10.1029/2003JA010350, 2004a.

Milan, S. E., Dayside and nightside contributions to the cross polar cap potential: Placing an upper limit on a viscous-like interaction, *Ann. Geophys.*, 22,3771-3777, 2004b.

Milan, S. E., B. Hubert, and A. Grocott, Formation and motion of a transpolar arc in response to dayside and nightside reconnection, *J. Geophys. Res.*, 110, A01212, doi:1029/2004JA010835, 2005.

Mizera, P. F., D. J. Gorney, and D. S. Evans, On the conjugacy of the aurora: High and low latitudes. *Geophys. Res. Lett.* 14, 190, 1987.

Bibliography

Naehr, S. M., and F. R. Toffoletto, Quantitative modeling of the magnetic field configuration associated with the theta aurora, *J. Geophys. Res.*, 109, A07202, doi:10.1029/2003JA010191, 2004.

Newell, P. T.; Meng, Ching-I., Ion acceleration at the equatorward edge of the cusp - Low altitude observations of patchy merging, *Geophysical Research Letters* (ISSN 0094-8276), vol. 18, p. 1829-1832, 1991.

Nielsen, E., and K. Schlegel, A first comparison of STARE and EISCAT electron drift velocity measurements, *J. Geophys. Res.*, 90, 3495-3504, 1983.

Nielsen, E., W. Guttler, E.C. Thomas, C.P. Stewart, T.B. Jones, and A. Hedberg, SABRE: A new radar auroral backscatter experiment, *Nature*, 304, 712-714, 1983.

Nielsen, E., W. Guttler, E.C. Thomas, C.P. Stewart, T.B. Jones, and A. Hedberg, A new radar auroral backscatter experiment, *Nature*, 304, 712-714, 1983a.

Nielsen, E., J. D. Whitehead, L. A. Hedberg, and T.B. Jones, A test of the cosine relationship using three-radar velocity measurements, *Radio Sci.*, 18, 230, 1983b.

Nielsen, E., J. D. Craven, L. A. Frank, and R. A. Heelis, Ionospheric flows associated with a transpolar arc, *J. Geophys. Res.* 95, 21169, 1990.

Nishida, A. T. Mukai, T. Yamamoto, S. Kokubun, and K. Maezawa: A unified model of magnetotail convection in geomagnetically quiet and active times, *J. Geophys. Res.*, 103, 4409-4418, 1998.

Obara T., M. Kitayama, T. Mukai, N. Kaya, J. S. Murphree, L. L. Cogger, Simultaneous observations of sun-aligned polar cap arcs in both hemispheres by EXOS-C and Viking, *Geophys. Res. Lett.* 15, 713, 1988.

Obara T., T. Mukai, H. Hayakawa, A. Nishida, K. Tsuruda, S. Machida, and H. Fukunishi, Akebono (EXOS D) observations of small-scale electromagnetic signatures relating to polar cap precipitation, *J. Geophys. Res.* 98, 11153, 1993.

Øieroset, M., Raeder, J. Phan, T. D., Wing, S. Wing, J. P. McFadden, W. Li, M. Fujimoto, M. Reme, and A. Balogh: Global cooling and densification of the plasma sheet during an extended period of purely Northward IMF on October 22-24, 2003, *Geophys. Res. Lett.*, 32, L12S07, 2005.

Østgaard N., S. B. Mende, H. U. Frey, L. A. Frank, J. B. Sigwarth, Observations of non-conjugate theta aurora, *Geophys. Res. Lett.*, 30(21),2125, doi:10.1029/2003GL017914, 2003.

Parker. E. N., *J. Geophys. Res.* 62, 509, 1957.

Bibliography

Parker, E. N., Dynamics of the interplanetary gas and magnetic fields, *ApJ*, 128, 664, 1958.

Peterson, W. K., and E. G. Shelley, Origin of the plasma in a cross-polar cap auroral feature (theta aurora), *J. Geophys. Res.*, 89, 6729, 1984.

Phan, T. D., et al., (2003), Simultaneous Cluster and IMAGE observations of cusp reconnection and auroral proton spot for northward IMF, *Geophys. Res. Lett.*, 30(10), 1509, doi:10.1029/2003GL016885.

Rairden, R. L., and S. B. Mende, Properties of 6300-A auroral emission at south pole, *J. Geophys. Res.*, 94, 1402, 1989.

Reiff, P.H., R.W. Spiro, and T.W. Hill, Dependence of polar cap potential drop on interplanetary parameters, *J. Geophys. Res.*, 86, 7639, 1981.

Reiff, P.H., and J.L. Burch, IMF By-dependent plasma flow and Birkeland currents in the dayside magnetosphere 2: A global model for northward and southward IMF, *J. Geophys. Res.*, 90, 1595, 1985.

Rich, F. J., and M. Hairston, Large-scale convection patterns observed by DMSP, *J. Geophys. Res.*, 99, 3827-3844, 1994.

Richard, Robert L.; Walker, Raymond J.; Ashour-Abdalla, Maha, The population of the magnetosphere by solar winds ions when the interplanetary magnetic field is northward, *Geophysical Research Letters* (ISSN 0094-8276), vol. 21, no. 23, p. 2455-2458, 1994.

Richmond, A. D. and J. P. Thayer, Ionospheric Electrodynamics: A Tutorial, in *Magnetospheric Current Systems*, edited by S. Ohtani, R. Fujii, M. Hesse, and R. L. Lysak, Geophysical Monograph 118, *American Geophysical Union, Washington, D. C.*, pp, 131-146, 2000.

Ruohoniemi, J.M., and R.A. Greenwald, K.B. Baker, J.-P. Villain, and M.A. McCready, Drift motions of small-scale irregularities in the high-latitude F region: An experimental comparison with plasma drift motions, *J. Geophys. Res.*, 92, 4553-4564, 1987.

Ruohoniemi, J.M., R.A. Greenwald, O. de la Beaujardière, and M. Lester, The response of the high-latitude dayside ionosphere to a sudden southward IMF turning, *Ann. Geophysicae*, 11, 544, 1993.

Ruohoniemi, J.M., and K.B. Baker, Large-scale imaging of high-latitude convection with Super Dual Auroral Radar Network HF radar observations, *J.*

Bibliography

Geophys. Res., 103, 20, 797, 1998.

Ruohoniemi, J. M., and R. A. Greenwald, Dependencies of high-latitude plasma convection: Consideration of interplanetary magnetic field, seasonal, and universal time factors in statistical patterns, *J. Geophys. Res.* 110, A09 204, doi: 10.1029/2004JA010815, 2005.

Russell, C.T., The configuration of the magnetosphere, in *Critical Problems of Magnetospheric Physics*, Ed. E. R. Dyer, Inter-Union Committee on STP, National Academy of Sciences, Washington DC, 1, 1972.

Senior, C. J. –C. Cerisier, F. Rich, M. Lester, and G. K. Parks, Strong sunward propagation flow bursts in the night sector during quiet solar wind conditions, SuperDARN and satellite observations, *Ann. Geophys.*, 20, 771-779, 2002.

Siscoe, G. L. and Huang, T. S.: Polar cap inflation and deflation, *J. Geophys. Res.*, 90, 543-547, 1985.

Smith, C.W., Acuña, M. H., Burlaga, L. F., L'Heureux, J., Ness, N. F., and Scheifele, J.: The ACE Magnetic Fields Experiment, *Space Sci. Rev.*, 86, 613-632, 1998.

Sofko, G. J., R. Greenwald and W. Bristow, Direct determination of large-scale magnetospheric field-aligned currents with SuperDARN, *Geophys. Res. Lett.*, 22, 2041-2044, 1995.

Song, P., and C. T. Russell, Model of the formation of low-latitude boundary layer for strongly northward interplanetary magnetic field, *J. Geophys. Res.*, 97, 1411-1420, 1992.

Stone, E.C., A.M. Frandsen, R.A. Mewaldt, E.R. Christian, D. Margolies, J.F. Ormes, and F. Snow, The Advance Composition Explorer, *Space Sci. Rev.*, 86, 1, 1998.

Sugiura, M., T. Iyemori, R. A. Hoffman, N. C. Maynard, J. L. Burch, and J. D. Winningham, Relationships between field-aligned currents, electric fields, and particle precipitation as observed by Dynamics Explorer-2, in *Magnetospheric Currents*, Geophysical Monograph Series, vol. 28, edited by T. Potemra, pp. 96-103, American Geophysical Union, Washington, D. C., 1984.

Svalgaard, L., Polar cap magnetic variations and their relationship with the interplanetary magnetic sector structure, *J. Geophys. Res.*, 78, 2064-2078, 1973.

Sweet, P. A. In *Electromagnetic Phenomena in Cosmical Physics* (edited by B. LEHNERTC).a mbridge, University Press, London, 1958.

Bibliography

Todd, H., S.W.H. Cowley, M. Lockwood, D.M. Willis, and H. Lühr, Response time of the high-latitude dayside ionosphere to sudden changes in the north-south component of the IMF, *Planet. Space Sci.*, 36, 1415, 1988.

Valladares, C. E., and H. C. Carlson, The electrodynamics, thermal and energetic character of intense sun-aligned arcs in the polar cap, *J. Geophys. Res.*, 96, 1379, 1991.

Valladares, C. E., H. C. Carlson, and K. Fukui, Interplanetary magnetic field dependency of stable Sun-aligned polar cap arcs, *J. Geophys. Res.*, 99, 6247-6272, 1994.

Villain, J.-P., G. Caudal, and C. Hanuise, A SAFARI-EISCAT comparison between the velocity of F-region small-scale irregularities and the ion drift, *J. Geophys. Res.*, 90, 8433-8443, 1985.

Walker, A. D. M, M. Pinnock, K. B. Baker, J. R. Dudeney, and J. P. S. Rash, Strong flow bursts in the nightside ionosphere during extremely quiet solar wind conditions, *Geophys. Res. Lett.*, Vol. 25, No. 6, 881-884, 1998.

Watanabe, M., T. Iijima, and F. J. Rich, Synthesis models of dayside field-aligned currents for strong interplanetary magnetic field By, *J. Geophys. Res.*, 101, 13, 303, 1996.

Waters, C. L., B. J. Anderson, and K. Liou, Estimation of global field aligned currents using the Iridium System magnetometer data, *Geophys. Res. Lett.*, 28, 2165-2168, 2001.

Waters, C. L., B. J. Anderson, R. A. Greenwald, R. J. Barnes, and J. M. Ruohoniemi, High Latitude Poynting Flux From Combined Iridium and SuperDARN Data, *Ann. Geophys.*, 22, 2861-2875, 2004.

Weimer, D. R., Maps of ionospheric field-aligned currents as a function of the interplanetary magnetic field derived from dynamics Explorer 2 data, *J. Geophys. Res.*, 106, 12889-12902, 2001.

Yamauchi, M., R. Lundin, L. Eliasson, S. Ohtani, and J. H. Clemmons, Relationships between large-, meso-, and small-scale field-aligned currents and their current carriers, in *Polar Cap Boundary Phenomena*, edited by: J. Moen et al., 173-188, Kluwer Academic Publishers, Netherlands, 1998.

Zhu L., J. J. Sojka, R. W. Schunk, D. J. Crain, A time-dependent model of polar cap arcs, *J. Geophys. Res.* 98, 6139, 1993a.

Bibliography

Zhu, L., R. W. Schunk, and J. J. Sojka, Polar cap arcs: A review, *J. Atmos. Sol.-Terr. Phys.*, 59, 1087, 1997.

Zmuda, A. J., J. H. Martin, and F. T. Heuring, Transverse magnetic disturbances at 1100 km in the aurora region, *J. Geophys. Res.*, 71, 5033, 1966.